# CO2 SWEEP BASED ON GEOCHEMICAL, AND RESERVOIR CHARACTERIZATION OF THE RESIDUAL OIL ZONE OF HESS'S SEMINOLE SAN ANDRES UNIT

**Type of Report:** Final Scientific

**SUBMITTED UNDER FUNDING OPPORTUNITY ANNOUNCEMENT: DEFE0024375**

**Reporting Period Start Date: 12/01/2014**

**Reporting Period End Date: 11/30/2019**

**Submitted by:** The University of Texas at Austin, Jackson School of Geosciences, Bureau of Economic Geology, University Station, Box X Austin, Texas 78713

**Submitted to:** U.S. Department of Energy National Energy Technology Laboratory

**PRINCIPAL INVESTIGATOR**

Ian Duncan, Ph.D.
(512) 471-5117

ian.duncan@beg.utexas.edu

## Acknowledgement of Government Support and Government License

This work was generated with financial support from the U.S. Government through Contract/Award No. DE-FE0024375, and as such the U.S. Government retains a paid-up, nonexclusive, irrevocable, world-wide license to reproduce, prepare derivative works, distribute copies to the public, and display publicly, by or on behalf of the Government, this work in whole or in part, or otherwise use the work for Federal purposes.

# INTRODUCTION

The discovery of ROZ (residual oil zone) underlying and lateral to major oil fields in the Permian of Texas have provided the potential for sequestering very large volume of CO2. The purpose of this study is to understand the nature of ROZs in the context of CO2EOR and geosequestration. The study was the first to gather detailed information on ROZs. It also provides a detailed and comprehensive analysis of the role of ROZ compared to MPZ (main pay zones) in achieving long term CO2 storage. This study has a wide scope and the potential to guide to the impacts of geological storage on GHG in the atmosphere. This report was developed based on a series of published papers.

# CONCLUSIONS

This study has provided the understanding that allows accurate estimates of the $CO_2$ sequestration capacity of $CO_2$-EOR in ROZs. This required an understanding of the incidental storage based on many years of production history and computer reservoir simulation. This project completed a detailed characterization of the largest producing ROZ, Hess's Seminole San Andres Unit. The project used the detailed reservoir characterization of the field, to constrain reservoir simulations of multiphase fluid flow. These simulations were designed to evaluate strategies to increase CO2 storage as well as maximize oil production. A comprehensive reservoir characterization of Hess's Seminole San Andres Unit was based on core logging, petrography, and stratigraphic correlation of faces using core and wireline logging results. We have investigated what controls sweep efficiency in ROZ reservoirs. This efficiency has a large impact on both the effectiveness of oil recovery and the volume of CO2 that will be sequestered. To understand what can be done to improve sweep efficiency we have used this new reservoir model. We have developed for the ROZ to design sophisticated multiphase fluid flow simulations to test different injection strategies for the ROZ. These simulations have allowed us to identify the WAG ratio that maximizes sweep. We have also completed an economic analysis of flooding ROZ reservoirs, based on simulations of flooding and using a Net Present Value (NPV) criteria.

# SUMMARY

The study of the ROZ (residual oil zone) versus the MPZ (main pay zone) of the Seminole Field provided a unique insight into the nature of ROZ. This is because we had access to an order of magnitude of core available in other fields. We were also able to use an extensive petrophysical data base with one-foot sampling interval made available by the operator. We also obtained an extensive and unique data base containing the entire production history for the field at full resolution. The data set also includes a unique complete, highly-granular information on volumes of CO2 injection and CO2 production. We created a unique high-resolution model of the reservoir. This is the first such model that has been created. Using this very high-resolution data base we were able to make high resolution, multiphase fluid flow simulations. These fluid flow simulations have enabled our team to evaluate CO2 sweep in the ROZ in comparison with the MPZ.

## TABLE OF CONTENTS

## EXECUTIVE SUMMARY

ROZs (residual oil zones) have the potential for very large-scale CO2 sequestration and will likely play a major role in CCUS (carbon capture utilization and storage). Although significant DOE funding has gone into ROZ investigations little if any quantitative information have been made available on the geology, mineralogy, and geochemistry (particularly diagenesis and isotope geochemistry).

The study of the ROZ (residual oil zone) versus the MPZ (main pay zone) of the Seminole Field provided a unique insight into the nature of ROZ. This is because we had access to an order of magnitude of core available in other fields. We were also able to use an extensive petrophysical data base with one-foot sampling interval made available by the operator. We also obtained an extensive and unique data base containing the entire production history for the field at full resolution. The data set also includes a unique complete, highly-granular information on volumes of CO2 injection and CO2 production. We created a unique high-resolution model of the reservoir. This is the first such model that has been created. Using this very high-resolution data base we were able to make high resolution, multiphase fluid flow simulations. These fluid flow simulations have enabled our team to evaluate CO2 sweep in the ROZ in comparison with the MPZ.

## Section 1 Nature of ROZs

A residual oil zone (ROZ) is characterized by oil saturations close to residual values, similar to those found at the termination of waterflooding. It has been proposed that ROZs are formed from an original oil saturated or main pay zone (MPZ) that has been flushed by a regional aquifer ("natural waterflooding" (NWF)) over geological time scales. An alternative model for the origin of ROZ as the result of capillary trapping along oil migration pathways. This type of oil zone is widely distributed in the Permian basin, West Texas

Steve Melzer of Melzer Consulting and Trentham of the Geology Department of the University of Texas Permian Basin (together with their co-authors Koperna, Kruuska, Hill, Hovorka and others), have pioneered the study of ROZs and generated significant interest from the DOE.

These researchers have had a significant impact on interest in ROZs in the context of oil production and CO2 sequestration.

Naturally occurring ROZs in carbonate reservoirs in the Permian Basin of Texas were initially interpreted from wireline logs as being productive oil zones. However, if these zones were subjected to drill stem tests or were completed for production, they produced water, occasionally with minor oil. Given that by definition that the ROZ will only produce water through primary or secondary (waterflood) production, the fields that are currently producing from the ROZ use CO2 injection.

Residual oil zones (ROZs) are characterized by oil volumes near to residual saturation, underlying (brown field) and lateral (greenfield) to oil reservoirs. The oil in the ROZ is largely immobile (at or near irreducible saturation) and cannot be produced by primary or secondary recovery means.

ROZs have been defined by Sue Hovorka in 2014, as a reservoir volume of “significant scale”, that has accumulated oil that was later naturally displaced [presumably by aquifer flow], leaving “behind a low, largely immobile remaining oil saturation”. Hovorka suggests that “ROZs are predictable at the regional scale according to the principles of buoyancy and hydrodynamics”.

Melzer described three types of ROZs, each begins with an MPZ that subsequent to trapping is impacted by the structural and hydrodynamic history of an area: ROZ Type 1. Regional tilt of a basin; ROZ Type 2. Breach of the reservoir seal with secondary healing; and ROZ Type 3. Changed hydrodynamic conditions within the underlying aquifer. Type 1 and Type 3 ROZs are characterized by OWCs that are tilted. Such tilted OWCs can be developed in response larger pressure on one side of the structure. If there is a significant increase the water velocity of the original MPZ it becomes naturally water flooded forming a ROZ. it has been suggested that in the Permian Basin the direction of tilted OWC form a coherent pattern across the San Andres reservoirs in the north CBP and NWS

A Type 1 ROZ occurs when an existing hydrocarbon accumulation in a structural or stratigraphic trap is subjected to a regional (tectonically induced) tilt. Type 1 ROZ is related to a gravity-dominated shift of the oil water contact (OWC).

The origin of ROZs is controversial however their significance to CCUS is becoming well characterized, with computer simulation and ongoing production over that last two decades. The Permian Basin is the largest area with CCUS projects focused on ROZ. Several operators are flooding this resource, exclusively now through the use of CO2 injection. Currently, there are twelve commercial and field pilots in the west Texas Permian Basin region exploiting CO2-EOR technology to target this oil.

## Section 2: CO2 Sweep in ROZ

The volumetric sweep efficiency is the pore volume swept (or contacted by injected by CO2) typically normed by the total pore volume. The macroscopic sweep efficiency is that portion of the reservoir volume swept by CO2. The macroscopic sweep efficiency for CO2 WAG injection, is in large part controlled by the reservoir's heterogeneity. The key heterogeneity is in the petrophysical properties such as porosity and permeability. Poor sweep efficiency is associate with high residual-water-saturation that may degrade reservoir-performance. A systematic approach to improved sweep-efficiency is lacking.

The sweep-efficiency of a segment of a reservoir, in some cases can be engineered to improve the sweep. For example, surfactants can be used to lower the interfacial tension between CO2 and water and as a result improve displacement efficiency of oil may be increased. For example, WAG (water alternating gas) lowers the propency of CO2 to focus flow dominantly in high permeability. In the current study we conducted multi-phase computer simulations of WAG to examine the difference in sweep between the ROZ and MPC.

Improvement in sweep efficiencies have been observed in vertical displacement experiments as the capillary number $C_n$ increases. The capillary number characterizes the ratio of viscous forces to interfacial tension forces. CO2 flooding is often characterized by poor volumetric-sweep-efficiency, a result of the high CO2 mobility and formation heterogeneity. The volumetric, macro sweep-efficiency also is dependent on the injection pattern used, nature of reservoir fracturing, location of gas-oil and oil-water contacts, reservoir thickness, mobility ratio, and the density difference between the displacing and displaced fluid. However, this definition of Cn is an oversimplification as the ratio of viscous and capillary force is scale-dependent. As a result, predicting the role of volumetric sweep efficiency on oil production for specific reservoirs requires multiphase flow simulations.

Two key metrics for WAG-injection are “WAG ratios” and “CO2 half-cycle sizes”. WAG injections are characterized by the ratio of volumes of water slugs to CO2 slugs utilized. Experimental studies of oil saturated sand packs concluded that WAG ratios for CO2 of 1 maximize oil production. The same result was obtained from simulations of real reservoirs. Also, most of the most common reported WAG ratio in fields are around 1.0.

The optimization of this process has been studied extensively in the past. It has been observed that the optimum slug sizes are 0:1 (continuous slug process) and 1:1 for tertiary oil recovery by CO2 injection for water-wet and oil-wet systems, respectively. They noted that maximum recovery is a stronger function of slug size in secondary CO2 flood than in tertiary flooding. Tertiary floods in the water-wet models were dominated by gravity forces while tertiary floods in an oil-wet medium were controlled by viscous fingering.

If the maximizing oil production is desired, the WAG ratios resulting in the minimum- retention fractions should be implemented. In contrast continuous CO2 injection that corresponds to a WAG ratio of zero. In this case Ren and Duncan have shown that in this case the fraction of CO2 retained can be nearly 70% of injected CO2. The sizes of CO2 half-cycle sizes are best characterized in terms of the %HCPV (hydrocarbon pore volumes). %HCPV is a proxy for time scaled to the nature of the reservoirs. In a mature CCUS project, WAG injections, recycling of over half of the CO2 may be achieved.

In reservoirs that are very heterogeneous, continuous $CO_2$ flooding displaces less of the OOIP, with oil in low permeability layers not being produced as a result of the high $CO_2$ mobility. The effect of wettability on the performance of WAG is crucial, especially at high WAG ratios. High WAG ratios result in less oil recovery by extraction. In water-wet rocks, this effect is significant and no extraction at high WAG ratios is observed. In mixed-wet rocks, however, significant oil recovery is obtained due to extraction regardless of WAG ratio. In the case of oil-$CO_2$ miscibility, the IFT of oil–CO2 becomes zero obviously less than the oil-water IFT, resulting in more effective mobilization of oil trapped oil pores with complex geometries, resulting in an increase of oil recovery.

It was discovered that WAG had the effect of temporarily blocking CO2 from flowing through high permeability/porosity. This has the effect of forcing the CO2 to contact more of the volume of the reservoir. WAG injection results in increasing the effectiveness of displacement by $CO_2$ and improved sweep efficiency of water. In WAG injections, a result of alternating slugs of $CO_2$ and water, is the reduction of viscous instability and an increase in the effectiveness of oil production. WAG has been used by most operators to increase overall oil recovery,

Two $CO_2$ /WAG injection rate patterns were distinguished by in the SACROC field as either WAG-sensitive or WAG insensitive. It has been noted that WAG-sensitive portions of the reservoir were characterized by injectivity losses for $CO_2$, sometimes on the order of 80%. They suggested that the WAG-insensitive patterns were characterized by fracture flow rather than by flow in the matrix. Their study of SACROC showed that over time, the injectivity of $CO_2$ mostly returned to the initial levels before WAG was initiated. The analysis of concluded WAG-insensitive patterns was characterized by fracture flow not matrix flow. Their simulations, in the context of injection and production rates (for the SACROC field) suggest that WAG injections with “longer $CO_2$ cycles and shorter water cycles improved the injectivity and pattern production”.

The WAG process, is the mobility control strategy of choice for injection $CO_2$. Despite its popularity, limited fluid phase simulations, have been published in journals with history matching, detailed static reservoir models, and well-based injection and production data. In water-wet reservoirs, it has been argued that the oil recovery for $CO_2$–WAG scenarios is lower when the injection pressure is less than the MMP (minimum miscibility pressure) and the spreading coefficient is negative. The bypassed oil in the reservoir in these circumstances will have the smallest contacted surface area per volume. Current research is focused on such thing as manipulating the system to enhance the surface area contacted. For example, using a pre-flush of $CO_2$ saturated reservoir water can impact the interfacial tensions (IFT) between the reservoir fluids and the spreading coefficient. A pre-flush of $CO_2$-saturated water can result of changing the spreading coefficient from negative to positive. As a result (In a water-wet reservoir), this increases surface contact area between the $CO_2$ and oil, improving oil production. It has been suggested that WAG injection increases the storage on CO2 in the reservoir relative to continuous $CO_2$ injection. This conclusion is not supported by our simulations.

The effectiveness of $CO_2$ injection as EOR is in part a function of the sweep efficiency. The mobility ratio, is a metric for the factors influencing the volumetric sweep. This ratio for injected $CO_2$ predicts a poor sweep, because of the low viscosity of the gas relative to that of the oil. Both the microscopic and macroscopic sweep efficiencies are important metrics.

Macroscopic heterogeneity determines the parts of the reservoir swept by the $CO_2$. The macroscopic efficiency is driven in part by the density contrast between the water, oil and $CO_2$ phases as well as the heterogeneity of the reservoir. In highly heterogenous reservoirs, in zones undergoing high permeability water flooding, has effective volumetric sweep that results in low residual oil saturations.

Improved microscopic displacement efficiency is typically related to changes in capillary number. The capillary number (Nc), is based on the ratio of viscous to capillary forces. The factors controlling microscopic sweep are complex, including the interfacial tensions, dynamic fluid-fluid and fluid mineral contact angles, the shape of pores and their wettability. As a result, surface tension, viscosity, and wettability may be the only properties that can be manipulated to increase oil recovery through increased microscopic displacement. These issues can be included in the design of the WAG injection.

Storage of $CO_2$ in depleted oil reservoirs has the advantage that they are typically are well characterized. Currently there are over 100 $CO_2$-EOR projects most in Texas. The first commercial scale $CO_2$-EOR project was at the Kelly Snyder field (now known as SACROC) began in 1972 in West Texas. Hence, $CO_2$-EOR technology has been used as CCUS for five decades. The initial SACROC $CO_2$ floods were carried out with anthropogenic $CO_2$ captured from a natural gas field.

We conducted flow simulations of $CO_2$ injection into both synthetic and realistic geologic reservoirs to find the optimal injection strategies for several scenarios. These simulations of $CO_2$ injection follow either man-made waterflooding or long-term natural waterflooding. We examined the effects of $CO_2$ injection rates, well patterns, reservoir heterogeneity, and permeability anisotropy, on optimal WAG ratios. Optimal is defined as being at minimal net $CO_2$ utilization ratios or maximal oil production rates.

Simulations of $CO_2$ EOR show that the optimal WAG ratio (the ratio of injected water and $CO_2$, in reservoir volumes) for the ROZs is less than 1, and it depends, but in qualitatively different ways, upon the well pattern and reservoir heterogeneity. The optimal WAG ratio tends to increase with changing from inverted 9-spot (80-acres) to inverted 5-spot (40-acre) or increasing reservoir heterogeneity. The ratios for ROZs are consistently less than those observed in the same geologic models experiencing $CO_2$ injection after traditional (man-made) waterflooding. This is because the water saturation caused by slow regional aquifer flow (~1ft/yr) differs from that created by traditional waterflooding. In ROZs, water prevails almost everywhere and thus it is less needed to ease $CO_2$ channeling as compared to MPZs.

This work demonstrates that optimal WAG ratios for oil production in ROZs are different from those in traditional MPZs because of oil saturation differences. Thus, commingled $CO_2$ injection into both zones or directly copying WAG injection designs from MPZs to ROZs might not maximize oil production.

Our simulation results show that the $CO_2$ net utilization ratios for the WAG after NWF found in the current study are larger than those for the WAG after MMWF. The large differences found are apparently the result of the relative magnitudes of initial oil saturation at the beginning of WAG injection. The utilization ratios for both types of WAG (after NWF versus after MMWF) are dependent on the WAG ratios, reservoir heterogeneity, and well patterns, but with different trends and extents. In the case of WAG following NWF, there is a WAG ratio (approximately 1.0) that yields the lowest net utilization ratios, irrespective of the well pattern. However, for WAG following MMWF, the net utilization ratio monotonically decreases with the WAG ratio. The different trend is essentially because of the oil saturation magnitudes at the beginning of WAG injection.

Reservoir heterogeneity does not alter the trends described above, however it leads to different net utilization ratios. Heterogeneity influences net utilization ratios in different ways for the cases of WAG following NWF versus following MMWF. The presence of heterogeneity results in larger utilization ratios relative to homogeneous reservoirs, for WAG following NWF. This is not the case for WAG following MMWF. Simulated production data indicates that heterogeneity for the WAG after NWF results in the rate of increasing production of $CO_2$ being less than the rate at which oil production decreases. This results in higher net utilization ratios for the heterogeneous case compared to the homogeneous one.

Several conclusions can be drawn based on our work on simulations:

- Capillary pressure influences remaining oil saturation more significantly for NWF than for MMWF. Small aquifer rates for the geologically-lasting NWF enhances capillary spreading and thus cancels the effect of heterogeneity in sweep. This reduces oil saturation to be close to residual levels in every portion of ROZs.

- WAG ratios for either minimizing net utilization ratios or maximizing averaged oil production rates) for virgin ROZs are consistently smaller than those for MPZs after MMWF. This is because of the prevalent high-water saturation (and low oil saturation) in the ROZs.

- The optimal WAG ratio (at the minimal net utilization ratio) increases when: (i) increasing initial oil saturation (before WAG); (ii) the ratio of $k_v/k_h$ increases; and (iii) the well pattern changes from inverted 9-spot to inverted 5-spot.

- The $CO_2$ net utilization ratios during $CO_2$ WAG injection for virgin ROZs are about 2-3 times larger than those for MPZs after MMWF. The utilization ratios depend on well patterns, reservoir heterogeneity, and WAG ratios.

- Both averaged oil production rates and oil recovery factors for the WAG in virgin ROZs are around ¼-¾ of those for the WAG in the MPZs after MMWF.

The results of this study are important for designing injection strategies for WAG in stacked MPZ and ROZ reservoirs. Four main trapping mechanisms for CO2 are typically recognized: structural/ stratigraphic trapping; residual trapping of CO2; solubility trapping; and mineral trapping:

1. Geological trapping is based on either structural or stratigraphic traps. Structural traps are formed by folding, in some cases combined with faulting of a seal (a non-permeable rock forming a capillary barrier to flow. Stratigraphic traps are formed by the overlapping of

relatively high porosity/permeability reservoir facies and low permeability seal facies. Local and regional unconformities are also form common geologic configuration for stratigraphic traps.

2. Residual trapping: Injection of $CO_2$, flushes a portion of the oil and water in the reservoir's pores. Of this volume of $CO_2$ is in part split into many micrometer-sized bubbles so that only a portion of the CO2 is mobile, the rest is immobilized by fixing in pores due to capillary forces. This process is known as residual trapping and thus presumably an effective mechanism for long-term storage. Voidage-trapping for $CO_2$ storage in oil reservoirs, is often referred to as voidage-replacement. In this case, injected-CO2 occupies the pore-volume that oil and water have been displaced from.
3. Solubility trapping is based on the dissolution of CO2 into formation fluids. Following the dissolution in the reservoir fluid their physical properties change. For example, dissolution of CO2 into oil results in it swelling as a very small molecule (CO2) dissolves into a fluid (oil), dominated by long chain hydrocarbon polymers. This results in oil that becomes lower in density (buoyancy) and viscosity. It also impacts the oil IFT. A significant portion of CO2 dissolves in the oil in the reservoir but is capillary trapped and thus not produced. CO2 solubility in a water phase is a function of pressure. temperature, and salinity. CO2 dissolution in the water phase results in lower pHs and a resultant increase in the solubility of some minerals.
4. Mineral trapping involves chemical reaction between injected CO2 and reservoir minerals that results in very long-term immobilization by the formation of carbonate minerals.

These trapping mechanisms reduce the portion of $CO_2$ that is mobile and that can potentially leak from a reservoir. By storing oil that has become a single phase via dissolution the relative volume of structurally trapped gas is decreased resulting in a reduced likelihood of leakage. The volume of mobile $CO_2$ varies within and between reservoirs. It depends on factors such as the solubility of $CO_2$ in the oil and the reservoir water, the wettability of the pore surface, and the interfacial tension (IFT) between the oil and $CO_2$, at pressures above the MMP. Solubility trapping in oil increases over time with a rate, during post injection periods, depending on the diffusion rate; the dimensions of oil in pore spaces; and convection. A strong aquifer at the base of a reservoir can carry away $CO_2$ dissolved in water resulting in further dissolution of $CO_2$ into the water leg of the field. WAG injection significantly increases the sweep efficiency and as a result increases $CO_2$ trapping.

We evaluate different development strategies and their associated uncertainties through integrated full-physics flow simulation and economic assessment for a San Andres Unit Brownfield residual oil zone. The assessment is based on a high-resolution geological model with integrated geological and reservoir characterization and careful calibration through historical primary and secondary production data matches.

To better compare development strategies, we defined and calculated a series of metrics (e.g., cumulative oil production, $CO_2$ storage amount, $CO_2$ retention fraction, and net present value (NPV)) for $CO_2$ EOR and storage. Water alternating gas (WAG) ratios were tuned to maximize either oil production or NPV. The influence of economic parameters (e.g., oil price and carbon credit) on favorable WAG ratios were examined. We found that:

i) Simultaneous WAG injection into both the MPZ and ROZ maximizes oil production and NPV, as compared to other injection strategies.
ii) The NPV is more sensitive to the WAG ratio when co-developing the ROZ and MPZ than in MPZ-only flooding.
iii) When targeting $CO_2$ storage, switching from comingled injection to only ROZ injection after two decades of production is a viable strategy. The optimal switching time needs further study.
iv) As the $CO_2$ tax credit varies, the best WAG ratios to maximize NPV change to balance benefits from oil production and carbon storage.

This work provides a basis for future optimization of $CO_2$ EOR and storage in brownfield ROZs.

For six field-scale CO2 floods that the more CO2 is injected, the less is retained. For example, for the Means Unit when 20% of the pore volume was injected, about 15% of the pore volume of CO2 has been retained. Under ideal circumstances, the amount of CO2 retained or trapped by subsequent water injection should approximately be equal to the residual oil saturation to waterflooding. Note the difference between the different CO2 storage patterns between the Horse Shoe Atoll fields (SACROC and Salt Creek) and the Central Basic Platform and North West Shelf (Wasson, Means, Seminole, Goldsmith, Hanford etc.)

## Section 3: Geology and Geochemistry

An understanding of the impact of diagenesis on San Andres ROZ reservoirs is important for both understanding the heterogeneity of porosity and permeability at the reservoir scale and assessing/predicting the differences in oil productivity between ROZ and MPZ reservoirs.

One aim of our study was to investigate the diagenetic characteristics of the San Andres Formation (focusing on the ROZ) to elucidate the factors that control the reservoir quality and sweep. The current project is the first study of ROZs within the San Andreas based on studies of extensive cores, wireline logs, and petrophysical data. We document the petrography of the dolomite and anhydrite textures and attempt to quantify the conditions under they were formed, (2) the origin and evolution of the paleo-waters that modified the San Andres carbonates inferred from the isotopic geochemistry, and (3) the sequence and timing of diagenetic events that these deposits have subsequently undergone.

In this study, 130 thin sections were prepared from 5 cores of wells SSAU #2714, SSAU #2921, SSAU #3903R, SSAU #5309, and SSAU #5505R. These thin sections were impregnated with blue dye to highlight megapores (>~10 µm) and with blue-fluorescent dye to highlight micropores (<~10 µm). For the petrographic observations the thin sections were examined by transmitted-light microscopy and cathodoluminescence microscopy (optical-CL) using a Reliotron III Cathodoluminescence attachment operated at 10-18 kV gun potential and 0.5-0.6 V beam current.

Textural characteristics of dolomites and diagenetic cements were investigated using a Zeiss Sigma High Vacuum Field Emission scanning electron microscope (HV FE-SEM) at the Bureau of Economic Geology, The University of Texas at Austin. Carbon-coated samples (~15 µm) were imaged under SEM-CL with a Gatan MonoCL4 detector operated at 5 kV and 120 µm aperture. Elemental analysis were analyzed by energy dispersive x-ray spectroscopy (EDS).

Powder samples (~30-50 mg per single sample) of dolostone were extracted for carbon and oxygen isotope measurements. The powered samples were heated to remove organic materials and then reacted with anhydrous phosphoric acid, under vacuum, to release $CO_2$ at 50°C for 24 hours. The $CO_2$ was then analyzed for carbon and oxygen isotopes on a Finnigan MAT251 mass spectrometer standardized with NBS-18. All carbon and oxygen data are reported in ‰ units relative to the Vienna Pee Dee Belemnite (VPDB) standard. The precision for both $\delta^{13}C$ and $\delta^{18}O$ measurements is better than ±0.1‰.

Eight dolomite and six anhydrite samples were leached in 0.2 M ammonium acetate with a pH of 8 prior to acid digestion for Sr isotopic analysis. Dolomite in 8% acetic acid for 15 minutes and anhydrite Sr was separated in 3M $HNO_3$ using Eichrom Sr Specific resin in 70 ul columns. Total procedure blank for Sr samples was l<30 pg. Sr samples were loaded onto single Re filaments with tantalum fluoride and 0.05M phosphoric acid and subsequently analyzed on a ThermoFisher Triton thermal ionization mass spectrometer in static mode. Intensity of $^{88}Sr$ of 8 V (using $10^{-11}$ Ohm resistors) ± 5 % was maintained for 8 blocks of 20 cycles with 8 second integration time. The $^{87}Sr/^{86}Sr$ ratio was corrected for mass fractionation using $^{88}Sr/^{86}Sr = 8.375209$ and an exponential law.

Two types of dolomite and two types of dolomitic sediments are distinguished based on crystal size and geometry (Sibley and Gregg, 1987). Type-1 dolomites (Dol-1 in Figure 3a) consists on a very finely crystalline brownish dolomite, non-planar and anhedral dolomite crystals, up to 10 μm in size, typically showing red, dull, luminescence (Figure 3b and 3c). Under SEM-CL the crystals are relatively homogeneous, dark gray in color. This type of dolomite appears within the skeletal components and thus is dominant in dolo-wackestones, dolo-packstones, and skeletal-peloid-bryozoan dolo-baffelstone/dolo-rudstone (microfacies b, c and d). Type-2 dolomite (Dol-2 in

Figure 4a), is constituted by medium to coarse crystalline, planar-s and subhedral-dolomite crystals, ranging from 50 to 200 µm in size, and showing red bright luminescence (Figure 4 a-c). This dolomite shows relatively lighter (white) CL color. This type of dolomite appears in all microfacies.

Dolomite sediment-1 is made up red bright luminescent anhedral dolomite crystals, 25-150 µm in size. The sediment has yellow color and is abundant in packstones, grainstones and wackestones (microfacies b, c and f).

Dolomite sediment-2 consist of white-brownish sediment made up of dull red luminescent anhedral dolomite crystals, <10 µm in size, partially filling the moldic porosity. The sediment includes reworked dolomite crystals, medium crystalline (up to 75 µm in size). Under the SEM-CL, the fined grained sediment is dark luminescent whereas the reworked dolomite crystals are light (white) color. This dolomite sediment is very common within microfacies b and c.

Sulfate cemented dolomite reservoir rocks in Seminole San Andres Unit (SSAU) in Central Basin platform have been widely studied for decades due to the importance of these reservoirs to oil production in one for the great petroleum provinces. Understanding the role of diagenesis in controlling the porosity and permeability of these reservoirs has proved a challenge. With the recent surge in development of residual oil zones, occurring at the base of many (perhaps all) of these reservoirs there have been and increased interest in the factors controlling porosity and permeability distribution in these San Andreas reservoirs.

Melzer has suggested that sweeping low salinity water through the lower parts of the reservoir resulting Type III ROZs. He sees the results as late-stage, “pervasive dolomitization with enhanced porosities and permeabilities”. He also suggests anaerobic processes are responsible for the release off sulfur as $H_2S$. He suggested that $H_2S$ results souring of the oil and gas, as well as alteration of disseminated anhydrite to calcite. He also asserted that aquifer “flushing” converts the calcite to dolomite via abiotic chemical reactions such as $CaCO_3 + Mg\ (aq) = 1/2MgCa(CO_3\ )$ and that biogenic (microbial mediated) chemical reactions consume hydrocarbons and produce native sulfur such as $CaSO_4 + HC = CaCO_3 + H_2O + S$ (Melzer, 2012). He suggests that this “late stage pervasive dolomitization” results in enhanced porosities and permeabilities.

Trentham and Melzer have suggested that the common characteristics of ROZs in the Permian Basin are:

(1) Enhanced porosity and permeability, resulting from diagenesis of the carbonate reservoir rocks, specifically dissolution of anhydrites

(2) “What is typically referred to as sulfur water” in contrast to higher salinity “connate water” in the main pay zone.

(3) Porosities and permeability’s slightly higher than in the main pay zone, which he ascribes to an “overlay of late (sweep stage) dolomitization”

(4) The occurrence of native sulfur associated with anhydrite nodules. Melzer (2013) asserted that another characteristic of the diagenesis on ROZs is the presence of native sulfur. He further asserts that sulfate reducing bacteria mediate “anhydrite dissolution and the precipitation of sulfur”.

It has been asserted that porosities and permeabilities can be higher in the ROZ than in the main pay zone as a result of the meteoric dissolution due to pervasive “late” dolomitization caused by sweep of meteoric aquifers.

Assuming that dolomite formation is occurring in shallow conditions where the initial dolomite is characterized by carbon and oxygen stable isotopes that were consistent with formation from evaporated Permian (Guadalupian) sea water. Such brines were the dolomitizing fluids. Gypsum apparently precipitated during the main dolomitization event. At a later stage anhydrite formed replacement nodules and cement.

The assertion that dolomitic reservoirs in ROZs underlying dolomitic MPZs are chemically modified and recrystallized is not supported by any mineralogical, chemical, or isotopic data. This data demonstrates that there are no changes in the mineralogical, chemical or isotopic data between the MPZ and the ROZ of the Seminole field. This field (known as the gold standard of

ROZs) is the only ROZ that has been quantitively studied. None of the four characteristics of ROZs enumerated above are found in the Seminole Field. This undermines their model for the genesis of ROZs. Hovorka's assertion that "Oils in ROZs and main reservoir zones of the Permian Basin are known to be biodegraded as a result of interaction with inflowing meteoric waters" is not supported by any evidence.

## Section 4: Overall Conclusions

This study has provided the understanding that allows accurate estimates of the $CO_2$ sequestration capacity of $CO_2$-EOR in ROZs. This required an understanding of the incidental storage based on many years of production history and computer reservoir simulation. This project completed a detailed characterization of the largest producing ROZ, Hess's Seminole San Andres Unit. The project used the detailed reservoir characterization of the field, to constrain reservoir simulations of multiphase fluid flow. These simulations were designed to evaluate strategies to increase CO2 storage as well as maximize oil production. A comprehensive reservoir characterization of Hess's Seminole San Andres Unit was based on core logging, petrography, and stratigraphic correlation of faces using core and wireline logging results. We have investigated what controls sweep efficiency in ROZ reservoirs. This efficiency has a large impact on both the effectiveness of oil recovery and the volume of CO2 that will be sequestered. To understand what can be done to improve sweep efficiency we have used this new reservoir model. We have developed for the ROZ to design sophisticated multiphase fluid flow simulations to test different injection strategies for the ROZ. These simulations have allowed us to identify the WAG ratio that maximizes sweep. We have also completed an economic analysis of flooding ROZ reservoirs, based on simulations of flooding and using a Net Present Value (NPV) criteria.

Several conclusions can be drawn based on our work on simulations:

- Capillary pressure influences remaining oil saturation more significantly for NWF than for MMWF. Small aquifer rates for the geologically-lasting NWF enhances capillary spreading and thus cancels the effect of heterogeneity in sweep. This reduces oil saturation to be close to residual levels in every portion of ROZs.

- WAG ratios for either minimizing net utilization ratios or maximizing averaged oil production rates) for virgin ROZs are consistently smaller than those for MPZs after MMWF. This is because of the prevalent high-water saturation (and low oil saturation) in the ROZs.
- The optimal WAG ratio (at the minimal net utilization ratio) increases when: (i) increasing initial oil saturation (before WAG); (ii) the ratio of $k_v/k_h$ increases; and (iii) the well pattern changes from inverted 9-spot to inverted 5-spot.
- The $CO_2$ net utilization ratios during $CO_2$ WAG injection for virgin ROZs are about 2-3 times larger than those for MPZs after MMWF. The utilization ratios depend on well patterns, reservoir heterogeneity, and WAG ratios.
- Both averaged oil production rates and oil recovery factors for the WAG in virgin ROZs are around ¼-¾ of those for the WAG in the MPZs after MMWF.

Assuming that dolomite formation is occurring in shallow conditions where the initial dolomite is characterized by carbon and oxygen stable isotopes that were consistent with formation from evaporated Permian (Guadalupian) sea water. Such brines were the dolomitizing fluids. Gypsum apparently precipitated during the main dolomitization event. At a later stage anhydrite formed replacement nodules and cement.

The assertion that dolomitic reservoirs in ROZs underlying dolomitic MPZs are chemically modified and recrystallized is not supported by any mineralogical, chemical, or isotopic data. This data demonstrates that there are no changes in the mineralogical, chemical or isotopic data between the MPZ and the ROZ of the Seminole field. This field (known as the gold standard of ROZs) is the only ROZ that has been quantitively studied. None of the four characteristics of ROZs enumerated above are found in the Seminole Field. This undermines their model for the genesis of ROZs. Hovorka’s assertion that “Oils in ROZs and main reservoir zones of the Permian Basin are known to be biodegraded as a result of interaction with inflowing meteoric waters” is not supported by any evidence.

# APPENDIX: PAPERS FROM THE PROJECT

# 1 Maximizing oil production from water alternating gas (CO2) injection into residual oil zones: The impact of oil saturation and heterogeneity

Bo Ren, Ian J. Duncan*

*Bureau of Economic Geology, The Jackson School of Geosciences, The University of Texas at Austin, Austin, TX, USA*

ARTICLE INFO

*Article history:*
Received 4 June 2020
Received in revised form
12 January 2021
Accepted 15 January 2021
Available online 20 January 2021

*Keywords:*
Residual oil zone
Oil saturation
Reservoir heterogeneity
$CO_2$-EOR
Water alternating gas

ABSTRACT

Residual oil zones (ROZs) are widespread reservoirs, characterized by oil at residual saturation, either underlying oil fields (brownfield) or lateral (greenfield) to such fields. These reservoirs have the potential to produce volumes of oil sufficiently significant to make appreciable impacts on the US's oil reserves and associated incidental $CO_2$ sequestration. The objective of this study is to improve our understanding the impact of heterogeneous and low oil saturations, in brownfield ROZs, on the effectiveness of water alternating gas (WAG) injection strategies. ROZs occur in the Permian Basin and elsewhere, and operators are using $CO_2$ injection for enhanced oil recovery (EOR) in these zones. The consensus model for the formation of ROZs is that they were formed by the effect of faster regional aquifer flow, acting over millions of years. Both the magnitude of oil saturation and the spatial distribution of oil differ from water-flooded main pay zones (MPZs). To explore the most effective injection strategies, we conducted simulations of $CO_2$ injection into synthetic geologic reservoirs. These simulations focused on injection into reservoirs subject to either man-made waterflooding or long-term natural waterflooding. By exploring the impact of varying: oil saturation; well patterns; reservoir heterogeneity; and permeability anisotropy, we attempt to quantify the factors that most influence the effectiveness of WAG injection. WAG ratios (the ratio of injected water and $CO_2$, in reservoir volumes) of interest are those that either minimize the net $CO_2$ utilization ratios or maximize oil production rates. In general, the most effective WAG ratios for ROZs, are consistently less than those observed undergoing $CO_2$ injection in the same geologic reservoir models after traditional (man-made) waterflooding. This work demonstrates that most favorable WAG ratios for oil production in ROZs are different from those in traditional MPZs because of oil saturation differences. Thus, $CO_2$ injection into both zones or directly copying WAG injection designs from MPZs to ROZs might not maximize oil production.

## 1. Introduction

Residual oil zones (ROZs) are widespread reservoirs, characterized by oil close to residual saturation, underlying (brown field) and lateral (greenfield) to oil reservoirs [1]. The oil resource in ROZs is not yet well characterized but is almost certainly substantial. For example, the volume of oil in-place in the ROZs of the San Andres formation within a twelve county in the Permian Basin of Texas and New Mexico has been estimated as 191 billion barrels with 42 billion barrels of oil underlying existing oil fields [2]. Very little information has been published on ROZ reservoirs. Any information or modeling that is published, will be novel and potentially important in understanding ROZ reservoirs. A key question is are ROZs essentially the same in their geology, petrophysical properties, and production potential as the main pay zones (MPZs) after waterflooding.

It has been proposed that ROZs are formed from an original oil-saturated MPZ that has been flushed by a regional aquifer ("natural waterflooding" or NWF) over geological time scales. The previously proposed mechanisms for the formation of ROZs result in the oil content coming to a quasi-equilibrium with water flows on a time scale of thousands of years. Such quasi-equilibrium values will effectively be the residual oil saturation [1,3,4]. An alternative model for the origin of ROZs as the result of capillary trapping along oil migration pathways [5]. It has been asserted that ROZs are characterized by oil saturations close to those found at the termination of waterflooding [4,6]. However, there is little if any high-quality data that supports this. In reality waterfloods are

---

* Corresponding author.
*E-mail address:* ian.duncan@beg.utexas.edu (I.J. Duncan).

https://doi.org/10.1016/j.energy.2021.119915
0360-5442/

terminated for economic reasons not because they reduce the oil content to the level of residual saturation. When $CO_2$-EOR is planned for a reservoir, waterflooding may be terminated earlier than economic cutoff.

Despite the significant potential of both ROZs and MPZs for oil production and incidental $CO_2$ storage the differences between the two are controversial. While the controlling physics of $CO_2$-EOR are the same for ROZs and MPZs, the specific characteristics of ROZs will influence the effectiveness of $CO_2$ WAG injection and $CO_2$ retention. One important issue is possible differences in oil saturation between ROZs and MPZs (after MMWF). Differences in oil saturation influence the interaction of $CO_2$ and in-situ fluids, and this in turn, impacts overall sweep and displacement efficiencies. In this sense, different strategies may have to be used to maximize the effectiveness of $CO_2$ WAG injection either for oil production or $CO_2$ sequestration.

Almost all previous $CO_2$-EOR studies focused on injection into MPZs, rather than ROZs. There have been two published studies of WAG injection into ROZs based on full physics simulations [7,8]. The study by Jamali and Ettehadtavakkol focused on evaluating the “Natural Aquifer” model for the origin of ROZs and their potential for $CO_2$ storage. Our earlier study [8] provided an understanding of the nature of WAG injection of $CO_2$ and the factors controlling $CO_2$ storage. It also explored varying $CO_2$ WAG injection strategies to improve oil production in ROZ reservoirs. Ren and Duncan [8] showed the WAG ratio (at maximum oil production) for the Seminole ROZ reservoir are smaller than the published WAG ratios for MPZ reservoirs. The reasons behind this observation were not addressed in that paper. The current study provides one possible explanation for this observation.

The difference in oil saturation between MPZs (after water flooding) and ROZs depends in part on both the efficiency of primary production and the time elapsed between initiation of waterflooding and the transition to $CO_2$ flooding. This transition is typically either an economic decision or based on some corporate strategic reasons. In all cases waterflooding is almost always terminated long before the reservoir approaches residual saturation.

From an industry perspective considering $CO_2$ flooding processes in residual oil zones (ROZs) versus main pay zones (MPZs), is essential to develop strategies to maximize oil production and minimize $CO_2$ utilization. This work investigated $CO_2$ water alternating gas (WAG) injection into relatively simple synthetic reservoir models of the ROZ underlying MPZ reservoirs. The reasoning for using these synthetic (and therefor accurately characterized) models was to clearly understand the factors that enable maximizing oil production and minimizing $CO_2$ utilization. The effects of oil saturation on the foregoing metrics were investigated by utilizing full physics reservoir simulations with varying WAG ratios and reservoir heterogeneity.

The main objective of the current study is to understand how the effectiveness of oil recovery from $CO_2$ WAG injection is affected by the differences in oil saturation between a ROZ and a MPZ (after MMWF). This understanding will help answer questions such as: are the WAG ratios that maximize oil recovery from MPZs, applicable to ROZs? Or, can a WAG strategy be found that maximizes oil recovery from both the ROZ and MPZ at the same time? To accomplish the objective, we conducted a series of simulations of $CO_2$ WAG injection following on from NWF and MMWF. These simulations were run on synthetic reservoir models. This enabled us to clearly evaluate how variations in reservoir heterogeneity impact oil saturation distributions after NWF and MMWF and thus $CO_2$ WAG ratios. This study investigates the desired WAG ratios that will maximize oil production, and understand how MPZs differ from ROZs in their response. Such a comparison has not been conducted or reported by others. The issues explored on the current study have important implications to field designs of WAG injection into ROZs and understanding when to switch from MPZ to ROZ injection or to institute commingled injection/production.

## 2. Theory and approach

### 2.1. Multi-phase flow simulations

The reservoir flow simulator used in this study is Eclipse-300 [9]. This simulator is an efficient, equation-of-state (EOS) based, multi-phase flow simulator. It utilizes robust equation-solvers that can achieve efficient numerical solutions for the flow of $CO_2$, water, and oil in porous-media. The simulator is reliable and widely used for evaluating oil production and carbon storage performance during $CO_2$-EOR (e.g., Refs. [8,10e12].

A flow chart summarizing our approach is illustrated in Fig. 1. All simulated cases started from synthetic geological models. After this step, we conducted flow simulation of both NWF and MMWF. Subsequently, $CO_2$ injection was started at the end of NWF or MMWF to evaluate $CO_2$-EOR performance and find favorable WAG ratios. The details of each step are given below.

### 2.2. Factors impacting WAG injection

The mechanisms of $CO_2$-EOR are well-understood [13]. The WAG ratio, defined as the cumulative volume of water injected divided by the gas injected into the reservoir, is an important metric to describe the nature of $CO_2$-EOR [14]. At large WAG ratios, water film blocking is known to occur [15], resulting oil trapping. In these circumstances, WAG injection essentially becomes ineffective-waterflooding. Small WAG ratios typically result in channeling and early breakthrough of injected $CO_2$. Both of these phenomena result in less than optimal oil production. Thus, in most circumstances, the maximum oil production rate or recovery factor will correspond to the most favorable WAG ratio [15e18]. Also, the effects of heterogeneity and injection strategies on the production efficiency of $CO_2$-EOR have been well studied (e.g. Refs. [19e23,52,53]). Others (e.g. Refs. [24e28]) have examined optimizing $CO_2$ WAG injection. A focus of these WAG injection studies for MPZs has been to identify the WAG ratios that yield maximum oil production.

### 2.3. Generation of reservoir models

We generated a series of statistical realizations of permeability fields using sequential Gaussian simulation [29,30]. The properties

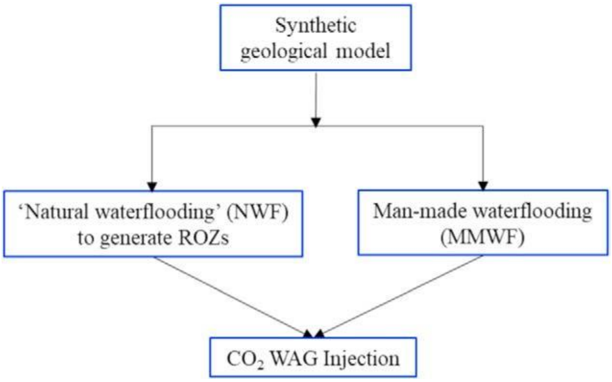

Fig. 1. Work flow chart of each simulated case.

of these fields were listed in Table 1. Both inverted 5- and 9-spot well patterns were considered. The permeability fields have different horizontal auto-correlation lengths ($l_x$), and we made the length dimensionless following the work of Li and Lake [31]. Dimensionless horizontal autocorrelation length ($l_{Dx}$) is defined as the ratio of $l_x$ over the domain width in the corresponding direction. $l_x$ indicates how close or how far the permeability is spatially auto-correlated, which is mainly controlled by sedimentary environments and diagenesis processes. The typical value of $l_{Dx}$ is 2. A series of auto-correlated permeability fields (Table 1) are generated to test the effect of autocorrelation length on simulation results. Specifically, layered geological models are considered through assigning the permeability field with a large $l_{Dx}$ (100, as shown by Tavassoli et al. [32]). The permeability anisotropy ($k_v/k_h$) is varied through decreasing $k_v$ while keeping $k_h$ unchanged: 0.001, 0.01, and 0.1. The horizontal permeability ($k_h$) field were statistically realized with different natural-log standard deviation ($s_{lnk}$): 0, 1, 2. The corresponding values of the Dykstra-Parsons coefficient are 0, 0.62, 0.85 (with increasing heterogeneity). The permeability natural-log mean ($m_{lnk}$) is set to be 5, which is close to that of the Seminole residual oil zone [8]. Changing $m_{lnk}$ will cause different recovery factors for a given time period, but that should not alter the desired WAG ratios that are focused in this study. Additionally, considering several different permeability spatial distributions can be characterized by one single set of heterogeneity indicators, we generated three realizations of the base permeability field (see Table 1) to evaluate the influence of permeability uncertainties on oil production during $CO_2$ injection.

Then, using the Holtz's [33] porosity-permeability correlation (refer to Eq. (1)), we calculated the porosity fields corresponding to the generated permeability fields. In Eq. (1), the unit of permeability is mD. The Holtz correlation might be applicable for rock types between the lithofacies packstone and mudstone of carbonate reservoirs.

$$4 = \left(\frac{k}{7E + 7}\right)^{1/9.61} \tag{1}$$

After generating permeability and porosity fields, the corresponding capillary entry pressure fields were calculated using the Leverett j-function [34], following the procedures as detailed by Ren [35]. The reason for considering capillary entry pressure heterogeneity in simulations is the small regional aquifer flux during ROZ formation. The reported aquifer flux during NWF within the Permian Basin is around 10e15 cm/yr (0.33e0.83 ft/yr, Trentham [36]), which is much less than that (~1 ft/day) of MMWF. Such small flux pronounces the effect of capillary pressure ($P_c$) heterogeneity on fluid migration and oil saturations, as demonstrated in the work by Ren and Duncan [37] and other works [38]. Thus, capillary pressure heterogeneity should be considered, and the implementation procedures are given in the following Section of Rock/Fluid Interaction Models.

## 3. Flow simulation of NWF and MMWF

### 3.1. Rock/Fluid Interaction Models

We assume the oil phase properties for the ROZ and MPZ are the same, so we use one set of PVT equations for both. The oil properties are adopted from the publication of Honarpour et al. [39]; whose analysis is based on the Seminole San Andres ROZ oil samples. A black oil model is built for the flow modeling of both NWF and MMWF. At the reservoir condition (2119.9 psi and 104 °F), the oil density is 657.71 kg/m$^3$, and the oil viscosity is 1.21 cp. The gas oil ratio (GOR) is 688.15 scf/bbl.

When simulating $CO_2$ WAG injection, we employ a compositional model with the oil compositions shown in Table 2. The Peng Robinson equation of state (PR EOS) is used with the parameter settings in Table 2. The binary interaction coefficients are listed in Table 3. The minimum miscibility pressure for the $CO_2$/oil mixture is around 1400 psi [39], and the $CO_2$ flooding is miscible in simulations.

For simplicity, we assume the relative permeability and capillary pressure curves (shown in Fig. 2a and b) are the same for the two processes of NWF and MMWF.

For flow simulation of NWF, the effect of capillary pressure heterogeneity on water/oil flow was considered. To capture this effect, the capillary pressure curve in Fig. 2b was assigned to the cells with the arithmetic mean of the permeability of a given field, the corresponding capillary pressure curves for other cells were scaled using the Leverett j-function [37]. Additionally, we also tested how ignoring capillary pressure or utilizing a single capillary pressure in our simulations influenced the resultant oil saturation in ROZs. A “single capillary pressure” corresponds to a model where the same capillary pressure curve (Fig. 2b) is assigned to all the cells in a simulated domain.

For the flow simulation of $CO_2$ WAG injection, the used relative permeability curves are in Fig. 2a and c. The Stone I model [40] is adopted to describe the oil relative permeability during 3-phase flow. The hysteresis in both the relative permeability and capillary pressure curves are omitted for computational efficiency. Both hysteresis and relative permeability has been experimentally shown to be cycle-dependent [41e43]. We believe that considering these cycle-dependent properties will not alter the observations of the relative magnitude of favorable WAG ratios for MPZs versus ROZs, although they have been shown to cause the difference in oil production rate prediction [23,44].

Table 1
Properties of synthesized permeability fields.

| Well pattern | Inverted 5-spot | Inverted 9-spot |
|---|---|---|
| Patter size, acre | 40 | 80 |
| Synthetic domain sizes, ft | 1320 × 1320 × 96 | 1860 × 1860 × 96 |
| Model cell sizes, ft | 30 × 30 × 3 | 30 × 30 × 3 |
| Model dimensions | 44 × 44 × 32 | 62 × 62 × 32 |
| Permeability horizontal dimensionless auto-correlation length, $l_{Dx}$ | 0, 2*, 100 | |
| Horizontal permeability log mean, $m_{lnk}$ | 5* | |
| Horizontal permeability log standard deviation, $s_{lnk}$ | 0, 1*, 2 | |
| Horizontal permeability Dykstra-Parsons coefficient, $V_{DP}$ | 0, 0.62*, 0.85 | |

*means base permeability field (i.e., base case).

Table 2
Crude oil compositions representative of the Seminole San Andres ROZ and the parameter settings for PR EOS (modified from Honarpour et al. [39], and Jamali and Ettehadtavakkol [7].

| Component | $CO_2$ | $C_1N_2$ | $C_2C_3H_2S$ | $C_4eC_6$ | $C_7eC_{10}$ | $C_{11}eC_{16}$ | $C_{17+}$ |
|---|---|---|---|---|---|---|---|
| Mole fraction, % | 0.02 | 20.14 | 15.9 | 8.99 | 17.29 | 18.42 | 19.24 |
| Critical temperature (R) | 547.56 | 339.21 | 619.38 | 835.43 | 1117.84 | 1344.62 | 1686.57 |
| Critical pressure (psi) | 1071.34 | 666.77 | 722.56 | 491.3 | 389.65 | 277.42 | 159.29 |
| Critical volume ($ft^3$/lb-mole) | 1.51 | 1.56 | 2.71 | 5.02 | 7.73 | 12.13 | 22.15 |
| Critical Z-factor | 0.275 | 0.287 | 0.295 | 0.275 | 0.251 | 0.233 | 0.195 |
| Molecular weights (g/mol) | 44.01 | 16.29 | 36.19 | 70.06 | 114.17 | 180.94 | 358.25 |
| Acentric Factor | 0.225 | 0.0139 | 0.125 | 0.245 | 0.383 | 0.582 | 1.0054 |
| Coefficient $U_a$ | 0.457 | 0.457 | 0.457 | 0.457 | 0.457 | 0.457 | 0.457 |
| Coefficient $U_b$ | 0.077 | 0.077 | 0.077 | 0.077 | 0.077 | 0.077 | 0.077 |

Table 3
Settings of binary interaction coefficients.

| Component | $CO_2$ | $C_1N_2$ | $C_2C_3H_2S$ | $C_4eC_6$ | $C_7eC_{10}$ | $C_{11}eC_{16}$ | $C_{17+}$ |
|---|---|---|---|---|---|---|---|
| $CO_2$ | 0 | | | | | | |
| $C_1N_2$ | 0.0976 | 0 | | | | | |
| $C_2C_3H_2S$ | 0.1289 | 0.0103 | 0 | | | | |
| $C_4eC_6$ | 0.1271 | 0.0019 | 0.0063 | 0 | | | |
| $C_7eC_{10}$ | 0.1105 | 0.0241 | 0.0196 | 0.003 | 0 | | |
| $C_{11}eC_{16}$ | 0.0943 | 0.0494 | 0.0333 | 0.0061 | 0 | 0 | |
| $C_{17+}$ | 0.0997 | 0.1365 | 0.0588 | 0.012 | 0 | 0 | 0 |

## 4. Injection/production schemes

To simulate the NWF process, a line drive geometry was used (Fig. 3a): water injectors are put into every left boundary cell, and producers are put into every right boundary cell. Such uniformly-distributed inlet and outlet conditions are to mimic regional aquifer flow, which has been demonstrated to be physically-applicable in reproducing ROZs [37]. The inlet water flux is set to be 0.5 ft/yr (15.24 cm/yr). With the inlet flux, the water injection rate is calculated to be 0.0368 rb/day (reservoir bbl/day). The ultimately-injected water pore volume (PV) is 86 for the single inverted 5-spot pattern and 43 for the inverted 9-spot pattern. All these models are saturated with oil as initial conditions.

For MMWF, both the inverted 5-spot 40-acre pattern (Fig. 3b) and inverted 9-spot 80-acre pattern are considered. The middle table in the figure shows the simulation parameter settings for both types of patterns. The ultimately-injected water PV is 5.8 and 2.9 for the inverted 5-spot and inverted 9-spot well pattern, respectively.

For $CO_2$ WAG injection (Fig. 3c), the flow simulation parameters are listed in the lower row of Fig. 3. The $CO_2$ injection rate is set to be constant at 3000 Mscf/day; varying rates has no effect on favorable WAG ratios although it changed oil production rates [8]. The $CO_2$ half-cycle size is 2.5% hydrocarbon pore volume (HCPV), based on the balance of good oil production and the operation ability of WAG cycle switches [8,45]. The HCPV is calculated at the end of NWF or MMWF. WAG ratio is varied from 0 to 5, through changing water injection duration while keeping $CO_2$ injection duration unchanged in each WAG cycle (see Appendix B for detailed illustration).

The other parameters of the flow simulation of NWF, MMWF and $CO_2$ WAG are included in Fig. 3. The boundaries of all simulation domains are closed (no flow). All the injectors and producers involved in simulations are vertical, and they are completely perforated along the depth range of simulation models.

Additionally, to specifically examine the effect of oil saturation

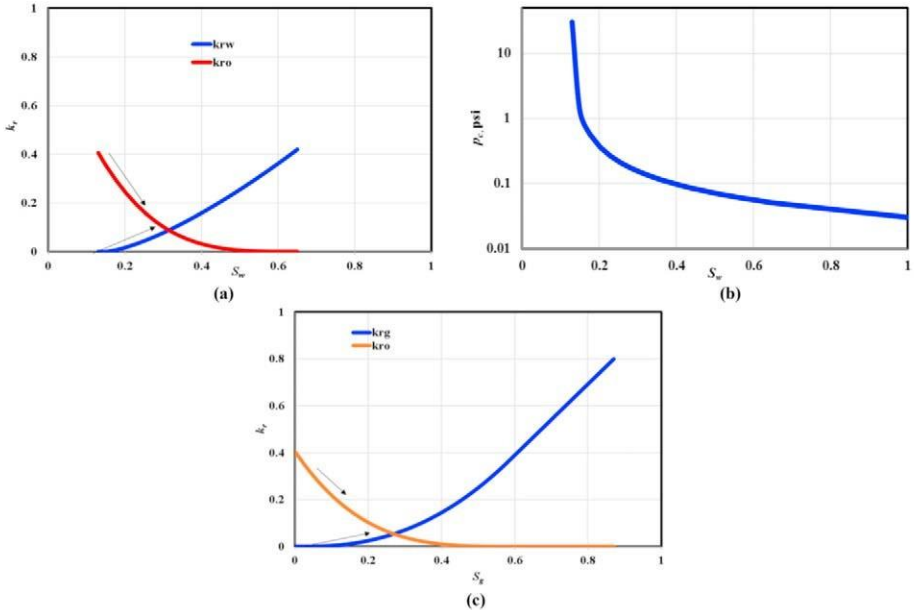

(a) (b) (c)

Fig. 2. (a) Water/oil relative permeability curves; (b) capillary pressure ($p_c$) curve for water/oil, here the capillary pressure is defined as non-wetting phase (water) pressure minus wetting phase (oil) pressure, and the reservoir is presumed to be completely oil-wet; (c) gas/oil relative permeability curves.

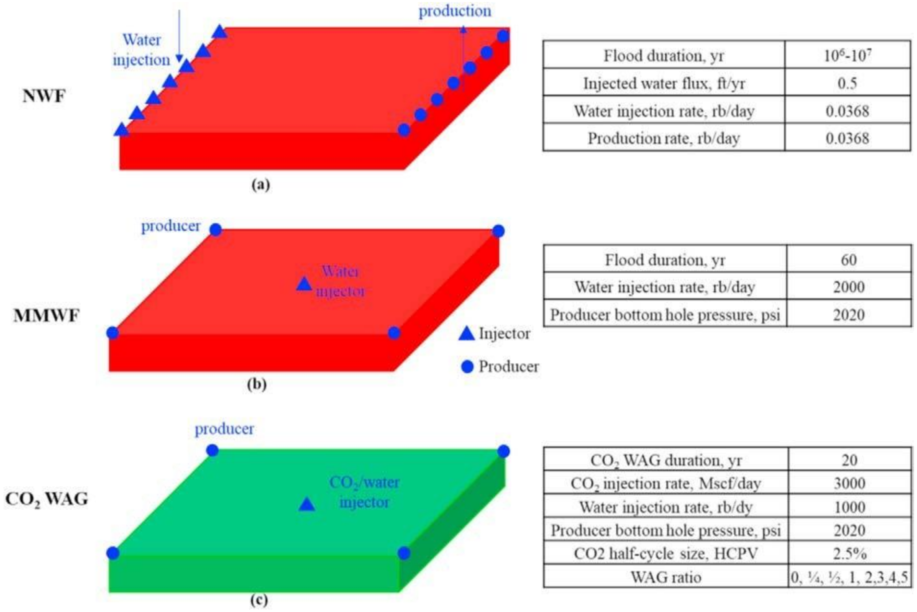

| Flood duration, yr | $10^6$-$10^7$ |
|---|---|
| Injected water flux, ft/yr | 0.5 |
| Water injection rate, rb/day | 0.0368 |
| Production rate, rb/day | 0.0368 |

| Flood duration, yr | 60 |
|---|---|
| Water injection rate, rb/day | 2000 |
| Producer bottom hole pressure, psi | 2020 |

| $CO_2$ WAG duration, yr | 20 |
|---|---|
| $CO_2$ injection rate, Mscf/day | 3000 |
| Water injection rate, rb/dy | 1000 |
| Producer bottom hole pressure, psi | 2020 |
| CO2 half-cycle size, HCPV | 2.5% |
| WAG ratio | 0, ¼, ½, 1, 2,3,4,5 |

Fig. 3. Illustration of NWF, MMWF, and $CO_2$ WAG simulation setup. The embedded tables on the right column show the corresponding simulation settings for each flow simulation process.

on WAG ratios, we manually assign uniform oil saturation ($S_{or}$) to geological models at the beginning of WAG injection. We consider several values of $S_{or}$: 0.3, 0.35, 0.4, and 0.5. They cover the range of oil saturation observed for the virgin ROZ in the Permian Basin [1,37].

### 4.1. Metrics of $CO_2$-EOR performance

We report how varying WAG ratios influences the following $CO_2$-EOR performance metrics: net $CO_2$ utilization ratio, averaged oil production rate, and dimensionless oil recovery factor. Their definitions are:

Net $CO_2$ utilization ratio¼(Total $CO_2$ injectedetotal $CO_2$ produced)/total oil produced, (MScf/Stb).

Averaged oil production rate¼Total oil produced/injection duration/number of oil producers, (Stbd/Well, standard tank barrel per day per well).

Dimensionless oil recovery factor ¼ cumulative oil produced during $CO_2$ injection/oil in place after MMWF and NWF, (%).

The metric of net $CO_2$ utilization ratio indicates the net use of $CO_2$ to produce 1 bbl of oil. It measures the cost-effectiveness of $CO_2$ injection for enhanced oil recovery. Typically, the largest cost of implementing WAG floods is acquiring $CO_2$ [46]. The dimensionless oil recovery factor is defined based on the oil remaining after either NWF or MMWF, rather than on the traditional original oil in place (OOIP). Thus, it can be expected the calculated dimensionless factors here are larger than those reported in the literature. Adding ‘dimensionless’ into our definition is to differentiate it from the traditional term.

## 5. Results

### 5.1. Influence of multiple realizations on oil production

The multiple realizations of the base permeability field showed minor influence on ultimate oil production (see Appendix A). Thus, we employed a single realization of the permeability fields in this work.

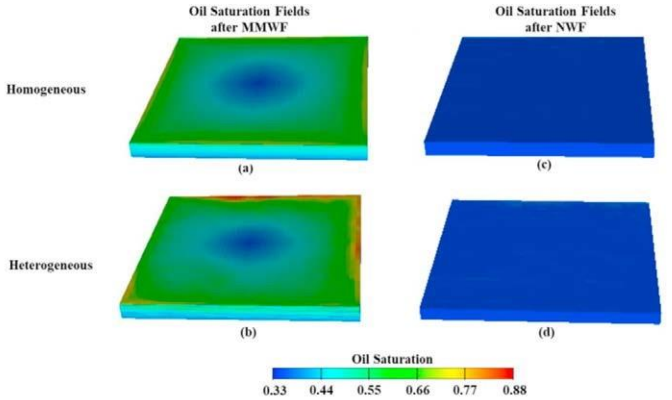

Fig. 4. Oil saturation fields at the end of MMWF (a and b, after 60 years of waterflooding) and at the end of NWF (c and d). For the heterogeneous geological model used, $V_{DP}$ ¼ 0.62, $l_{Dx}$ ¼ 2. Inverted 5-spot patterns were used, and heterogeneity capillary pressure was considered in these flow simulations.

### 5.2. Oil saturation magnitude and patterns after MMWF vs. after NWF

The oil saturation fields at the end of MMWF versus those at the end of NWF are shown in Fig. 4. After 60 years of MMWF (Fig. 4a-b), waterflooding has swept much of the oil from the lower part of the reservoir, and the remaining oil is mainly in the upper portion and edges. In contrast, after $10^6$ years of NWF, the oil saturations for most of the cells of the reservoir have almost reached the end point of relative permeability (0.35) (Fig. 4c-d).

The effect of capillary pressure on oil saturation histograms after MMWF versus after NWF has been explored, and histograms for computed oil saturations are shown in Fig. 5. For MMWF (Fig. 5a), the three histograms for the cases of without $P_c$, single $P_c$, and heterogeneous $P_c$ overlap. For the NWF case, the different assumptions for the $P_c$ yield result in different histograms as shown in Fig. 5b and elaborated in the figure caption.

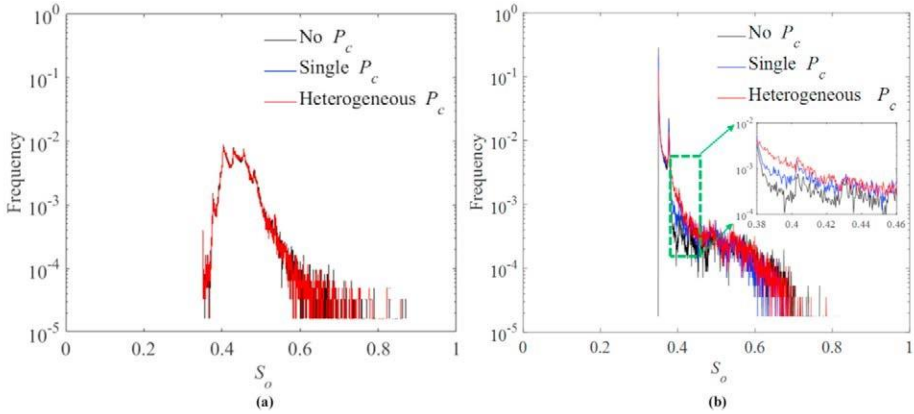

Fig. 5. The histograms of remaining oil saturation ($S_o$) at the end of MMWF (a) and at the end of NWF (b) when considering no $P_c$, single $P_c$, and heterogeneous $P_c$. In Fig. 5b, the case of No $P_c$ shows the greatest number of cells with the oil saturation close to 0.35 (the endpoint of relative permeability as shown in Fig. 2a). However, the zoom-in plot into the $S_o$ interval of 0.38e0.48 shows that the case of heterogeneous $P_c$ yields the largest frequency around this interval (note the logarithmic scale in the Y-axis). In Fig. 5a, the arithmetic mean of oil saturation for the three different considerations of $P_c$ is the same (0.43), however, in Fig. 5b, the mean varies. It is 0.376, 0.380, 0.384 for the case considering no $P_c$, single $P_c$, and heterogeneous $P_c$ correspondingly. The heterogeneous geological model was used with $V_{DP}$ ¼ 0.62, l$_{Dx}$ ¼ 2, and inverted 5-spot patterns.

### 5.3. Cumulative dimensionless oil recovery factors during continuous $CO_2$ injection after NWF vs. MMWF

A key objective of this study was to evaluate the dimensionless oil recovery factors for continuous $CO_2$ injection following MMWF, compared to those following NWF. Fig. 6a and b show the metric for the continuous $CO_2$ injection after MMWF, and for the WAG after NWF, respectively. The final oil recovery factor for the inverted 5-spot pattern in the homogenous ROZ model is about 21.8%, which is less that the corresponding value (around 28.9%) for the continuous $CO_2$ injection after MMWF. The oil remaining in the upper portion of the reservoir after MMWF was effectively swept by the injected $CO_2$. Qualitatively similar observation of oil recovery factors is made for the inverted 9-spot patterns. Table 4 lists the dimensionless oil recovery for the WAG injection into the different heterogeneous synthetic models. The recovery factors for the WAG after MMWF is overall larger than those for the WAG after NWF, and the differences between the factors for the two processes increases with the WAG ratio.

Another noteworthy difference between Fig. 6a and b is the oil production starting time during WAG injection. Oil production response is quick for the WAG after MMWF versus delayed production for WAG after NWF (the oil starts to produce at around 0.12 PV of $CO_2$ injection for WAG after NWF in the inverted 9-spot pattern). This delay is longer for the inverted 5-spot patterns than for the inverted 9-spot.

### 5.4. $CO_2$ net utilization ratios

The $CO_2$ net utilization ratios for the WAG after NWF and after MMWF are shown in Fig. 7a and 7b, respectively. The latter ratios are in the range of 2e10 MScf/Stb, and the former ones can be as high as 35 MScf/Stb. Obvious inflection points exist in the curves of $CO_2$ utilization ratios versus WAG ratios for the WAG after NWF, However, the equivalent curves for the WAG after MMWF become almost flat as the WAG ratio increases. The WAG ratios (at the minimum net utilization ratios) for the latter WAG are around 1.5, larger than that (around 1) for the former WAG. The simulations completed in this study found that the utilization ratios for WAG after NWF versus after MMWF depend on the WAG ratios, reservoir heterogeneity, and well patterns area/configuration (Fig. 7a and b).

The net utilization ratios for the inverted 9-spot pattern are overall larger than those for the inverted 5-spot (dashed curves are above solid curves in both Fig. 7a and b). Similar observations of the

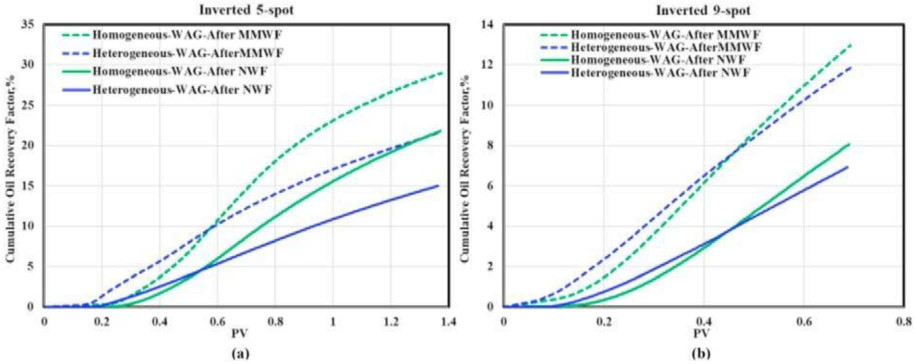

Fig. 6. Dimensionless oil recovery factors versus pore volume (PV) of $CO_2$ injected during continuous $CO_2$ injection after MMWF vs. after NWF. For the heterogeneous geological model used, $V_{DP}$ ¼ 0.62, l$_{Dx}$ ¼ 2. The homogeneous models show slower oil production response than heterogeneous ones because of the uniform $CO_2$ flood conformances, however, the final oil production for homogeneous models are apparently always better than heterogeneity ones. The ultimately-injected $CO_2$ PV for the inverted 9-spot is about half of that for the inverted 5-spot, due to both the pattern coverage area difference and the same WAG injection duration (refer to Fig. 3).

Table 4
Dimensionless oil recovery factors for WAG injection in both inverted 5-spot and 9-spot well patterns. The recovery factors for both WAG ratio 0 (continuous $CO_2$) and 1 are listed in the table. For the heterogeneous geologic models, $s_{lnk}$ ¼ 1, $m_{lnk}$ ¼ 5.

| Well pattern | Model Heterogeneity | WAG after MMWF: WAG ratio ¼ 0 | WAG after NWF: WAG ratio ¼ 0 | WAG after MMWF: WAG ratio ¼ 1 | WAG after NWF: WAG ratio ¼ 1 |
|---|---|---|---|---|---|
| Inverted 5-spot | $V_{DP}$ ¼ 0, $l_{Dx}$ ¼ 0 | 28.9% | 21.8% | 22.7% | 12.4% |
| | $V_{DP}$ ¼ 0.62, $l_{Dx}$ ¼ 2 | 21.7% | 13.8% | 26.1% | 11.9% |
| | $V_{DP}$ ¼ 0.62, $l_{Dx}$ ¼ 100 | 23.2% | 15.6% | 27.1% | 13.2% |
| Inverted 9-spot | $V_{DP}$ ¼ 0, $l_{Dx}$ ¼ 0 | 12.9% | 8.1% | 11.9% | 6.2% |
| | $V_{DP}$ ¼ 0.62, $l_{Dx}$ ¼ 2 | 11.8% | 6.9% | 13.6% | 5.9% |
| | $V_{DP}$ ¼ 0.62, $l_{Dx}$ ¼ 100 | 10.2% | 6.4% | 11.9% | 5.6% |

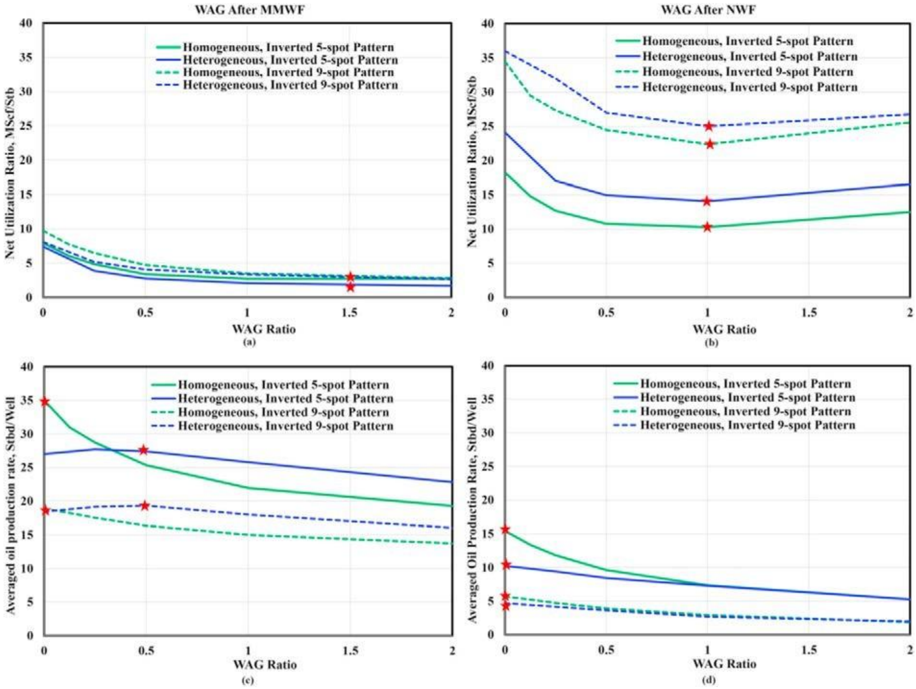

Fig. 7. $CO_2$ net utilization ratios and averaged oil production rates for the inverted 5-spot (40 acre) and inverted 9-spot (80 acre) well patterns. $CO_2$ WAG injection is simulated following the processes of NWF or MMWF. For the heterogeneous geological model used, $V_{DP}$ ¼ 0.62, $l_{Dx}$ ¼ 2. A WAG ratio of 0 means continuous $CO_2$ injection. Note that for WAG following NWF, there is a favorable WAG ratio that yields the lowest net utilization ratios irrespective of the well pattern, and this ratio is around 1. However, for WAG after MMWF, the net utilization ratio monotonically decreases with the WAG ratio. The unit of Stbd/Well means standard tank barrel per well. The WAG injection here is started following 30 years of MMWF.

effect of well patterns on these metrics are made in the layered geological models (see Appendix C). Therefore, using inverted 5-spot patterns can improve the effectiveness of WAG injection to enhance oil recovery.

### 5.5. Averaged oil production rates and oil recovery factors

For the synthetic reservoir models utilized in this study, the average oil production rates for the WAG following MMWF are larger than those for the WAG following NWF (Fig. 7c vs. 7d). The average rates are impacted negatively by increasing WAG ratios for the $CO_2$ after NWF, whereas, for the WAG after MMWF, heterogeneity necessitates a small (0.25e0.5) WAG ratio to achieve the maximum oil production rates. For simulations of the heterogeneous models shown in Fig. 7c and d, the WAG ratios at maximum oil production rates are less for virgin ROZs than for the MPZs subject to MMWF.

### 5.6. Effect of oil saturation ($S_{or}$) on favorable WAG ratios

Net utilization ratios and average oil production during WAG injection with different initial oil saturation ($S_{or}$) are shown in Fig. 8. $S_{or}$ controls the curve trend of the net utilization ratio versus the WAG ratio (Fig. 8a and c). At a low $S_{or}$, there is a favorable WAG ratio (at the minimum net utilization ratio). However, when $S_{or}$ increases to 0.5, the net utilization ratio becomes almost flat as the WAG ratio increases. The approximate inflection point (labelled by a star) moves to the right as the $S_{or}$ increases. As a result, small $S_{or}$ results in small WAG ratios minimizing net utilization.

For average oil production rates (Fig. 8b and d), the point of optimal return tends to move to a higher WAG ratio as $S_{or}$ increases. Larger $S_{or}$ requires larger WAG ratios to maximize oil production rates.

Well patterns slightly influence the favorable WAG ratios. As the well pattern changes from inverted 5-spot to inverted 9-spot, the favorable WAG ratio (either at minimum net utilization ratio or at maximum oil production rates) decreases marginally (Fig. 8a vs.

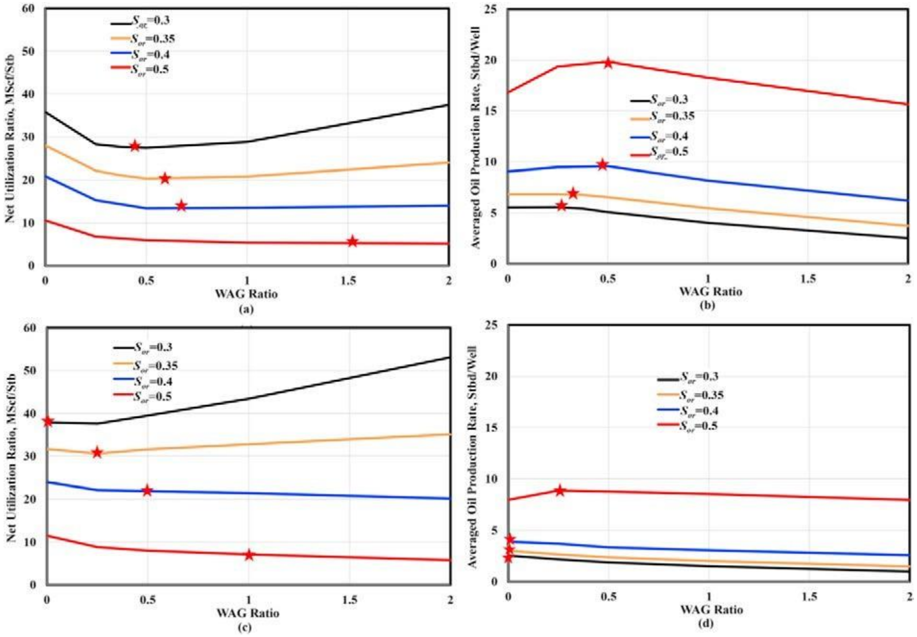

Fig. 8. $CO_2$ net utilization ratios and averaged oil production rates for the inverted 5-spot pattern (a and b) and for the inverted 9-spot pattern (c and d). The initial oil saturation ($S_{or}$) at the beginning of $CO_2$ WAG injection is manually set to be constant. For the heterogeneous geological model used, $V_{DP}$ ¼ 0.85, l$_{Dx}$ ¼ 2. The stars indicate the inflection or optimal points in the curves.

Fig. 8c and b vs. Fig. 8d). For example, for the inverted 5-spot pattern, as $S_{or}$ increases from 0.3 to 0.5, the favorable WAG ratio increases from 0.45 to 1.5 (Fig. 8a), whereas, the corresponding ratio for the inverted 9-spot pattern are comparatively small, increasing from 0 to 1 (Fig. 8c).

### 5.7. Effect of permeability anisotropies ($k_v/k_h$) on favorable WAG ratios for ROZs

Increasing permeability anisotropy (the ratio of $k_v/k_h$) improves $CO_2$ net utilization efficiency (Fig. 9a) for ROZs. The net utilization ratio decreases from 20 to 10 Mscf/Stb when $k_v/k_h$ increases from 0.01 to 1, given a WAG ratio of 1. Large $k_v$ favors $CO_2$ production more than oil production. That is the reason that the $CO_2$ net utilization ratios for the case of $k_v/k_h$¼1 are the smallest, even though the corresponding oil production rate rapidly decreases with the increase in the WAG ratio. Adjusting $k_v/k_h$ has a similar effect on oil production rates (Fig. 9b) as adjusting reservoir heterogeneity does (Fig. 7c-f): oil production decreases as the WAG ratio increases.

Also, the ratio of $k_v/k_h$ increases the favorable WAG ratio (at the minimum net utilization) (Fig. 9a). Large $k_v$ necessities more water injection to divert injected $CO_2$, and thus $CO_2$ can better sweep the reservoir. This large $k_v$, within the context of structural geology, might be due to vertical fractures. Some vertical fractures have been observed in the cores of the Seminole San Andres ROZ (Duncan, unpublished data). In this sense, the heterogeneity associated vertical natural fractures should be carefully characterized as they have a significant effect on $CO_2$ net utilization ratios.

## 6. Discussion

Our companion paper [8] set out to make a comparison between WAG injection into the ROZ versus the MPZ for the Seminole San Andres Unit. Simulations presented in that study showed that the desired WAG ratios (at maximum oil production) for the ROZ are smaller than the published WAG ratios (arithmetic mean is 1.6, and

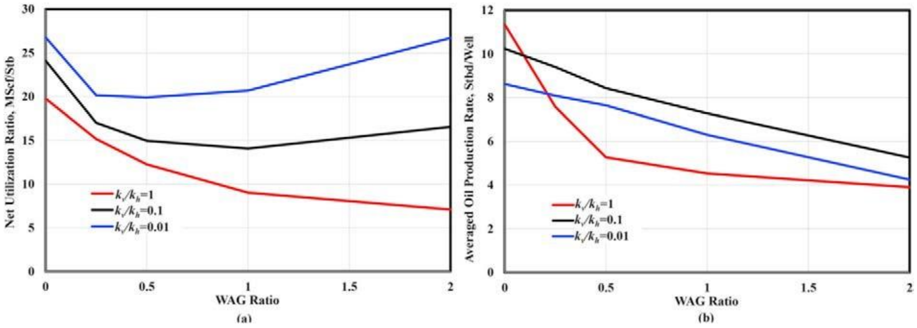

Fig. 9. $CO_2$ net utilization ratios (a) and averaged oil production rates (b) for the heterogeneous model with different permeability anisotropies. Inverted 5-spot patterns are used. The initial oil saturation ($S_{or}$) at the beginning of $CO_2$ WAG injection is manually set to be constant (0.35). For the heterogeneous geological model used, $V_{DP}$ ¼ 0.62, and l$_{Dx}$ ¼ 2.

standard deviation is 1.0) by Christensen et al. [14] for typical MPZ reservoirs. Ren and Duncan [8] did not identify the underlying reasons behind this observation. The current study explored a possible explanation by examining the impact of oil saturation differences on WAG injection between ROZs and MPZs.

### 6.1. *Magnitude and patterns of oil saturation after MMWF vs. NWF*

The interplay between flow rates and capillary pressure, and its effect on flow and oil saturation is illustrated in Fig. 5. High injection rates for MMWF create relatively large viscous forces that override capillary pressure effects. As a result, the frequency histograms for oil saturation (Fig. 5a) are almost the same for the scenarios of without $P_c$, single $P_c$, and heterogeneous $P_c$. However, for NWF, the lower flow rates enhance the effect of $P_c$. The histograms, shown in Fig. 5b, vary significantly in the oil saturation interval of 0.35e0.46. As the simulation inputs are changed from no $P_c$ to heterogeneous $P_c$, the frequency of occurrence for the endpoint oil saturation (0.35) decreases, whereas, the frequency of occurrence for the oil saturation in the range 0.38e0.46 increases. This is consistent with both relative permeability and capillary pressure controlling oil saturation for NWF. The relative permeability curves in these flow simulations apparently dominate the result of oil saturation. As a consequence, the maximum points of the histograms are always around the endpoint saturation (0.35, in Fig. 5b).

It should be noted that pore-scale capillary trapping, which is an '*implicit*' capillary pressure effect [13], controls relative permeability endpoints. The '*explicit*' capillary pressure effect is reflected in the frequency change of the oil saturation interval 0.38e0.46 when the way of incorporating the capillary pressure curve differs. Heterogeneous $P_c$ causes capillary entry pressure effects, and the oil surrounded by capillary barriers (with high entry capillary pressure) is not swept. Thus, the case considering heterogeneous $P_c$ retains large (0.6e0.8) oil saturation (refers to Fig. 5b).

### 6.2. *$CO_2$ net utilization ratios*

The simulation results presented in Fig. 7a and b show that the $CO_2$ net utilization ratios for the WAG after NWF found in the current study are larger than those for the WAG after MMWF. The large differences found are apparently the result of the relative magnitude of initial oil saturation at the beginning of WAG injection. The utilization ratios for both types of WAG (after NWF versus after MMWF) depend on the WAG ratios, reservoir heterogeneity, and well patterns, but with different trends and extents (Fig. 7a and b): in the case of WAG following NWF, there exists a WAG ratio (approximately 1.0) that yields the lowest net utilization ratio, irrespective of the well pattern. However, for WAG following MMWF (Fig. 7a), the net utilization ratio monotonically decreases with the WAG ratio. The different trends are due to the oil saturation variations as supported by Fig. 8a and c.

Reservoir heterogeneity does not alter the trends described above, however it leads to different net utilization ratios (Fig. 7a and b). Heterogeneity influences net utilization ratios in different ways for the cases of WAG following NWF versus following MMWF. The presence of heterogeneity results in larger utilization ratios relative to homogeneous reservoirs for WAG following NWF, but not for WAG following MMWF. Simulated production data indicates that heterogeneity for the WAG after NWF results in the rate of increasing production of $CO_2$ being less than the rate at which oil production decreases. This causes the higher net utilization ratios for the heterogeneous case compared to the homogeneous one.

Table 5
Comparison of remaining oil saturation statistics between core measurement of oil saturation in the Seminole ROZ by Honarpour et al. [39] and NWF flow simulation results in this work.

| Parameters | Measurements[a] | Simulations[b] |
|---|---|---|
| Mean | 0.388 | 0.383 |
| Median | 0.368 | 0.361 |
| Standard deviation | 0.045 | 0.058 |
| Maximum | 0.499 | 0.811 |
| Minimum | 0.350 | 0.350 |

[a] The original measurement is every 1 ft, averaging over every 3 ft was made here to be consistent with the scale that is used in flow simulations.

[b] this is corresponding to the flow simulation using heterogeneous capillary pressure as shown in Fig. 5b.

### 6.3. *Averaged oil production and recovery factor*

For heterogeneous reservoir models, the WAG ratios corresponding with maximum rates of oil production are less for ROZs than for the MPZs after MMWF (Fig. 7c vs. 7d). The $CO_2$ WAG into virgin ROZs starts with high water saturation and a large portion of the injected $CO_2$ is suspected to displace water, rather than oil. Consequently, $CO_2$ tends to break through late as a result of the relative small mobility ratio contrast between $CO_2$ and water compared to the $CO_2$/oil system. Under these conditions, the large water saturation in virgin ROZs attenuates the need for water injection during WAG.

Oil production rates are more sensitive to WAG ratios for the homogeneous models than for the heterogeneous ones (Fig. 7c vs. 7d). The average oil rate for the two models crosses at a WAG ratio around 0.5. WAG injection is much more effective for heterogeneous models than for homogenous ones to improve oil production rates. As the pattern changes from inverted 5-spot to inverted 9-spot, the average oil production rate decreases, as does the oil recovery factor.

### 6.4. *Favorable WAG ratios at maximum oil production or minimum net utilization ratio*

One of the key findings from the flow simulations is that the favorable WAG ratios for the WAG injection after NWF, is smaller than those for the WAG after MMWF. This has implications in the design of $CO_2$ injection projects. When an operator prepares to target Greenfield ROZs for $CO_2$ flooding, they might benefit from starting the ROZ flood with a small (<1) WAG ratio. For Brownfields, ROZs are hydraulically connected with MPZs. Since the favorable WAG ratio for the two zones is different, additional characterization and simulations need to be conducted to choose the WAG ratio when considering WAG injection into the ROZ. One might not simply deepen wells targeting the MPZ and continue injecting at the same WAG ratio. WAG injection might be started in the MPZ followed by the ROZ with the most desired WAG ratio specific to each zone. When switching to the ROZ, the commingled production of both zones can be adopted because the injected $CO_2$ into the ROZ might move into the MPZ and help produce oil. Determining the optimal switching time merits further study.

Our flow simulations consider the geological heterogeneity variations that essentially control the sweep efficiency of $CO_2$ during WAG injection. In this sense, these favorable WAG ratios should lead to maximum *sweep* efficiencies. However, it is not sure that whether such ratios lead to maximum *displacement* efficiencies. To examine this point, the analysis method proposed by Walsh and Lake [47]; based on the fractional flow theory, is recommended.

### 6.5. Comparison to field/Lab measurements and observations

We compared the statistics of simulated remaining oil saturation after MMWF to those of Seminole ROZ cores by Honarpour et al. [39]. These sponge cores were extracted from the virgin ROZ interval, and the in-situ remaining oil saturation was measured using Dean Stark analysis and a spectrophotometer technique [39]. As shown in Table 5, the remaining oil saturation statistics between core measurements and our simulations are close, including the mean, median, standard deviation, and minimum of oil saturation. The maximum remaining oil saturation show discrepancy between measurements and simulations. This discrepancy should be due to the un-swept cells with low permeability/porosity in flow simulations.

Additionally, Gong and Gu [48] conducted coreflooding simulation of ROZ generation using carbonate cores, and the measured remaining oil saturation was in the range of 34.33e36.86%. This range is covered by our simulation results. This makes sense since cores tend be much more homogeneous compared to the statistically-generalized permeability fields used in this work.

For the median of remaining oil saturation (0.361), it is very close to the residual oil saturation to waterflooding or minimum oil saturation (0.350). At such low oil saturation, oil production response was delayed till $CO_2$ breakthrough (as shown in Fig. 6b). Such delay has been observed and confirmed in Tall Cotton ROZ reservoir (not associated with a MPZ) undergoing $CO_2$ injection [49].

### 6.6. Limitations and further considerations

The results from flow simulations are based several simplifications. First, inclined producing oil/water contacts, as have been inferred for some ROZ fields \[39,54,57,58], are not considered in the study. This contact is the oil saturation transition from a MPZ to a ROZ. Considering this contact might have some effects on favorable WAG ratios since such a contact is an oil saturation change. Second, this study assumes the same oil phase properties for both ROZs and MPZs. The experimental characterization of oil samples by Aleidan et al. [50] demonstrates that the global compositions and overall quality for the both zones are very similar. However, Honarpour et al. [39] showed that the oil API gravity is different for the MPZ and the ROZ. Further studies are needed to investigate how significant phase property differences would influence WAG ratios. Third, the favorable WAG ratios were estimated on the basis of the $CO_2$ utilization ratios or oil production rates averaged over 20 year of WAG injection. Since the oil production response varies significantly with time, changing WAG duration would give different favorable WAG ratios. However, their relative magnitude for ROZs versus MPZs will not be altered. Last, our work assumed the same geological models for both MPZs and ROZs, in order to focus on the effect of oil saturation differences (as caused by distinct flow regimes) on favorable WAG ratios. For the effect of other differences between the two oil zones, particularly reservoir permeability/porosity properties, needs to be further studied through invoking realistic geological models, which is our next step.

## 7. Summary and conclusions

We conducted a systematic numerical simulation of i) the oil saturation characteristics between main pay zones (MPZs) after man-made waterflooding (MMWF) and virgin residual oil zone (ROZs) ii) the influence of this difference on the performance and strategies of water alternating gas (WAG) injection in both zones. Since the whole study is mostly based on numerical assessment, the conclusions could be tempered by the limitations and simplifications involved in our work. Several qualitative, rather than quantitative, conclusions are tentatively drawn below based on this work:

- Favorable WAG ratios (either minimizing net utilization ratios or maximizing oil production rates) for virgin ROZs are consistently smaller than those for MPZs after MMWF. This is speculated to be due to the prevalent large water saturation in ROZs.
- Capillary pressures influence oil saturations more significantly for natural waterflooding (NWF) than for MMWF. Small aquifer flow rates for NWF enhance the effect of capillary heterogeneity on water/oil flow, and thus small portions of the ROZ retain large (0.4e0.5) remaining oil saturation. This capillary effect, however, is not shown for MMWF, mainly due to relatively large injection rates (viscous pressure).
- The favorable WAG ratio, corresponding to the minimum net utilization ratio, appears to increases when: (i) initial oil saturation (before WAG) increases; (ii) the ratio of $k_v/k_h$ increases; and (iii) the well pattern changes from inverted 9-spot to inverted 5-spot.
- The $CO_2$ net utilization ratios during $CO_2$ WAG injection for virgin ROZs are overall larger than those for MPZs after MMWF. The net utilization ratios depend, in qualitatively different ways, upon well patterns, reservoir heterogeneity, and WAG ratios.
- Both averaged oil production rates and oil recovery factors for the WAG in virgin ROZs appear to be less than those for the WAG in the MPZs after MMWF. This is mainly because remaining oil after NWF is comparatively less than that after MMWF.

## Author statement

Bo Ren: Conceptualization, Methodology, Validation, Writing e original draft. Ian Duncan: review, rewriting, and editing.

## Declaration of competing interest

The authors declare that they have no known competing financial interests or personal relationships that could have appeared to influence the work reported in this paper.

## Acknowledgements

This study is part of a long-term project investigating ROZ reservoirs in the Permian Basin of Texas being carried out by the Bureau of Economic Geology's (BEG's) State of Texas Advanced Resource Recovery (STARR) Program and funded in part by a US Department of Energy contract under DOE Award Number FE0024375 (PI: Duncan). We greatly appreciate suggestions on the research from Professor Larry Lake. We also appreciate useful edits and comments on an earlier version of the paper by Dr.s Larry Lake, Jerry Jensen, and Frank Male. Bo Ren wishes to thank William

Ambrose for his mentoring and support during this work. This research was sponsored the United States Department of Energy (DOE). The views and opinions expressed herein are those of the authors, do not necessarily reflect those of the DOE.

## Nomenclature

### *Roman Symbols*

| | |
|---|---|
| $k$ | Permeability, mD |
| $k_h$ | Horizontal permeability, mD |
| $k_v$ | Vertical permeability, mD |
| $P_c$ | Capillary pressure, psi |
| $S_{or}$ | Initial oil saturation before WAG injection |
| $V_{DP}$ | Dykstra-Parson coefficient |

### *Greek Symbols*

| | |
|---|---|
| $l_x$ | Horizontal autocorrelation length, ft |
| $l_{Dx}$ | Dimensionless horizontal autocorrelation length |
| $m_{lnk}$ | Horizontal permeability log mean, mD |
| $s_{lnk}$ | Horizontal permeability log standard deviation, mD |
| 4 | Porosity, fraction |

### *Acronyms*

| | |
|---|---|
| EOR | Enhanced Oil Recovery |
| HCPV | Hydrocarbon Pore Volume |
| PR EOS | Peng Robinson Equation of State |
| GOR | Gas Oil Ratio |
| MPZs | Main Pay Zones |
| MMWF | Man-made Waterflooding |
| NWF | Natural Waterflooding |
| rb | Reservoir Barrel |
| ROZs | Residual Oil Zones |
| Stbd/Well | Standard Tank Barrel per Day per Well |
| WAG | Water Alternating Gas |

## Appendix A. Influence of Multiple Realizations on Oil Production

This appendix shows the influence of multiple realizations of a permeability field on oil production. Three realizations of the base permeability field (refer to Table 1) were created and then used for the flow simulation of continuous $CO_2$ injection (i.e., WAG ratio ¼ 0). As shown in Fig. A-1, multiple realizations show a minor effect on the ultimate oil production (all the curves almost overlap with each at the end). This means that the ultimate oil production performance is controlled by global heterogeneity indicators as shown in Table 1. The initial cumulative oil production varies for multiple realizations due to the different local heterogeneity inside synthesized permeability fields.

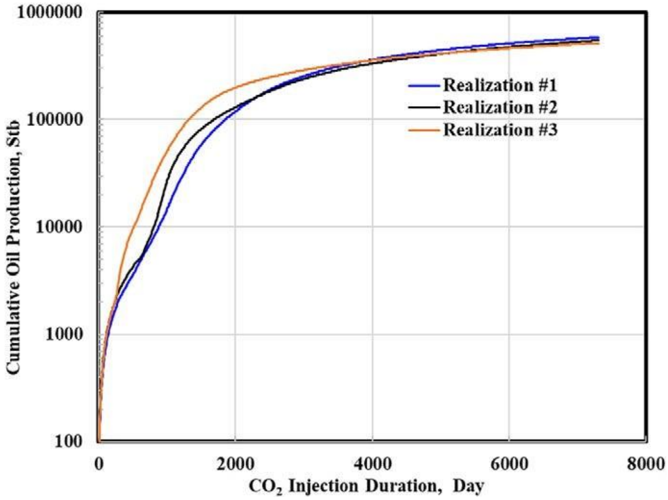

Fig. A1. Cumulative oil production versus CO2 injection duration for three realizations of the base permeability field during continuous CO2 injection into an inverted 5-spot well pattern. The CO2 injection follows 60 years of waterflooding as illustrated in the section of 'Flow Simulation of NWF and MMWF'.

## Appendix B. WAG Ratio Illustration

This appendix illustrates the design of $CO_2$ WAG injection for different WAG ratios. The ratio is defined as the reservoir volume ratio between injected water and injected $CO_2$ in each WAG cycle. It is increased through increasing water injection duration in each cycle while keeping $CO_2$ injection duration unchanged (Fig. A-1). Thus, when the WAG ratio increases, the amount of cumulatively-injected $CO_2$ is decreased with total water amount increased.

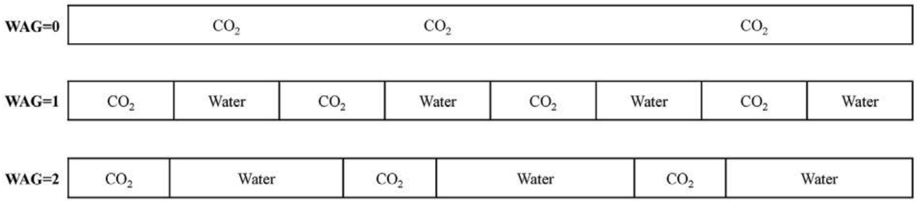

Fig. B1. Schematic illustration of WAG injection schemes for different WAG ratios.

## Appendix C. Production Metrics for Layered Geological Models

This appendix shows the effect of the WAG ratio and well patterns on the $CO_2$ net utilization ration, average oil production rates, and oil recovery factor during WAG injection in layered synthetic geological models.

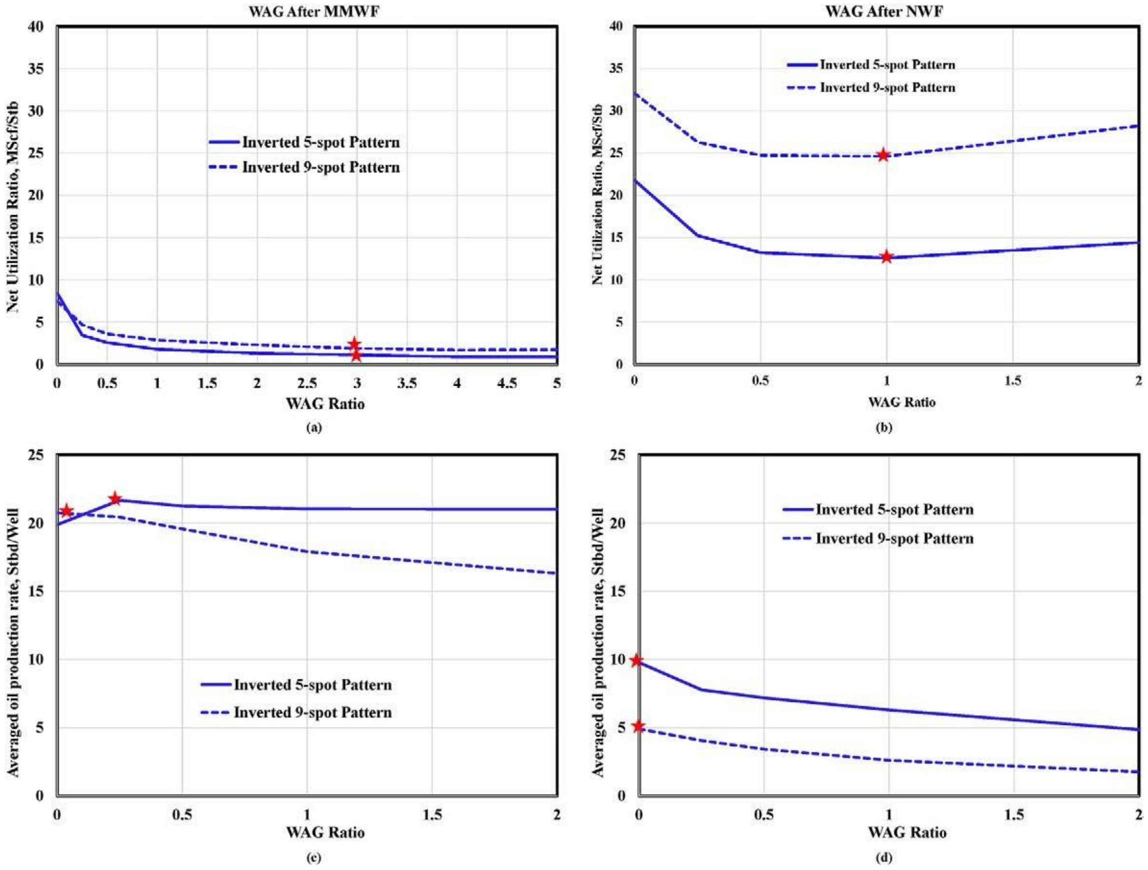

Fig. C1. $CO_2$ net utilization ratio and averaged oil production rates for the inverted 5-spot and inverted 9-spot well patterns. $CO_2$ WAG injection is simulated following the processes of NWF or MMWF. The layered geological model is used with $V_{DP}$ ¼ 0.62, $l_{Dx}$ ¼ 100. The WAG injection here is started following 30 years of MMWF.

## References

[1] Harouaka A, Trentham B, Melzer S. Long overlooked residual oil zones (ROZ's) are brought to the limelight. In: SPE-167209-MS presented at SPE unconventional resources conference Canada, calgary, alberta, Canada, 5-7 november; 2013. https://doi.org/10.2118/167209-MS.

[2] Kuuskraa V, Petrusak R, Wallace M. Residual oil zone "fairways" and discovered oil resources: expanding the options for carbon negative storage of CO2. Energy Procedia 2017;114:5438e50. https://doi.org/10.1016/j.egypro.2017.03.1688.

[3] Melzer LS, Kuuskraa VA, Koperna GJ. The origin and resource potential of residual oil zones. In: SPE 102964 presented at the annual technical conference and exhibition, san antonio, Texas, 24-27 september; 2006. https://doi.org/10.2118/102964-MS.

[4] Koperna GJ, Melzer LS, Kuuskraa VA. Recovery of oil resources from the residual and transitional oil zones of the Permian Basin. In: SPE 102972 presented at the annual technical conference and exhibition, san antonio, Texas, 24-27 september; 2006. https://doi.org/10.2118/102972-MS.

[5] Duncan IJ, Ren B, Male F, Baques V. Origin and exploitation of residual oil zones (ROZ) in the Permian Basin of Texas. In: Abstract presented at AAPG 2019 international conference and exhibition, buenos aires, Argentina, 27-30 august; 2019.

[6] Melzer LS. In: Melzer LS, editor. Residual oil zones (ROZs): a review of ROZ science and engineering; 2013.

[7] Jamali A, Ettehadtavakkol A. CO2 storage in residual oil zones: field-scale modeling and assessment. International Journal of Greenhouse Gas Control 2017;56:102e15.

[8] Ren B, Duncan IJ. Reservoir simulation of carbon storage associated with CO2 EOR in residual oil zones, san Andres formation of west Texas, Permian Basin, USA. Energy 2019a;167:391e401. https://doi.org/10.1016/j.energy.2018.11.007.

[9] Eclipse. Eclipse User's Guide. France: Schlumberger; 2016.

[10] Ampomah W, Balch RS, Grigg RB, McPherson B, Will RA, Lee SY, Dai Z, Pan F. Co-optimization of CO2-EOR and storage processes in mature oil reservoirs. Greenhouse Gases: Sci Technol 2017;7(1):128e42. https://doi.org/10.1002/ghg.1618.

[11] Pan F, McPherson BJ, Dai Z, Jia W, Lee SY, Ampomah W, Viswanathan H, Esser R. Uncertainty analysis of carbon sequestration in an active CO2-EOR field. International Journal of Greenhouse Gas Control 2016;51:18e28. https://doi.org/10.1016/j.ijggc.2016.04.010.

[12] Sifuentes WF, Marie AG, Martin JB. Modeling CO2 storage in aquifers: assessing the key contributors to uncertainty. In: SPE-123582 presented at SPE offshore europe oil and gas conference and exhibition, aberdeen, UK, 8-11 september; 2009. https://doi.org/10.2118/123582-MS.

[13] Lake LW, Johns R, Rossen B, Pope G. Enhanced oil recovery. second ed. Richardson TX: Society of Petroleum Engineers; 2014.

[14] Christensen JR, Stenby EH, Skauge A. Review of WAG field experience. SPE Reservoir Eval Eng 2001;4(2):97e106. https://doi.org/10.2118/71203-PA.

[15] Stalkup FI. Displacement of oil by solvent at high water saturation. SPE J 1970;10(4):337e48. https://doi.org/10.2118/2419-PA.

[16] Afzali S, Rezaei N, Zendehboudi S. A comprehensive review on enhanced oil recovery by water alternating gas (WAG) injection. Fuel 2018;227:218e46. https://doi.org/10.1016/j.fuel.2018.04.015.

[17] Wu X, Ogbe DO, Zhu T, Khataniar S. Critical design factors and evaluation of recovery performance of miscible displacement and WAG process. In: PET-SOC-2004-192 presented at the Canadian international petroleum conference, calgary, alberta, 8-10 june; 2004. https://doi.org/10.2118/2004-192.

[18] Rogers JD, Grigg RB. A literature analysis of the WAG injectivity abnormalities in the CO2 process. SPE Reservoir Eval Eng 2001;4(5):375e86. https://doi.org/10.2118/73830-PA.

[19] Bermudez L, Johns RT, Parakh HC. Parametric investigation of WAG floods above the MME. SPE J 2007;12(2):224e34. https://doi.org/10.2118/84366-PA.

[20] Kulkarni MM, Rao DN. Experimental investigation of miscible and immiscible water-alternating-gas (WAG) process performance. J Petrol Sci Eng 2005;48(1e2):1e20. https://doi.org/10.1016/j.petrol.2005.05.001.

[21] Malik QM, Islam MR. CO2 injection in the weyburn field of Canada: optimization of enhanced oil recovery and greenhouse gas storage with horizontal wells. In: SPE-59327-MS presented at SPE/DOE improved oil recovery symposium, Tulsa, Oklahoma, 3-5 April; 2000. https://doi.org/10.2118/59327-MS.

[22] Song Z, Li Z, Wei M, Lai F, Bai B. Sensitivity analysis of water-alternating-CO2 flooding for enhanced oil recovery in high water cut oil reservoirs. Comput Fluids 2014;99:93e103. https://doi.org/10.1016/j.compfluid.2014.03.022.

[23] Zuo L, Chen Y, Zou DE, Kamath J. Three-phase relative permeability modeling in the simulation of WAG injection. SPE Reservoir Eval Eng 2014;17(3):326e39. https://doi.org/10.2118/166138-PA.

[24] Chen S, Li H, Yang D, Tontiwachwuthikul P. Optimal parametric design for water-alternating-gas (WAG) process in a CO2-miscible flooding reservoir. J Can Petrol Technol 2010;49(10):75e82. https://doi.org/10.2118/141650-PA.

[25] Chen B, Reynolds AC. Ensemble-based optimization of the water-alternating-gas-injection process. SPE J 2016;21(3):786e98. https://doi.org/10.2118/173217-PA.

[26] Ettehadtavakkol A, Lake LW, Bryant SL. CO2-EOR and storage design optimization. International Journal of Greenhouse Gas Control 2014;25:79e92. https://doi.org/10.1016/j.ijggc.2014.04.006.

[27] Nwachukwu A, Jeong H, Sun A, Pyrcz M, Lake LW. Machine learning-based optimization of well locations and WAG parameters under geologic uncertainty. In: SPE 190239 presented at the SPE improved oil recovery conference, tulsa, Oklahoma, USA, 14-18 april; 2018. https://doi.org/10.2118/190239-MS.

[28] Shehata AM, El-banbi AH, Sayyouh H. Guidelines to optimize CO2 EOR in heterogeneous reservoirs. In: SPE-151871 presented at the north africa technical conference and exhibition, cario, Egypt, 20-22 february; 2012. https://doi.org/10.2118/151871-MS.

[29] Jensen J, Lake LW, Corbett PW, Goggin D. Statistics for Petroleum Engineers and Geoscientists. second ed. Netherlands: Elsevier Publishing; 2000pp270.

[30] Remy N, Boucher A, Wu J. Applied Geostatistics with SGeMS: a User's Guide. Cambridge University Press; 2009pp135.

[31] Li D, Lake LW. Scaling fluid flow through heterogeneous permeable media. SPE Adv Technol 1995;3(1):188e97. https://doi.org/10.2118/26648-PA.

[32] Tavassoli S, Pope GA, Sepehrnoori K. Investigation and optimization of the effects of geologic parameters on the performance of gravity-stable surfactant floods. SPE J 2016;21(3):761e75. https://doi.org/10.2118/178915-PA.

[33] Holtz MH. Residual gas saturation to aquifer influx: a calculation method for 3-D computer reservoir model construction. In: SPE-75502-MS presented at SPE gas technology symposium, calgary, alberta, Canada, 30 april-2 may; 2002. https://doi.org/10.2118/75502-MS.

[34] Leverett MC. Capillary behavior in porous solids. AIME Petroleum Transactions 1941;142:152e69. https://doi.org/10.2118/941152-G.

[35] Ren B. Local capillary trapping and permeability-Retarded Accumulation during geological carbon sequestration. Ph.D. Dissertation. Austin, Texas: The University of Texas at Austin; 2017. p. 17e8. https://repositories.lib.utexas.edu/handle/2152/62236.

[36] Trentham CR, Melzer LS, Vance DB. Commercial Exploitation and the origin of residual oil zones: Developing a case history in the Permian Basin of New Mexico and west Texas. RPSEA Final Report; 2012.

[37] Ren B, Duncan IJ. Modeling oil saturation evolution in residual oil zones: implications for CO2 EOR and sequestration. J Petrol Sci Eng 2019b;177:528e39. https://doi.org/10.1016/j.petrol.2019.02.072.

[38] Arab D, Kantzas A, Bryant SL. Water flooding of oil reservoirs: effect of oil viscosity and injection velocity on the interplay between capillary and viscous forces. J Petrol Sci Eng 2019;186. https://doi.org/10.1016/j.petrol.2019.106691.

[39] Honarpour MM, Nagarajan NR, Grijalba Cuenca A, Valle M, Adesoye K. Rock-fluid characterization for miscible CO2 injection: residual oil zone, Seminole field, Permian Basin. In: SPE-133089 presented at the annual technical conference and exhibition, florence, Italy, 19-22 september; 2010. https://doi.org/10.2118/133089-MS.

[40] Stone HL. Probability model for estimating three-phase relative permeability. J Petrol Technol 1970;22(2):214e8. https://doi.org/10.2118/2116-PA. SPE-2116-PA.

[41] Egermann P, Vizika O, Dallet L, Requin C, Sonier F. Hysteresis in three-phase flow: experiments, modeling and reservoir simulations. In: Paper SPE-65127-MS presented at SPE European petroleum conference, paris, France, 24-25 october; 2000. https://doi.org/10.2118/65127-MS.

[42] Element DJ, Masters JHK, Sargent NC, Jayasekera AJ, Goodyear SG. Assessment of three-phase relative permeability models using laboratory hysteresis data. In: Paper SPE-84903-MS presented at SPE international improved oil recovery conference in asia pacific, kuala lumpur, Malaysia, 20-21 october; 2003. https://doi.org/10.2118/84903-MS.

[43] Skauge A, Sorbie K. Status of fluid flow mechanisms for miscible and immiscible WAG. In: SPE-169747 presented at SPE EOR conference at oil and gas west asia, muscat, Oman, 31 march e 2 april; 2014. https://doi.org/10.2118/169747-MS.

[44] Spiteri EJ, Juanes R. Impact of relative permeability hysteresis on the numerical simulation of WAG injection. J Petrol Sci Eng 2006;50(2):115e39. https://doi.org/10.1016/j.petrol.2005.09.004.

[45] Ettehadtavakkol A. CO2 EOR-storage design Optimization under uncertainty. Ph.D. Dissertation. The University of Texas at Austin; 2013pp46.

[46] Jarrell PM, Fox CE, Stein MH, Webb SL. Practical aspects of CO2 flooding, vol. 22. Richardson, TX: Society of Petroleum Engineers; 2002.

[47] Walsh MP, Lake LW. Applying fractional flow theory to solvent flooding and chase fluids. J Petrol Sci Eng 1989;2(4):281e303. https://doi.org/10.1016/0920-4105(89)90005-3.

[48] Gong Y, Gu Y. Experimental study of water and CO2 flooding in the tight main pay zone and vuggy residual oil zone of a carbonate reservoir. Energy Fuels 2015;29(10):6213e23. https://doi.org/10.1021/acs.energyfuels.5b01185.

[49] KM (Kinder Morgan). Tall Cotton (san Andres) field. In: Presentation at the CO2 & ROZ conference, midland, Texas, 3e6 december; 2018. https://www.co2conference.net/wp-content/uploads/2019/01/Dec-2018-CO2-ROZ-Conf_____-Presentation_Tall-Cotton-vfinal.pdf.

[50] Aleidan A, Kwak H, Muller H, Zhou X. Residual-oil zone: paleo-oil characterization and fundamental analysis. SPE Reservoir Eval Eng 2017;20(2):260e8. https://doi.org/10.2118/179545-PA.

[52] Bunge AL, Radke CJ. CO2 flooding strategy in a communicating layered reservoir. J Petrol Technol 1982;34(12):2746e56. https://doi.org/10.2118/10289-PA.

[53] Chang YB, Lim MT, Pope GA, Sepehrnoori K. CO2 flow patterns under multiphase flow: heterogeneous field-scale conditions. SPE Reservoir Eng 1994;9:208e16. https://doi.org/10.2118/22654-PA.

[54] Chen B, Pawar RJ. Characterization of CO2 storage and enhanced oil recovery in residual oil zones. Energy 2019;183:291e304. https://doi.org/10.1016/j.energy.2019.06.142.

[57] Rassenfoss S. New permian oil play requires pumping and persistence. J Petrol Technol 2017;69(2):28e31. https://doi.org/10.2118/0217-0028-JPT.

[58] Sanguinito S, Singh H, Myshakin EM, Goodman AL, Dilmore RM, Grant TC, Morgan D, Bromhal G, Warwick PD, Brennan ST, Freeman PA, et al. Methodology for estimating the prospective CO2 storage resource of residual oil zones at the national and regional scale. International Journal of Greenhouse Gas Control 2020;96:103006. https://doi.org/10.1016/j.ijggc.2020.103006.

# 2

# Economic analysis of CCUS: Accelerated development for $CO_2$ EOR and storage in residual oil zones under the context of 45Q tax credit

Bo Ren [a], Frank Male [b,*], Ian J. Duncan [a]

[a] *Bureau of Economic Geology, Jackson School of Geosciences, The University of Texas at Austin, Austin, TX, USA*
[b] *Pennsylvania State University, State College, PA, USA*

## HIGHLIGHTS

- Residual oil zone development improves $CO_2$ utilization and storage economics.
- Joint development of MPZ and underlying ROZ are the best production strategy.
- Ideal water–gas injection ratio depends on a balance of oil prices and carbon credit.

## ABSTRACT

Residual oil zones (ROZ) undergoing $CO_2$ Enhanced Oil Recovery ($CO_2$-EOR) may benefit from specific strategies to maximize their value. We evaluated several strategies for producing from a Permian Basin, West Texas, USA field's ROZ. This ROZ lies below the main pay zone (MPZ) of the field. Such brownfield ROZs occur in the Permian Basin and elsewhere. Since brownfield ROZs are hydraulically connected to the MPZs, development sequences and schemes influence oil production, $CO_2$ storage, and net present value (NPV). We conducted economic assessments of various $CO_2$ injection/production schemes in the stacked ROZ-MPZ reservoir based on flow simulations of a high-resolution geocellular model built from wireline logs and core data and calibrated through production history matching. Flow simulations of water alternating gas (WAG) injection, such as switching injection from the MPZ to the ROZ and commingled production, were studied. Simulation results showed that simultaneous $CO_2$ injection into the MPZ and ROZ lead to the largest oil production and, generally, the largest NPV. If instead, $CO_2$ was simultaneously injected into the MPZ and ROZ, then into the ROZ alone, this maximized $CO_2$ storage. $CO_2$ storage can be used as a tax credit under the Internal Revenue Code, Section 45Q. Storage performance depends on the development approach and WAG ratio. Developing the ROZ increased storage compared to only producing from the MPZ. The WAG ratio to maximize oil production did not always yield the largest NPV. These findings are potentially applied to other Brownfield ROZs, which are common below San Andres reservoirs in the Permian Basin and other basins. ROZ development can increase oilfields' NPV and carbon storage potential. Our study can serve as an analog for similar reservoirs. This work provides valuable insights into the further optimization of brownfield ROZ development and information for operators to plan to develop stacked ROZ-MPZ reservoirs.

## 1. Introduction

$CO_2$ enhanced oil recovery ($CO_2$-EOR) is an established technology that can provide revenue and long-term $CO_2$ storage [1]. CCUS (carbon capture utilization and storage) is based on integration of $CO_2$-EOR with long term storage of anthropogenic $CO_2$ ($CO_2$-sequestration). Also, if the $CO_2$ used in the CCUS is anthropogenic, Section 45Q of the US Internal Revenue Code provides tax credits for capturing and sequestering the carbon during EOR.

For Section 45Q, as described in the Congressional Research Service [2], the US Internal Revenue Service lays out ways in which companies can receive tax credits if they capture $CO_2$ that would otherwise be in the atmosphere and geologically sequester it. There are different rates depending on when the carbon capture equipment began service and whether it was used in $CO_2$-EOR. For instance, a facility that began construction before 2026 and was finished in 2026 could earn $50/ton credits if the $CO_2$ was subsequently geologically sequestered, and $35/ton if it was used to enhance oil recovery.

Most $CO_2$ injection projects in oilfields target the main pay zones (MPZs) that were under primary production or being waterflooded. However, operators have also used this technology to target residual oil zones (ROZs). In ROZs, the oil saturation is too low for oil to flow

---

*Abbreviations:* CCUS, Carbon Capture Utilization and Storage; EOR, Enhanced Oil Recovery; MPZ, Main Pay Zone; ROZ, Residual Oil Zone; NPV, Net Present Value; CAPEX, Capital Expenditures; OPEX, Operational Expenditures.

* Corresponding author.
*E-mail address:* frank.male@psu.edu (F. Male).

https://doi.org/10.1016/j.apenergy.2022.119393
Received 18 November 2021; Received in revised form 8 April 2022; Accepted 29 May 2022

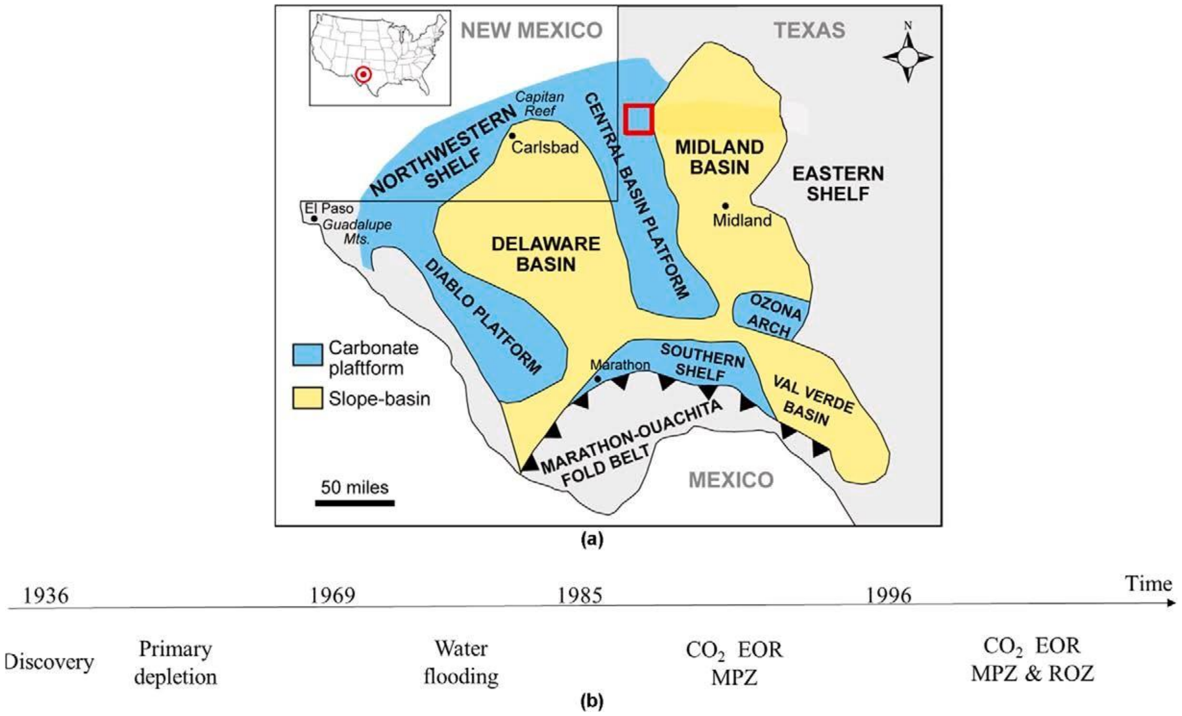

**Fig. 1.** (a) Tectonic map of the Permian Basin showing the location of the study area (red box) in west Texas. Modified from Ruppel et al. [41] and Dutton et al. [42]. (b) brief production history of the oilfield. (For interpretation of the references to color in this figure legend, the reader is referred to the web version of this article.)

without intervention [3,4,5]. ROZs cannot be successfully waterflooded but can be produced by $CO_2$-EOR or de-watering [6]. Brownfield ROZs underlie and connect to conventional oil reservoirs, whereas greenfield ROZs are laterally far from traditional MPZs [7]. Many brownfield ROZs occur in the US Permian Basin [8,3] and around the world, such as in Canada [9], China [10], the North Sea [11], and the Norwegian Continental Shelf [12].

ROZs are a good candidate for $CO_2$ EOR and storage. Reservoir processes make storing $CO_2$ in the ROZ easier than using aquifers [13]. Sanguinito et al. [14] evaluated $CO_2$ storage capacities in ROZs at the national and regional scales, and the results showed a large potential of $CO_2$ storage. $CO_2$ injection has produced oil from ROZs in several San Andres reservoirs in the Permian Basin [3]. There are disagreements about how to better exploit the ROZ reservoirs. Koperna et al. [15] concluded that “simultaneously implementing the flood in both the ROZ and MPZ” is a superior approach to “separately completing either the MPZ or the ROZ” in term of cumulative oil production. Jamali and Ettehadtavakkol [16] asserted that early expansion into brownfield ROZs compromises project economics. There is an increasing interest in oil production and incidental sequestration associated with ROZs [17].

A future challenge for $CO_2$ injection into ROZs will be to balance two economic drivers, producing oil and sequestering anthropogenic $CO_2$. The best strategy may be different for the ROZ versus the MPZ. Thus, there are advantages and disadvantages for co-developing the zones versus developing them in sequence. Since these ROZs are connected to MPZs, the interaction between the two zones will influence both production performance and the best development strategies. Such strategies include:

1) Co-developing the MPZ and ROZ
2) Developing only the MPZ
3) Expanding to the ROZ years or decades after developing the MPZ
4) Co-developing the MPZ and ROZ, but eventually stopping MPZ injection.

Selecting between these strategies should be based on:

- understanding the reservoir and geological characteristics,
- estimating the potential for $CO_2$ EOR and storage in the reservoirs, and
- strategic goals for oil production and carbon storage.

Several groups have performed economic analysis of $CO_2$ sequestration and evaluated the economics of different strategies for $CO_2$ injection (see for example [18,19]). These issues have also been studied by van ‘t Veld et al. [20], Wang et al. [21], Farajzadeh et al. [22], and Attanasi and Freeman [23], among others. Ettehadtavakkol et al [24] evaluated the impact of carbon tax credits for sequestration on economics of $CO_2$-EOR in conjunction with sequestration. Tayari et al. [25] investigated the impact of reservoir heterogeneity on the economics of $CO_2$ floods. They created a model based on three cost modules: injection, production, and $CO_2$ recycling, for valuing EOR projects. They then identified key model parameters including “production rate and composition, injection fluid rate and composition, and bottom-hole pressure,” combined with reservoir simulations to enable estimating injection, production, and $CO_2$ recycling, and thus the costs and revenue for specific development scenarios for different types of reservoirs. Zekri and Jerbi [19] determined that the nature and structure of the tax regime is critical to the viability of many EOR projects. Some projects are profitable only if there are tax incentives. Although the study of Tayari et al. [25] largely focused on $CO_2$ foam flooding, a topic outside the focus of the current study, these authors did explore how reservoir heterogeneity impacts project economics.

This paper is the first study to conduct a simulation of $CO_2$ injection into a ROZ using modern, a state-of-the-art simulator and a high-resolution static geologic model. Unlike previous studies by, for example, Wang et al. [26], Koperna et al. [15], Jamali and Ettehadtavakkol [16], Webb [27], and Liu and Ettehadtavakkol [17], who used static reservoir model that are low resolution and often highly upscaled, we minimized upscaling. We identified development strategies for brownfield ROZs that maximize either oil recovery, $CO_2$ storage, or NPV. This is the first study that uses high-resolution study of reservoir simulation, coupled to economic-analysis, to understand the economics of

ROZ versus MPZ and ROZ/MPZ being flooded at the same time.

A San Andres oilfield with a long history of commercial-scale ROZ production is used in this study. The static model was created from a comprehensive database of subsurface information, including well logs, core logs, and per-well production and injection data. We then conducted simulations to evaluate the influence of the four strategies on oil production as well as the utilization and retention (sequestration) of $CO_2$ in the reservoir. In comparison to many published studies, this high-quality reservoir model enabled decreasing the uncertainties in both our history match and prediction of oil production and $CO_2$ storage associated with $CO_2$-EOR. Based on this, we can conduct an extensive investigation of how various reservoir development scenarios impact the economic viability of brownfield ROZ projects.

Our analysis models the oil production and mass of $CO_2$ stored as a function of the WAG ratio and development scenarios. For each scenario, we focused on managing the development of brownfield ROZ to achieve the best financial outcome for the project, considering plausible values for carbon credits. We compared the optimal WAG ratios for NPV and cumulative oil production. The factors influencing economic results were used to conduct an economic sensitivity analysis. We also examined how tax credits impact economics. This study enhances our understanding of the economics of $CO_2$ EOR and storage in ROZs.

## 2. Background and methods

The field studied is in the northeast corner of the Central Basin Platform (Fig. 1a). The field has experienced primary production, waterflooding, and $CO_2$ injection (Fig. 1b). By 2010, the field had produced approximately 700 million barrels of oil, mostly from the MPZs of the Permian carbonate San Andres Formation. Fig. 1b shows a brief history of the field. $CO_2$ injection into the MPZ, begun in the early 1980s, slowed the production decline associated with the mature water flood operation. The operator began full-field ROZ development in 2007.

### 2.1. Geological characterization

The San Andres Formation is one of the several shallow water platform carbonates and mixed siliciclastic-carbonate units that developed on the shelves of the Permian basin in west Texas and New Mexico during the Permian (Leonardian-Guadalupian) [28]. This formation hosts the Upper Permian (Guadalupian) oil play. The sequence stratigraphy of the reservoir sequences by Kerans et al. [29] and Lucia et al. [30] found multiple, shallowing-up cycles. These cycles consist of mudstones and wackestones grading upward into grain-dominated packstones and grainstones. The reservoir caprock is a thick anhydrite layer. Seven carbonate microfacies and one anhydrite dominated microfacies have been described from 10 continuous cores in the northern and central part of the field [31]. The cores exhibit well-developed cyclic depositional sequences, with at least five cycles of sedimentation. The cores exhibit a very thick lower cycle of sedimentation, dominated almost entirely by open-marine facies. Upper cycles are thinner and exhibit a greater proportion of shallow restricted subtidal and tidal flat facies.

The facies within the reservoir studied are pervasively dolomitized. Ruppel and Cander [32] suggested that porosity preservation in these reservoirs was a consequence of dolomitization. Fusilinid mudstones/packstones exhibit variably preserved porosities. It has been suggested that the crinodal-rich facies, prevalent in the San Andres ROZ, is characterized by moderate to large (up to greater than 20%) porosity. Most of this porosity is secondary in origin [31]. Intercrystalline porosity is variably occluded by anhydrite cement. Bryozoan facies in the lower part of the cores have moderate porosities, generally ranging between 10 and 15%. Peloidal-oolitic shoal deposits have variable porosities, ranging from a few percent up to 22%. Most of the grainstones have their primary porosity reduced by anhydrite cements. Packstones exhibit high intercrystalline and leached dolomite rhomb porosity. A study by Duncan and Baqu´es (in prep) reveals no significant change in the nature of the facies or diagenesis between the MPZ and ROZ in the reservoir.

**Table 1**
Designed development scenarios for the brownfield ROZ.

| Scenario # | Injection Schemes | Production Schemes | Notes |
|---|---|---|---|
| 1 | MPZ & ROZ 40 yr commingled injection | MPZ & ROZ 40 yr comingled production | Develop MPZ & ROZ at the start |
| 2 | MPZ 40 yr injection | MPZ 40 yr production | Develop only MPZ |
| 3 | MPZ 20 yr injection + MPZ & ROZ 20 yr injection | MPZ 20 yr + MPZ & ROZ 20 yr | Develop MPZ initially and then develop MP & ROZ |
| 4 | MPZ & ROZ 20 yr injection + ROZ 20 yr injection | MPZ & ROZ 40 yr | Develop MPZ & ROZ and then develop ROZ |

### 2.2. Reservoir geomodeling and calibration

We integrated information from well logs, and core descriptions into a 3-D geological model. The cored-wells' logs (including spontaneous potential, gamma ray, density porosity, and neutron porosity) were analyzed, and through this we assigned facies to non-cored wells. Next, we conducted semi-variogram analysis of each facies group in each zone, adopting an exponential variogram model. Then, we used sequential indictor simulation to generate facies for the geomodel and sequential Gaussian simulation to generate porosity fields. The corresponding permeability fields were estimated as described in Ren and Duncan [5,33] and Ren et al. [13].

After building a full-field high resolution (cell size 20 × 20 × 2 ft) geological model, we generated a coarser model with cell sizes of 100 × 100 × 2 ft. We then cut a sector model and used it to history match the primary depletion and waterflooding for calibration of the MPZ portion of the reservoir model. More details are included in Appendix A.

### 2.3. Multiphase flow simulation of $CO_2$ injection and development scenarios

The calibrated reservoir model was then used to predict $CO_2$ EOR and storage potentials. For the simulation input, the rock/fluid interaction models (including fluid properties, relative permeability, and capillary pressure curves) refer to Ren et al. [13].

When predicting the performance of $CO_2$ EOR and storage, water alternating gas (WAG) injection was considered. Inverted 9-spot 80-acre patterns were adopted, which are currently being used in some cases to develop the MPZ (see for example [34]. The $CO_2$ injection rate is set to 3000 Mscf/day, and water injection rate is 1400 rb/day (reservoir barrel/day). The injection target pressure is at the reservoir fracturing pressure of 3900 psi [35]. Bottom hole pressure for producers is set to be the minimum miscibility pressure, which was measured as 1400 psi (based on the examples provided by [34]. The WAG ratio (i.e., reservoir volume ratio between injected water and $CO_2$) was varied from 0 to 4, through changing water injection duration while keeping $CO_2$ injection duration unchanged in each WAG cycle. The WAG ratio equal to 1 (base case) corresponds to 90 days of water injection alternating with 70 days of $CO_2$ injection. We run simulations of WAG injection for 40 years.

In our model scenarios, all injectors and producers involved in simulations are vertical and perforated according to the development scenarios as shown in Table 1. Different switching schedules and injection/production schemes were considered. Buffered boundary conditions as described by Ren and Duncan [5] were used in all simulations to mimic realistic flow scenarios.

**Table 2**
The settings of economic parameters in NPV calculation. These settings are based on the publications by Chen and Reynolds [43],Godec [44],Hultzsch et al. [45], and Tayari et al. [25].

| Component | Base Settings | Range |
|---|---|---|
| Oil price ($/STB) | 60 | 30–90 |
| Oil price basis ($/STB) | 1 | – |
| Gas price ($/Mscf) | 1.80 | 1.2–5 |
| Gas price basis ($/Mscf) | 0.25 | – |
| Tax credit for carbon storage ($/ton) | 0 | 0–90 |
| $CO_2$ purchase price ($/ton) | Oil price × 0.42 [*] | Oil price × (0.33–0.50) |
| Gas recycling cost ($/MSCF) | Oil price × 1% | – |
| Produced water management cost ($/STB)[ψ] | 0.85 | – |
| Liquid lifting cost ($/STB) [⁝] | 0.19 | 0.10–0.40 |
| Deepening cost ($/ft) | 150 | – |
| Annual discount rate | 0.12 | – |

[*] the price of $CO_2$ sold varies according to oil price.

[ψ] produced water management cost consists of water injection, water recycling, and water disposal.

[⁝] this is the liquid lifting cost for wells perforated in the MPZ only. The cost for other wells perforated in the ROZ or both the MPZ and ROZ is assumed to linearly increase with reservoir depth.

### 2.4. Economic modeling

The economics of $CO_2$ floods were studied by Flanders et al. [36] and are well understood. For most economic analyses of oil and gas projects the key approach is estimating the Net Present Value (NPV). The NPV is based on estimating the projects annual cash income; subtracting the capital and operational expenditures (CAPEX and OPEX); discounting the resultant cash flow to the time of the beginning of the project; and finally summing the annual estimates to compute the NPV. In some applications, the discount rate is based on the cost of borrowing money. In oil production projects, a higher discount rate is used to account for risk, particularly the risk that oil prices or the value of sequestering $CO_2$ may decrease during the lifetime of the project. In traditional $CO_2$-EOR projects, the cost of $CO_2$ has dominated the economics. When sequestration is considered, with some combination carbon credits and tax abatements, the economics can change significantly. In traditional $CO_2$-EOR operations, the CAPEX includes the cost of: infill drilling (where required); installation of a $CO_2$ cleanup plant; installation of a $CO_2$ compression system and pipeline networks for water and $CO_2$; well workovers (where required); and other surface installation expenses. OPEX includes the following major cost drivers: the cost of $CO_2$ purchase and the costs of electricity for running compressors to recycle $CO_2$ and pumps to produce fluids and to reinject water.

Project revenues come from sales of crude oil, short-chain hydrocarbon liquids (recovered from the $CO_2$ cleanup plant), and natural gas, as well as tax credits and carbon sequestration payments from the incidental storage of $CO_2$. In this analysis, the NPV consists of four components: oil revenue, carbon credits, operational expenses, and cost of well deepening into the ROZ. The OPEX (operational expenses) include $CO_2$ purchase, $CO_2$ recycling, produced water management, and liquid lifting costs.

The formula used to estimate NPV is equation (1). We consider the carbon storage credit a revenue term for simplicity. This is valid for comparing cases or for companies with sufficient tax liabilities. The following equations, 2–9, show how to calculate all of the components of NPV. We calculated the differences in cumulative net present values (NPV) between the various development scenarios. For these scenarios, we assumed the capital expenditures or CAPEX for MPZ development are sunk costs. This study focuses on the difference in calculated NPV that will be attributed exclusively to the development of brownfield ROZ projects. The current study investigates the impact of different $CO_2$ injection strategies on the project's NPV. It is assumed that the CAPEX for ROZ projects is limited to the cost of deepening wells from the MPZ to ROZ.

The cost assumptions are listed in Table 2. Sensitivity analysis of these parameters was also conducted using the range in Table 2. Specifically, our setting for the carbon storage tax credit was varied from $0 to $90/ton, with the base case at $0/ton. This covers the range of credit rates in Section 45Q. According to the Congressional Research Service [2], the carbon tax credits directly go to capture entities, and some operators are building capture facilities. The carbon credit was $11.91/ton in 2020 and inflation-adjusted annually for equipment set up before 2018. For equipment placed on or after that date, the carbon tax credit is $20.22/ton in 2020, increasing to $35/ton by 2026, and inflation-adjusted annually onward. Carbon credits can impact the oil prices, just as oil prices currently impact $CO_2$ costs. We examined the influence of this interaction on the optimal WAG ratio and NPV.

$$NPV = \sum_{n=1}^{N} \frac{Oil_{revenuen} + Carbon_{price_n} - Recurrent_{costn} - Welldeepen_{cost_n}}{(1+r)^n} \tag{1}$$

$$Oil_{revenuen} = \left[Q_{op(n)} - Q_{op(n-1)}\right] \times Oil_{price} \tag{2}$$

$$Carbon_{price}n = \left[Q_{gi(n)} - Q_{gi(n-1)}\right] - \left[Q_{gp(n)} - Q_{gp(n-1)}\right]) \times Storagetax \tag{3}$$

$$Recurrent_{costn} = Gaspurn + Gasrecyn + Water_{cost}n + Liquid_{lift}n \tag{4}$$

$$Gaspurn = \left[Q_{gi(n)} - Q_{gi(n-1)}\right] - \left[Q_{gp(n)} - Q_{gp(n-1)}\right]) \times Gaspur_{price} \tag{5}$$

$$Gasrecyn = \left[Q_{gp(n)} - Q_{gp(n-1)}\right] \times Gasrecy_{cost} \tag{6}$$

$$Water_{cost}n = \left[Q_{\wp(n)} - Q_{\wp(n-1)}\right] - \left[Q_{wi(n)} - Q_{wi(n-1)}\right]) \times Water_{cost} \tag{7}$$

$$Liquid_{Lift}n = \left[Q_{op(n)} - Q_{op(n-1)}\right] + \left[Q_{\wp(n)} - Q_{\wp(n-1)}\right]) \times Lift_{cost} \tag{8}$$

$$Welldeepen_{cost_n} = Cost_{perft} * Deepen_{length} \tag{9}$$

In the above equations,

$Oil_{revenuen}$, revenue from oil production at the $n_{th}$ year, $.

$Carbon_{price_n}$, price of carbon as incentive for carbon storage at the $n_{th}$ year, $.

$Recurrent_{costn}$, recurrent operation cost at the $n_{th}$ year, $.

$Welldeepen_{costn}$, well deepening cost for ROZ development at the $n_{th}$ year, $.

$r$, annual discount rate.

$n$, year numbering since the start of development.

$Q_{op(n)}$, cumulative oil production till the $n_{th}$ year, STB. $Q_{op(n-1)}$, cumulative oil production till the $(n\text{-}1)_{th}$ year, STB. $Oil_{price}$, the price of oil, $/STB.

$Q_{gi(n)}$, cumulative gas injection till the $n_{th}$ year, MSCF. $Q_{gi(n-1)}$, cumulative gas injection till the $(n\text{-}1)_{th}$ year, MSCF.

$Q_{gp(n)}$, cumulative gas production till the $n_{th}$ year, MSCF.

$Q_{gp(n-1)}$, cumulative gas production till the $(n\text{-}1)_{th}$ year, MSCF.

$Storagetax$, tax credit for carbon storage, $/Tonne.

$Gaspurn$, $CO_2$ purchase cost at the $n_{th}$ year, $.

$Gasrecyn$, $CO_2$ recycling cost at the $n_{th}$ year, $.

$Water_{cost}n$, produced water management cost at the $n_{th}$ year, $.

$Liquid_{lift}n$, produced liquid lifting cost at the $n_{th}$ year, $.

$Gaspur_{price}$, $CO_2$ purchase price, $/Tonne.

$Gasrecy_{cost}$, $CO_2$ recycling cost, $/MSCF.

$Q_{\wp(n)}$, cumulative water production till the $n_{th}$ year, STB.

$Q_{\wp(n-1)}$, cumulative water production till the $(n\text{-}1)_{th}$ year, STB.

$Q_{wi(n)}$, cumulative water injection till the $n_{th}$ year, STB. $Q_{wi(n-1)}$, cumulative water injection till the $(n\text{-}1)_{th}$ year, STB.

$Water_{cost}$, cost of produced water management, $/STB.

$Lift_{cost}$, cost of liquid lifting, $/STB.

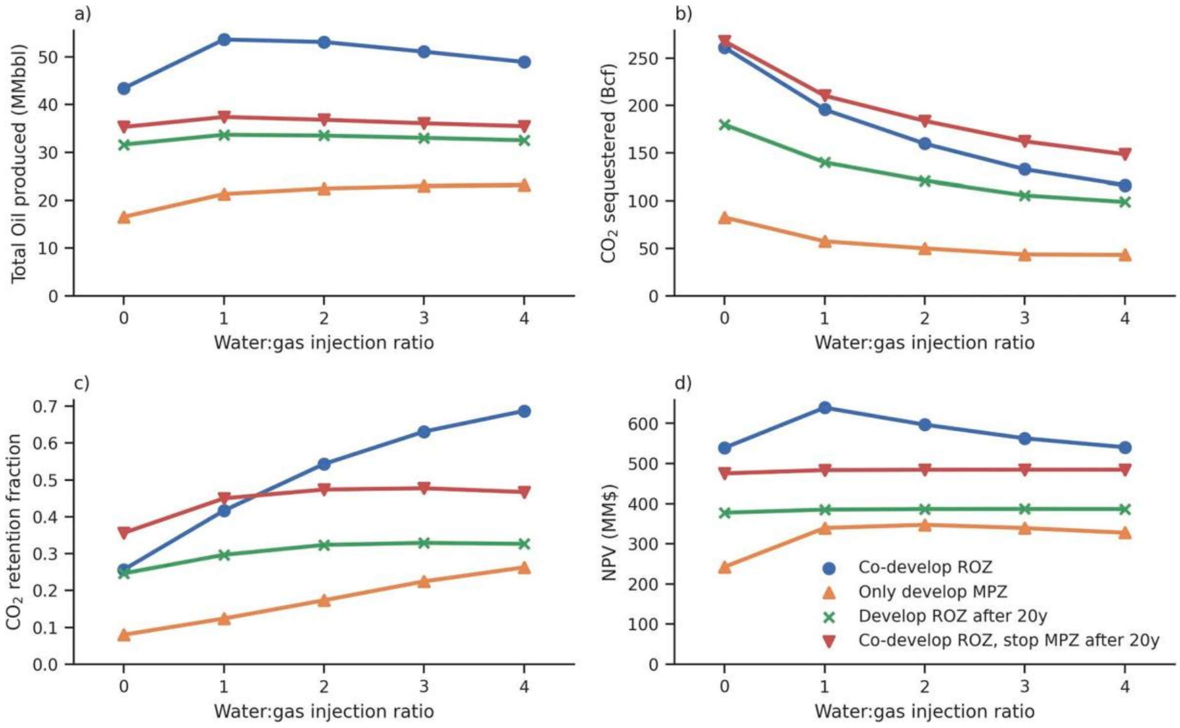

**Fig. 2.** Comparison of $CO_2$ EOR and storage metrics for different development scenarios at the end of WAG injection (at 40 years). Blue shows scenario #1, orange scenario #2, green scenario #3, and red scenario #4. (a) final oil production; (b) final amount of $CO_2$ stored; (c) final retention fraction of $CO_2$; (d) final NPV. The WAG ratio is in the range of 0–4. The final NPV is calculated using the base settings in Table 2. (For interpretation of the references to color in this figure legend, the reader is referred to the web version of this article.)

$Cost_{perft}$, cost of deepening wells into ROZ, \$/ft.
$Deepen_{length}$, depth of deepening for wells into ROZ, \$.

### 2.5. Metrics used to evaluate $CO_2$ EOR and storage performance

In addition to traditional EOR performance metrics (e.g., cumulative oil production), we also calculated metrics used to measure the performance of $CO_2$ storage in the brownfield ROZ.

Stored $CO_2$ amount = injected $CO_2$ amount – produced $CO_2$ amount.
$CO_2$ retention fraction = stored $CO_2$ amount / injected $CO_2$ amount.

All these $CO_2$ EOR and storage metrics change with time; the results given here are the values after 40 years.

## 3. Results

In this section, we show results for the simulation and economic

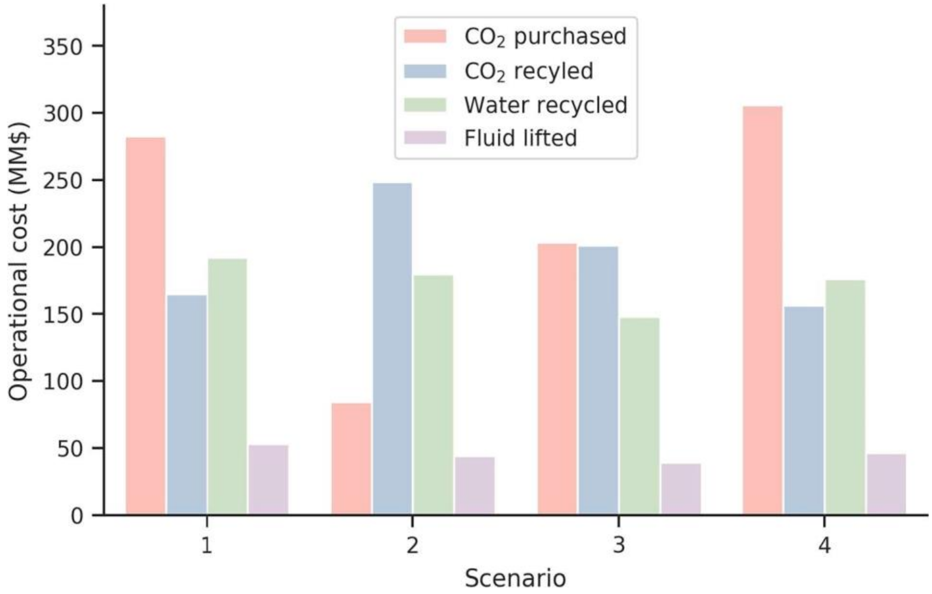

**Fig. 3.** Bar charts for 40 years of cost for development scenarios 1 through 4. The WAG ratio is 1 (70 days of $CO_2$ half-cycle alternating with 90 days of water half-cycle). We used the base case economics (see Table 2). The scenarios are as follows: 1) Co-developing the MPZ and ROZ 2) Developing only the MPZ 3) Expanding to the ROZ years or decades after developing the MPZ 4) Co-developing the MPZ and ROZ, but eventually stopping MPZ injection.

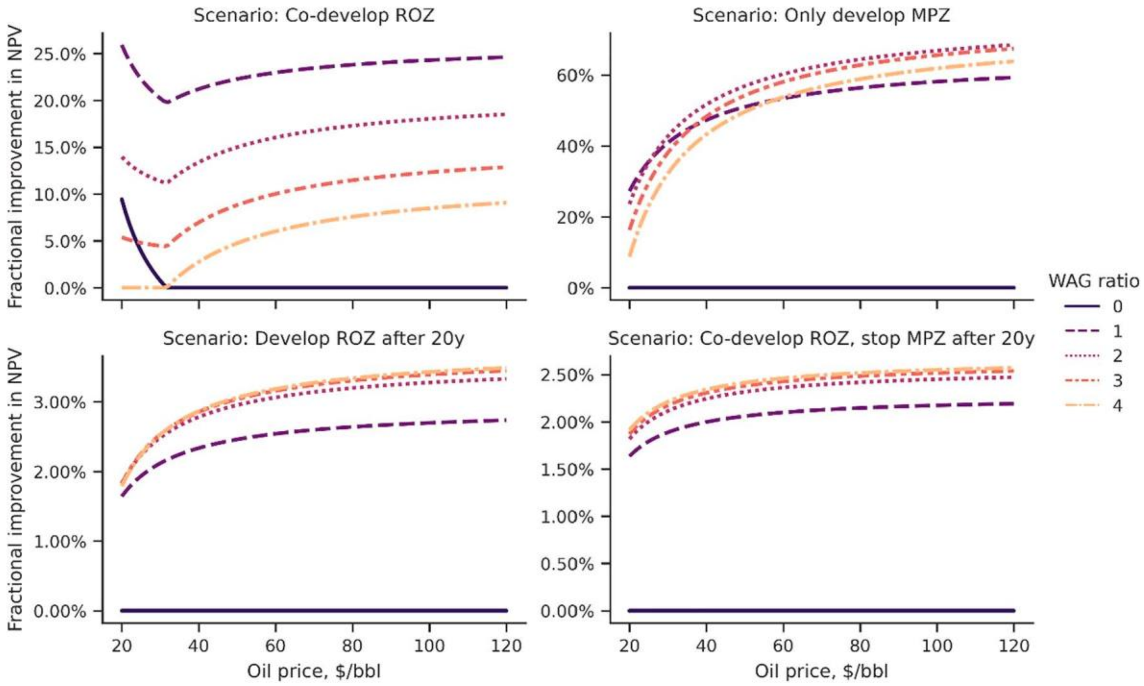

**Fig. 4.** Dependence of the NPV for different WAG ratios corresponding to maximum cumulative NPV on oil price. The vertical axis is the fraction improvement to the NPV compared to the worst WAG ratio (usually zero, for these cases). A fractional improvement of 100% means 2x better NPV than the worst WAG ratio at that oil price. The settings for other economic parameters match the base case (refer to Table 2). Note the different vertical scales.

metrics from developing a sector of the field in several different ways over 40 years. First are the development scenario comparisons, then we show the sensitivity to several uncertain economic variables.

### *3.1. Comparing different development scenarios*

Fig. 2 compared the $CO_2$ EOR and storage metrics for each development scenario (Table 1). Comingled injection and production (scenario #1) yield the largest oil production and NPV at all WAG ratios, and comingled injection followed by ROZ injection only (scenario #4) leads

**Fig. 5.** Dependence of the NPV for different WAG ratios corresponding to maximum cumulative NPV on carbon credit. The vertical axis is improvement to the NPV compared to the worst WAG ratio. 100% improvement means twice the NPV over the worst WAG ratio. The $CO_2$ purchasing cost is $50/Ton. The settings for other economic parameters match the base case (refer to Table 2). Note the different vertical scales. Inflection points occur when $CO_2$ credits are high enough that oil production is less important.

**Fig. 6.** Dependence of the NPV on different WAG ratios and development scenarios for the three levels of carbon credit reported in Section 45Q. The x-axis is the water-to-gas injection ratio, where 0 is all gas injection and 4 is four reservoir bbl of water injection to one reservoir bbl of gas injection. The y-axis is the net present value in million dollars. Color of the lines indicate different development scenarios, and the line style is the carbon tax credit.

to the largest $CO_2$ storage amount for each WAG ratio. The lowest NPV is for scenario #2, which is MPZ development only. Not developing the ROZ leads to the lowest oil production and $CO_2$ storage.

Injecting into the ROZ (scenarios #1, 3, and 4) increases the volume $CO_2$ accesses compared to MPZ injection only (scenario #2). Scenario 4 has the largest $CO_2$ storage because MPZ injection perforations were squeezed after 20 years of production, limiting $CO_2$ recycling. In some cases, the WAG ratio impacts project economics via oil sales. In scenarios 1 and 2, oil production depends on WAG ratio, but scenarios 3 and 4 do not display this sensitivity (Fig. 2a). For most scenarios, a WAG ratio of 1 achieves optimal or near-optimal NPV.

Storage is heavily dependent upon WAG ratio (Fig. 2b). As WAG ratio increases, less $CO_2$ is sequestered because less $CO_2$ is purchased, leading to increasing $CO_2$ retention fractions (Fig. 2c). This WAG effect on $CO_2$ retention is strongest when ROZ and MPZ are co-developed (scenario #1). At a WAG ratio of 1, constant MPZ + ROZ production leads to 40%

**Fig. 7.** Dependence of the NPV for high, low, and base cases of six key parameters, where the NPV-maximizing WAG ratio has been selected for each scenario. The x-axis of each subplot shows the modified variable. Along the y-axis is the project net present value (same scale for each plot). Different colors represent the different development scenarios. Shading shows the uncertainty in the average NPV for these sensitivities.

more oil being produced, but roughly the same amount of $CO_2$ sequestered as stopping MPZ production after 20 years. We examined the $CO_2$ saturation at the end of simulation, and it appears that $CO_2$ did not largely migrate from the ROZ to the MPZ.

The largest NPV came from adopting a WAG ratio of 1 and jointly developing the ROZ and MPZ. The lowest NPVs came from never developing the ROZ. The main difference between these extremes came from oil sales; operating costs were comparable (Fig. 3).

Operational costs far outweigh capital costs when considering developing the ROZ after having built an MPZ $CO_2$ flood. It costs roughly \$150/ft to deepen vertical wells in a conventional onshore field (not including lost production). The cost of deepening all 119 wells into the ROZ is 4.5 million dollars. This is equivalent to purchasing about 200 thousand tons of $CO_2$, whereas in scenario #1, 6–15 million tons of $CO_2$ are purchased.

Most of the costs for all scenarios come from recycling and purchasing of $CO_2$. Fig. 3 shows the operational cost bar charts after 40 years of development, given a WAG ratio of 1. The total OPEX of the scenario #1 is the most (\$871 million), and scenario 2 is the least (\$700 million). The other two are in between. For MPZ-only development (scenario #2), $CO_2$ purchasing costs are far lower than recycling cost. When moving from the MPZ to ROZ development, the large ROZ water saturation does not greatly increase lifting and water management costs. Therefore, there are few differences in these costs between scenarios, except some water management savings in scenario #3 from delayed ROZ development.

### 3.2. Sensitivity analysis

We performed a sensitivity analysis on the economic assumptions and WAG ratio. This included oil price, carbon sequestration tax credits, $CO_2$ purchasing price, and lifting cost. Geologic and fluid parameters were held fixed during this analysis since we focused on economic assessment. To focus on the effect of WAG ratio rather than the obvious (and linear) effect of price, we generated plots normalized to the lowest NPV WAG ratio to see the uplift for selecting a better water–gas injection ratio.

WAG ratios can significantly change the NPV for both EOR and CCUS applications (Figs. 4-5). This uplift varies from over 100% for only developing the MPZ and focusing on carbon tax credits to less than 1% for co-developing the ROZ and MPZ but stopping MPZ exploitation after 20 years. Without considering carbon credits, the benefit of selecting the best WAG ratio can be from 65% at high oil prices when developing only the MPZ to less than 2% at low oil prices when delaying ROZ development.

The optimal WAG ratio depends on the oil price and is not necessarily the WAG ratio for the largest oil production (Fig. 4). When co-developing the ROZ, selecting a WAG ratio of 1 is consistently the best option, but when only developing the MPZ, at low prices a WAG ratio of 1 is ideal, but above \$30/bbl, a WAG ratio of 2 is better. When delaying development of the ROZ, higher WAG ratios improve the NPV.

For almost all scenarios and oil prices, a WAG ratio of 0 is the worst choice. This is due to lower total oil production and higher $CO_2$ purchasing and recycling costs. Both $CO_2$ purchasing and recycling scale with oil price. However, when co-developing the ROZ at sub-\$30/bbl oil prices, it is better than a high WAG ratio because of lower operational costs from fluid lifting and water recycling.

Carbon storage tax credits for CCUS also affect the ideal WAG ratio (Fig. 5). In Scenario #3, where the operator develops the ROZ 20 years after starting $CO_2$ injection in the MPZ, the ideal WAG ratio varies from 4 at no tax credit to 0 for a tax credit of greater than \$70/ton carbon dioxide sequestered. The increase in NPV from optimizing WAG ratio can be from over 100% to about 1% for different scenarios and carbon tax credits.

The maximum $CO_2$-EOR related tax credit proposed in 45Q is \$35/Ton. We show the NPV for different development scenarios and 45Q carbon credits in Fig. 6. At all carbon credit levels, co-developing the ROZ maximizes NPV, followed by co-developing the ROZ and stopping MPZ exploitation after 20 years, then developing the ROZ after 20 years, and finally, developing the MPZ has the lowest NPV.

Fig. 7 shows the sensitivity of NPV to several economic parameters (i.e., oil price, natural gas sales price, lifting cost, and recycling water and $CO_2$ prices). We selected the WAG ratio that maximized NPV for each scenario. The most important parameters, in order, are oil price, $CO_2$ cost, and gas sales price. Co-developing the ROZ leads to the best NPV expectations at all oil prices greater than \$6/bbl. After development costs for the MPZ $CO_2$ flood have been paid off, all scenarios have a breakeven price for oil prices between \$2/bbl (MPZ only) and \$5/bbl (develop ROZ, close MPZ after 20 years) for base case operating expenditures and the costs of extending to the ROZ (if the scenario includes ROZ development).

## 4. Discussion

The focus of this paper is on the economics, but the simulations of these different development scenarios tell us a few things about $CO_2$-EOR. For instance, for MPZ-only development, most of the injected $CO_2$ channels into producers and is recycled (as illustrated in Fig. 2). This channeling is less prominent in the ROZ. A comparison between scenarios #1 and #4 shows a large difference in oil production (Fig. 2a) but similar $CO_2$ storage (Fig. 2b). The lack of $CO_2$ migration we see is consistent with surveys we conducted of the $CO_2$ saturation fields.

### 4.1. Economics for ROZ versus MPZ $CO_2$ flood projects

Brownfield ROZ projects are able to use the same recycle plant and other infrastructure as the original $CO_2$ EOR development in the MPZ. Therefore, expanding an MPZ $CO_2$ flood to the ROZ requires little capital expenditure. As a result, in the payback period (the time from the initiation of the project to the time at which positive cash flow begins) is shorter. Co-developing the ROZ also accelerates the oil production and maximizes the ultimate recovery (Fig. 2). Accelerating the production improves the NPV, further improving the economics over MPZ-only $CO_2$ floods.

### 4.2. Role of varying the WAG ratios on the economics of $CO_2$ floods

Previous studies (e.g., [37,38]) of optimal WAG ratios for $CO_2$-EOR projects have largely ignored economics. As the WAG ratio represents the relative volume of $CO_2$ versus water being injected, $CO_2$ prices and tax breaks mean the ratio will significantly affect the operational expenses.

The NPV is more sensitive to the WAG ratio when only developing the MPZ than for scenarios where the ROZ is also developed (Figs. 3 and 4). In the MPZ, continuous $CO_2$ injection leads to early breakthrough and more $CO_2$ recycling, thus increasing operational expenses while simultaneously decreasing oil production when compared to WAG. In the ROZ, the low mobility of oil slows channeling, which decreases the effect of the WAG ratio on the NPV.

$CO_2$ tax breaks affect the ideal WAG ratio by over 20% for much of the range of carbon credits when either only developing the MPZ or co-developing the ROZ (Fig. 4). There are complex interactions between the oil price, carbon credit, WAG ratio, and their effects on the NPV for both MPZ and ROZ project development.

### 4.3. Role of $CO_2$ sequestration tax credits

Ettehadtavakkol et al. [24] modeled the economics of different rates of fluid injection, WAG ratio and pattern flood duration. They examined the discounted cash flows from $CO_2$ EOR projects. They examined breakeven oil prices as $CO_2$ utilization, oil production rate and purchase price of $CO_2$ are varied. Significantly, they also considered the impact of

**Fig. A1.** (a) The Petrel unit boundary of full-field geological model for the field with the dashed square in (a) representing the outer boundaries of a cut sector model. (b) Porosity fence diagram. (c) Permeability field with the two sectional cut for direct visualization. Four zones (gas cap, MPZ, ROZ, and water leg) are differentiated with different colors for easy look. The depth cutoff for the three contacts are 1725 ft (gas-oil-contact), 1935 ft (producing water-oil-contact or the contact between the MPZ and ROZ), and 2200 ft (free water level). (d) Permeability field of the cut sector with all the vertical well locations shown on the top of model.

$CO_2$ sequestration payments. Their main findings included a recommended range ($20 - $40/tonne) of $CO_2$ storage tax for sustainable $CO_2$ EOR-storage operations.

We found that carbon tax credits could be a significant source of income for $CO_2$-EOR projects. Even when the carbon credit is significantly less than the cost of acquiring anthropogenic $CO_2$, this can make $CO_2$-EOR projects more profitable. Also, as said above, adding carbon credits can lead to changes in the NPV-maximizing WAG ratio.

A significant point in the applicability of tax credits appears to be when $CO_2$ storage becomes more important than oil sales for selecting the NPV (Fig. 5). This is heavily scenario-dependent, and it happens at the lowest $CO_2$ credit for immediate ROZ development. Thus, we may conclude that ROZ development allows for more flexibility in selecting the best WAG ratio to balance oil sales with carbon credits.

Section 45Q requires projects to capture 500,000 metric tons/year to apply for this credit. In the most carbon-storage-intensive scenario, our whole field study sequestered 59 million metric tons for the first 20 years (note, our simulations only covered a portion of the field), or about 1.6 million metric tons/year. The least carbon-intensive development scenario would still sequester 0.2 million metric tons per year.

For comparison, a 500-megawatt coal-fired power plant emits about 3 million metric tons a year [39]. Thus, it is possible to use the full $CO_2$ output of a power plant to supply $CO_2$ to a ROZ flood of this size and meet the minimum requirements for Section 45Q.

Furthermore, the Permian basin has an extensive $CO_2$ pipeline network, so a $CO_2$ storage project in this area would have many potential $CO_2$ CCUS sites to supply. There are 71 projects in West Texas served by the Denver City $CO_2$ Hub [40].

### 4.4. *Sensitivity of results to variations in income and costs*

The WAG ratio that yields the maximum oil production does not necessarily give the maximum NPV. Oil prices from $40–80/bbl tend to have the same ideal WAG ratio (Fig. 4). For carbon storage, though at sufficiently large carbon credits, the ideal WAG ratio drops (Fig. 5). While oil prices, gas prices, and $CO_2$ costs affect the project NPV significantly, the best NPV always resulted from co-developing the ROZ when developing the MPZ $CO_2$ flood. The lift cost, $CO_2$ recycling cost, and water management cost did not greatly affect project economics (Fig. 7).

## 5. Summary and conclusions

We evaluated different development strategies and their associated uncertainties through integrated full-physics flow simulation and economic assessment for a San Andres Unit Brownfield residual oil zone.

**Fig. A2.** History matching of oil production rate (a), water cut (b), gas-oil-ratio (c), and reservoir pressure (d) during primary depletion and waterflooding periods. Large dots are field measurements, and lines represent simulation results.

The assessment is based on a high-resolution geological model with integrated geological and reservoir characterization and careful calibration through historical primary and secondary production data matches. To better compare development strategies, we defined and calculated a series of metrics (*e.g.*, cumulative oil production, $CO_2$ storage amount, $CO_2$ retention fraction, and net present value (NPV)) for $CO_2$ EOR and storage. Water alternating gas (WAG) ratios were tuned to maximize either oil production or NPV. The influence of economic parameters (e.g., oil price and carbon credit) on favorable WAG ratios were examined. We found that:

i) Simultaneous WAG injection into both the MPZ and ROZ maximizes oil production and NPV, as compared to other injection strategies.
ii) The NPV is more sensitive to the WAG ratio when co-developing the ROZ and MPZ than in MPZ-only flooding.
iii) When targeting $CO_2$ storage, switching from comingled injection to only ROZ injection after two decades of production is a viable strategy. The optimal switching time needs further study.
iv) As the $CO_2$ tax credit varies, the best WAG ratios to maximize NPV change to balance benefits from oil production and carbon storage.

This work provides a basis for future optimization of $CO_2$ EOR and storage in brownfield ROZs.

## Author contribution

**Bo Ren:** Conceptualization, Methodology, Economic modeling, Writing – original draft, Editing. **Frank Male:** Economic analysis, Figure preparation, Writing - second draft, Editing. **Ian Duncan:** Conceptualization, Management, Review, Rewriting, Editing.

## Declaration of Competing Interest

The authors declare that they have no known competing financial interests or personal relationships that could have appeared to influence the work reported in this paper.

## Acknowledgements

We thank Robin Dommisse for valuable assistance in the geomodelling aspects of this work. Bo Ren wishes to thank William Ambrose for advice and mentoring during the project. Bo Ren also wants to thank Dr. Victor del Carpio Neyra for discussing storage tax credit. Our colleague Dr. Jerry Jensen also made useful suggestions and comments. This study is part of a long-term project investigating ROZ reservoirs in the Permian Basin of Texas being carried out by the Bureau of Economic Geology's (BEG's) State of Texas Advanced Resource Recovery (STARR) CCUS Team and was funded in part by a US Department of Energy contract through the National Energy Technology Laboratory under DOE Award Number FE0024375 (PI: Duncan). The opinions of the authors do not necessarily reflect those of the United States Government or any agency thereof. We thank Professor Larry W. Lake, who holds the Shahid and Sharon Ullah Endowed Chair at the University of Texas, for his ongoing interest in our work and for his insightful questions. This paper is published with the permission of the Director of the BEG.

## Appendix A:. Model construction and validation

### *Geological Models*

Fig. A1 shows the full-field porosity and permeability, along with permeability for the sector model. We selected this porosity/permeability distribution from the batch of realizations that conform to geological characterizations and reservoir heterogeneity. The cut sector consists of 25 inverted 9-spot 80-acre patterns, with 25 vertical injectors and 94 vertical producers.

### *History Matching*

The simulation in this study were based in part on a reservoir model for the MPZ that was used to history match the oil production, water cut, gas-oil-ratio (GOR), and mean reservoir pressure. The static model is calibrated, and a good match was found for oil production rate, water cut, and reservoir pressure (Fig. A2). The history match of GOR is challenging. GOR matching is hindered by the both the lack of information about the gas cap size and lack of knowledge of the vertical fracture permeability of the reservoir. Still, the overall trend and peak GOR rates are captured.

## References

[1] IPCC (Intergovernmental Panel on Climate Change). IPCC Special Report on Carbon Dioxide Capture and Storage. Cambridge, UK: Cambridge University Press; 2005.

[2] Congressional Research Service. The Tax Credit for Carbon Sequestration (Section 45Q). Accessed 11 October 2021, https://sgp.fas.org/crs/misc/IF11455.pdf; 2021.

[3] Melzer LS. Residual Oil Zones Changing Commercial Reservoir Models. Oil Gas J 2017;115(4):52–5.

[4] Rouech´e JN, Karacan CO¨. Zone Identification and Oil Saturation Prediction in a Waterflooded Field: Residual Oil Zone, East Seminole Field, Texas, USA, Permian Basin. In: SPE-190170-MS presented at the SPE Improved Oil Recovery Conference; 2018. https://doi.org/10.2118/190170-MS.

[5] Ren B, Duncan IJ. Reservoir Simulation of Carbon Storage Associated with $CO_2$ EOR in Residual Oil Zones, San Andres Formation of West Texas, Permian Basin. USA *Energy* 2019;167:391–401. https://doi.org/10.1016/j.energy.2018.11.007.

[6] Jamali, A., Ettehadtavakkol, A., Watson, M., Zeinuddin, O. 2017. Depressurizing Permian Basin San Andres Residual Oil Zones: A Feasibility Study. SPE-187482-MS presented at SPE Liquids-Rich Basins Conference - North America, Midland, Texas, 13-14 September. https://doi.org/10.2118/187482-MS.

[7] Harouaka, A., Trentham, B., Melzer, S. 2013. Long Overlooked Residual Oil Zones (ROZ's) Are Brought to the Limelight. SPE-167209-MS presented at SPE Unconventional Resources Conference Canada, Calgary, Alberta, Canada, 5-7 November. https://doi.org/10.2118/167209-MS.

[8] Melzer, L. S., Kuuskraa, V. A., Koperna, G. J. 2006. The Origin and Resource Potential of Residual Oil Zones. SPE-102964-MS presented at the SPE Annual Technical Conference and Exhibition, San Antonio, Texas, 24-27 September. https://doi.org/10.2118/102964-MS.

[9] Gong Y, Gu Y. Experimental Study of Water and $CO_2$ Flooding in the Tight Main Pay Zone and Vuggy Residual Oil Zone of a Carbonate Reservoir. Energy Fuels 2015;29(10):6213–23. https://doi.org/10.1021/acs.energyfuels.5b01185.

[10] Fang H, Xu H, Wang Z, Jiang T, Zhao Y, Li J. Formation Mechanism of the Donghe Sandstone Residual Oil Zone in the Tarim Basin, NW China. J Petrol Sci Eng 2018; 171:1023–32. https://doi.org/10.1016/j.petrol.2018.08.009.

[11] Stewart RJ, Johnson G, Heinemann N, Wilkinson M, Haszeldine RS. Low Carbon Oil Production: Enhanced Oil Recovery with $CO_2$ from North Sea Residual Oil Zones. Int J Greenhouse Gas Control 2018;75:235–42. https://doi.org/10.1016/j.ijggc.2018.06.009.

[12] Bergmo PE, Grimstad AA, Kurtev K. Mapping of Paleo Residual Oil Zones on the NCS and the Potential for Production by $CO_2$-EOR. Int J Greenhouse Gas Control 2018;75:254–61. https://doi.org/10.1016/j.ijggc.2018.06.005.

[13] Ren, B., Male, F., Wang, Y., Baqu´es, V., Duncan, I.J., Lake, L.W. 2019. Oil Saturation in Residual Oil Zones and Its Effect on $CO_2$ WAG Injection Strategies. SPE-196230-MS presented at the SPE Annual Technical Conference and Exhibition, Calgary, Alberta, 30 September-2 October. https://doi.org/10.2118/196230-MS.

[14] Sanguinito S, Singh H, Myshakin EM, Goodman AL, Dilmore RM, Grant TC, et al. Methodology for Estimating the Prospective $CO_2$ Storage Resource of Residual Oil Zones at the National and Regional Scale. Int J Greenhouse Gas Control 2020;96: 103006. https://doi.org/10.1016/j.ijggc.2020.103006.

[15] Koperna, G.J., Melzer, L.S. and Kuuskraa, V.A. 2006. Recovery of Oil Resources from the Residual and Transitional Oil Zones of the Permian Basin. SPE-102972-MS presented at the SPE Annual Technical Conference and Exhibition, San Antonio, Texas, 24-27 September. https://doi.org/10.2118/102972-MS.

[16] Jamali A, Ettehadtavakkol A. $CO_2$ Storage in Residual Oil Zones: Field-scale Modeling and Assessment. Int J Greenhouse Gas Control 2017;56:102–15. https://doi.org/10.1016/j.ijggc.2016.10.005.

[17] Liu J, Ettehadtavakkol A. A Technical Turning Point-Based Framework to Optimize $CO_2$ EOR-Storage: Capacity Dynamics of Brownfield Residual Oil Zones. J Petrol Sci Eng 2022;210:109889. https://doi.org/10.1016/j.petrol.2021.109889.

[18] Jiang J, Rui Z, Hazlett R, Lu J. An Integrated Technical-economic Model for Evaluating $CO_2$ Enhanced Oil Recovery Development. Appl Energy 2019;247: 190–211. https://doi.org/10.1016/j.apenergy.2019.04.025.

[19] Zekri A, Jerbi KK. Economic Evaluation of Enhanced Oil Recovery. Oil & Gas Science and Technology 2002;57(3):259–67. https://doi.org/10.2516/ogst:2002018.

[20] Veld KVt, Mason CF, Leach A. The Economics of $CO_2$ Sequestration through Enhanced Oil Recovery. Energy Procedia 2013;37:6909–19. https://doi.org/10.1016/j.egypro.2013.06.623.

[21] Wang X, van 't Veld K, Marcy P, Huzurbazar S, Alvarado V. Economic co-optimization of oil recovery and CO2 sequestration. Appl Energy 2018;222: 132–47. https://doi.org/10.1016/j.apenergy.2018.03.166.

[22] Farajzadeh R, Eftekhari AA, Dafnomilis G, Lake LW, Bruining J. On the Sustainability of $CO_2$ Storage through $CO_2$–Enhanced Oil Recovery. Appl Energy 2020;261:114467. https://doi.org/10.1016/j.apenergy.2019.114467.

[23] Attanasi ED, Freeman PA. Decision Analysis and $CO_2$–Enhanced Oil Recovery Development Strategies. Nat Resour Res 2022;31(1):735–49. https://doi.org/10.1007/s11053-021-09983-6.

[24] Ettehadtavakkol, A., Lake, L. W., Bryant, S. L. 2014. Impact of Storage Tax Credit on Economic Viability of $CO_2$ Storage With EOR. SPE-169838-MS presented at the SPE Hydrocarbon Economics and Evaluation Symposium, Houston, Texas, 19-20 May 2014. https://doi.org/10.2118/169838-MS.

[25] Tayari F, Blumsack S, Johns RT, Tham S, Ghosh S. Techno-economic Assessment of Reservoir Heterogeneity and Permeability Variation on Economic Value of Enhanced Oil Recovery by Gas and Foam Flooding. J Petrol Sci Eng 2018;166: 913–23. https://doi.org/10.1016/j.petrol.2018.03.053.

[26] Wang FP, Lucia FJ, Kerans C. Integrated Reservoir Characterization Study of a Carbonate Ramp Reservoir: Seminole San Andres Unit, Gaines County, Texas. SPE Reservoir Evaluation & Engineering 1998;1(02):105–13. https://doi.org/10.2118/36515-PA.

[27] Webb, N. 2019. A Nonconventional $CO_2$ -EOR Target in the Illinois Basin: Oil Reservoirs of the Thick Cypress Sandstone (No. DOE-UofI-24431). United States. https://www.osti.gov/servlets/purl/1545654.

[28] Ward R, Kendall CG, St C, Harris PM. Upper Permian (Guadalupian) Facies and Their Association with Hydrocarbons Permian Basin: West Texas and New Mexico. AAPG 1986;70:239–62. https://doi.org/10.1306/9488566F-1704-11D7-8645000102C1865D.

[29] Kerans C, Lucia FJ, Senger RK. Integrated Characterization of Carbonate Ramp Reservoirs Using Permian San Andres Formation Outcrop Analogs. AAPG Bull 1994;78(2):181–216. https://doi.org/10.1306/BDFF905A-1718-11D7-8645000102C1865D.

[30] Lucia FJ, Kerans C, Wang FP. Fluid-Flow Characterization of Dolomitized Carbonate-Ramp Reservoirs: San Andres Formation (Permian) of Seminole Field and Algerita Escarpment. Permian Basin, Texas and New Mexico SEPM 1995;SC34: 129–53. https://doi.org/10.2110/scn.95.34.0129.

[31] Duncan, I.J. and Baqu´es, V., in prep. Diagenetic Evolution of the Residual Oil Zone (ROZ) Platform Carbonates San Andres Seminole Unit, Permian Basin, West Texas: Constraints from C, O and Sr isotopes. Unpublished.

[32] Ruppel, S.C., Cander, H.S., 1988, Dolomitization of Shallow Water Platform Carbonates by Seawater and Seawater-Derived Brines: the San Andres Formation (Guadalupian), West Texas, in Shukla, V., and Baker, P.A., eds., Sedimentology and Geochemistry of Dolostones: SEPM Spec. Publ. 43, 245–262. https://doi.org/10.2110/pec.88.43.0245.

[33] Ren B, Duncan IJ. Modeling Oil Saturation Evolution in Residual Oil Zones: Implications for $CO_2$ EOR and Sequestration. J Petrol Sci Eng 2019;177:528–39. https://doi.org/10.1016/j.petrol.2019.02.072.

[34] Honarpour MM, Nagarajan NR, Grijalba Cuenca A, Valle M, Adesoye K. Rock-Fluid Characterization for Miscible $CO_2$ Injection: Residual Oil Zone, Seminole Field, Permian Basin. In: SPE-133089 presented at the Annual Technical Conference and Exhibition; 2010. https://doi.org/10.2118/133089-MS.

[35] Alcorn ZP, Fredriksen SB, Sharma M, Rognmo AU, Føyen TL, Fernø MA, et al. An Integrated Carbon-Dioxide-Foam Enhanced-Oil-Recovery Pilot Program with Combined Carbon Capture, Utilization, and Storage in an Onshore Texas Heterogeneous Carbonate Field. SPE Reservoir Eval Eng 2019;78(2):181–216. https://doi.org/10.2118/190204-PA.

[36] Flanders, W.A., McGinnis, R.A. and Shatto, A.G. 1993, October. $CO_2$ EOR Economics for Small-to-Medium-Size Fields. SPE-26391-MS presented at the SPE Annual Technical Conference and Exhibition, Houston, Texas, 3-6 October. https://doi.org/10.1016/j.apenergy.2019.114467.

[37] Chen S, Li H, Yang D, Tontiwachwuthikul P. Optimal Parametric Design for Water-Alternating-Gas (WAG) Process in a CO2-Miscible Flooding Reservoir. J Can Pet Technol 2010;49(10):75–82. https://doi.org/10.2118/141650-PA.

[38] Wu, X., Ogbe, D. O., Zhu, T., Khataniar, S. 2004. Critical Design Factors and Evaluation of Recovery Performance of Miscible Displacement and WAG Process. PETSOC-2004-192 presented at the Canadian International Petroleum Conference, Calgary, Alberta, 8-10 June. https://doi.org/10.2118/2004-192.

[39] Li K, Yu H, Feron P, Tade M, Wardhaugh L. Technical and Energy Performance of an Advanced, Aqueous Ammonia-Based $CO_2$ Capture Technology for a 500 MW

Coal-fired Power Station. Environ Sci Technol 2015;49(16):10243–52. https://doi.org/10.1021/acs.est.5b02258.

[40] Wallace, M., and others. 2021. The U.S. $CO_2$ Enhanced Oil Recovery Survey. https://adv-res.com/pdf/ARI-2021-EOY-2020-CO2-EOR-Survey-OCT-21-2021.pdf Accessed 4 April 2022.

[41] Ruppel, S. C., Kerans, C., Major, R. P., Holtz, M. H., 1995, Controls on Reservoir Heterogeneity in Permian Shallow Water Carbonate Platform Reservoirs, Permian Basin: Implications for Improved Recovery: The University of Texas at Austin, Bureau of Economic Geology Geological Circular GC9502.

[42] Dutton SP, Kim EM, Broadhead RF, Raatz WD, Breton CL, Ruppel SC, et al. Play Analysis and Leading-Edge Oil-Reservoir Development Methods in the Permian Basin: Increased Recovery through Advanced Technologies. AAPG Bull 2005;89(5): 553–76. https://doi.org/10.1306/12070404093.

[43] Chen B, Reynolds AC. Ensemble-based Optimization of the Water-Alternating-Gas-Injection Process. SPE J 2016;21(03):786–98. https://doi.org/10.2118/173217-PA.

[44] Godec ML. Acquisition and Development of Selected Cost Data for Saline Storage and Enhanced Oil Recovery (EOR). United States 2014. https://www.osti.gov/servlets/purl/1557133.

[45] Hultzsch P, Lake LW, Gilbert RB. Decision and Risk Analysis Through the Life of the Field. In: In Hydrocarbon Economics and Evaluation Symposium. SPE-107704-MS presented at SPE Hydrocarbon Economics and Evaluation Symposium; 2007. https://doi.org/10.2118/107704-MS.

# 3

# Reservoir simulation of carbon storage associated with $CO_2$ EOR in residual oil zones, San Andres formation of West Texas, Permian Basin, USA

Bo Ren [a], [*], Ian J. Duncan [b]

[a] Hildebrand Department of Petroleum and Geosystems Engineering, The University of Texas at Austin, USA
[b] Bureau of Economic Geology, The University of Texas at Austin, USA

## ARTICLE INFO

*Article history:*
Received 25 June 2018
Received in revised form
2 November 2018
Accepted 3 November 2018
Available online 5 November 2018

*Keywords:*
Residual oil zone
Carbon sequestration
$CO_2$ retention
Reservoir properties
Injection strategies

## ABSTRACT

Residual oil zones (ROZs) are reservoirs in which oil is largely at levels of residual saturation. Such reservoirs cannot be produced by conventional techniques; rather some forms of enhanced oil recovery (EOR), such as $CO_2$ injection is required. As a result, these zones have a potential for $CO_2$ storage associated with EOR activities. In West Texas, the oil production potential of these zones, associated with the San Andres Formation alone, has been estimated as on the order of tens of billions of barrels. A series of numerical simulations of $CO_2$ miscible flooding were conducted on 11 Sub-Volumes cut from a larger static reservoir that represents the range of heterogeneity in permeability and porosity found in San Andres ROZs. This work set out to evaluate the effects of injection strategies and reservoir heterogeneities on the performance of $CO_2$ sequestration. The injection techniques investigated were: continuous $CO_2$ injection and water alternating gas (WAG). Multiple factors were examined, including domain boundary conditions, well patterns, injection rates, permeability anisotropies, and natural fractures. It was found that ROZs could have higher retention fractions (i.e., volume fraction of injected $CO_2$ retained in ROZs) for a combination of inverted five-spot well patterns and large WAG ratios. Based on the results of these numerical simulations, the long-term potential for $CO_2$ storage associated with $CO_2$-EOR of ROZs can be assessed. Our results provide key insights into how future $CO_2$ storage projects associated with EOR in ROZs within carbonate sequences may be implemented.

## 1. Introduction

Residual oil zones (ROZs) are reservoirs in which oil is largely at levels near those for residual saturation [1]. The oil in ROZ reservoirs cannot be produced by conventional techniques, but rather requires either $CO_2$ enhanced oil recovery ($CO_2$-EOR) or unconventional strategies, such as horizontal drilling and intense depressurization by dewatering (see Ref. [2]). ROZs are widely distributed in the Permian Basin of West Texas. The volume of oil recoverable from ROZs in both the San Andres and Canyon Reef formations of Permian Basin, have been estimated by Koperna et al. [3] as 12 billion barrels, with unpublished estimates an order of magnitude or more. Thus, the potential for large scale $CO_2$ sequestration associated with future $CO_2$-EOR projects is very significant. Such projects are already underway with commercial scale WAG injections into ROZs currently taking place in eight San Andres oil fields in the Permian Basin utilizing WAG (water alternating gas) injection of $CO_2$ [4].

This study presents a series of simulations of the outcomes of WAG injections designed to give insights into oil production and $CO_2$ storage associated with EOR projects in the ROZs of the San Andres Formation. Apart from a limited, preliminary simulation study by Jamali and Ettehadtavakkol [5] there have been no published full-physics studies of WAG injections into ROZ reservoirs.

Given that the use of depleted oil reservoirs for $CO_2$ sequestration was suggested at least 25 years ago [6,7], surprisingly few detailed studies were based on both full-physics simulation and real heterogeneous reservoir data, designed to elucidate the nature of incidental storage associated with EOR. The comprehensive review of $CO_2$-EOR by WAG injection by Afzali et al. [8] did not reference any publications on this topic, equivalent in scope and

---

[*] Corresponding author.
*E-mail addresses:* boren@utexas.edu (B. Ren), ian.duncan@beg.utexas.edu (I.J. Duncan).

https://doi.org/10.1016/j.energy.2018.11.007

detail to the current study. Numerous core flooding and rock-water-$CO_2$ interaction studies have been made on $CO_2$ injections (for example [9e12]). Such experiments are useful to understand the processes involved in WAG flooding. However, they provide only limited insights into the field scale response of real reservoirs, which have multiple spatial scales of heterogeneity.

Many studies that have used multi-phase fluid flow simulations to evaluate $CO_2$ injection strategies, at the level of individual 5-spot (or similar patterns). Of these, only a few have attempted to understand the factors impacting both $CO_2$ storage and oil recovery in the saturated zones of oil reservoirs (see for example [13e17]). The applicability of most of these studies to field-based EOR operations is limited, in that they: have not utilized fact-based, high-resolution, three-dimensional static models; do not include realistic representations of the natural heterogeneity found in real reservoirs; fail to evaluate the validity of the no-flow conditions they assume at the boundaries of the "5-spot" or other injection patterns being studied; do not compute metrics such a $CO_2$ utilization and $CO_2$ retention that can be compared to those in characterizing actual oilfields; make no evaluation of the impact of reservoir model cell size on the simulation results; and often use injection conditions that are incompatible with the operational requirements of $CO_2$-EOR projects. The current study makes a unique contribution in that it addresses these issues. The study by Ettehadtavakkol et al. [18] was based on synthetic reservoirs with simulated heterogeneous properties. Their analysis included a study of the impact of varying the WAG ratio (the volume ratio between a water slug and a $CO_2$ slug at the reservoir condition) on $CO_2$ utilization and oil production. Compared with [18], the current study is more comprehensive, evaluates the role of boundary conditions, cell size, and variations in reservoir heterogeneity in permeability. In addition, the current study extends their study to ROZ reservoirs.

It has been suggested [19] that, oil recovery from WAG injection of $CO_2$ is more sensitive to heterogeneity than is water flooding. No studies designed to understand the effects of the heterogeneity of ROZ reservoirs on their oil production and $CO_2$ storage response appear to have been published. Simulation of WAG injection strategies into model reservoirs that do not account for observed heterogeneity in parameters such as porosity and permeability, are unlikely to yield realistic oil production and $CO_2$ storage performance.

The capacity of ROZs to sequester $CO_2$ through EOR is not well understood as commercial scale ROZ floods have only been implemented in the last decade. Although Bachu et al. [20] asserted that ROZs are regarded by the oil industry as superior targets for geological $CO_2$ sequestration, there is little published supporting information or analysis.

The objective of the current work is to understand the factors controlling the performance of $CO_2$ injection for EOR and the volume of associated $CO_2$ storage in ROZs. Initially this study examined the impact of varying the: (1) the size of the cells in the simulated model; (2) the nature of domain boundary conditions; (3) the nature of well conditions (perforation length, injection rate, and bottom hole pressure); and (4) injection strategies (such as continuous $CO_2$ injection and WAG). As noted above the impact of these factors on the results of simulations of WAG injections have largely been ignored in previous work. The current study demonstrates that these issues can have a significant effect on the estimates of the efficiency of $CO_2$ storage associated with EOR and has broad applicability to simulations of EOR in general. This study set out to evaluate the influence on $CO_2$ storage and EOR performance of: varying WAG injection strategies; well configurations (by comparing 40-acre, 5-spot injection patterns with 80-acre, 9-spot patterns); and simulating reservoir volumes with the range of heterogeneous reservoir properties found in a real San Andreas ROZ reservoir. The work presented here would help us to better understand the future of ROZ reservoirs as targets for both $CO_2$ storage and EOR.

## 2. Theory and approach

The simulator used in the study, Eclipse-300 [21], is an efficient, multidimensional, equation-of-state based, compositional simulator. The software uses robust equation solvers and algorithms that enable efficient numerical solutions to solve mass and energy balance (continuum equations) describing the multi-phase flow of $CO_2$, water, and oil in a heterogeneous porous media. The flow governing equations used in this work are the same as those described in Zuloaga et al. [22]. The dispersion of $CO_2$ in oil reservoirs is not considered in simulations.

We employ a single rather than a dual permeability model for the carbonate reservoir. In this reservoir fractures are limited in occurrence and frequently filled by anhydrite cements (Duncan, unpublished data based on extensive core and thin section observations). To understand the sensitivity of flow to the limited open fractures observed, we employ matrix permeability multipliers to approximate their effect.

### *2.1. Description of geology of selected study-areas*

A carbonate ramp is the consensus depositional model used by geologists in interpreting the depositional environment of the carbonate hosted oil reservoirs in the San Andres Formation [23e25]. This ramp sloped seaward at less than 2° and was characterized by sedimentary facies belts, roughly parallel to the shelf margin. San Andres oil reservoirs are typically found in the ramp crest facies where wave energy belt is sufficient to produce "grain-dominated rock-fabric facies" [23]. We utilized the three-dimensional static reservoir model for a ROZ reservoir built by Ren and Duncan [4] constructed to represent a typical San Andres ROZ reservoir in carbonate ramp environment on the margin of the Central Basin Platform. The ROZ reservoir consists largely of a facies association of wackestones, packstones and rare grainstones that formed on the seaward, deeper-water side of the ramp crest. The overlying facies belts that formed the main reservoir prograded over these rocks (Duncan, unpublished data). The reservoirs have been pervasively dolomitized. The interaction of this event with the original rock fabrics, together with later stage dolomite and anhydrite cementing of pores spaces, created the heterogeneity in permeability and porosity observed today. From this model, we cut out three dimensional reservoir volumes representing eleven Sub-Volumes. These were selected to represent the likely range in variability of the petrophysical properties (Table 1). Sub-Volumes

Table 1
Statistics of permeability fields for the study area before and after incorporating the whole-core permeability-porosity correlation.

| Study area model | $m_{k\_before}$, mD | $s_{k\_before}$, mD | $m_{k\_after}$, mD | $s_{k\_after}$, mD |
|---|---|---|---|---|
| #1 | 5.3 | 22.7 | 6.1 | 22.3 |
| #2 | 21.0 | 44.0 | 21.3 | 43.7 |
| #3 | 22.3 | 54.6 | 22.7 | 54.3 |
| #4 | 27.7 | 69.4 | 28.2 | 69.1 |
| #5 | 11.5 | 59.8 | 11.6 | 59.2 |
| #6 | 14.4 | 38.8 | 14.8 | 38.3 |
| #7 | 17.4 | 54.6 | 18.0 | 54.3 |
| #8 | 18.9 | 46.7 | 19.3 | 46.3 |
| #9 | 15.2 | 73.3 | 15.2 | 72.8 |
| #10 | 22.0 | 62.1 | 22.5 | 61.8 |
| #11 | 21.1 | 56.4 | 21.4 | 56.1 |

#1, 2, 3, 4, 5, 10, 11 represent the variability of the ROZ reservoir along the long axis of the reservoir paralleling to the coastal margin (along the strike). Sub-Volumes #7, 2, 6 and #9, 3, 8 represent two parallel transects orthogonal to the long axis of the reservoir (across the strike or along the dip, with #7 and 9 being close to the shelf margin and #6 and 8 being on the interior side of the Central Basin platform). These selected Sub-Volumes represent the range of reservoir facies associated the San Andres ROZ. Computing the arithmetic mean and standard deviation of the permeability's in each Sub-Volume is used to represent the reservoir heterogeneity in each.

The Sub-Volumes #1 through #9 (Table 1) were created with inverted 5-spot (40-acre) well patterns where the model dimensions (number of cells in each direction) are 41 × 41 × 398 cells, with a cell size of 100 ft × 100 ft × 2 ft. The cell size in the vertical direction varies in different layers with the average 2 ft. For Sub-Volumes #10 and #11 (Table 1), 9-spot (80-acre) well patterns were used with the model dimensions of the modeled volume being 80 × 80 × 398 cells, with the same cell sizes as for the 5-spot (40-acre) patterns. The initial pressure is assumed to be hydrostatic, and the reservoir temperature is set to be 105 °F.

The average and standard deviations of permeability and porosity computed for these nine Sub-Volumes were listed in Table 1. To incorporate the effects of core-scale heterogeneity on permeability, we utilized the permeability data published by Honarpour et al. [26]. These data sets include the measurements from core plugs and whole cores (Fig. 1b). Whole-core measurements reveal the effects of core-scale heterogeneity and natural fractures on a larger spatial scale than core plugs. The arithmetic mean and standard deviation of the permeability in Table 1 are both before and after incorporating the effects of large-scale heterogeneity represented in the whole-core measurements. The permeability fields before incorporation were generated through using the rock type model (Fig. 1a) that were developed by Lucia [27].

Some adjustments were made in order to properly incorporate the whole-core permeability-porosity correlation into the reservoir model. As shown in Fig. 1b, the permeability measured on the wholes cores can be orders of magnitudes larger than the permeability of the core plugs when porosity is less than 15%. Considering this, for cells with porosity larger than 15%, the permeability-porosity transformation derived from the whole cores is used to populate permeability in these cells in the geocellular model. Permeability in the other cells is the same as before when using the rock type method. After using the correlation, the mean of permeability increases and the standard deviation decreases (Table 1). The fields with a large fraction of low porosity should have a large increase in permeability.

The ROZ oil properties used in this study are those reported by Honarpour et al. [26]. At the reservoir conditions, the minimum miscibility pressure for the $CO_2$/oil mixture is approximately 1300e1450 psi [26]. Miscible flooding is easily achieved, and the following flow simulation is based on this flood mode.

The relative permeability and capillary pressure curves were adapted from Refs. [26,28]. Both the drainage and imbibition modes were considered, and the settings in the relative permeability curves were consistent with those in the capillary pressure curves.

### 2.2. Injection/production simulation schemes

The overall injection and production scheme designs were based on the typical field operation in San Andres and similar reservoirs in the Permian Basin. In the field, WAG injections are run with injection pressures controlled by the depth of the reservoir, together with the pipeline/recycle pressure and production pressures. Our simulation designs were intended to be general and thus cover different types of operational scenarios, including injection strategies, well patterns, and pressures. Only vertical injectors are considered in this work as the current practice of operators is to deepen the current vertical wells into the ROZs.

For the lateral boundary conditions of the domain (Fig. 2), two different types were investigated: closed and ‘buffered’ boundaries. Closed boundaries are almost universally implemented in the simulation of hydrocarbon production [29,30]. The buffered boundaries introduced in this study are an attempt to create a more realistic evaluation of the results of storage operations. For the buffered boundaries, the pattern volume of interest, is surrounded by the same well patterns by cutting a larger sub-volume from the geocellular model. The outer boundaries of these rimming patterns were closed. For example, in Fig. 2, eight well patterns were employed to surround the middle one, and we called this buffered boundary as “one rimming layer”. Similarly, two and three rimming layers were also tested through cutting larger models. All the quantitative evaluations were made only on the middle well pattern.

For the domain upper boundary, it was assumed to be closed or no-flow since our study is focused on ROZs. Some ROZs in the San

Fig. 1. (a) Rock type model used in building the permeability field, and the model is adapted from Lucia [27]; (b) the blue curve was the permeability-porosity correlation built on the whole-core data. The green curve was built on the permeability-porosity data measured on core-plugs. These two curves were adapted from the publication by Honarpour et al. [26]. (For interpretation of the references to colour in this figure legend, the reader is referred to the Web version of this article.)

Fig. 2. Different lateral boundary conditions tested in this study. For the buffered boundaries, the middle well pattern was rimmed by eight of the same well patterns to approximate realistic flow conditions. The evaluation was made only on the middle pattern.

Andres Formation underlie the main pay zones (MPZs). In this case, some portion of the $CO_2$ injected through ROZs would be likely to move upward into the MPZs. For the domain lower boundary, it was connected to an underlying aquifer with different body size tested in the study. The nature of this underlying aquifer was modeled by using the Carter-Tracy analytical aquifer [21].

Table 2 summarized the nature of the cases studied. Note that the variable parameters are divided into three groups: domain boundaries and sizes; injection parameters; and static reservoir parameters. The first group consists of closed boundaries, buffered boundaries, different sizes of underlying aquifers, and different cell areal sizes ($L_x$ and $L_y$ in Table 2). The second group is comprised of: injection rates; the depth of well perforations, the magnitude of injected pore volumes (or PV), WAG ratios, $CO_2$ half-cycle sizes, well patterns (inverted 5-spot or 9-spot), and pattern coverage areas. The third group of parameters are permeability anisotropies, heterogeneity differences between the dip and strike directions, natural fractures, and the thickness of the underlying aquifer. All the simulations were run for 25 years, which is a typical duration for a pattern in a commercial $CO_2$ EOR operation.

### 2.3. *Metrics for $CO_2$ EOR and storage performance*

The use of metrics to evaluate the behavior of $CO_2$ floods dates back at least to the work of Hadlow [6] who plotted the "cumulative $CO_2$ retention versus cumulative $CO_2$ injection" for five major $CO_2$ EOR projects in the Permian Basin. Hadlow also used a metric he termed overall or gross $CO_2$ utilization, defined as the volume of $CO_2$ injected per incremental barrel of oil produced.

Azzolina et al. [31] have presented a more comprehensive set of metrics. Following Melzer's definition [32], we defined $CO_2$ retention by the relation:

$CO_2$ retention fraction = (total $CO_2$ injected — $CO_2$ produced) / total $CO_2$ injected

Where: $CO_2$ retention = percent of injected $CO_2$ retained in the reservoir (%); total $CO_2$ injected = total injected volumes of $CO_2$ [purchased plus recycled $CO_2$] (% of the total hydrocarbon pore volume (HCPV)); and $CO_2$ produced = total produced volumes of $CO_2$ [recycled $CO_2$] (%HCPV).

## 3. Results

In the following, we examined the results of simulations in the context of systematically varying the nature of the models, the boundary conditions, and the nature of the reservoir Sub-Volumes selected. The relevant physics were added into the flow simulations

Table 2
Summary of conditions for simulations.

| $L_x$, ft | $L_y$, ft | Domain lateral boundary conditions | Sub-Volume model label | Well pattern, size | $CO_2$ injection rate, MScf/d | $CO_2$ injector perforation | Underlying aquifer thickness, ft | WAG ratio | $CO_2$ half-cycle size, HPCV | Incorporating the hole-core perm-porosity correlation | $k_v/k_h$ | Mainly tested parameters |
|---|---|---|---|---|---|---|---|---|---|---|---|---|
| 100 | 100 | Closed, Buffered: one layer, two-layer, three-layer | #1 | Inverted 5-spot, 40-acre | 3000 | Complete | 0 | 0 | NA | No | 0.1 | Boundary conditions |
| 20 | 20 | Buffered: one layer | #1 | Inverted 5-spot, 40-acre | 3000 | Complete | 0 | 0 | NA | No | 0.1 | Cell areal sizes |
| 100 | 100 | Buffered: one layer | #1 | Inverted 5-spot, 40-acre | 3000 | Complete | 0 | 0 | NA | No | 0.1 | |
| 200 | 200 | Buffered: one layer | #1 | Inverted 5-spot, 40-acre | 3000 | Complete | 0 | 0 | NA | No | 0.1 | |
| 100 | 100 | Buffered: one layer | #1 | Inverted 5-spot, 40-acre | 3000 | Lower quarter | 0 | 0 | NA | No | 0.1 | Perforation lengths |
| 100 | 100 | Buffered: one layer | #1 | Inverted 5-spot, 40-acre | 6000 | Complete | 0 | 0 | NA | No | 0.1 | Injection rates |
| 100 | 100 | Buffered: one layer | #1 | Inverted 5-spot, 40-acre | 3000 | Complete | 0 | 0.25, 0.5, 1, 2 | 2.5% | No | 0.1 | WAG ratios |
| 100 | 100 | Buffered: one layer | #1 | Inverted 5-spot, 40-acre | 3000 | Complete | 0 | 0.25 | 1.0%, 2.5%, 5.0% | No, Yes | 0.1 | $CO_2$ half-cycle sizes, natural fractures |
| 100 | 100 | Buffered: one layer | #1 | Inverted 5-spot, 40-acre | 3000 | Complete | 0 | 0, 0.25, 0.5, 1, 2 | 2.5% | Yes | 0.1, 1, 10 | Permeability anisotropies, WAG ratios |
| 100 | 100 | Buffered: one layer | #1 | Inverted 5-spot, 40-acre | 3000 | Complete | 125, 250, 500, 1000 | 0.25 | 2.5% | Yes | 0.1 | Underlying aquifer thickness |
| 100 | 100 | Buffered: one layer | #2 | Inverted 5-spot, 40-acre | 3000 | Complete | 0 | 0, 0.25 | 1.0%, 2.5%, 5.0% | No, Yes | 0.1 | Different sub-volume models, Continuous $CO_2$ injection vs. WAG injection |
| 100 | 100 | Buffered: one layer | #3 | Inverted 5-spot, 40-acre | 3000 | Complete | 0 | 0, 0.25 | 1.0%, 2.5%, 5.0% | No, Yes | 0.1 | |
| 100 | 100 | Buffered: one layer | #4 | Inverted 5-spot, 40-acre | 3000 | Complete | 0 | 0, 0.25 | 1.0%, 2.5%, 5.0% | No, Yes | 0.1 | |
| 100 | 100 | Buffered: one layer | #5 | Inverted 5-spot, 40-acre | 3000 | Complete | 0 | 0, 0.25 | 1.0%, 2.5%, 5.0% | No, Yes | 0.1 | |
| 100 | 100 | Buffered: one layer | #5 | Inverted 5-spot, 40-acre | 3000 | Complete | 0 | 0, 0.25, 0.5, 1, 2 | 2.5% | Yes | 0.1, 1, 10 | |
| 100 | 100 | Buffered: one layer | #6 | Inverted 5-spot, 40-acre | 3000 | Complete | 0 | 0, 0.25 | 1.0%, 2.5%, 5.0% | No, Yes | 0.1 | |
| 100 | 100 | Buffered: one layer | #7 | Inverted 5-spot, 40-acre | 3000 | Complete | 0 | 0, 0.25 | 1.0%, 2.5%, 5.0% | No, Yes | 0.1 | |
| 100 | 100 | Buffered: one layer | #8 | Inverted 5-spot, 40-acre | 3000 | Complete | 0 | 0, 0.25 | 1.0%, 2.5%, 5.0% | No, Yes | 0.1 | |
| 100 | 100 | Buffered: one layer | #9 | Inverted 5-spot, 40-acre | 3000 | Complete | 0 | 0, 0.25 | 1.0%, 2.5%, 5.0% | No, Yes | 0.1 | |
| 100 | 100 | Buffered: one layer | #10 | Inverted 9-spot, 80-acre | 3000 | Complete | 0 | 0, 0.25, 0.5, 1, | 2.5% | Yes | 0.1 | Well patterns, Different sub-volume models |
| 100 | 100 | Buffered: one layer | #11 | Inverted 9-spot, 80-acre | 3000 | Complete | 0 | 0, 0.25, 0.5, 1, | 2.5% | Yes | 0.1 | |

in steps to explore their specific contribution to $CO_2$ retention.

Varying the parameters in Table 2 affect both $CO_2$ retention and oil production. The impact on associated storage can be quantified in two ways: the time-averaged retention fractions (averaged over the whole injection period) and the instantaneous retention fraction. These metrics can be computed by using both numerical results and field data. These metrics do not measure the relative importance of $CO_2$ storage modes such as the free state and capillary trapped $CO_2$ [33,34]. As oil reservoirs appear to have a very low leakage risk during $CO_2$ storage [35], our work focused on $CO_2$ retention, rather than the detailed quantification of storage modes.

### 3.1. Effect of cell size

The size of cells in the geocellular model used for simulations is a key modeling parameter that has been little studied. We conducted a sensitivity analysis to find the optimal size that balances numerical accuracy and computational efficiency. Fig. 3 shows the cumulative oil production as a function of elapsed time for different combinations of cell areal sizes. The cell thickness was not changed (around ~2 ft) when varying the areal sizes. After 10 years, the oil production for the coarsest grid (largest cell size) is about 20% higher than that for the finer grids. When the cell areal dimensions are 100 × 100 ft, the changes in predicted oil volumes from the simulations are minimal. There is a reasonable trade-off between apparent accuracy and computational time. Thus, we will use this cell size in the following.

### 3.2. Effect of domain lateral boundary conditions

This study set out to explore the relationship between choosing different boundary conditions and the results from the associated simulations. Fig. 4 shows the effect of varying the lateral boundary conditions imposed on the modeled domain on the metrics for oil production and associated $CO_2$ storage. The retention fraction is sensitive to the nature of boundary conditions (Fig. 4a). The buffered boundary conditions yield a higher retention fraction than those for the closed boundary conditions. Application of these two types of boundary conditions result in similar gross $CO_2$ utilization ratios. For the buffered boundaries, the number of rimming layers affect the evaluation of retention fractions. The retention fractions for the three types of buffered boundaries (namely, one, two, and three rimming layers) in one set of simulations showed a difference of 18%. This large difference arises from the different levels of heterogeneity for the rimming patterns. Such a large difference indicates the magnitude of uncertainty involved in the evaluation of retention fractions for realistic reservoir models. For simplicity, buffered boundaries with one rimming layer will be used in the rest of the simulations.

Fig. 3. Cumulative oil production vs. time for the different areal cell sizes.

Fig. 4. Effect of domain lateral boundary conditions on $CO_2$ retention fractions (a) and gross $CO_2$ utilization ratios (b).

### 3.3. Effect of well conditions (perforation and injection/production pressure)

Two different scenarios for the perforation of injection wells are considered: (1) complete perforation of the depth range of the ROZ reservoir; and (2) the perforation of the lower quarter. The complete perforation case is equivalent to the open-hole injection of $CO_2$, which was a common practice when many of the San Andres reservoirs were first produced. The results of our simulations (first two rows in Table 3) show that $CO_2$ retention fractions are largely insensitive to perforation intervals (0.698 versus 0.696). In the same simulation, the two perforation strategies have a significant influence on the oil production rates (4.9 vs. 12.8 Stbd/well). The complete perforations result in an increased sweep efficiency compared with the lower-quarter perforations. This higher sweep efficiency reflects the layered nature of the reservoir, with high permeability "flow units" interlayered with low permeability (<0.01mD) flow barriers and baffles (discontinuous flow barriers). These largely constrain $CO_2$ to laterally push oil towards producers.

Two $CO_2$ injection strategies were considered: constant pressure and constant rate. Simulation results (1st and 3rd row in

Table 3
$CO_2$ rention and oil production for differently combined well conditions during continuous $CO_2$ injection.

| Well conditions[b] | $CO_2$ retention fraction | Stbd[a]/Well |
|---|---|---|
| Inj_rate ¼ 3 MM Scf/d; Pro_bhp ¼ 2020 psi; Complete perforation in injectors (base case settings) | 0.696 | 12.8 |
| Inj_rate ¼ 3 MM Scf/d; Pro_bhp ¼ 2020 psi; Lower-quarter perforation in injectors | 0.698 | 4.9 |
| Inj_rate ¼ 6 MM Scf/d; Pro_bhp ¼ 2020 psi; Complete perforation in injectors | 0.629 | 19.6 |
| Inj_bhp ¼ 2600 psi; Pro_bhp ¼ 2020 psi (bubble point) Complete perforation in injectors | 0.696 | 4.3 |
| Inj_bhp ¼ 2600 psi; Pro_bhp ¼ 1400 psi (MMP) Complete perforation in injectors | 0.647 | 9.6 |

[a] Stbd, standard tank barrel per day.
[b] Inj ¼ injectors, Pro ¼ producers, bhp ¼ bottom hole pressure.

Table 3) show that, when imposing a constant rate on injectors, large $CO_2$ injection rates typically enhance oil production (12.8 stbd/well for base case vs. 19.6 stbd/well). For these two cases the time-averaged $CO_2$ retention fraction decreased from 0.696 to 0.629. The injection rate can have a significant effect on $CO_2$ retention. Injection/production pressure shows the similar effect on the retention fraction as injection rates (the last two row in Table 3). When the production bottom hole pressure decreased from 2020 psi (bubble point pressure) to 1400 psi (MMP), the retention fraction shows a significant decrease (from 0.696 to 0.647), and oil production rate for the well doubled (from 4.3 to 9.6 Stbd/well).

### 3.4. Effect of half-cycle size and WAG ratio

Two important parameters involved in WAG injection are WAG ratios and $CO_2$ half-cycle sizes (measured in terms of the %HCPV. The impact of these two parameters on $CO_2$ retention and oil production are shown in Fig. 5a and b. For a given $CO_2$ half-cycle size, the $CO_2$ retention fraction first decreases with the increasing WAG ratio, followed by a steady increase (Fig. 5a). Note that continuous $CO_2$ injection (at zero WAG ratio) enhances sequestration as the $CO_2$ retention fraction can be as high as 0.69.

If the oil production is the priority, the WAG ratios corresponding to the smallest retention fractions should be considered as these ratios result in the highest oil production (Fig. 5b). Based on these simulations, the retention fraction does not decrease significantly (from 0.69 to only 0.67) when changing from continuous $CO_2$ injection (WAG ratio ¼ 0) to optimized WAG injection for oil production (WAG ratio ¼ 0.25) (Fig. 5a vs. Fig. 5b).

Fig. 5. Effect of WAG ratio and $CO_2$ half-cycle size on $CO_2$ retention (a) and oil production (b) for the Sub-Volume model #1. The used geologic models are without incorporating the whole-core permeability-porosity correlation.

### 3.5. Effect of permeability anisotropy

To examine the $CO_2$ retention sensitivity to the anisotropy of permeability, the ratio of the vertical to horizontal permeability ($k_z/k_x$) was varied from 0.1 to 10 while keeping $k_z$ unchanged. Anisotropic permeabilities on the order of $10\times k_x$ can be caused by vertical natural-fractures. As the permeability anisotropy increases, the $CO_2$ retention fraction decreases (Fig. 6). With increasing WAG ratio, the effect of permeability anisotropies on the $CO_2$ retention fraction becomes more pronounced. At a small WAG ratio, the permeability anisotropy has a weak effect on $CO_2$ retention. However, as the WAG ratio increases, the retention enhancement caused by decreasing vertical permeability becomes large (Fig. 6).

### 3.6. Effect of injection techniques and reservoir heterogeneity

The retention fractions for the two different $CO_2$ injection techniques (i.e., continuous $CO_2$ injection and WAG injection) are compared in Fig. 7. The retention fraction changes marginally

Fig. 6. Effect of permeability anisotropy on $CO_2$ retention for the Sub-Volume mode #1. The whole-core permeability-porosity correlation was incorporated into the reservoir model.

Fig. 7. $CO_2$ retention for different Sub-Volumes under both continuous $CO_2$ injection and WAG injection. The $CO_2$ retention fractions for the WAG injection correspond to the optimal WAG ratio (i.e., the WAG ratio that gives the largest oil production).

Fig. 8. Cross plot of $CO_2$ retention fractions versus the permeability standard deviations for the nine Sub-Volumes (from #1 to #9 in Table 1) undergoing continuous $CO_2$ injection. The retention fractions for WAG injection were not shown here as they are close to those for continuous $CO_2$ injection (Fig. 7). These simulations are based on the whole-core permeability-porosity correlation.

(around ± 0.04) between these two injection strategies.

The range of $CO_2$ retention fractions for the 9 Sub-Volumes from 0.36 to 0.70, appears to be correlated with reservoir heterogeneity (Fig. 8) as measured by the standard deviation of permeabilities within each Sub-Volume. Generally, the retention fraction increase with decreasing heterogeneity (i.e., decreasing permeability standard deviation). Homogeneity enhances $CO_2$ sweep efficiency and a larger percentage of the $CO_2$ injected occupies the pore spaces where the in-situ oil or water has been displaced.

All the above $CO_2$ storage efficiencies are time-averaged over 25 yrs. Fig. 9 shows the evolution of retention fractions for the nine Sub-Volumes during continuous $CO_2$ injection. The evolution of $CO_2$ retention reflects the varying production rates of $CO_2$. For example, consider the results for the Sub-Volume #7 (the lowest red dashed curve in Fig. 9) the $CO_2$ retention fraction decreases rapidly, i.e., most of the injected $CO_2$ is produced rapidly. This appears to be due to the large heterogeneity in permeability (refer to Table 1) in this Sub-Volume, resulting in early $CO_2$ breakthrough. WAG injection into this Sub-Volume will increase the volume of $CO_2$ retained in the reservoir. In contrast, Sub-Volume #1 has the largest retention fraction, and the standard deviation of the permeability in this reservoir volume is estimated to be the smallest among the nine Sub-Volumes (refer to Table 1).

Fig. 9. Evolution of $CO_2$ retention fractions for the nine (from #1 to #9 in Table 1) Sub-Volumes with 5-spot well patterns. Dashed lines correspond to the Sub-Volumes across the strike direction.

### 3.7. Effect of well patterns and pattern volume

Overall, the $CO_2$ retention fractions for the 80-acre inverted 9-

Fig. 10. Effect of WAG ratios on $CO_2$ retention (a) and oil production (b). The inverted 5-spot results are for the Sub-Volume #1, which partially overlaps the 9-spot Sub-Volume #10 in space. The assessment employed the reservoir model that incorporated the whole-core permeability-porosity correlation.

spot pattern are less than those for the 40-acre inverted 5-spot pattern (Fig. 10 a). This may be because of the high producer/injector ratio (more production wells) involved in the inverted 9-spot pattern. It also may be related to the larger areal extent (80-acre) of the 9-spot patterns compared with the 40-acre, 5-spot patterns. The difference in retention fractions between the two patterns becomes smaller as the WAG ratio increases. For the 9-spot pattern, the smaller $CO_2$ retention can be compensated by using a large WAG ratio (Fig. 10 a).

If oil production is the priority, employing a large (>1) WAG ratio is a poor choice (Fig. 10 b). For 9-spot well patterns, the averaged oil production rate rapidly decreases with the increase in the WAG ratio (less $CO_2$ cumulatively injected), whereas the retention fraction shows the opposite trend. At the point of the maximum oil production rate, only 45% of injected $CO_2$ is stored for the 80-acre, 9-spot pattern. However, for the 40-acre, 5-spot pattern, the WAG ratio, at which the maximum oil production is achieved, yields the high retention fraction of 70%.

## 4. Discussion and conclusions

### 4.1. Impact of model cell size, boundary conditions and operational parameters on simulation results

The first step taken in this study, was to evaluate the impact of increasing the resolution of the static reservoir model on the results from simulations of WAG injection of $CO_2$. This study showed that simulation of a coarser geocellular grid ($200 \times 200 \times 2$ ft) results in oil production ~20% higher than for grids with the cells size $100 \times 100 \times 2$ ft and smaller. As the majority of published studies of $CO_2$ injection did not conduct grid size sensitivity study (for example [17,36]), our result is sobering. It is likely that the cell size dependency on these metrics is a function of the heterogeneity modeled by the geocellular model. This is worthy of further study.

The second step in our study, was examining the impact of the choice of boundary conditions on simulation results. Again, the impact of boundary conditions imposed on modeling of WAG injection appear to have been largely, if not entirely ignored by previous published studies. Many studies do not document the boundary conditions used, but those who do largely use no flow boundary conditions. The simulations performed in the current study resulted in values for $CO_2$ retention for closed boundary conditions lower by as much as 35% compared with what is referred to in this paper as “buffered boundary conditions”. The buffering used in this study was created by cutting a volume one, two, or three patterns wide from the whole reservoir static reservoir model of Ren and Duncan [4]. As the buffer zone is populated by real reservoir data these are arguably significantly more realistic than closed boundaries. Previous studies that assume no flow between adjacent patterns may give inaccurate estimates of the amount of $CO_2$ retained in ROZs. Of course, model simulations that do not include reservoir heterogeneity will not be impacted by choice of boundary conditions. Unfortunately, such simulations are highly unlikely to produce realistic results.

Although our study has shown that increasing the $CO_2$ injection rate from 3 to 6 MM Scf/d resulted in an increase in oil production from 12.8 to 19.6 Stbd/well and a decrease in the time-averaged $CO_2$ retention fraction from 0.696 to 0.629. However, in the field operation of reservoirs injection rate is not an independent variable but rather is controlled by the imposed injection pressures. Injection pressures are constrained by factors such as the delivery pressure of $CO_2$ pipelines or the sizing of $CO_2$ recycle compressors, together with the depth of the fluid column in injection wells.

### 4.2. Analysis of the impact of the nature of WAG injection

A systematic numerical assessment has been conducted on $CO_2$ storage associated with EOR utilizing WAG injection into ROZ reservoirs. The simulations are based on vertical injectors that have been adopted by the great majority of field operators implementing $CO_2$ EOR projects. In addition, the numerical assessment employs WAG injection and continuous $CO_2$ injection, which have been widely employed in oilfields [37]. A set of 3-D Sub-Volumes cut from the detailed static reservoir model was utilized in the current study. Each was centered on an inverted 40-acre, 5-spot or 80-acre, 9-spot injection pattern. These volumes were selected to enable modeling of a range of reservoir heterogeneity as measured by the standard deviation of permeability. The aim was to understand how reservoir heterogeneity in ROZ reservoirs influences $CO_2$ storage incidental to $CO_2$-EOR. Multi-phase flow simulations were conducted on these volumes.

The results of these numerical experiments is consistent with the conclusion that maximum $CO_2$ retention in ROZs can be achieved by a combination of large WAG ratios (around 1e3), and the implementation of inverted 5-spot well patterns. Reservoirs with homogeneous permeability fields and small permeability anisotropies will have larger retention of $CO_2$. In contrast, for 5-spot well patterns, a combination of complete perforation, high $CO_2$ injection rates, small WAG ratios (around 0.1 to 0.6) increase oil production. Both oil production and $CO_2$ retention fractions in ROZs can be simultaneously high when using a combination of 5-spot well patterns and continuous $CO_2$ injection. If maximizing oil production is the priority, a combination of 9-spot well patterns and WAG injection appears to be a superior strategy. The optimal WAG ratio for achieving the maximum oil production differs for the reservoir subareas in our study that have different levels of heterogeneity. This appears to be because heterogeneity influences the effectiveness and necessity of injecting water during WAG.

### 4.3. The role of the heterogeneity of the reservoir on $CO_2$ storage

The current study appears to be the first published attempt to systematically understand the role of reservoir heterogeneity on metrics such as $CO_2$ retention. This study has shown that the more homogeneous the permeability field (and presumably the greater the sweep efficiency), the higher the retention fraction. This is consistent with our traditional understanding that reservoir homogeneity is also favorable to enhancing oil recovery [29]. In contrast, reservoir heterogeneity tends to cause early $CO_2$ breakthrough and poor $CO_2$ retention (Fig. 9 and Table 1).

The simulations in this study are consistent with the retention fraction for $CO_2$ varying by a factor of two, from 0.36 to 0.70 for Sub-Volumes modeled within the ROZ reservoir. This range difference appears to be attributable, at least in part, to reservoir heterogeneity. The data presented in the current study is consistent with the retention fraction increasing with decreasing heterogeneity (i.e., decreasing permeability standard deviation). Homogeneity enhances $CO_2$ sweep efficiency and a larger percentage of the $CO_2$ injected occupies the pore spaces where the in-situ oil or water has been displaced. In evaluating the $CO_2$ storage associated with the future carbon capture and storage (CCS) projects in ROZ reservoirs a range of this magnitude is very significant.

The WAG simulations presented in this study were designed to understand the impact of reservoir heterogeneity. The approach was motivated in part by the whole-core versus core plug-based permeability-porosity correlation presented by Honarpour et al. [26]. The differences in permeability between traditional core plug data versus the whole-core measurement reveal significant heterogeneities in permeability at a scale of inches. In studies of ROZ reservoirs, the heterogeneity associated with natural fractures should be carefully characterized as they can have a significant effect on $CO_2$ retention. The design of WAG injections should consider the intensities of natural fractures in different Sub-Volumes of a given reservoir model. The use of a single WAG ratio for the whole field might not be the best strategy.

### *4.4. Implications to the future projects of carbon sequestration associated with EOR in ROZs*

The overall assessment shows that $CO_2$ storage in ROZs is impacted by both injection strategies and reservoir heterogeneity. For vertical $CO_2$ injectors, larger WAG ratios always result in higher retention fractions, however the cumulative volume of $CO_2$ injected is also decreased.

If maximizing oil production is the priority, $CO_2$ injection alternating with relatively small slugs of water (i.e., small WAG ratio, around 0.25) is a good choice. This injection is different from the WAG in traditional (originally oil saturated) reservoirs. For such reservoirs, published optimized WAG ratios have been reported in the range of 0.9e3 [38], which is much higher than the optimized WAG ratios derived from this current study. The reasons for this difference are not clear and are worthy of further study. As noted by Ren and Duncan [4], the oil saturation in ROZs is different from that in originally oil saturated reservoirs. In these reservoirs, much of the remaining oil after man-made water flooding (and before $CO_2$ injection) resides in reservoir regions not swept during water flooding. In ROZs the oil saturation is apparently developed through relatively slow regional water flushing. In virgin ROZ reservoirs, oil saturation tends to be relatively uniform, except where some low porosity/permeability patches have retained relatively high oil saturation [4].

### *4.5. Final thoughts*

It is important to accurately estimate the magnitude of $CO_2$ storage affected by WAG based EOR into ROZs with a range of injection strategies. The current study has shown that such accurate estimates require careful consideration of: (1) the nature of imposed boundary conditions; (2) the impact of the size of the cells in the simulations grid; (3) the nature of reservoir heterogeneity; and (4) the nature of WAG protocols. Most previously-published simulation studies fail to take into account most or all of these critical issues.

In the simulation results presented in the current study, $CO_2$ retention is found to be strongly influenced by the heterogeneity and anisotropy of the permeability field. Portions of the reservoir with both less permeability heterogeneity and anisotropies (ratio between vertical and horizontal permeability) have higher $CO_2$ retention fractions.

The results of this study, based on real static reservoir models, for the first time, provide a robust understanding of the factors controlling $CO_2$ storage associated with WAG $CO_2$ injection to improve oil production in ROZ reservoirs. Simulation of WAG injection strategies into model reservoirs that do not account for observed heterogeneity in parameters such as porosity and permeability, are unlikely to yield realistic oil production and $CO_2$ storage performance.

The results of this study provide key insights into how future $CO_2$ storage projects associated with EOR in ROZs within carbonate sequences may be evaluated and then implemented.

## Acknowledgement

This study is part of a long term project investigating ROZ reservoirs in the Permian Basin of Texas being carried out by the Bureau of Economic Geology's (BEG's) State of Texas Advanced Resource Recovery (STARR) Program and funded in part by a U.S. Department of Energy contract under DOE Award Number FE0024375 (PI: Duncan). The first author wishes to thank Dr. Larry Lake and Dr. Frank Male for helpful discussion and comments during the project. Great thanks are due to the two anonymous reviewers for their constructive comments.

## Abbreviations

| | |
|---|---|
| BHP | Bottom hole pressure |
| CCS | Carbon capture and storage |
| $CO_2$-EOR | $CO_2$ enhanced oil recovery |
| HCPV | Hydrocarbon pore volume |
| MPZs | Main pay zones |
| PV | Pore volume |
| ROZs | Residual oil zones |
| Stbd | Standard tank barrel per day |
| WAG | Water alternating gas |

## References

[1] Melzer LS. In: Melzer LS, editor. Residual oil zones (ROZs): a review of ROZ science and engineering; 2013.

[2] Jamali A, Ettehadtavakkol A. $CO_2$ storage in residual oil zones: field-scale modeling and assessment. Int J Greenh Gas Contr 2017;56:102e15.

[3] Koperna GJ, Melzer LS, Kuuskraa VA. Recovery of oil resources from the residual and transitional oil zones of the Permian Basin. In: SPE-102972-MS presented at the SPE annual technical conference and exhibition, 24-27 september, San Antonio, Texas, USA; 2006.

[4] Ren B, Duncan I. Modeling oil saturation evolution in residual oil zones: implications for $CO_2$ EOR and sequestration. Accepted J Petrol Sci Eng 2018, 12827.

[5] Jamali A, Ettehadtavakkol A. $CO_2$ storage in residual oil zones: field-scale modeling and assessment. Int J Greenh Gas Contr 2017;56:102e15.

[6] Hadlow RE. Update of industry experience with $CO_2$ injection. In: 1992. SPE 24928-MS presented at the SPE annual technical conference and exhibition, 4-7 October, Washington, Texas; 1992.

[7] Holt T, Jensen JI, Lindeberg E. Underground storage of $CO_2$ in aquifers and oil reservoirs. Energy Convers Manag 1995;36(6e9):535e8.

[8] Afzali S, Rezaei N, Zendehboudi S. A comprehensive review on enhanced oil recovery by water alternating gas (WAG) injection. Fuel 2018;227:218e46.

[9] Jackson DD, Andrews GL, Claridge EL. Optimum WAG ratio vs. Rock wettability in $CO_2$ flooding. In: SPE-14303-MS presented at SPE annual technical conference and exhibition, 22-26 september, Las Vegas, Nevada; 1985.

[10] Kulkarni MM, Rao DN. Experimental investigation of miscible and immiscible water-alternating-gas (WAG) process performance. J Petrol Sci Eng 2005;48(1e2):1e20.

[11] Luhmann AJ, Tutolo BM, Tan C, Moskowitz BM, Saar MO, Seyfried WE. Whole rock basalt alteration from $CO_2$-rich brine during flow-through experiments at 150° C and 150bar. Chem Geol 2017;453:92e110.

[12] Cui G, Zhang L, Tan C, Ren S, Zhuang Y, Enechukwu C. Injection of supercritical $CO_2$ for geothermal exploitation from sandstone and carbonate reservoirs: $CO_2$ewatererock interactions and their effects. J CO2 Util 2017;20:113e28.

[13] Malik QM, Islam MR. $CO_2$ injection in the weyburn field of Canada: optimization of enhanced oil recovery and greenhouse gas storage with horizontal wells. In: SPE-59327-MS presented at the SPE/DOE improved oil recovery symposium, 3-5 April, Tulsa, Oklahoman, USA; 2000.

[14] Ghomian Y. Reservoir simulation studies for coupled $CO_2$ sequestration and enhanced oil recovery. The University of Texas at Austin; 2008.

[15] Dai Z, Middleton R, Viswanathan H, Fessenden-Rahn J, Bauman J, Pawar R, Lee SY, McPherson B. An integrated framework for optimizing $CO_2$ sequestration and enhanced oil recovery. Environ Sci Technol 2013;1(1):49e54.

[16] Ren B, Ren S, Zhang L, Chen G, Zhang H. Monitoring on $CO_2$ migration in a tight oil reservoir during CCS-EOR in Jilin oilfield China. Energy 2016;98:108e21.

[17] Safi R, Agarwal RK, Banerjee S. Numerical simulation and optimization of $CO_2$ utilization for enhanced oil recovery from depleted reservoirs. Chem Eng Sci 2016;144:30e8.

[18] Ettehadtavakkol A, Lake LW, Bryant SL. $CO_2$-EOR and storage design optimization. Int J Greenh Gas Contr 2014;25:79e92.

[19] Mathiassen OM. $CO_2$ as injection gas for enhanced oil recovery and estimation of the potential on the Norwegian continental shelf. Master Thesis. Trondheim, Norway: Norwegian University of Science and Technology; 2003.

[20] Bachu S, Pires P, Li MY, Guzman F, Eide LI, Aleidan A, Ackiewicz M, Melzer LS. Technical challenges in the conversion of $CO_2$-EOR projects to $CO_2$ storage projects, report prepared by the CSLF task force on technical challenges in the

transition from $CO_2$ EOR to CCS. 2013.

[21] Eclipse-300. Eclipse user's guide. France: Schlumberger; 2016.

[22] Zuloaga P, Yu W, Miao J, Sepehrnoori K. Performance evaluation of $CO_2$ Huff-n-Puff and continuous $CO_2$ injection in tight oil reservoirs. Energy 2017;134:181e92.

[23] Wang FP, Lucia FJ, Kerans C. Integrated reservoir characterization study of a carbonate ramp reservoir: seminole San Andres unit, Gaines County, Texas. SPE Reservoir Eval Eng 1998;1(02):105e13.

[24] Phelps RM, Kerans C, Scott SZ, Janson X, Bellian JA. Three-dimensional modelling and sequence stratigraphy of a carbonate ramp-to-shelf transition, Permian upper San Andres Formation. Sedimentology 2008;55(6):1777e813.

[25] Hurd GS, Kerans C, Fullmer S, Janson X. Large-scale inflections in slope angle below the shelf break: a first order control on the stratigraphic architecture of carbonate slopes: cutoff formation, Guadalupe Mountains National Park, West Texas, USA. J Sediment Res 2016;86(4):336e62.

[26] Honarpour MM, Nagarajan NR, Grijalba Cuenca A, Valle M, Adesoye K. Rock-fluid characterization for miscible CO2 injection: residual oil zone, seminole field, Permian Basin. Society of Petroleum Engineers; 2010.

[27] Lucia FJ. Carbonate reservoir characterization: an integrated approach. Springer Science & Business Media; 2007.

[28] Burnside NM, Naylor M. Review and implications of relative permeability of $CO_2$/brine systems and residual trapping of $CO_2$. Int J Greenh Gas Contr 2014;23:1e11.

[29] Lake LW, Johns RT, Rossen WR, Pope GA. Enhanced oil recovery. Richardson, Texas, USA: Society of Petroleum Engineers; 2014.

[30] Ren B, Zhang L, Huang H, Ren S, Chen G, Zhang H. Performance evaluation and mechanisms study of near-miscible $CO_2$ flooding in a tight oil reservoir of Jilin oilfield China. J Nat Gas Sci Eng 2015;27:1796e805.

[31] Azzolina NA, Nakles DV, Gorecki CD, Peck WD, Ayash SC, Melzer LS, Chatterjee S. CO2 storage associated with CO2 enhanced oil recovery: a statistical analysis of historical operations. Int J Greenh Gas Contr 2015;37:384e97.

[32] Melzer LS. Carbon dioxide enhanced oil recovery ($CO_2$ EOR): factors invovled in adding carbon capture, utilization and storage (CCUS) to enhanced oil recovery. In: Midland Texas: melzer consulting. National enhanced oil recovery initiative resources; 2012. http://neori.org/Melzer CO2EOR CCUS Feb2012.pdf/ . [Accessed 9 April 2014].

[33] Talman SJ, Perkins EH. Pembina cardium $CO_2$ monitoring project, Alberta, Canadadgeochemical interpretation of produced fluid compositions. Energy Procedia 2009;1:2151e9.

[34] Zhang L, Li X, Ren B, Cui G, Zhang Y, Ren S, Chen G, Zhang H. $CO_2$ storage potential and trapping mechanisms in the H-59 block of Jilin oilfield China. Int J Greenh Gas Contr 2016;49:267e80.

[35] Tao Q. Modeling $CO_2$ leakage from geological storage formation and reducing the associated risk. The University of Texas at Austin; 2012.

[36] Zhang L, Li X, Zhang Y, Cui G, Tan C, Ren S. $CO_2$ injection for geothermal development associated with EGR and geological storage in depleted high-temperature gas reservoirs. Energy 2017;123:139e48.

[37] Jarrell PM, Fox CE, Stein MH, Webb SL. Practical aspects of $CO_2$ flooding, vol. 22. Richardson, Texas, USA: Society of Petroleum Engineers; 2002.

[38] Christensen JR, Stenby EH, Skauge A. Review of WAG field experience. SPE Reservoir Eval Eng 2001;4:97e106.

# 4

# Reservoir simulation of carbon storage associated with $CO_2$ EOR in residual oil zones, San Andres formation of West Texas, Permian Basin, USA

Bo Ren [a, *], Ian J. Duncan [b]

[a] *Hildebrand Department of Petroleum and Geosystems Engineering, The University of Texas at Austin, USA*
[b] *Bureau of Economic Geology, The University of Texas at Austin, USA*

ARTICLE INFO

*Article history:*
Received 25 June 2018
Received in revised form
2 November 2018
Accepted 3 November 2018
Available online 5 November 2018

*Keywords:*
Residual oil zone
Carbon sequestration
$CO_2$ retention
Reservoir properties
Injection strategies

ABSTRACT

Residual oil zones (ROZs) are reservoirs in which oil is largely at levels of residual saturation. Such reservoirs cannot be produced by conventional techniques; rather some forms of enhanced oil recovery (EOR), such as $CO_2$ injection is required. As a result, these zones have a potential for $CO_2$ storage associated with EOR activities. In West Texas, the oil production potential of these zones, associated with the San Andres Formation alone, has been estimated as on the order of tens of billions of barrels. A series of numerical simulations of $CO_2$ miscible flooding were conducted on 11 Sub-Volumes cut from a larger static reservoir that represents the range of heterogeneity in permeability and porosity found in San Andres ROZs. This work set out to evaluate the effects of injection strategies and reservoir heterogeneities on the performance of $CO_2$ sequestration. The injection techniques investigated were: continuous $CO_2$ injection and water alternating gas (WAG). Multiple factors were examined, including domain boundary conditions, well patterns, injection rates, permeability anisotropies, and natural fractures. It was found that ROZs could have higher retention fractions (i.e., volume fraction of injected $CO_2$ retained in ROZs) for a combination of inverted five-spot well patterns and large WAG ratios. Based on the results of these numerical simulations, the long-term potential for $CO_2$ storage associated with $CO_2$-EOR of ROZs can be assessed. Our results provide key insights into how future $CO_2$ storage projects associated with EOR in ROZs within carbonate sequences may be implemented.

## 1. Introduction

Residual oil zones (ROZs) are reservoirs in which oil is largely at levels near those for residual saturation [1]. The oil in ROZ reservoirs cannot be produced by conventional techniques, but rather requires either $CO_2$ enhanced oil recovery ($CO_2$-EOR) or unconventional strategies, such as horizontal drilling and intense depressurization by dewatering (see Ref. [2]). ROZs are widely distributed in the Permian Basin of West Texas. The volume of oil recoverable from ROZs in both the San Andres and Canyon Reef formations of Permian Basin, have been estimated by Koperna et al. [3] as 12 billion barrels, with unpublished estimates an order of magnitude or more. Thus, the potential for large scale $CO_2$ sequestration associated with future $CO_2$-EOR projects is very significant. Such projects are already underway with commercial scale WAG injections into ROZs currently taking place in eight San Andres oil fields in the Permian Basin utilizing WAG (water alternating gas) injection of $CO_2$ [4].

This study presents a series of simulations of the outcomes of WAG injections designed to give insights into oil production and $CO_2$ storage associated with EOR projects in the ROZs of the San Andres Formation. Apart from a limited, preliminary simulation study by Jamali and Ettehadtavakkol [5] there have been no published full-physics studies of WAG injections into ROZ reservoirs.

Given that the use of depleted oil reservoirs for $CO_2$ sequestration was suggested at least 25 years ago [6,7], surprisingly few detailed studies were based on both full-physics simulation and real heterogeneous reservoir data, designed to elucidate the nature of incidental storage associated with EOR. The comprehensive review of $CO_2$-EOR by WAG injection by Afzali et al. [8] did not reference any publications on this topic, equivalent in scope and

---

[*] Corresponding author.
*E-mail addresses:* boren@utexas.edu (B. Ren), ian.duncan@beg.utexas.edu (I.J. Duncan).

https://doi.org/10.1016/j.energy.2018.11.007

detail to the current study. Numerous core flooding and rock-water-$CO_2$ interaction studies have been made on $CO_2$ injections (for example [9e12]). Such experiments are useful to understand the processes involved in WAG flooding. However, they provide only limited insights into the field scale response of real reservoirs, which have multiple spatial scales of heterogeneity.

Many studies that have used multi-phase fluid flow simulations to evaluate $CO_2$ injection strategies, at the level of individual 5-spot (or similar patterns). Of these, only a few have attempted to understand the factors impacting both $CO_2$ storage and oil recovery in the saturated zones of oil reservoirs (see for example [13e17]). The applicability of most of these studies to field-based EOR operations is limited, in that they: have not utilized fact-based, high-resolution, three-dimensional static models; do not include realistic representations of the natural heterogeneity found in real reservoirs; fail to evaluate the validity of the no-flow conditions they assume at the boundaries of the "5-spot" or other injection patterns being studied; do not compute metrics such a $CO_2$ utilization and $CO_2$ retention that can be compared to those in characterizing actual oilfields; make no evaluation of the impact of reservoir model cell size on the simulation results; and often use injection conditions that are incompatible with the operational requirements of $CO_2$-EOR projects. The current study makes a unique contribution in that it addresses these issues. The study by Ettehadtavakkol et al. [18] was based on synthetic reservoirs with simulated heterogeneous properties. Their analysis included a study of the impact of varying the WAG ratio (the volume ratio between a water slug and a $CO_2$ slug at the reservoir condition) on $CO_2$ utilization and oil production. Compared with [18], the current study is more comprehensive, evaluates the role of boundary conditions, cell size, and variations in reservoir heterogeneity in permeability. In addition, the current study extends their study to ROZ reservoirs.

It has been suggested [19] that, oil recovery from WAG injection of $CO_2$ is more sensitive to heterogeneity than is water flooding. No studies designed to understand the effects of the heterogeneity of ROZ reservoirs on their oil production and $CO_2$ storage response appear to have been published. Simulation of WAG injection strategies into model reservoirs that do not account for observed heterogeneity in parameters such as porosity and permeability, are unlikely to yield realistic oil production and $CO_2$ storage performance.

The capacity of ROZs to sequester $CO_2$ through EOR is not well understood as commercial scale ROZ floods have only been implemented in the last decade. Although Bachu et al. [20] asserted that ROZs are regarded by the oil industry as superior targets for geological $CO_2$ sequestration, there is little published supporting information or analysis.

The objective of the current work is to understand the factors controlling the performance of $CO_2$ injection for EOR and the volume of associated $CO_2$ storage in ROZs. Initially this study examined the impact of varying the: (1) the size of the cells in the simulated model; (2) the nature of domain boundary conditions; (3) the nature of well conditions (perforation length, injection rate, and bottom hole pressure); and (4) injection strategies (such as continuous $CO_2$ injection and WAG). As noted above the impact of these factors on the results of simulations of WAG injections have largely been ignored in previous work. The current study demonstrates that these issues can have a significant effect on the estimates of the efficiency of $CO_2$ storage associated with EOR and has broad applicability to simulations of EOR in general. This study set out to evaluate the influence on $CO_2$ storage and EOR performance of: varying WAG injection strategies; well configurations (by comparing 40-acre, 5-spot injection patterns with 80-acre, 9-spot patterns); and simulating reservoir volumes with the range of heterogeneous reservoir properties found in a real San Andreas ROZ reservoir. The work presented here would help us to better understand the future of ROZ reservoirs as targets for both $CO_2$ storage and EOR.

## 2. Theory and approach

The simulator used in the study, Eclipse-300 [21], is an efficient, multidimensional, equation-of-state based, compositional simulator. The software uses robust equation solvers and algorithms that enable efficient numerical solutions to solve mass and energy balance (continuum equations) describing the multi-phase flow of $CO_2$, water, and oil in a heterogeneous porous media. The flow governing equations used in this work are the same as those described in Zuloaga et al. [22]. The dispersion of $CO_2$ in oil reservoirs is not considered in simulations.

We employ a single rather than a dual permeability model for the carbonate reservoir. In this reservoir fractures are limited in occurrence and frequently filled by anhydrite cements (Duncan, unpublished data based on extensive core and thin section observations). To understand the sensitivity of flow to the limited open fractures observed, we employ matrix permeability multipliers to approximate their effect.

### 2.1. *Description of geology of selected study-areas*

A carbonate ramp is the consensus depositional model used by geologists in interpreting the depositional environment of the carbonate hosted oil reservoirs in the San Andres Formation [23e25]. This ramp sloped seaward at less than 2° and was characterized by sedimentary facies belts, roughly parallel to the shelf margin. San Andres oil reservoirs are typically found in the ramp crest facies where wave energy belt is sufficient to produce "grain-dominated rock-fabric facies" [23]. We utilized the three-dimensional static reservoir model for a ROZ reservoir built by Ren and Duncan [4] constructed to represent a typical San Andres ROZ reservoir in carbonate ramp environment on the margin of the Central Basin Platform. The ROZ reservoir consists largely of a facies association of wackestones, packstones and rare grainstones that formed on the seaward, deeper-water side of the ramp crest. The overlying facies belts that formed the main reservoir prograded over these rocks (Duncan, unpublished data). The reservoirs have been pervasively dolomitized. The interaction of this event with the original rock fabrics, together with later stage dolomite and anhydrite cementing of pores spaces, created the heterogeneity in permeability and porosity observed today. From this model, we cut out three dimensional reservoir volumes representing eleven Sub-Volumes. These were selected to represent the likely range in variability of the petrophysical properties (Table 1). Sub-Volumes

Table 1
Statistics of permeability fields for the study area before and after incorporating the whole-core permeability-porosity correlation.

| Study area model | $m_{k\_before}$, mD | $s_{k\_before}$, mD | $m_{k\_after}$, mD | $s_{k\_after}$, mD |
|---|---|---|---|---|
| #1 | 5.3 | 22.7 | 6.1 | 22.3 |
| #2 | 21.0 | 44.0 | 21.3 | 43.7 |
| #3 | 22.3 | 54.6 | 22.7 | 54.3 |
| #4 | 27.7 | 69.4 | 28.2 | 69.1 |
| #5 | 11.5 | 59.8 | 11.6 | 59.2 |
| #6 | 14.4 | 38.8 | 14.8 | 38.3 |
| #7 | 17.4 | 54.6 | 18.0 | 54.3 |
| #8 | 18.9 | 46.7 | 19.3 | 46.3 |
| #9 | 15.2 | 73.3 | 15.2 | 72.8 |
| #10 | 22.0 | 62.1 | 22.5 | 61.8 |
| #11 | 21.1 | 56.4 | 21.4 | 56.1 |

#1, 2, 3, 4, 5, 10, 11 represent the variability of the ROZ reservoir along the long axis of the reservoir paralleling to the coastal margin (along the strike). Sub-Volumes #7, 2, 6 and #9, 3, 8 represent two parallel transects orthogonal to the long axis of the reservoir (across the strike or along the dip, with #7 and 9 being close to the shelf margin and #6 and 8 being on the interior side of the Central Basin platform). These selected Sub-Volumes represent the range of reservoir facies associated the San Andres ROZ. Computing the arithmetic mean and standard deviation of the permeability's in each Sub-Volume is used to represent the reservoir heterogeneity in each.

The Sub-Volumes #1 through #9 (Table 1) were created with inverted 5-spot (40-acre) well patterns where the model dimensions (number of cells in each direction) are $41 \times 41 \times 398$ cells, with a cell size of $100\ \text{ft} \times 100\ \text{ft} \times 2$ ft. The cell size in the vertical direction varies in different layers with the average 2 ft. For Sub-Volumes #10 and #11 (Table 1), 9-spot (80-acre) well patterns were used with the model dimensions of the modeled volume being $80 \times 80 \times 398$ cells, with the same cell sizes as for the 5-spot (40-acre) patterns. The initial pressure is assumed to be hydrostatic, and the reservoir temperature is set to be 105 °F.

The average and standard deviations of permeability and porosity computed for these nine Sub-Volumes were listed in Table 1. To incorporate the effects of core-scale heterogeneity on permeability, we utilized the permeability data published by Honarpour et al. [26]. These data sets include the measurements from core plugs and whole cores (Fig. 1b). Whole-core measurements reveal the effects of core-scale heterogeneity and natural fractures on a larger spatial scale than core plugs. The arithmetic mean and standard deviation of the permeability in Table 1 are both before and after incorporating the effects of large-scale heterogeneity represented in the whole-core measurements. The permeability fields before incorporation were generated through using the rock type model (Fig. 1a) that were developed by Lucia [27].

Some adjustments were made in order to properly incorporate the whole-core permeability-porosity correlation into the reservoir model. As shown in Fig. 1b, the permeability measured on the wholes cores can be orders of magnitudes larger than the permeability of the core plugs when porosity is less than 15%. Considering this, for cells with porosity larger than 15%, the permeability-porosity transformation derived from the whole cores is used to populate permeability in these cells in the geocellular model. Permeability in the other cells is the same as before when using the rock type method. After using the correlation, the mean of permeability increases and the standard deviation decreases (Table 1). The fields with a large fraction of low porosity should have a large increase in permeability.

The ROZ oil properties used in this study are those reported by Honarpour et al. [26]. At the reservoir conditions, the minimum miscibility pressure for the $CO_2$/oil mixture is approximately 1300e1450 psi [26]. Miscible flooding is easily achieved, and the following flow simulation is based on this flood mode.

The relative permeability and capillary pressure curves were adapted from Refs. [26,28]. Both the drainage and imbibition modes were considered, and the settings in the relative permeability curves were consistent with those in the capillary pressure curves.

## 2.2. Injection/production simulation schemes

The overall injection and production scheme designs were based on the typical field operation in San Andres and similar reservoirs in the Permian Basin. In the field, WAG injections are run with injection pressures controlled by the depth of the reservoir, together with the pipeline/recycle pressure and production pressures. Our simulation designs were intended to be general and thus cover different types of operational scenarios, including injection strategies, well patterns, and pressures. Only vertical injectors are considered in this work as the current practice of operators is to deepen the current vertical wells into the ROZs.

For the lateral boundary conditions of the domain (Fig. 2), two different types were investigated: closed and ‘buffered’ boundaries. Closed boundaries are almost universally implemented in the simulation of hydrocarbon production [29,30]. The buffered boundaries introduced in this study are an attempt to create a more realistic evaluation of the results of storage operations. For the buffered boundaries, the pattern volume of interest, is surrounded by the same well patterns by cutting a larger sub-volume from the geocellular model. The outer boundaries of these rimming patterns were closed. For example, in Fig. 2, eight well patterns were employed to surround the middle one, and we called this buffered boundary as “one rimming layer”. Similarly, two and three rimming layers were also tested through cutting larger models. All the quantitative evaluations were made only on the middle well pattern.

For the domain upper boundary, it was assumed to be closed or no-flow since our study is focused on ROZs. Some ROZs in the San

Fig. 1. (a) Rock type model used in building the permeability field, and the model is adapted from Lucia [27]; (b) the blue curve was the permeability-porosity correlation built on the whole-core data. The green curve was built on the permeability-porosity data measured on core-plugs. These two curves were adapted from the publication by Honarpour et al. [26]. (For interpretation of the references to colour in this figure legend, the reader is referred to the Web version of this article.)

Fig. 2. Different lateral boundary conditions tested in this study. For the buffered boundaries, the middle well pattern was rimmed by eight of the same well patterns to approximate realistic flow conditions. The evaluation was made only on the middle pattern.

Andres Formation underlie the main pay zones (MPZs). In this case, some portion of the $CO_2$ injected through ROZs would be likely to move upward into the MPZs. For the domain lower boundary, it was connected to an underlying aquifer with different body size tested in the study. The nature of this underlying aquifer was modeled by using the Carter-Tracy analytical aquifer [21].

Table 2 summarized the nature of the cases studied. Note that the variable parameters are divided into three groups: domain boundaries and sizes; injection parameters; and static reservoir parameters. The first group consists of closed boundaries, buffered boundaries, different sizes of underlying aquifers, and different cell areal sizes ($L_x$ and $L_y$ in Table 2). The second group is comprised of: injection rates; the depth of well perforations, the magnitude of injected pore volumes (or PV), WAG ratios, $CO_2$ half-cycle sizes, well patterns (inverted 5-spot or 9-spot), and pattern coverage areas. The third group of parameters are permeability anisotropies, heterogeneity differences between the dip and strike directions, natural fractures, and the thickness of the underlying aquifer. All the simulations were run for 25 years, which is a typical duration for a pattern in a commercial $CO_2$ EOR operation.

### 2.3. *Metrics for $CO_2$ EOR and storage performance*

The use of metrics to evaluate the behavior of $CO_2$ floods dates back at least to the work of Hadlow [6] who plotted the "cumulative $CO_2$ retention versus cumulative $CO_2$ injection" for five major $CO_2$ EOR projects in the Permian Basin. Hadlow also used a metric he termed overall or gross $CO_2$ utilization, defined as the volume of $CO_2$ injected per incremental barrel of oil produced.

Azzolina et al. [31] have presented a more comprehensive set of metrics. Following Melzer's definition [32], we defined $CO_2$ retention by the relation:

$CO_2$ retention fraction = (total $CO_2$ injected — $CO_2$ produced) / total $CO_2$ injected

Where: $CO_2$ retention = percent of injected $CO_2$ retained in the reservoir (%); total $CO_2$ injected = total injected volumes of $CO_2$ [purchased plus recycled $CO_2$] (% of the total hydrocarbon pore volume (HCPV)); and $CO_2$ produced = total produced volumes of $CO_2$ [recycled $CO_2$] (%HCPV).

## 3. Results

In the following, we examined the results of simulations in the context of systematically varying the nature of the models, the boundary conditions, and the nature of the reservoir Sub-Volumes selected. The relevant physics were added into the flow simulations

Table 2
Summary of conditions for simulations.

| $L_x$, ft | $L_y$, ft | Domain lateral boundary conditions | Sub-Volume model label | Well pattern, size | $CO_2$ injection rate, MScf/d | $CO_2$ injector perforation | Underlying aquifer thickness, ft | WAG ratio | $CO_2$ half-cycle size, HPCV | Incorporating the hole-core perm-porosity correlation | $k_v/k_h$ | Mainly tested parameters |
|---|---|---|---|---|---|---|---|---|---|---|---|---|
| 100 | 100 | Closed, Buffered: one layer, two-layer, three-layer | #1 | Inverted 5-spot, 40-acre | 3000 | Complete | 0 | 0 | NA | No | 0.1 | Boundary conditions |
| 20 | 20 | Buffered: one layer | #1 | Inverted 5-spot, 40-acre | 3000 | Complete | 0 | 0 | NA | No | 0.1 | Cell areal sizes |
| 100 | 100 | Buffered: one layer | #1 | Inverted 5-spot, 40-acre | 3000 | Complete | 0 | 0 | NA | No | 0.1 | |
| 200 | 200 | Buffered: one layer | #1 | Inverted 5-spot, 40-acre | 3000 | Complete | 0 | 0 | NA | No | 0.1 | |
| 100 | 100 | Buffered: one layer | #1 | Inverted 5-spot, 40-acre | 3000 | Lower quarter | 0 | 0 | NA | No | 0.1 | Perforation lengths |
| 100 | 100 | Buffered: one layer | #1 | Inverted 5-spot, 40-acre | 6000 | Complete | 0 | 0 | NA | No | 0.1 | Injection rates |
| 100 | 100 | Buffered: one layer | #1 | Inverted 5-spot, 40-acre | 3000 | Complete | 0 | 0.25, 0.5, 1, 2 | 2.5% | No | 0.1 | WAG ratios |
| 100 | 100 | Buffered: one layer | #1 | Inverted 5-spot, 40-acre | 3000 | Complete | 0 | 0.25 | 1.0%, 2.5%, 5.0% | No, Yes | 0.1 | $CO_2$ half-cycle sizes, natural fractures |
| 100 | 100 | Buffered: one layer | #1 | Inverted 5-spot, 40-acre | 3000 | Complete | 0 | 0, 0.25, 0.5, 1, 2 | 2.5% | Yes | 0.1, 1, 10 | Permeability anisotropies, WAG ratios |
| 100 | 100 | Buffered: one layer | #1 | Inverted 5-spot, 40-acre | 3000 | Complete | 125, 250, 500, 1000 | 0.25 | 2.5% | Yes | 0.1 | Underlying aquifer thickness |
| 100 | 100 | Buffered: one layer | #2 | Inverted 5-spot, 40-acre | 3000 | Complete | 0 | 0, 0.25 | 1.0%, 2.5%, 5.0% | No, Yes | 0.1 | Different sub-volume models, Continuous $CO_2$ injection vs. WAG injection |
| 100 | 100 | Buffered: one layer | #3 | Inverted 5-spot, 40-acre | 3000 | Complete | 0 | 0, 0.25 | 1.0%, 2.5%, 5.0% | No, Yes | 0.1 | |
| 100 | 100 | Buffered: one layer | #4 | Inverted 5-spot, 40-acre | 3000 | Complete | 0 | 0, 0.25 | 1.0%, 2.5%, 5.0% | No, Yes | 0.1 | |
| 100 | 100 | Buffered: one layer | #5 | Inverted 5-spot, 40-acre | 3000 | Complete | 0 | 0, 0.25 | 1.0%, 2.5%, 5.0% | No, Yes | 0.1 | |
| 100 | 100 | Buffered: one layer | #5 | Inverted 5-spot, 40-acre | 3000 | Complete | 0 | 0, 0.25, 0.5, 1, 2 | 2.5% | Yes | 0.1, 1, 10 | |
| 100 | 100 | Buffered: one layer | #6 | Inverted 5-spot, 40-acre | 3000 | Complete | 0 | 0, 0.25 | 1.0%, 2.5%, 5.0% | No, Yes | 0.1 | |
| 100 | 100 | Buffered: one layer | #7 | Inverted 5-spot, 40-acre | 3000 | Complete | 0 | 0, 0.25 | 1.0%, 2.5%, 5.0% | No, Yes | 0.1 | |
| 100 | 100 | Buffered: one layer | #8 | Inverted 5-spot, 40-acre | 3000 | Complete | 0 | 0, 0.25 | 1.0%, 2.5%, 5.0% | No, Yes | 0.1 | |
| 100 | 100 | Buffered: one layer | #9 | Inverted 5-spot, 40-acre | 3000 | Complete | 0 | 0, 0.25 | 1.0%, 2.5%, 5.0% | No, Yes | 0.1 | |
| 100 | 100 | Buffered: one layer | #10 | Inverted 9-spot, 80-acre | 3000 | Complete | 0 | 0, 0.25, 0.5, 1, | 2.5% | Yes | 0.1 | Well patterns, Different sub-volume models |
| 100 | 100 | Buffered: one layer | #11 | Inverted 9-spot, 80-acre | 3000 | Complete | 0 | 0, 0.25, 0.5, 1, | 2.5% | Yes | 0.1 | |

in steps to explore their specific contribution to $CO_2$ retention.

Varying the parameters in Table 2 affect both $CO_2$ retention and oil production. The impact on associated storage can be quantified in two ways: the time-averaged retention fractions (averaged over the whole injection period) and the instantaneous retention fraction. These metrics can be computed by using both numerical results and field data. These metrics do not measure the relative importance of $CO_2$ storage modes such as the free state and capillary trapped $CO_2$ [33,34]. As oil reservoirs appear to have a very low leakage risk during $CO_2$ storage [35], our work focused on $CO_2$ retention, rather than the detailed quantification of storage modes.

### 3.1. Effect of cell size

The size of cells in the geocellular model used for simulations is a key modeling parameter that has been little studied. We conducted a sensitivity analysis to find the optimal size that balances numerical accuracy and computational efficiency. Fig. 3 shows the cumulative oil production as a function of elapsed time for different combinations of cell areal sizes. The cell thickness was not changed (around ~2 ft) when varying the areal sizes. After 10 years, the oil production for the coarsest grid (largest cell size) is about 20% higher than that for the finer grids. When the cell areal dimensions are 100 × 100 ft, the changes in predicted oil volumes from the simulations are minimal. There is a reasonable trade-off between apparent accuracy and computational time. Thus, we will use this cell size in the following.

### 3.2. Effect of domain lateral boundary conditions

This study set out to explore the relationship between choosing different boundary conditions and the results from the associated simulations. Fig. 4 shows the effect of varying the lateral boundary conditions imposed on the modeled domain on the metrics for oil production and associated $CO_2$ storage. The retention fraction is sensitive to the nature of boundary conditions (Fig. 4a). The buffered boundary conditions yield a higher retention fraction than those for the closed boundary conditions. Application of these two types of boundary conditions result in similar gross $CO_2$ utilization ratios. For the buffered boundaries, the number of rimming layers affect the evaluation of retention fractions. The retention fractions for the three types of buffered boundaries (namely, one, two, and three rimming layers) in one set of simulations showed a difference of 18%. This large difference arises from the different levels of heterogeneity for the rimming patterns. Such a large difference indicates the magnitude of uncertainty involved in the evaluation of retention fractions for realistic reservoir models. For simplicity, buffered boundaries with one rimming layer will be used in the rest of the simulations.

Fig. 3. Cumulative oil production vs. time for the different areal cell sizes.

Fig. 4. Effect of domain lateral boundary conditions on $CO_2$ retention fractions (a) and gross $CO_2$ utilization ratios (b).

### 3.3. Effect of well conditions (perforation and injection/production pressure)

Two different scenarios for the perforation of injection wells are considered: (1) complete perforation of the depth range of the ROZ reservoir; and (2) the perforation of the lower quarter. The complete perforation case is equivalent to the open-hole injection of $CO_2$, which was a common practice when many of the San Andres reservoirs were first produced. The results of our simulations (first two rows in Table 3) show that $CO_2$ retention fractions are largely insensitive to perforation intervals (0.698 versus 0.696). In the same simulation, the two perforation strategies have a significant influence on the oil production rates (4.9 vs. 12.8 Stbd/well). The complete perforations result in an increased sweep efficiency compared with the lower-quarter perforations. This higher sweep efficiency reflects the layered nature of the reservoir, with high permeability "flow units" interlayered with low permeability (<0.01mD) flow barriers and baffles (discontinuous flow barriers). These largely constrain $CO_2$ to laterally push oil towards producers.

Two $CO_2$ injection strategies were considered: constant pressure and constant rate. Simulation results (1st and 3rd row in

Table 3
$CO_2$ rention and oil production for differently combined well conditions during continuous $CO_2$ injection.

| Well conditions[b] | $CO_2$ retention fraction | Stbd[a]/Well |
|---|---|---|
| Inj_rate ¼ 3 MM Scf/d; Pro_bhp ¼ 2020 psi; Complete perforation in injectors (base case settings) | 0.696 | 12.8 |
| Inj_rate ¼ 3 MM Scf/d; Pro_bhp ¼ 2020 psi; Lower-quarter perforation in injectors | 0.698 | 4.9 |
| Inj_rate ¼ 6 MM Scf/d; Pro_bhp ¼ 2020 psi; Complete perforation in injectors | 0.629 | 19.6 |
| Inj_bhp ¼ 2600 psi; Pro_bhp ¼ 2020 psi (bubble point) Complete perforation in injectors | 0.696 | 4.3 |
| Inj_bhp ¼ 2600 psi; Pro_bhp ¼ 1400 psi (MMP) Complete perforation in injectors | 0.647 | 9.6 |

[a] Stbd, standard tank barrel per day.

[b] Inj ¼ injectors, Pro ¼ producers, bhp ¼ bottom hole pressure.

Table 3) show that, when imposing a constant rate on injectors, large $CO_2$ injection rates typically enhance oil production (12.8 stbd/well for base case vs. 19.6 stbd/well). For these two cases the time-averaged $CO_2$ retention fraction decreased from 0.696 to 0.629. The injection rate can have a significant effect on $CO_2$ retention. Injection/production pressure shows the similar effect on the retention fraction as injection rates (the last two row in Table 3). When the production bottom hole pressure decreased from 2020 psi (bubble point pressure) to 1400 psi (MMP), the retention fraction shows a significant decrease (from 0.696 to 0.647), and oil production rate for the well doubled (from 4.3 to 9.6 Stbd/well).

### 3.4. Effect of half-cycle size and WAG ratio

Two important parameters involved in WAG injection are WAG ratios and $CO_2$ half-cycle sizes (measured in terms of the %HCPV. The impact of these two parameters on $CO_2$ retention and oil production are shown in Fig. 5a and b. For a given $CO_2$ half-cycle size, the $CO_2$ retention fraction first decreases with the increasing WAG ratio, followed by a steady increase (Fig. 5a). Note that continuous $CO_2$ injection (at zero WAG ratio) enhances sequestration as the $CO_2$ retention fraction can be as high as 0.69.

If the oil production is the priority, the WAG ratios corresponding to the smallest retention fractions should be considered as these ratios result in the highest oil production (Fig. 5b). Based on these simulations, the retention fraction does not decrease significantly (from 0.69 to only 0.67) when changing from continuous $CO_2$ injection (WAG ratio ¼ 0) to optimized WAG injection for oil production (WAG ratio ¼ 0.25) (Fig. 5a vs. Fig. 5b).

Fig. 5. Effect of WAG ratio and $CO_2$ half-cycle size on $CO_2$ retention (a) and oil production (b) for the Sub-Volume model #1. The used geologic models are without incorporating the whole-core permeability-porosity correlation.

### 3.5. Effect of permeability anisotropy

To examine the $CO_2$ retention sensitivity to the anisotropy of permeability, the ratio of the vertical to horizontal permeability ($k_z/k_x$) was varied from 0.1 to 10 while keeping $k_z$ unchanged. Anisotropic permeabilities on the order of $10\times k_x$ can be caused by vertical natural-fractures. As the permeability anisotropy increases, the $CO_2$ retention fraction decreases (Fig. 6). With increasing WAG ratio, the effect of permeability anisotropies on the $CO_2$ retention fraction becomes more pronounced. At a small WAG ratio, the permeability anisotropy has a weak effect on $CO_2$ retention. However, as the WAG ratio increases, the retention enhancement caused by decreasing vertical permeability becomes large (Fig. 6).

### 3.6. Effect of injection techniques and reservoir heterogeneity

The retention fractions for the two different $CO_2$ injection techniques (i.e., continuous $CO_2$ injection and WAG injection) are compared in Fig. 7. The retention fraction changes marginally

Fig. 6. Effect of permeability anisotropy on $CO_2$ retention for the Sub-Volume mode #1. The whole-core permeability-porosity correlation was incorporated into the reservoir model.

Fig. 7. $CO_2$ retention for different Sub-Volumes under both continuous $CO_2$ injection and WAG injection. The $CO_2$ retention fractions for the WAG injection correspond to the optimal WAG ratio (i.e., the WAG ratio that gives the largest oil production).

Fig. 8. Cross plot of $CO_2$ retention fractions versus the permeability standard deviations for the nine Sub-Volumes (from #1 to #9 in Table 1) undergoing continuous $CO_2$ injection. The retention fractions for WAG injection were not shown here as they are close to those for continuous $CO_2$ injection (Fig. 7). These simulations are based on the whole-core permeability-porosity correlation.

(around ± 0.04) between these two injection strategies.

The range of $CO_2$ retention fractions for the 9 Sub-Volumes from 0.36 to 0.70, appears to be correlated with reservoir heterogeneity (Fig. 8) as measured by the standard deviation of permeabilities within each Sub-Volume. Generally, the retention fraction increase with decreasing heterogeneity (i.e., decreasing permeability standard deviation). Homogeneity enhances $CO_2$ sweep efficiency and a larger percentage of the $CO_2$ injected occupies the pore spaces where the in-situ oil or water has been displaced.

All the above $CO_2$ storage efficiencies are time-averaged over 25 yrs. Fig. 9 shows the evolution of retention fractions for the nine Sub-Volumes during continuous $CO_2$ injection. The evolution of $CO_2$ retention reflects the varying production rates of $CO_2$. For example, consider the results for the Sub-Volume #7 (the lowest red dashed curve in Fig. 9) the $CO_2$ retention fraction decreases rapidly, i.e., most of the injected $CO_2$ is produced rapidly. This appears to be due to the large heterogeneity in permeability (refer to Table 1) in this Sub-Volume, resulting in early $CO_2$ breakthrough. WAG injection into this Sub-Volume will increase the volume of $CO_2$ retained in the reservoir. In contrast, Sub-Volume #1 has the largest retention fraction, and the standard deviation of the permeability in this reservoir volume is estimated to be the smallest among the nine Sub-Volumes (refer to Table 1).

Fig. 9. Evolution of $CO_2$ retention fractions for the nine (from #1 to #9 in Table 1) Sub-Volumes with 5-spot well patterns. Dashed lines correspond to the Sub-Volumes across the strike direction.

### 3.7. *Effect of well patterns and pattern volume*

Overall, the $CO_2$ retention fractions for the 80-acre inverted 9-

Fig. 10. Effect of WAG ratios on $CO_2$ retention (a) and oil production (b). The inverted 5-spot results are for the Sub-Volume #1, which partially overlaps the 9-spot Sub-Volume #10 in space. The assessment employed the reservoir model that incorporated the whole-core permeability-porosity correlation.

spot pattern are less than those for the 40-acre inverted 5-spot pattern (Fig. 10 a). This may be because of the high producer/injector ratio (more production wells) involved in the inverted 9-spot pattern. It also may be related to the larger areal extent (80-acre) of the 9-spot patterns compared with the 40-acre, 5-spot patterns. The difference in retention fractions between the two patterns becomes smaller as the WAG ratio increases. For the 9-spot pattern, the smaller $CO_2$ retention can be compensated by using a large WAG ratio (Fig. 10 a).

If oil production is the priority, employing a large (>1) WAG ratio is a poor choice (Fig. 10 b). For 9-spot well patterns, the averaged oil production rate rapidly decreases with the increase in the WAG ratio (less $CO_2$ cumulatively injected), whereas the retention fraction shows the opposite trend. At the point of the maximum oil production rate, only 45% of injected $CO_2$ is stored for the 80-acre, 9-spot pattern. However, for the 40-acre, 5-spot pattern, the WAG ratio, at which the maximum oil production is achieved, yields the high retention fraction of 70%.

## 4. Discussion and conclusions

### 4.1. Impact of model cell size, boundary conditions and operational parameters on simulation results

The first step taken in this study, was to evaluate the impact of increasing the resolution of the static reservoir model on the results from simulations of WAG injection of $CO_2$. This study showed that simulation of a coarser geocellular grid ($200 \times 200 \times 2$ ft) results in oil production ~20% higher than for grids with the cells size $100 \times 100 \times 2$ ft and smaller. As the majority of published studies of $CO_2$ injection did not conduct grid size sensitivity study (for example [17,36]), our result is sobering. It is likely that the cell size dependency on these metrics is a function of the heterogeneity modeled by the geocellular model. This is worthy of further study.

The second step in our study, was examining the impact of the choice of boundary conditions on simulation results. Again, the impact of boundary conditions imposed on modeling of WAG injection appear to have been largely, if not entirely ignored by previous published studies. Many studies do not document the boundary conditions used, but those who do largely use no flow boundary conditions. The simulations performed in the current study resulted in values for $CO_2$ retention for closed boundary conditions lower by as much as 35% compared with what is referred to in this paper as “buffered boundary conditions”. The buffering used in this study was created by cutting a volume one, two, or three patterns wide from the whole reservoir static reservoir model of Ren and Duncan [4]. As the buffer zone is populated by real reservoir data these are arguably significantly more realistic than closed boundaries. Previous studies that assume no flow between adjacent patterns may give inaccurate estimates of the amount of $CO_2$ retained in ROZs. Of course, model simulations that do not include reservoir heterogeneity will not be impacted by choice of boundary conditions. Unfortunately, such simulations are highly unlikely to produce realistic results.

Although our study has shown that increasing the $CO_2$ injection rate from 3 to 6 MM Scf/d resulted in an increase in oil production from 12.8 to 19.6 Stbd/well and a decrease in the time-averaged $CO_2$ retention fraction from 0.696 to 0.629. However, in the field operation of reservoirs injection rate is not an independent variable but rather is controlled by the imposed injection pressures. Injection pressures are constrained by factors such as the delivery pressure of $CO_2$ pipelines or the sizing of $CO_2$ recycle compressors, together with the depth of the fluid column in injection wells.

### 4.2. Analysis of the impact of the nature of WAG injection

A systematic numerical assessment has been conducted on $CO_2$ storage associated with EOR utilizing WAG injection into ROZ reservoirs. The simulations are based on vertical injectors that have been adopted by the great majority of field operators implementing $CO_2$ EOR projects. In addition, the numerical assessment employs WAG injection and continuous $CO_2$ injection, which have been widely employed in oilfields [37]. A set of 3-D Sub-Volumes cut from the detailed static reservoir model was utilized in the current study. Each was centered on an inverted 40-acre, 5-spot or 80-acre, 9-spot injection pattern. These volumes were selected to enable modeling of a range of reservoir heterogeneity as measured by the standard deviation of permeability. The aim was to understand how reservoir heterogeneity in ROZ reservoirs influences $CO_2$ storage incidental to $CO_2$-EOR. Multi-phase flow simulations were conducted on these volumes.

The results of these numerical experiments is consistent with the conclusion that maximum $CO_2$ retention in ROZs can be achieved by a combination of large WAG ratios (around 1e3), and the implementation of inverted 5-spot well patterns. Reservoirs with homogeneous permeability fields and small permeability anisotropies will have larger retention of $CO_2$. In contrast, for 5-spot well patterns, a combination of complete perforation, high $CO_2$ injection rates, small WAG ratios (around 0.1 to 0.6) increase oil production. Both oil production and $CO_2$ retention fractions in ROZs can be simultaneously high when using a combination of 5-spot well patterns and continuous $CO_2$ injection. If maximizing oil production is the priority, a combination of 9-spot well patterns and WAG injection appears to be a superior strategy. The optimal WAG ratio for achieving the maximum oil production differs for the reservoir subareas in our study that have different levels of heterogeneity. This appears to be because heterogeneity influences the effectiveness and necessity of injecting water during WAG.

### 4.3. The role of the heterogeneity of the reservoir on $CO_2$ storage

The current study appears to be the first published attempt to systematically understand the role of reservoir heterogeneity on metrics such as $CO_2$ retention. This study has shown that the more homogeneous the permeability field (and presumably the greater the sweep efficiency), the higher the retention fraction. This is consistent with our traditional understanding that reservoir homogeneity is also favorable to enhancing oil recovery [29]. In contrast, reservoir heterogeneity tends to cause early $CO_2$ breakthrough and poor $CO_2$ retention (Fig. 9 and Table 1).

The simulations in this study are consistent with the retention fraction for $CO_2$ varying by a factor of two, from 0.36 to 0.70 for Sub-Volumes modeled within the ROZ reservoir. This range difference appears to be attributable, at least in part, to reservoir heterogeneity. The data presented in the current study is consistent with the retention fraction increasing with decreasing heterogeneity (i.e., decreasing permeability standard deviation). Homogeneity enhances $CO_2$ sweep efficiency and a larger percentage of the $CO_2$ injected occupies the pore spaces where the in-situ oil or water has been displaced. In evaluating the $CO_2$ storage associated with the future carbon capture and storage (CCS) projects in ROZ reservoirs a range of this magnitude is very significant.

The WAG simulations presented in this study were designed to understand the impact of reservoir heterogeneity. The approach was motivated in part by the whole-core versus core plug-based permeability-porosity correlation presented by Honarpour et al. [26]. The differences in permeability between traditional core plug data versus the whole-core measurement reveal significant heterogeneities in permeability at a scale of inches. In studies of ROZ reservoirs, the heterogeneity associated with natural fractures should be carefully characterized as they can have a significant effect on $CO_2$ retention. The design of WAG injections should consider the intensities of natural fractures in different Sub-Volumes of a given reservoir model. The use of a single WAG ratio for the whole field might not be the best strategy.

### 4.4. Implications to the future projects of carbon sequestration associated with EOR in ROZs

The overall assessment shows that $CO_2$ storage in ROZs is impacted by both injection strategies and reservoir heterogeneity. For vertical $CO_2$ injectors, larger WAG ratios always result in higher retention fractions, however the cumulative volume of $CO_2$ injected is also decreased.

If maximizing oil production is the priority, $CO_2$ injection alternating with relatively small slugs of water (i.e., small WAG ratio, around 0.25) is a good choice. This injection is different from the WAG in traditional (originally oil saturated) reservoirs. For such reservoirs, published optimized WAG ratios have been reported in the range of 0.9e3 [38], which is much higher than the optimized WAG ratios derived from this current study. The reasons for this difference are not clear and are worthy of further study. As noted by Ren and Duncan [4], the oil saturation in ROZs is different from that in originally oil saturated reservoirs. In these reservoirs, much of the remaining oil after man-made water flooding (and before $CO_2$ injection) resides in reservoir regions not swept during water flooding. In ROZs the oil saturation is apparently developed through relatively slow regional water flushing. In virgin ROZ reservoirs, oil saturation tends to be relatively uniform, except where some low porosity/permeability patches have retained relatively high oil saturation [4].

### 4.5. Final thoughts

It is important to accurately estimate the magnitude of $CO_2$ storage affected by WAG based EOR into ROZs with a range of injection strategies. The current study has shown that such accurate estimates require careful consideration of: (1) the nature of imposed boundary conditions; (2) the impact of the size of the cells in the simulations grid; (3) the nature of reservoir heterogeneity; and (4) the nature of WAG protocols. Most previously-published simulation studies fail to take into account most or all of these critical issues.

In the simulation results presented in the current study, $CO_2$ retention is found to be strongly influenced by the heterogeneity and anisotropy of the permeability field. Portions of the reservoir with both less permeability heterogeneity and anisotropies (ratio between vertical and horizontal permeability) have higher $CO_2$ retention fractions.

The results of this study, based on real static reservoir models, for the first time, provide a robust understanding of the factors controlling $CO_2$ storage associated with WAG $CO_2$ injection to improve oil production in ROZ reservoirs. Simulation of WAG injection strategies into model reservoirs that do not account for observed heterogeneity in parameters such as porosity and permeability, are unlikely to yield realistic oil production and $CO_2$ storage performance.

The results of this study provide key insights into how future $CO_2$ storage projects associated with EOR in ROZs within carbonate sequences may be evaluated and then implemented.

## Acknowledgement

This study is part of a long term project investigating ROZ reservoirs in the Permian Basin of Texas being carried out by the Bureau of Economic Geology's (BEG's) State of Texas Advanced Resource Recovery (STARR) Program and funded in part by a U.S. Department of Energy contract under DOE Award Number FE0024375 (PI: Duncan). The first author wishes to thank Dr. Larry Lake and Dr. Frank Male for helpful discussion and comments during the project. Great thanks are due to the two anonymous reviewers for their constructive comments.

## Abbreviations

| | |
|---|---|
| BHP | Bottom hole pressure |
| CCS | Carbon capture and storage |
| $CO_2$-EOR | $CO_2$ enhanced oil recovery |
| HCPV | Hydrocarbon pore volume |
| MPZs | Main pay zones |
| PV | Pore volume |
| ROZs | Residual oil zones |
| Stbd | Standard tank barrel per day |
| WAG | Water alternating gas |

## References

[1] Melzer LS. In: Melzer LS, editor. Residual oil zones (ROZs): a review of ROZ science and engineering; 2013.

[2] Jamali A, Ettehadtavakkol A. $CO_2$ storage in residual oil zones: field-scale modeling and assessment. Int J Greenh Gas Contr 2017;56:102e15.

[3] Koperna GJ, Melzer LS, Kuuskraa VA. Recovery of oil resources from the residual and transitional oil zones of the Permian Basin. In: SPE-102972-MS presented at the SPE annual technical conference and exhibition, 24-27 september, San Antonio, Texas, USA; 2006.

[4] Ren B, Duncan I. Modeling oil saturation evolution in residual oil zones: implications for $CO_2$ EOR and sequestration. Accepted J Petrol Sci Eng 2018, 12827.

[5] Jamali A, Ettehadtavakkol A. $CO_2$ storage in residual oil zones: field-scale modeling and assessment. Int J Greenh Gas Contr 2017;56:102e15.

[6] Hadlow RE. Update of industry experience with $CO_2$ injection. In: 1992. SPE 24928-MS presented at the SPE annual technical conference and exhibition, 4-7 October, Washington, Texas; 1992.

[7] Holt T, Jensen JI, Lindeberg E. Underground storage of $CO_2$ in aquifers and oil reservoirs. Energy Convers Manag 1995;36(6e9):535e8.

[8] Afzali S, Rezaei N, Zendehboudi S. A comprehensive review on enhanced oil recovery by water alternating gas (WAG) injection. Fuel 2018;227:218e46.

[9] Jackson DD, Andrews GL, Claridge EL. Optimum WAG ratio vs. Rock wettability in $CO_2$ flooding. In: SPE-14303-MS presented at SPE annual technical conference and exhibition, 22-26 september, Las Vegas, Nevada; 1985.

[10] Kulkarni MM, Rao DN. Experimental investigation of miscible and immiscible water-alternating-gas (WAG) process performance. J Petrol Sci Eng 2005;48(1e2):1e20.

[11] Luhmann AJ, Tutolo BM, Tan C, Moskowitz BM, Saar MO, Seyfried WE. Whole rock basalt alteration from $CO_2$-rich brine during flow-through experiments at 150° C and 150bar. Chem Geol 2017;453:92e110.

[12] Cui G, Zhang L, Tan C, Ren S, Zhuang Y, Enechukwu C. Injection of supercritical $CO_2$ for geothermal exploitation from sandstone and carbonate reservoirs: $CO_2$ewatererock interactions and their effects. J CO2 Util 2017;20:113e28.

[13] Malik QM, Islam MR. $CO_2$ injection in the weyburn field of Canada: optimization of enhanced oil recovery and greenhouse gas storage with horizontal wells. In: SPE-59327-MS presented at the SPE/DOE improved oil recovery symposium, 3-5 April, Tulsa, Oklahoman, USA; 2000.

[14] Ghomian Y. Reservoir simulation studies for coupled $CO_2$ sequestration and enhanced oil recovery. The University of Texas at Austin; 2008.

[15] Dai Z, Middleton R, Viswanathan H, Fessenden-Rahn J, Bauman J, Pawar R, Lee SY, McPherson B. An integrated framework for optimizing $CO_2$ sequestration and enhanced oil recovery. Environ Sci Technol 2013;1(1):49e54.

[16] Ren B, Ren S, Zhang L, Chen G, Zhang H. Monitoring on $CO_2$ migration in a tight oil reservoir during CCS-EOR in Jilin oilfield China. Energy 2016;98:108e21.

[17] Safi R, Agarwal RK, Banerjee S. Numerical simulation and optimization of $CO_2$ utilization for enhanced oil recovery from depleted reservoirs. Chem Eng Sci 2016;144:30e8.

[18] Ettehadtavakkol A, Lake LW, Bryant SL. $CO_2$-EOR and storage design optimization. Int J Greenh Gas Contr 2014;25:79e92.

[19] Mathiassen OM. $CO_2$ as injection gas for enhanced oil recovery and estimation of the potential on the Norwegian continental shelf. Master Thesis. Trondheim, Norway: Norwegian University of Science and Technology; 2003.

[20] Bachu S, Pires P, Li MY, Guzman F, Eide LI, Aleidan A, Ackiewicz M, Melzer LS. Technical challenges in the conversion of $CO_2$-EOR projects to $CO_2$ storage projects, report prepared by the CSLF task force on technical challenges in the

transition from $CO_2$ EOR to CCS. 2013.

[21] Eclipse-300. Eclipse user's guide. France: Schlumberger; 2016.

[22] Zuloaga P, Yu W, Miao J, Sepehrnoori K. Performance evaluation of $CO_2$ Huff-n-Puff and continuous $CO_2$ injection in tight oil reservoirs. Energy 2017;134:181e92.

[23] Wang FP, Lucia FJ, Kerans C. Integrated reservoir characterization study of a carbonate ramp reservoir: seminole San Andres unit, Gaines County, Texas. SPE Reservoir Eval Eng 1998;1(02):105e13.

[24] Phelps RM, Kerans C, Scott SZ, Janson X, Bellian JA. Three-dimensional modelling and sequence stratigraphy of a carbonate ramp-to-shelf transition, Permian upper San Andres Formation. Sedimentology 2008;55(6):1777e813.

[25] Hurd GS, Kerans C, Fullmer S, Janson X. Large-scale inflections in slope angle below the shelf break: a first order control on the stratigraphic architecture of carbonate slopes: cutoff formation, Guadalupe Mountains National Park, West Texas, USA. J Sediment Res 2016;86(4):336e62.

[26] Honarpour MM, Nagarajan NR, Grijalba Cuenca A, Valle M, Adesoye K. Rock-fluid characterization for miscible CO2 injection: residual oil zone, seminole field, Permian Basin. Society of Petroleum Engineers; 2010.

[27] Lucia FJ. Carbonate reservoir characterization: an integrated approach. Springer Science & Business Media; 2007.

[28] Burnside NM, Naylor M. Review and implications of relative permeability of $CO_2$/brine systems and residual trapping of $CO_2$. Int J Greenh Gas Contr 2014;23:1e11.

[29] Lake LW, Johns RT, Rossen WR, Pope GA. Enhanced oil recovery. Richardson, Texas, USA: Society of Petroleum Engineers; 2014.

[30] Ren B, Zhang L, Huang H, Ren S, Chen G, Zhang H. Performance evaluation and mechanisms study of near-miscible $CO_2$ flooding in a tight oil reservoir of Jilin oilfield China. J Nat Gas Sci Eng 2015;27:1796e805.

[31] Azzolina NA, Nakles DV, Gorecki CD, Peck WD, Ayash SC, Melzer LS, Chatterjee S. CO2 storage associated with CO2 enhanced oil recovery: a statistical analysis of historical operations. Int J Greenh Gas Contr 2015;37:384e97.

[32] Melzer LS. Carbon dioxide enhanced oil recovery ($CO_2$ EOR): factors invovled in adding carbon capture, utilization and storage (CCUS) to enhanced oil recovery. In: Midland Texas: melzer consulting. National enhanced oil recovery initiative resources; 2012. http://neori.org/Melzer CO2EOR CCUS Feb2012.pdf/ . [Accessed 9 April 2014].

[33] Talman SJ, Perkins EH. Pembina cardium $CO_2$ monitoring project, Alberta, Canadadgeochemical interpretation of produced fluid compositions. Energy Procedia 2009;1:2151e9.

[34] Zhang L, Li X, Ren B, Cui G, Zhang Y, Ren S, Chen G, Zhang H. $CO_2$ storage potential and trapping mechanisms in the H-59 block of Jilin oilfield China. Int J Greenh Gas Contr 2016;49:267e80.

[35] Tao Q. Modeling $CO_2$ leakage from geological storage formation and reducing the associated risk. The University of Texas at Austin; 2012.

[36] Zhang L, Li X, Zhang Y, Cui G, Tan C, Ren S. $CO_2$ injection for geothermal development associated with EGR and geological storage in depleted high-temperature gas reservoirs. Energy 2017;123:139e48.

[37] Jarrell PM, Fox CE, Stein MH, Webb SL. Practical aspects of $CO_2$ flooding, vol. 22. Richardson, Texas, USA: Society of Petroleum Engineers; 2002.

[38] Christensen JR, Stenby EH, Skauge A. Review of WAG field experience. SPE Reservoir Eval Eng 2001;4:97e106.

# 5

# Modeling oil saturation evolution in residual oil zones: Implications for $CO_2$ EOR and sequestration

Bo Ren*, Ian Duncan

*The University of Texas at Austin, United States*

ARTICLE INFO

*Keywords:*
Oil saturation
Residual oil zone
$CO_2$ EOR and storage
Flow modeling
Capillary pressure heterogeneity

ABSTRACT

Residual oil zones (ROZs) are extensively developed in carbonate formations in the Permian Basin, West Texas. These ROZs have the potential both for economically-viable $CO_2$ enhanced oil recovery ($CO_2$-EOR) and for significant volumes of associated $CO_2$ sequestration. The accepted model for ROZ formation is based on the hydrodynamic effects of tectonically-controlled increased water flow in aquifers at the base of oil fields. The nature of this process is modelled using a commercial reservoir simulator in this work. These simulations explore the effects of strength of aquifer flow, flow direction, and capillary pressure on the nature and distribution of oil saturations in ROZs. A special emphasis was on understanding the impact of heterogeneity of capillary pressures in ROZ reservoirs. These factors determine the thickness of ROZs, the magnitude of oil saturation, and the slope of water-oil contacts. Understanding the magnitude of oil saturation and how it varies within ROZs is important in determining reserves, and evaluating both EOR and sequestration potential. The geometry of ROZs are established slowly, especially for small regional water fluxes, however oil saturations achieve almost steady states in relatively short time scales. The simulated oil saturation profiles found in this study are in reasonable agreement with the measured profile published for the San Andres Seminole Unit's ROZ. The results support the plausibility of the hydrodynamic model, but do not rule out other models for the origin of ROZs.

## 1. Introduction

Residual oil zones (ROZs) can be defined as an oil reservoir or portion of a reservoir in which the oil is at, or is close to, residual oil saturation (Melzer et al., 2006). ROZs have the apparent characteristics of a reservoir after the completion of a waterflood. ROZs in carbonate reservoirs in the Permian Basin of Texas were initially interpreted from wireline logs as being productive oil zones. However, if these zones were completed for production, they produced water, only occasionally with traces of oil. Thus, ROZs can be produced by neither conventional pumping nor water flooding. Rather, producing from these zones requires some form of enhanced oil recovery such as $CO_2$-EOR. This also provides incidental sequestration of $CO_2$. Bachu et al. (2013) noted that ROZs are “regarded in the industry as the most optimum part of oil reservoirs to store $CO_2$”. They based this on: the typically large volume of ROZs; their high water saturation; and “hydrocarbon availability”. Many similar studies (e.g., Koperna et al., 2006; Godec et al., 2013; Kuuskraa et al., 2013; Melzer, 2013; Trentham and Melzer, 2015; Kuuskraa et al., 2017; Stewart et al., 2018) have been conducted to assess the feasibility and potential of $CO_2$ EOR and storage in ROZs.

ROZs have different types in terms of their origin and evolution. Harouaka et al. (2013) classified these occurrences of ROZs into two types: (i) Brownfield ROZs, that are located below the water-oil contact of oil reservoirs; and (ii) Greenfield ROZs, that are not associated with normal oil reservoirs or main pay zones (MPZ). Melzer (2013) divided ROZs into three types, resulting from the following different scenarios for their origin: (i) an oil accumulation is subject to a tilt (from differential subsidence or tectonic movements), resulting in re-equilibration of water-oil contacts and the formation of ROZs; (ii) the original oil accumulation leaks through seal (perhaps temporally), again leading to ROZ formation; (iii) a change in the hydrodynamics of an underlying aquifer. The water flow scenarios sweep the lower portion of oil columns, resulting in the development of ROZs (Fig. 1). The consensus of opinions is that the ROZs in the Permian Basin represent the third of these categories and the simulations made in the current study are based on this scenario.

Unfortunately, almost all the research on ROZ formation and characteristics has not been published in refereed journals but rather is available in contract reports, presentations, and conference proceedings. Dennis et al. (2000, 2005) studied the tilted oil-water contacts in the North Sea through numerical simulation and laboratory experiments. They focused on the response of fluid contacts to aquifer

---

* Corresponding author.
*E-mail address:* boren@utexas.edu (B. Ren).

https://doi.org/10.1016/j.petrol.2019.02.072
Received 2 May 2018; Received in revised form 18 February 2019; Accepted 22 February 2019

Fig. 1. A schematic diagram showing the formation of hydrodynamic ROZ. Before the increase in regional water flow rates, the spill point (labelled by the red arrow) controls an original oil water contact at the base of the MPZ. After increasing water flow rates, part of the oil at the bottom of the original MPZ is flooded to be as a ROZ (Adapted from Melzer, 2013). (For interpretation of the references to colour in this figure legend, the reader is referred to the Web version of this article.)

heterogeneity and flow rates, without detailed investigation of oil saturation characteristics in ROZs. Trentham and his coworkers (Trentham, 2011; Trentham et al., 2012) assumed that, high aquifer flow rates would have been initially established across the San Andres formation due to the uplift of the Guadalupe Mountains (along the western margin of the Permian Basin). This uplift apparently peaked around 20 Ma (Horak, 1985), and, subsequent erosion of these mountains would have reduced hydraulic heads in the regional aquifer thus lowering flow rates. Harouaka et al. (2013) suggested that the hydrodynamic impact continued unabated, “albeit at a very slow pace like one foot/1000 years”, an assertion they based on “analytical modeling” using the analysis of Hubbert (1953). In this view, the slope of ROZ-MPZ contacts would reflect the most recent aquifer flow regime. Only limited basin scale hydrological data and modeling have been published for regions within the Permian Basin (McNeal, 1965; Bein and Dutton, 1993; Lee and Williams, 2000). A recent study by Trentham and Melzer (2015) attempted to model the probable flow pathways, of what they termed “hydrodynamic fairways”. However, absent a creation of a set of robust regional groundwater flow models extending back to the regional uplift event in the Permian Basin, the groundwater flow directions cannot be well constrained. Jamali and Ettehadtavakkol (2017) modelled the ROZ formation process through mimicking the natural waterflooding process; however, their specific simulation was based on a simplified static reservoir model and physics.

This paper is the first attempt to use multiphase and full-physics flow simulations to make a comprehensive study of the hydrodynamic model for the development of ROZs in the San Andres Formation. In the following, we describe our modeling approach and analyze several factors that are potentially significant in the evolution of ROZs. Finally, we analyzed the implications of these results to both oil production and $CO_2$ sequestration in future $CO_2$-EOR projects in these zones.

## 2. Theory and approach

This project sets out to study the formation of ROZs in the San Andres Formation. We mimick the “natural waterflood” scenario using flow simulation. These simulations aim to explore the nature and spatial patterns of oil saturation in ROZs in response to the variations in the flow of regional aquifers. The flow simulator used is Eclipse-E100 (2016), an efficient and multidimensional black-oil simulator.

### 2.1. Reservoir properties

Our modeling is based on the reservoir characteristics of the residual oil zone associated with the Seminole Field, however, we do not model this field specifically. A three-dimensional (3D) static reservoir model, representative of the geology and petrophysical variation of the ROZ underlying the Seminole Field, built in part from the published reservoir property data. Lucia (2007) and Wang et al. (1998) have published extensive porosity and permeability data from Seminole cores. The data presented in Honarpour et al. (2010) include porosity versus permeability plots, and vertical as well as horizontal permeability measurements. These are particularly important as all from the ROZ. These authors also supply data from sponge cores on residual-oil-saturation versus depth in the ROZ and versus permeability. The model is populated using data from these published sources and from petrophysical measurements made on cores in the Bureau of Economic Geology (BEG) core warehouse, and interpretation of wireline logs from the BEG log library.

Two 2-D section geologic models were cut from the 3-D whole reservoir model: one is along the E-W (X-Z slice, the approximate dip direction), and the other is along the N-S (Y-Z slice, the approximate strike direction). The purpose of selecting these two sections is to examine how flow direction affects oil saturation evolution in the ROZ. The two 2D vertical sections cross along a vertical line. This line overlaps a drilled vertical well with detailed well properties published by Honarpour et al. (2010). Specifically, this well has the oil saturation profile that is based on measurements made prior to $CO_2$ injection into the ROZ. This data provides an important way for us to validate the reasonableness of our simulations. Additionally, a small 3D sector model is also cut with the above well in the middle. So these two 2-D slices and one 3D sector model are used to simulate the natural water flooding process in forming ROZs.

The corner point grid system is used. The dimensions of each 2D model is 63 × 398 with the horizontal cell size of 100 ft, and the vertical cell size varies in different layers with the average ~2 ft. The 3D sector model has the dimensions of 20 × 20 × 398 with the cell size of 100 ft × 100 ft × ~2 ft. These sector models have similar means and standard deviation for the porosity and permeability (Table 1). The porosity and permeability fields for the E-W model are shown in Fig. 2. Published permeability measurements by Honarpour et al. (2010) show that the horizontal and vertical permeability's are largely similar. However, these authors note that the presence of low permeability layers of fine-grained, anhydrite-rich facies, creates strongly anisotropic

Table 1
Statistics of petrophysical properties for the 2D and 3D sector models.

| Measures | 2D | | 3D |
|---|---|---|---|
| | W-E slice | N-S slice | |
| Porosity arithmetic mean, [] | 0.11 | 0.11 | 0.11 |
| Porosity standard deviation, [] | 0.042 | 0.044 | 0.044 |
| Permeability arithmetic mean, mD | 17.2 | 15.9 | 16 |
| Permeability standard deviation, mD | 80.9 | 44.8 | 53.9 |
| Capillary entry pressure arithmetic mean, psi | 0.44 | 0.43 | 0.43 |
| Capillary entry pressure standard deviation, psi | 1.08 | 1.06 | 1.07 |

Fig. 2. (a) The horizontal permeability field along the W-E direction; (b) the corresponding porosity field; (c) the capillary entry pressure field corresponding to the above permeability and porosity fields. The dip angle (w.r.t to the horizontal direction) of the top boundary of the domain is around 2°.

permeability. They suggested the resultant vertical component is approximately one tenth of the horizontal component, so we use this ratio in our study. Initially, hydrostatic pressure is set for the reservoir with the middle depth pressure at 2119.9 psi, and the reservoir temperature is 104 °F. The oil saturation is initialized using the gravity-capillary equilibrium method.

A capillary entry pressure field (Fig. 2c) is generated using the Leverett j-function (Leverett, 1941) that links permeability, porosity, and capillary pressure. A general Leverett j-function has been proposed by Mirzaei-Paiaman et al. (2018), which incorporated two more rock microstructure-related parameters into the function (i.e., tortuosity and shape factor). For our current study, we used the traditional Leverett j-function (Eq. (1)) for simplicity:

$$J\,(S_w) = -\frac{p_c\,(S_w)}{\sigma_{o/w}\,\cos\theta}\sqrt{\frac{k}{\phi}} \tag{1}$$

where $p_c$ is capillary pressure, $\sigma$ is the interfacial tension between oil and brine water, $\theta$ is contact angle, $k$ is permeability, $\phi$ is porosity, $S_w$ is water saturation. The base or reference capillary pressure curve (Fig. 3b) is assigned to the cells with the permeability of 16 mD as this reference curve is measured on the core with this permeability. These cells are considered as reference cells. The other cells in the model are assigned with different capillary pressure curves by scaling the capillary pressure of each cell with its permeability and porosity. The interfacial tension for each cell is assumed to be the same, and contact angle has the same assumption. Then, the capillary pressure for other cells can be calculated by the following Eq. (2).

Fig. 3. (a) Drainage relative permeability curves; (b) the reference drainage capillary pressure curve. This curve is measured on a 16-mD core sample; (c) the fractional flow curve for water.

$$p_{c,nonref} = p_{c,ref}\sqrt{\frac{k_{ref}}{k_{nonref}}\frac{\phi_{nonref}}{\phi_{ref}}} \tag{2}$$

$p_{c,nonref}$ is the capillary pressure for other cells (nonreference cells), $p_{c,ref}$ is the capillary pressure for the reference cells, $k_{ref}$ and $k_{nonref}$ is the permeability for the reference cells, and the other cells, respectively Porosity naming follows the same rules as permeability. Through using Eq. (2), each cell is assigned with a capillary pressure curve that is consistent with its upscaled permeability and porosity while omitting interfacial tension and contact angle. The detailed procedure of scaling the reference capillary pressure curve for each cell has been elaborated by Saadatpoor (2012) and Ren (2017). Fig. 2c shows the generated

Table 2
Injection simulation schemes in the 2D models.

| Water flux entering formation from wellbore, ft/yr | Injection rate, rb/d[b] | Injection duration, yrs | Totally injected water, PV | $N_{gr}$ along the wellbore, (Eq. (3)) | Dominant force |
|---|---|---|---|---|---|
| 5.0 | 183.4 | 50 k | 268 | 4.7E+3 | Gravity |
| 0.5[a] | 18.3[a] | 50 k[a] | 26.8[a] | 4.7E+4[a] | Gravity |
| 0.05 | 1.83 | 50 k | 2.7 | 4.7E+5 | Gravity |

[a] Means base case settings.
[b] rb means reservoir barrel.

capillary entry pressure field for the E-W model. The statistics for all the capillary entry pressure fields are listed in Table 1.

The importance of considering capillary pressure heterogeneity is driven by the impact of the small regional water flux during ROZ formation. It has been suggested that regional water flux in the Permian Basin that drove the formation of the ROZ in the San Andres Formation was on the order of 10–25 cm/yr (Trentham et al., 2012). Such small water fluxes would be associated with a minimal viscous force, comparable to the magnitude of water-oil capillary pressures.

### 2.2. Petrophysical and fluid properties

Relative permeability and capillary pressure curves are shown in Fig. 3a and b, respectively. The relative permeability curves are adapted from published data (Honarpour et al., 2010). The capillary pressure curve are based on the fitting to the lab measurement using the centrifuge technique (Chen and Ruth, 1995). These curves describe the dynamic flow properties during the drainage process, which applies to the regional water infiltration since the reservoir tends to be oil-wet (Honarpour et al., 2010). Using these relative permeability curves, we plot the fractional flow curve for water (Fig. 3c). When water saturations are greater than 0.4, the fractional flow of oil is reduced to be negligible (< 0.04). This means that the remaining oil is effectively immobile, and oil production will be minimal with further water flow, even at a long time scale.

### 2.3. Flow simulation schemes

The flow simulations are designed to model the key relevant physics for understanding the formation of ROZs associated with the San Andres Formation in the Permian Basin. To understand the relevant physics, we first introduce a gravity number ($N_{gr}$), and this number describes the influence of competitive gravity versus viscous forces on water flooding. $N_{gr}$ is a dimensionless ratio of the gravitational force acting on the fluids to the viscous force that drives water migration. Several definitions of gravity number are possible. Here, we use the ratio of a nominal speed of vertical flow $u_v$ to a nominal speed of horizontal flow $u_h$, combined with the ratio of reservoir horizontal length $L$, thickness $H$, and formation dip angle $\alpha$. We write the gravity number based on the definition of Shook et al. (1992):

$$N_{gr} = \frac{\Delta\rho g k_v H \cos\alpha}{u_h \mu L} \tag{3}$$

In the above, $\Delta\rho$ is the density difference between water and oil. $g$ is the gravitational acceleration. $k_v$ is the arithmetic mean of vertical permeability. $H$ is the vertical dimension of the portion of a aquifer impacting the base of an oil reservoir (equivalent to the length characterized by a pressure boundary condition). $\alpha$ is formation dip angle with respect to the horizontal direction, $\mu$ is water viscosity at the reservoir condition. $L$ is reservoir horizontal length. The nominal horizontal flux ($u_h$) is the regional water flux as mentioned above. Under the reservoir condition (2119.9 psi and 104 °F), water density is 1060.4 kg/m$^3$, oil density is 832.9 kg/m$^3$, and water viscosity is 0.7 cp.

All terms, except for $u_h$, in Eq. (3) are fixed for a given residual oil zone. The horizontal water flux boundary condition is imposed in the Eclipse model by setting the water injection rate for an injector well (described below). Thus, $N_{gr}$ is essentially a dimensionless regional water flux or water injection rate (a reciprocal injection rate). Large values of $N_{gr}$ ($\sim 10^3$) correspond to small water flux and the water movement is dictated by gravity. Table 1 shows the examined water flux magnitude, gravity number and the corresponding dominant force for flow simulations. For the base case water flux, the corresponding pressure gradient across the simulation domain (from the injector side to produce side) is $1.4 \times 10^{-3}$ psi/ft. For all the cases simulated, the gravity number $N_{gr}$ is much larger than 1. Thus, the regional water flow should be dominated by gravity.

In the 2D models, the volume of water injected is approximately 27 pore volumes (PV) for the base case (corresponding to the regional water flux of 0.5 ft/yr and injection duration of 50 k years, Table 2). This PV is consistent with the suggestions of Trentham et al. (2012) about the time scale and flux of regional natural waterflood impacting the ROZs within the Permian Basin. The sensitivity of the magnitude of oil saturation in the ROZs to varying the magnitude and duration of regional hydraulic head, is also investigated (Table 2). The regional hydraulic head was varied over three orders of magnitude (reflected in the water flux settings in Table 2). Additionally, changes in the nature of ROZs (e.g., oil saturation and geometry) in response to the lowering of hydraulic head are examined. This lowering decreases regional water flow rate, and this study is designed to approximate the decreasing rate of flow through three sequential simulation processes with the water fluxes decreasing from 5 ft/yr, 0.5 ft/yr to 0.05 ft/yr, with each modelled for 50,000 years (refer to case #12 in Table 3). More importantly, both single and heterogeneous capillary pressures functions are considered in these simulations. A single capillary pressure function means that the capillary pressure curve (shown in Fig. 3b) is used for all the cells in the domain, whereas, heterogeneous capillary pressure functions are based on scaled capillary pressure curves.

For boundary and well settings, Fig. 4 shows a schematic illustration of well locations and perforations for the 2D W-E slice model. A vertical injector and a producer are used to mimic regional water filtration in

Table 3
Summary of conditions for simulations.

| Case # | Water flux, ft/yr | Totally-injected PV | Injection duration, yr | Flow direction | Capillary pressure |
|---|---|---|---|---|---|
| 1 | 0.5 | 26.8 | 50 k | W-E | w/o |
| 2 | 0.5 | 32.1 | 60 k | W-E | w/o |
| 3 | 0.5 | 26.8 | 50 k | W-E | Single |
| 4 | 0.5 | 26.8, 268, 536 | 50 k, 0.5 Ma, 1 Ma | W-E | Heterogeneous |
| 5 | 5.0 | 268 | 0.5 Ma | W-E | Single |
| 6 | 5.0 | 268 | 60 k | W-E | Heterogeneous |
| 7 | 0.05 | 2.7 | 50 k | W-E | Single |
| 8 | 0.05 | 2.7, 27, 54 | 50 k, 0.5 Ma, 1 Ma | W-E | Heterogeneous |
| 9 | 0.5 | 26.8 | 50 k | N-S | Single |
| 10 | 0.5 | 26.8 | 50 k | N-S | Heterogeneous |
| 11 | 5, 0.5, 0.05 | 297.5 | 0.15 Ma | W-E | Heterogeneous |
| 12 | 0.5 (3D) | 26.8 | 50 k | W-E | Heterogeneous |

Fig. 4. A schematic illustration of the water injector and the producer used to mimic the regional water flush in the ROZ for the 2D W-E slice model. The perforation intervals in both wells are along the producing ROZ and the water leg. The lateral extension of the domain is 6300 ft with the thickness around 1113 ft.

the ROZ, and the two wells are placed on the left and right boundary cells, respectively. Both wells are perforated along the intervals of both the producing ROZ and the water leg, for which, their heights are approximated through the field tests and measurements (Honarpour et al., 2010). Constant water rate is imposed on the injector with the values shown in Table 2, and the same rate of liquid production is imposed on the right producer. Boundary settings in the N-S slice are the same. For the 3D sector model, each slice along the X-direction in 3D are assigned with the same boundaries as does for 2D. Through doing this, the regional water flow should be properly mimicked. The condition settings for all the simulated cases are summarized in Table 3. Most of the simulation cases are designed on the 2D slices considering both the computational efficiency and easy settings when examining different factors. The last simulation case is on the 3D sector model in order to study possible differences.

## 3. Results

Most of the following analyses is restricted on the 2D slice models. Difference between 3D and 2D are highlighted. We firstly describe the evolution of oil saturation fields during the ROZ formation process. Particularly, we emphasize the effect of the interplay between water flux magnitude and capillary pressure on the remaining oil saturation in ROZs. Next, we compare our simulation results to the field measurement.

### 3.1. *Effect of the duration of regional aquifer flow on oil saturation in ROZs*

To evaluate the effect of the duration of regional aquifer flow on the nature of ROZ formation, we start with the case that considers no capillary pressure (#1 in Table 3). This case shows a similar oil saturation field as another case that considers single capillary pressure (#3 in Table 3). Fig. 5 shows the evolution of oil saturation fields for the case #3. In the uppermost oil saturation field (T = 0 yrs), the red area is the original "oil saturated zone" or the MPZ, and the blue area is the water leg. For the MPZ, the oil saturation is initialized using the gravity-capillary equilibrium, and the initial oil saturation is high and around 0.8. The capillary transition zone in these simulations is very small and almost not observable as shown around the interface between the yellow and blue areas. As water influx proceeds (T = 10,000 to 50,000 yrs), the vertical extent of the ROZ increases. At a timescale of 50,000 years, further changes in the magnitude and spatial distribution of oil saturation values are negligible.

Fig. 5. The evolution of oil saturation fields considering single capillary pressure. The water inlet flux is 0.5 ft/yr. The overall tilt of the producing water-oil contact in the bottom field is around 100 ft per mile, downward to the east.

The variation of oil saturation with depth is perhaps the most important feature of ROZs. To quantify oil saturation vertical profiles, we plot the change of oil saturation along depth at different times (Fig. 6). Overall, the oil saturation profiles attained an approximate or pseudo-steady state after approximately 50,000 years. The intervals with high saturation represent the low permeability/low porosity ($< 0.05$) areas, and this oil cannot be efficiently displaced by water. The attainment of pseudo-steady-state oil saturation is further illustrated in Fig. 7 that shows the evolution of cell oil saturations in several selected depths. It appears that, in this simulation, the upper part of the ROZ requires a much longer time to reach the pseudo-steady state (note the light blue line in Fig. 7).

### 3.2. *Effect of the interplay between inlet flux magnitude and capillary pressure*

We first analyze the effect of water flux magnitude (aquifer flowrate) on ROZs when considering single capillary pressure (left column in Fig. 8). ROZ thickness is sensitive to the magnitude of the upstream water flux in the aquifer. This is because of the competition between the viscous and gravitational forces (the ratio is gravity number $N_{gr}$, Eq. (3)): large viscous force (large water flux) suppresses the effect of water gravity on the displacement profile, and a thick ROZ is created. Additionally, the contact between the MPZ (yellow in Fig. 8) and the ROZ (light blue) becomes less inclined as water flux decreases; this is obviously because decreasing water flux tends to create hydrostatic

Fig. 6. The change of oil saturation vertical oil saturation profiles with time. These profiles correspond to the middle column cells (along the well with measured oil saturation in the ROZ) of the oil saturation fields in Fig. 5.

distribution of oil/water.

Next, we focus on the imposed upstream water flux of 0.5 ft/yr (the middle row in Fig. 8) and analyze the effect of capillary pressure heterogeneity on the development of ROZs in response to this water flow. When capillary pressure heterogeneity is taken into account, the producing water-oil contact is enlarged (relative to single capillary pressure). In addition, the transition zone (black circled area in the middle row) between the ROZ and the MPZ is distinct, with a thickness of 10–15 ft. The oil saturation in this transition zone varies significantly, from around 0.30 in light green spots to 0.80 in the light yellow patches. However, for the case considering single capillary pressure, the transition zone is thin and poorly defined (refer to the middle left oil saturation field in Fig. 8).

More importantly, the interplay between capillary pressure heterogeneity and upstream water flux largely influences the thickness of the upper transition zone (the dashed circle area). Through comparing the middle saturation field to the lower one in the right column in Fig. 8, it can be seen that the upper transition zone becomes thick as the upstream water flux decreases. Again, this is because of the lower viscous force, which in turn enhances the effect of capillary dispersion on oil saturation.

The above analyses concentrate on the evolution of oil saturation in ROZs. The time scale of achieving quasi steady-state oil saturation in a ROZ is much less than the geologic time of mountain uplift and erosion (~Ma). Generally, the evolution of oil saturation in a given cell is mainly controlled by both relative permeability curves and imposed pressure gradient (equivalent to inlet water flux). Thus, any changes in both of them would cause different time consumed to achieve steady states.

Fig. 7. The change of cell oil saturation with time at several different selected depth points. These points are all in the ROZ: 5370 ft is around the ROZ top, the two depths of 5425 and 5450 ft are in the middle, and 5475 ft is at the bottom.

Fig. 8. Oil saturation fields at 50000 yrs of flow simulation. Each row represents different regional water fluxes. The left column considers single capillary pressure, whereas, the right column considers heterogeneous capillary pressure. The dashed lines represent the approximated transition areas between the top of the producing ROZs and the base of producing MPZs. As water flux decreases, the overall tilt of the producing water-oil contact decreases from about 100 ft per mile (upper) to 30 ft per mile (lower).

### *3.3. Effect of the duration of regional aquifer flow on the thickness of ROZ*

ROZ thickness takes a longer time to establish itself than oil saturation does (Fig. 9). After 50 k yrs, the thickness of the ROZ continues growing for the small regional water flux of 0.05 ft/yr, and it becomes asymptotic as flow simulation proceeds to 1 MM yrs. For the large flux of 0.5 ft/yr, however, it takes a short time in establishing the ROZ geometry, and the ROZ has already been fully fledged around 0.5 MM yrs. So the thickness of ROZs are impacted by flush duration and water flux magnitudes.

Fig. 9. The evolution of ROZ thickness for the two regional water fluxes (0.05 vs. 0.5 ft/yr). Capillary pressure heterogeneity is considered. The overall tilt of the producing water-oil contact is the left lower field is approximately 20 ft per mile, and it is 100 ft per mile in the right lower field.

Fig. 10. Impact of flow direction on oil saturation fields in the ROZ. The oil saturation is at the 50,000 yrs of flow simulation with capillary pressure heterogeneity considered. The black dashed lines circle the oil stripes with large oil saturation in the ROZ, and the blue dashed lines approximate the inclined producing water-oil contacts. The imposed water flux for both oil saturation fields is 0.5 ft/yr. The tilt of producing water-oil contacts is stronger in the W-E slice than that in the N-S slice, 100 ft per mile vs. 55 ft per mile. (For interpretation of the references to colour in this figure legend, the reader is referred to the Web version of this article.)

### 3.4. Effect of direction of regional water flow

The direction of regional water flow is not well constrained by available data. However, this direction influences the pattern of oil saturation in the ROZ (Fig. 10). This pattern is significantly different between the two orthogonal directions. For the W-E section (orthogonal to the edge of the Central Basin Platform), the streaks with high oil saturation are of limited lateral extent compared to than those in the N-S section (approximately parallel to the shelf edge of the platform). These differences in the spatial variation of oil saturation reflect the significant variation in the heterogeneity of capillary pressures. The origin of this heterogeneity is rooted in the changes of depositional environments from the inner-mid ramp to the outer ramp from west to east. However, for the section parallel to the shelf edge, the sedimentary facies reflect a more limited range of sedimentary environments with more limited heterogeneity in capillary pressures. This gives rise to a very large laterally-extended strip of higher oil saturations in the ROZ. This important observation is useful in guiding the configurations of injectors and producers during $CO_2$-EOR operations.

Another noteworthy issue is the nature of water-oil contacts (dashed blue lines in Fig. 10) for the two different regional water flow directions. The inclination of the contact along the strike direction is smaller than that along the dip direction. This observation is consistent with greater lateral sedimentary continuity along the strike.

### 3.5. Effect of the change of regional water flux

A key question is the extent to which the nature and geometry of ROZs are impacted by low flow rates following after a period of high flow rates, a scenario expected based on the tectonic history of the Basin. The overall shape of the ROZ undergoes negligible modification when the regional water rate is reduced by an order of magnitude for 50,000 years (Fig. 11a), i.e., the ROZ interval thickness has not altered during the sequential change of regional water rate. However, oil saturation is impacted by the sequential change of water flux. Specifically, the oil saturation in the downstream of regional water flow increases as regional water flux decreases (Fig. 11b). This reflects the displacement of oil downstream. Additionally, the ROZ in the upstream is thicker than that in the downstream (comparing the ROZ depth interval between Fig. 11a and b). This is consistent with the above observation of ROZ geometries (in both Figs. 5 and 8).

### 3.6. Differences between 2D and 3D

The resultant oil saturation magnitude and pattern in 3D are found to be very similar to the results of 2-D simulations with marginally higher oil saturation in 3-D than in 2-D along some depth intervals (Fig. 12). This might be counterintuitive since the added one dimension in 3D normally enhances lateral flow and causes an overall large oil saturation compared to 2D. However, such lateral flow is restrained by the specific boundary settings in this study; each X-Z slice in the 3D model has close pressure gradient from the injection side to the production one, so most of the flow are along the X-Z direction. This is similar to what happens in the 2D X-Z slice model. In other words, the water/oil flow dynamics is marginally altered by the added one dimension in 3D. This analysis also supports our observation that the time-scale of attaining quasi steady-state oil saturation in 3D is close to that in 2D.

### 3.7. Comparison with field measurements in the Seminole ROZ

Our study has compared the vertical variation in oil saturation in our ROZ simulations carried out at different water fluxes with down the well measurements for the ROZ in the San Andres Seminole Unit, published by Honarpour et al. (2010). The vertical pattern of variation in oil saturation most closely resembles the pattern produced by simulations using a water flux of 0.5 ft/yr. Fig. 13 shows the predicted oil saturation profile at this water flux. The simulated oil saturation profile in the N-S slice (red line in Fig. 13) shows a better agreement with the measured oil saturation in the main interval of the ROZ than that in the E-W slice. Meanwhile, it is worthwhile to notice the fluctuation of measured oil saturations. The controls of these fluctuation are under the investigation now.

## 4. Discussion

This study has not attempted to specifically model the Seminole Field. Rather, we have modelled the formation of a generic ROZ by starting with an oil-saturated reservoir. Its thickness is equivalent to the sum of the current SSAU ROZ and producing MPZ. Our simulations reproduce many of the features reported from the San Andres ROZ. The simulation results are consistent with an effectively steady state being reached (at least with respect to oil saturation) on a time scale of 50 thousand years. It is significant that, even after 1 MM yrs of regional water flush, the oil saturation in several patches remains similar to the initialized values (0.7–0.8). These patches are local areas of lower porosity and permeability. This observation is consistent with the observed presence of oil stains in the less permeable patches of San Andres core samples.

### 4.1. The tilt and measurability of ROZ boundaries

The estimated tilt of the top boundary of the ROZ has been regarded as the key evidence for the validity of the hydrodynamic model. The tilts vary significantly (3–200 m/km, 15.8–1056 ft/mile) for different oilfields worldwide (Dennis et al., 2000; Connor and Swarbrick, 2008). The estimates for the dip in our simulations is small (in our base-case simulations approximately 100 ft per mile, Fig. 5). This is comparable to the earlier suggestions by Melzer et al. (2006), and it is also consistent with other reduced-physics modeling results (e.g., Koperna et al., 2006; Jamali and Ettehadtavakkol, 2017). However, the accuracy limitations of wireline log measurements of oil saturation are significant (Pathak et al., 2012) and the dip estimates available for real San Andres ROZs in unpublished reports and presentation do not

Fig. 11. The selected two oil saturation profiles and their changes in response to the lowering water flux. The regional water flow is from west to east. The profile#1 is on the upstream of water flow, whereas, the profile#2 is on the downstream. The exact locations of these two columns are along $I = 22$ and $I = 43$, respectively. $I$ is the numbering of cells from west to east in the horizontal direction. This figure is corresponding to the case#11 in Table 3.

appear to be robust. Another complication is that, as demonstrated in our simulations and by the data presented by Honarpour et al. (2010), the variability in oil saturations is related to local heterogeneity in reservoir properties, particularly capillary pressure heterogeneity. This heterogeneity significantly blurs the transitions between MPZs and ROZs, as well as the ROZ-water contacts (see Fig. 8, for example).

### 4.2. *Influence of heterogeneous capillary pressure*

The results of our simulations show the significant influence of capillary pressure heterogeneity on the flow paths of water/oil and thus on the characteristics, including the producing water-oil contact, as well as the pattern, and magnitude of oil saturation in ROZs. To our best knowledge, this is first time that such a physic is incorporated in flow simulations of ROZ formation processes. Heterogeneous capillary pressures have also been found to be important in other slow subsurface dynamics processes, e.g., buoyant flow of $CO_2$ during geological carbon sequestration (Saadatpoor et al., 2009; Trevisan et al., 2017) and secondary hydrocarbon migration/accumulation (Carruthers, 1998). Even for conventional water flooding with the water speed three orders of magnitudes larger than that associated with the hydraulic head gradient and consequent subsurface regional aquifer flow rates preferred in this study, capillary pressure heterogeneity apparently significantly affects oil saturation under some conditions (Chang and Yortsos, 1992; Lasseter et al., 1986).

Fig. 12. Comparison of oil saturation profiles between the 2D W-E slice model and the 3D sector model. The profile are along the well with measured oil saturation as mentioned above. Capillary pressure heterogeneity is considered in these simulations.

### 4.3. *Limitations of this study*

This study is subject to several limitations. First, the predictions of average oil saturation in the ROZs from our simulations are marginally larger than those measured by Honarpour et al. (2010). One possibility is that, in some cells, the 50,000 years of the flow simulations presented is insufficient to achieve a steady state. This is the consequence of the fractional flow curve for water (Fig. 3c). The fractional flow of oil is reduced to a very small value ($< 0.008$) when water saturation increases to 0.5. Another complication is the impact of our limited ability to accurately model the heterogeneous nature of the reservoir. The simulations in this study utilized a cell size of 100 ft × ~2 ft (in 2D models). However, the estimates of porosity and permeability were based on measurements of core plugs with the size of 1–2 inches. Upscaling these detailed measurements to the scale of the simulation grids inevitably averages out the true heterogeneous nature of the reservoir. Additionally, the study employs injectors to represent regional water influx. Whether such a representation is proper in creating hydrodynamically-representative tilts, need to be further validated by more field/well data.

### 4.4. *Implications to future $CO_2$-EOR and associated sequestration in ROZs*

The current study provides useful insights into how these residual oil reservoirs can best be exploited to maximize both oil production and $CO_2$ storage. For example, heterogeneities in permeability, porosity, and capillary pressures are highly likely to result in three-dimensional spatial heterogeneities in oil saturation. Such patches and layers of high saturation could be exploited by using multiple horizontal wells. The volume and saturation of water in ROZs should impact the selection and optimization of $CO_2$ injection strategies. The nature of water occurrence in ROZs differs from that of MPZs subsequent to man-made water flooding. In these circumstances, the water saturations in MPZs typically will be locally high around the water streamlines connecting injectors and producers. This difference would result in differing optimal parameters for WAG injection such as water cycle size and WAG ratio (see for example Ren and Duncan, 2019) as well as the $CO_2$/water/rock interaction (Luhmann et al., 2017; Cui et al., 2017) for the geochemical

Fig. 13. Comparison of ROZ oil saturation profiles between reservoir simulations and field measurements. The oil saturation (black square dots) is originally measured in sponge cores and then corrected for reservoir conditions (Honarpour et al., 2010). The black squares are the corrected oil saturations. The comparison employs the simulated oil saturation with the water inlet flux 0.5 ft/yr. The selected time for the simulation result is at 50 k yrs.

sequestration purpose. Additionally, tilted contacts have been demonstrated to be important in affecting $CO_2$ storage capacities and security. Numerical simulations by Heinemann et al. (2016) show that $CO_2$ storage in hydrodynamic aquifers can be enhanced through accelerated $CO_2$ dissolution compared with static aquifers.

## 5. Conclusions and recommendations

Characterizing the variation of oil saturation in residual oil zones (ROZs) is essential to assess reserves, design $CO_2$-EOR projects, and estimate sequestration capacities. The simulations reported in this study have shown that the characteristics of ROZs can be reproduced using a commercial, full-physics, multi-phase flow simulator. The simulated oil saturation profiles are in reasonable agreement with the measured profile published for the San Andres Seminole Unit's ROZ. The results support the plausibility of the hydrodynamic model suggested by earlier researchers, but do not rule out other models for the origin of ROZs.

The interplay between the magnitudes of water flux (aquifer flow rate) and capillary pressure influences the variation of oil saturations (both spatially and temporally) and geometry of ROZs. Larger water fluxes result in thicker ROZs, and heterogeneity of capillary pressures results in diffuse water-oil contacts.

During the formation of ROZs, the evolution of oil saturations is essentially controlled by relative permeability curves, and in our specific study, oil saturation can achieve almost steady states in a time scale that is relatively short compared to the time over which increased aquifer flow rates are likely. However, the geometry of ROZs are slow to be established, especially for small regional water fluxes.

A considerable amount of oil resides in ROZ reservoirs. Thus, they should be considered as the attractive exploration targets for $CO_2$ EOR and storage. Additionally, the spatial distribution of oil in ROZs are different from that in MPZs undergoing water flooding. This difference should be emphasized in the optimization of injection strategies during $CO_2$ EOR and storage in ROZs.

## Acknowledgements

This study is part of a long term project investigating ROZ reservoirs in the Permian Basin of Texas being carried out by the Bureau of Economic Geology's (BEG's) State of Texas Advanced Resource Recovery (STARR) Program and funded in part by a U.S. Department of Energy contract under DOE Award Number FE0024375 (PI: Duncan). The first author would like to thank Dr. Sheng Peng for his review during the preparation of this manuscript. We wish to thank Robin Dommisse for his help in building the geologic model. The opinions of the authors do not necessarily reflect those of the United States Government or any agency thereof. The research was also supported by endowed funds from the Jackson School of Geological Sciences at The University of Texas at Austin. Publication authorized by the Director, Bureau of Economic Geology.

## Appendix A. Supplementary data

Supplementary data to this article can be found online at https://doi.org/10.1016/j.petrol.2019.02.072.

## References

Bachu, S., Pires, P., Li, M.Y., Guzman, F., Eide, L.I., Aleidan, A., Ackiewicz, M., Melzer, L.S., 2013. Technical challenges in the conversion of $CO_2$-EOR projects to $CO_2$ storage projects, report prepared by the CSLF task force on technical challenges in the transition from $CO_2$ EOR to CCS. http://www.cslforum.org/publications/documents/CO2-EORtoCCS_FinalReport.pdf.

Bein, A., Dutton, A.R., 1993. Origin, distribution, and movement of brine in the Permian Basin (USA): a model for displacement of connate brine. Geol. Soc. Am. Bull. 105 (6), 695–707.

Carruthers, D.J.F., 1998. Transport Modelling of Secondary Oil Migration Using Gradient-Driven Invasion Percolation Techniques. Ph.D. Dissertation. Heriot-Watt University, Edinburgh, UK.

Chang, J., Yortsos, Y.C., 1992. Effect of capillary heterogeneity on buckley-leverett displacement. SPE Reservoir Eng. 7 (2), 285–293. https://doi.org/10.2118/18798-PA.

Chen, Z.A., Ruth, D.W., 1995. Measurement and interpretation of centrifuge capillary pressure curves-the sca survey data. Log. Anal. 36 (5) SPWLA-1995-v36n5a2.

Connor, S.A., Swarbrick, R.E., 2008. Pressure regression, fluid drainage and a hydrodynamically controlled fluid contact in the North Sea, lower cretaceous, britannia sandstone formation. Petrol. Geosci. 14, 115–126.

Cui, G., Zhang, L., Tan, C., Ren, S., Zhuang, Y., Enechukwu, C., 2017. Injection of supercritical $CO_2$ for geothermal exploitation from sandstone and carbonate reservoirs: $CO_2$–water–rock interactions and their effects. J. $CO_2$ Util. 20, 113–128.

Dennis, H., Baillie, J., Holt, T., Wessel-Berg, D., 2000. Hydrodynamic Activity and Tilted Oil-Water Contacts in the North Sea. vol. 9. NPF Special Publication, pp. 171–185.

Dennis, H., Bergmo, P., Holt, T., 2005. Tilted oil-water contacts: modelling the effects of aquifer heterogeneity. In: In: Dore, A.G., Vining, B.A. (Eds.), Petroleum Geology: North-West Europe and Global Perspectives – Proceedings of the 6th Petroleum Geology Conference, vol. 6. pp. 145–158.

Eclipse-E100, 2016. Eclipse Users' Manual. Schlumberger, France.

Godec, M.L., Kuuskraa, V.A., Dipietro, P., 2013. Opportunities for using anthropogenic $CO_2$ for enhanced oil recovery and $CO_2$ storage. Energy Fuels 27 (8), 4183–4189.

Harouaka, A., Trentham, B., Melzer, L.S., 2013. Long overlooked residual oil zones (ROZ's) are brought to the limelight. In: SPE-167209 Presented at the SPE Unconventional Resources Conference, Calgary, Canada, 5-7 November, . https://doi.org/10.2118/167209-MS.

Heinemann, N., Stewart, R.J., Wilkinson, M., Pickup, G.E., Haszeldine, R.S., 2016. Hydrodynamics in subsurface $CO_2$ storage: tilted contacts and increased storage security. Int. J. Greenh. Gas ContR. 54, 322–329. https://doi.org/10.1016/j.ijggc.2016.10.003.

Honarpour, M.M., Nagarajan, N.R., Grijalba Cuenca, A., Valle, M., Adesoye, K., 2010. Rock-fluid characterization for miscible $CO_2$ injection: residual oil zone, Seminole field, Permian Basin. In: SPE-133089 Presented at the Annual Technical Conference and Exhibition, Florence, Italy, 19-22 September, . https://doi.org/10.2118/133089-MS.

Horak, R.L., 1985. Tectonic and hydrocarbon maturation history in the Permian Basin. Oil Gas J. 83 (21), 124–129.

Hubbert, M.K., 1953. Entrapment of petroleum under hydrodynamic conditions. Bull. Am. Assoc. Pet. Geol. 37 (8), 1954–2028.

Jamali, A., Ettehadtavakkol, A., 2017. $CO_2$ storage in residual oil zones: field-scale modeling and assessment. Int. J. Greenh. Gas ContR. 56, 102–115. https://doi.org/10.1016/j.ijggc.2016.10.005.

Koperna, G.J., Melzer, L.S., Kuuskraa, V.A., 2006. Recovery of oil resources from the residual and transitional oil zones of the Permian Basin. In: SPE 102972 Presented at the Annual Technical Conference and Exhibition, San Antonio, Texas, 24-27 September, . https://doi.org/10.2118/102972-MS.

Kuuskraa, V.A., Godec, M.L., Dipietro, P., 2013. $CO_2$ utilization from "next generation" $CO_2$ enhanced oil recovery technology. Energy Procedia 37, 6854–6866.

Kuuskraa, V., Petrusak, R., Wallace, M., 2017. Residual oil zone "fairways" and discovered oil resources: expanding the options for carbon negative storage of $CO_2$. Energy Procedia 114, 5438–5450.

Lasseter, T.J., Waggoner, J.R., Lake, L.W., 1986. Reservoir heterogeneities and their influence on ultimate recovery. In: Lake, L.W., Carroll, B.C. (Eds.), Reservoir Characterization. Elsevier Inc., Amsterdam, pp. 545–559.

Lee, M.K., Williams, D.D., 2000. Paleohydrology of the Delaware basin, western Texas: overpressure development, hydrocarbon migration, and ore genesis. AAPG (Am. Assoc. Pet. Geol.) Bull. 84 (7), 961–974.

Leverett, M.C., 1941. Capillary behavior in porous solids. AIME Petrol. Trans. 142, 152–169.

Lucia, F.J., 2007. Carbonate Reservoir Characterization: an Integrated Approach. Springer Science & Business Media, Berlin, Germany.

Luhmann, A.J., Tutolo, B.M., Tan, C., Moskowitz, B.M., Saar, M.O., Seyfried, W.E., 2017. Whole rock basalt alteration from $CO_2$-rich brine during flow-through experiments at 150° C and 150bar. Chem. Geol. 453, 92–110.

McNeal, R.P., 1965. Hydrodynamics of the Permian Basin. AAPG Mem. 4, 308–326.

Melzer, L.S., Kuuskraa, V.A., Koperna, G.J., 2006. The origin and Resource potential of residual oil zones. In: SPE-102964 Presented at the Annual Technical Conference and Exhibition, San Antonio, Texas, 24-27 September, . https://doi.org/10.2118/102964-MS.

Melzer, L.S., 2013. Residual oil zones (ROZ): a review of ROZ science and engineering. In: Enhanced Oil Recovery's Tensleep III Workshop. University of Wyoming.

Mirzaei-Paiaman, A., Ostadhassan, M., Rezaee, R., Saboorian-Jooybari, H., Chen, Z., 2018. A new approach in petrophysical rock typing. J. Petrol. Sci. Eng. 166, 445–464. https://doi.org/10.1016/j.petrol.2018.03.075.

Pathak, P., Fitz, D., Babcock, K., Wachtman, R.J., 2012. Residual oil saturation determination for EOR projects in means field, a mature west Texas carbonate field. SPE Reservoir Eval. Eng. 15 (05), 541–553. https://doi.org/10.2118/145229-PA.

Ren, B., 2017. Local Capillary Trapping and Permeability-Retarded Accumulation during Geological Carbon Sequestration. Ph.D. Dissertation. The University of Texas at Austin, Austin, Texas.

Ren, B., Duncan, I.J., 2019. Reservoir simulation of carbon storage associated with $CO_2$ EOR in residual oil zones, San Andres formation of west Texas, Permian Basin, USA. Energy 167, 391–401. https://doi.org/10.1016/j.energy.2018.11.007.

Saadatpoor, E., Bryant, S.L., Sepehrnoori, K., 2009. New trapping mechanism in carbon sequestration. Transport Porous Media 82 (1), 3–17. https://doi.org/10.1007/s11242-009-9446-6.

Saadatpoor, E., 2012. Local Capillary Trapping in Geological Carbon Storage. Ph.D. Dissertation. The University of Texas at Austin, Austin, Texas.

Shook, M., Li, D., Lake, L.W., 1992. Scaling immiscible flow through permeable media by inspectional analysis. Situ 16 (4), 311–350.

Stewart, R.J., Johnson, G., Heinemann, N., Wilkinson, M., Haszeldine, R.S., 2018. Low carbon oil production: enhanced oil recovery with $CO_2$ from North Sea residual oil zones. Int. J. Greenh. Gas Contr 75, 235–242. https://doi.org/10.1016/j.ijggc.2018.06.009.

Trentham, B., 2011. Residual oil zones: the long term future of enhanced oil recovery in the Permian Basin and elsewhere. In: AAPG Southwest Section Meeting, Jun 5-7, . http://www.searchanddiscovery.com/documents/2011/40787trentham/ndx_trentham.pdf.

Trentham, C.R., Melzer, L.S., Vance, D.B., 2012. Commercial Exploitation and the Origin of Residual Oil Zones: Developing a Case History in the Permian Basin of New Mexico and West Texas. RPSEA Final Report.

Trentham, C.R., Melzer, L.S., 2015. Case Studies of the ROZ $CO_2$ Flood and the Combined ROZ/MPZ $CO_2$ Flood at the Goldsmith Landreth Unit, Ector County, Texas. DOE Final Report.

Trevisan, L., Krishnamurthy, P.G., Meckel, T.A., 2017. Impact of 3D capillary heterogeneity and bedform architecture at the sub-meter scale on $CO_2$ saturation for buoyant flow in clastic aquifers. Int. J. Greenh. Gas ContR. 56, 237–249. https://doi.org/10.1016/j.ijggc.2016.12.001.

Wang, F., Lucia, F., Kerans, C., 1998. Integrated reservoir characterization study of a carbonate ramp reservoir: Seminole san Andres unit, gaines county, Texas. SPE Reservoir Eval. Eng. 1 (02), 105–113. https://doi.org/10.2118/183628-PA.

6

# Lessons for machine learning from the analysis of porosity-permeability transforms for carbonate reservoirs

Frank Male [a,*], Ian J. Duncan [b]

[a] Hildebrand Department of Petroleum and Geosystems Engineering, University of Texas at Austin, USA
[b] Bureau of Economic Geology, University of Texas at Austin, USA

ARTICLE INFO

*Keywords:*
Data analysis
Reservoir characterization
Permeability prediction

ABSTRACT

Prediction of permeability is one of the most difficult aspects of reservoir characterization because permeability cannot be directly measured by current well logging technology. This is particularly challenging for carbonate rocks. Machine learning (ML) and robust multivariate methods have been developed that have been used in many fields of study to make accurate estimators for variables of interest from both large and small datasets. ML has been criticized for utilizing approaches that are typically not interpretable. That is, it is not clear how the answers are arrived at and what aspects of input data may be resulting in inaccurate results. The current study uses a number of the mathematical algorithms that operate inside ML modules. It applies them to developing porosity-permeability transforms, with or without rock types, to two well-characterized data sets for carbonate reservoirs. One data set is from Jerry Lucia's 1995 study of carbonate rock types, and the other is from a study of the Seminole, West Texas, San Andres Unit. This study of statistical analysis of porosity-permeability transforms includes: transforming the data to normal distributions; performing cross-validation blind testing; and detecting heteroscedasticity by creating plots of residuals. Heteroscedastic data (populations with variable variance) may have an adverse impact on ML algorithms such as Random Forests (RF). We find that including lithofacies information does not greatly improve porosity-permeability transforms. We also propose a number of strategies to make ML analyses of reservoir (and other geosciences) data sets more robust and accurate.

## 1. Introduction

Predicting permeability from porosity measurements of heterogeneous carbonate reservoir facies is of considerable importance in reservoir characterization. A model developed a few decades ago by Jerry Lucia, 1995, 2007 was widely regarded as a major step forward in developing porosity-permeability transforms for such reservoirs. The Lucia (1995) model related rock fabric to the formulation of porosity-permeability transforms for carbonate lithologies. In recent years, Machine Learning (ML) models have been proposed as a different approach for classifying rock fabrics and predicting permeability.

Machine Learning is fast becoming a popular tool for attempting to solve a wide variety of problems in the earth sciences (Cranganu et al., 2015; Lary et al., 2016; Cat[illegible]e et al., 2017). ML uses algorithms such as Gradient Boosting Regressors, Random Forests, Support Vector Ma- chines, and Neural Networks (Mishra and Datta-Gupta, 2017). It also utilizes improved versions of conventional algorithms, such as ordinary least squares (OLS). Recently developed variants of OLS provide more robust solutions to accomplish regression of complex data sets (James et al., 2013). These algorithms can process large amounts of data to facilitate rapid pattern recognition for large multi-variable data sets, make predictive inferences, estimate the relative importance of contributing factors in determining a specific outcome, and "to make and improve predictions of behaviors based on data" (Molnar, 2019).

Unfortunately, ML models for are viewed by some practitioners (and many end users) as "Black Boxes." A black box model is either "too complicated for any human to comprehend," or a model that is proprietary (Rudin, 2019). Even if these models can be used to make accurate predictions, if the nature of the underling mathematical and/or statistical basis for these predictions is not clear, then such a characterization is justified. The forecasts from ML models cannot typically be explained in a way that can readily understood by the researcher or the end-user of the research.

Interpretable Machine Learning, the focus of Molnar (2019), attempts to make Black Box Models explainable. Molnar (2019) asserted that there is "no real consensus about what interpretability is." Others

---

* Corresponding author.
*E-mail address:* frmale@utexas.edu (F. Male).

https://doi.org/10.1016/j.petrol.2019.106825
Received 11 October 2019; Received in revised form 17 December 2019; Accepted 17 December 2019

**Table 1**
Lithological classifications for the SSAU, giving the group, rock name, and approximate depostional environment for each lithological group.

| Lithological group | Rock name | Depositional environment |
|---|---|---|
| 1 | Mudstone | Outer ramp below storm wave base |
| 2 | Bioclastic wackestone | Outer ramp to mid ramp |
| 3 | Bioclastic packstone, grainstone, and rudstone | Mid ramp to shoal |
| 4 | Ooid-peloid grainstone | Shoal |
| 5 | Peloidal wackestone, laminated mudstone, and anhydrite | Back shoal, tidal flat, and sabhka |

have suggested that interpretability is the capability to determine how an ML model arrives at its answers to the posed question. Interpretability requires understanding the effects that changes in the input data have on results (Gilpin et al., 2018; Murdoch et al., 2019). Interpretability is important in avoiding embedded bias as well as aiding researchers understanding the impact on the solution of trade-offs in their models. Attempting to explain Black Box models may elucidate some issues. However, as Rudin (2019) noted, “creating models that are interpretable in the first place” may be the preferred approach. Interpretable models include linear regression, logistic regression, other linear regression extensions, and decision trees (Molnar, 2019).

A particular ML research focus, of interest to geologists, has been classifying rock facies and predicting permeability from wireline log data (Hall, 2016; Al-Mudhafar, 2017; Ahmadi and Chen, 2018; Sudakov et al., 2019). Over the last decade, a variety of artificial intelligence and ML approaches have been brought to bear on the problem of estimating the permeability of carbonate reservoir rocks (see for example El-Sebakhy et al., 2012; Al-Mudhafar, 2015; Elkatatny et al., 2018).

In the current study, we examine the results from some specific ML models for predicting permeability. In addition, we utilize some of the key algorithms that are utilized in some ML models to test the validity (predictability) of permeability estimates made using regression-based transforms. The data comes from the seminal study of porosity-permeability relationships in carbonate reservoirs published by Lucia (1995) and from an ongoing study of the Seminole San Andres Unit (SSAU) reservoir by Baqués and Duncan.

Lucia’s methodology has been widely applied in rock typing and reservoir characterization studies. However, the Lucia transforms have not been subjected to a robust statistical analysis. In this paper, we study the uses and limitations of ML, using carbonate porosity-permeability measurements as an example. With machine learning approaches, we addressed the question, “Can rock typing techniques improve prediction of permeability from porosity?”

In order to address whether rock typing techniques assist in building porosity-permeability transforms, we used a number of approaches. First, we analyzed input data to establish its fitness for the application of ML algorithms. Then we made predictions of permeability based on models of differing degrees of complexity. The models included ordinary least squares (OLS) and regularized, Elastic-Net regressors. Finally, we analyzed the residuals from those predictions to determine how predictive the models are and whether their assumptions appear to be violated.

## 2. Materials and methods

### 2.1. Lucia’s model for porosity, permeability, and rock fabric

An important part of reservoir characterization is finding the spatial distribution of petrophysical properties for rocks. This is typically achieved through taking high confidence results from core and outcrop studies, generalizing them, and then applying these generalizations to lower confidence data set, such as well log interpretations. Two petrophysical properties are particularly important for reservoir characterization: porosity and permeability. Both can be measured in core samples, however only porosity can be directly estimated from wireline well logs. In clastic reservoirs, typically a tight correlation can be found between porosity and permeability. However, in carbonate reservoirs it is common to find 3 orders of magnitude variation in permeability for rocks of a specific porosity. Development of useful porosity-permeability transforms from core data proved elusive for many years.

There have been repeated attempts at relating porosity to permeability through the rock fabric of carbonate lithologies, starting with Gus Archie. Archie (1952) proposed a carbonate classification system that considered the pore-size distribution.

In the mid-1990s, Lucia proposed a new approach (Lucia, 1995). He split carbonate rocks into three classes, based on a modified Dunham texture nomenclature (Dunham, 1962) and on the average grain size. He also developed a set of transforms to predict permeability for a specific porosity and rock type. The Lucia rock type approach provided a framework to estimate the petrophysical parameters of carbonates. (Grötsch and Mercadier, 1999; Lucia, 2007; Wang et al., 1998).

### 2.2. Porosity/permeability data from the Seminole San Andres Unit, Permian Basin, Texas

In order to compare the rock typing approach to one utilizing lithological information, we built two complementary datasets. Cores from legacy wells in the Seminole San Andres Unit (SSAU) were put through routine core analysis, scanned using off-the-shelf desktop scanners, and logged to determine the lithofacies. The approach is documented in Baqués and Duncan (in prep.). Lucia rock types were based on a data set that spans many fields in the Permian Basin and Persian Gulf; it includes several SSAU wells.

The SSAU is a dolomitized carbonate ramp reservoir that has produced more than 700 million bbl of oil to date. It is located on the eastern shelf of the Central Basin Platform of the Permian Basin, West Texas, USA. There have been several reservoir characterization studies of the SSAU, including Wang et al. (1998), Sonnenfeld et al. (2003), Kerans et al. (1994), Honarpour et al. (2010), and Ren and Duncan (2019). The Seminole field was among those analyzed by Lucia (1995) during the development of his rock typing approach.

The lithological analysis dataset from the SSAU that we utilized includes 2803 porosity and permeability measurements. Lithological interpretations were placed into five facies groups (from deep to shallow deposition): 1) open marine mudstone, 2) bioclastic wackestone, 3) bioclastic grainstone-packstone-rudstone, 4) ooid-peloid grainstone, and 5) laminated mudstone, anhydrite and peloidal wackestone. These are shown in Table 1.

Another dataset comes from Lucia (1995). The Lucia rock types are 1, 2, and 3, which roughly correspond to grain-dominated grainstones, grain-dominated packstones, and mud-dominated fabrics (Lucia, 1995, Figure 16). These are derived from thin section analysis to determine the Lucia rock class and to estimate the interparticle porosity. This data is then merged with core measurements of the Klinkenberg-corrected permeability to air. The result is an approximately 400 sample dataset exactly corresponding to Lucia (1995) Figure 12.

### 2.3. Data exploration

Upon collecting the data, porosity and permeability univariate and bivariate distributions were plotted for each rock type. This included Q-Q plots, histograms and cross-plots. Q-Q plots are useful for identifying outliers, testing skewness of the data, testing the normality of the distribution, and determining the degree of difference between groups.

This data exploration provided the opportunity to consider how complex the model can be, for the available data. A highly unbalanced distribution of facies (if, for instance, one facies made up over 80% of the data) would indicate that facies splits could tell us little about the porosity-permeability relationships. If the histogram shows two distinct sub-distributions within one of the facies, that could indicate a natural division for an overbroad facies definition.

**Fig. 1.** Histograms of interparticle porosity (a) and permeability (b) distributions for each Lucia rock type in the Lucia (1995) dataset. Porosity for rock class three is bi-modal. Permeability values for each class do not follow a normal distribution.

Cross-plots between porosity and permeability by facies give an idea of the likely effectiveness of a linear model. Clearly linear trends lead to good accuracy of the model, and plots without clear trends generally lead to ineffective models.

### 2.4. *Preprocessing*

In order to select a model that is likely to perform effectively on blind tests, we must measure and minimize over-fitting. When a model over-fits, its predictions are being influenced by noise in the data rather than true effects. Over-fitting is tested for by creating a hold-out dataset (the testing set), fitting models on the training set, then testing their performance on the excluded data.

After the data is split into testing and training datasets, preprocessing is applied to the testing dataset. Permeability is log-transformed to simplify comparison between this work and others, and to make its distribution more nearly Gaussian. The porosity data set is transformed, using the Box-Cox method (Box and Cox, 1964). This method transforms non-normal variables to approximate a normal distribution. Normality is a necessary assumption for a number of statistical techniques, including linear regression. After the porosity dataset is transformed, it is centered to a mean of zero and scaled to a standard deviation of 1.

After variable transformation, regressions follow equations of the form

$$\log_e k = A\frac{\varphi^\lambda - 1}{\lambda} + B;$$

where $\lambda$ is the Box-Cox exponent used to transform porosity to approximate normality, $\varphi$ is porosity reported as a volume fraction, and $A$ and $B$ are fitting parameters. The Box-Cox exponent is estimated through optimization of a partial log-likelihood function (R Core Team, 2017, step_BoxCox documentation).

### 2.5. *Building regression models*

Regression models (also called regressors) are statistical techniques that approximate the relations between a dependent (response) and one or more independent (explanatory) variables. The OLS method has poor performance (in terms of bias and variance/uncertainty issues) for many data sets. The bias is the difference between the true value of a

**Fig. 2.** a) Cross-plot of porosity and permeability for each Lucia rock class (modified from Lucia, 1995). Both the x- and y-axes are logarithmic. Color indicates the rock class. b) Residuals plot for a regression of log-porosity against log-permeability by rock class. A black line shows zero residual. The color of the points indicates the Lucia rock type. (For interpretation of the references to color in this figure legend, the reader is referred to the Web version of this article.)

**Fig. 3.** a) Histograms for porosity for each lithology in the SSAU dataset. B) Histograms for log-permeability for each lithology in the SSAU dataset. While, for most lithologies, the property distributions are unimodal, the porosity and permeability distributions for lithology 4 are multimodal. Lithologies are listed in Table 1.

population parameter and the expected value from the model. It measures the accuracy (or deviation from truth) of the estimates. The variance is a measure of the uncertainty in these estimates. The best model minimizes both the bias and the variance. Statistical analysis has shown that the OLS linear regression model is often plagued by significant bias (Agterberg, 1974; Seber, 1977; Mann, 1987). For example, there are cases in which the predictor variables are cross-correlated with each other and with the response variable. When this cross-correlation exists, OLS regressions report high accuracy, but do not make accurate predictions of new data.

Alternatives to OLS regression include regularized linear regression approaches such as LASSO regression, Ridge regression, Elastic Net regression (that combines LASSO and Ridge regression), and non-parametric regressors, usually based on decision trees. Al-Mudhafar (2019) has applied LASSO regression to modeling the permeability of sandstone reservoirs. In contrast to the LASSO algorithm, the Elastic Net regression modifies the objective function to minimize a combination of the prediction error and the $L_1$-norm and $L_2$-norms of the coefficients (Zou and Hastie, 2005). Consequently, coefficients are shrunk (as happens in ridge regression) and specific coefficients may be zeroed out (as happens in LASSO regression). Elastic Net regression is generally considered to be the most robust linear regressor (Zou and Hastie, 2005) and is used in this study.

A common non-parametric regression approach is random forests (RF). Random forest regression aggregates an ensemble of decision trees in order to arrive at a result. The decision trees are generated in parallel, and each split is made from random subsets of the dependent variables. Breiman (2001) discovered that decision trees generated through taking random columns from the dependent variables are less prone to over-fitting. This technique allows random forests to be more robust than decision trees. We use random forests built with the Ranger library on the SSAU dataset.

After data exploration, preprocessing, and regressor selection comes regression model building. In selecting the regression to be used, several factors must be taken into account. First, the objective of the regression: to predict permeability from porosity and facies (a different regression would be built to predict porosity from permeability and facies, for instance). Aiding this objective would be measures of which facies are most important for the porosity to permeability transformation. With this information, models can be simplified and designed to rely on the most robust predictors and on fewer assumptions. Simple, robust models are preferred because they are 1) easier to implement and interpret and 2) more likely to perform well on blind tests.

### 2.6. Testing regression models

Testing models includes considering the questions of predictability on the training set and of generalizability to the testing set. Generalizability can be assessed by finding how reliable the process is on new wells that do not have permeability measurements. The methods for testing generalizability include assessing model accuracy for training, cross-validated, and testing (holdout) data (Kearns, 1996).

During cross-validation, the training data is split into several groups. Each group is excluded from the training data as the model is built, then predicted (Kohavi, 1995). The regression is tuned during cross-validation to optimize the regression. In order to achieve the best cross-validation scores, regularization is imposed on the model to minimize over-fitting.

There are three common metrics used for assessing the accuracy of a regression: explained variance ($R^2$), square root of the mean squared error (RMSE), and mean absolute error (MAE). Explained variance can be reported using the Pearson R, which assumes the target variable (log-transformed permeability) is normally distributed with no outliers and constant variance across predicted values. Q-Q plots of the inputs and residuals can be generated to test these assumptions. The equations for MAE, RMSE, and Pearson R are given by:

$$RMSE = \left( \sum_{i}^{n} \left( y_i - y_i' \right)^2 / n \right)^{1/2}$$

$$MAE = \sum_{i}^{n} \left| y_i - y_i' \right| / n$$

$$r = \frac{1}{n-1} \sum_{i}^{n} \left( \frac{y_i - \bar{y}}{\sigma_y} \right) \left( \frac{y_i' - \bar{y}'}{\sigma_{y'}} \right)$$

where $n$ is the sample size $i$ represents the sample number, $y$ is the actual value, $y'$ is the predicted value, a bar over a quantity is the mean of that quantity, and $\sigma$ is the standard deviation of a quantity.

RMSE is the metric most commonly used for measuring the accuracy of regression models. This metric is better than MAE when the objective of the model is to reduce the magnitude of the largest errors. The MAE is less sensitive to outliers than MSE, and thus is preferable when large errors are not a concern. In the case of carbonate permeability prediction, outliers are common and RMSE is a superior metric.

However, MAE is easier to understand than RMSE, because its value is the expected value of the error of the regression. Therefore, for instance, an MAE of 5% on a prediction of 100 mD permeability would suggest that the average absolute error on that measurement is 5 mD. In this work, models are trained to minimize RMSE of log-permeability

**Fig. 4.** Hexbin cross-plot of permeability versus porosity for each lithology in the SSAU dataset. Permeability and porosity axes are both log-transformed. The box at the top of each plot gives the lithology (listed in Table 1). Color indicates the number of points in the hexbin, from 1 (dark blue) to 40 (bright yellow). (For interpretation of the references to color in this figure legend, the reader is referred to the Web version of this article.)

**Table 2**
Measures of model accuracy for the predictions proposed by Lucia (1995) transforming interparticle porosity ($\varphi_{ip}$) to permeability to air ($k$). Values are reported in the natural logarithm of permeability in mD. RMSE = Root-mean squared error, and MAE = mean absolute error. The bias is the approximate amount the given equation will underestimate the permeability.

| Rock Type | Equation (mD) | $R^2$ | RMSE (log-e mD) | MAE (log-e mD) | Approximate Bias (%) |
|---|---|---|---|---|---|
| 1 | $k = (45.35 \times 10^8)\varphi_{ip}^{8.537}$ | 0.55 | 2.00 | 1.64 | 740% |
| 2 | $k = (1.595 \times 10^5)\varphi_{ip}^{5.184}$ | 0.69 | 1.20 | 0.99 | 200% |
| 2[a] | $k = (2.040 \times 10^6)\varphi_{ip}^{6.380}$ | 0.69 | 1.31 | 1.05 | 230% |
| 3 | $k = (2.884 \times 10^3)\varphi_{ip}^{4.275}$ | 0.66 | 1.04 | 0.82 | 170% |

[a] Lucia offers two transforms for rock type 2.

(such that the units of RMSE are log-mD), but both RMSE (in log-mD) and MAE (in log-mD) are reported.

Reporting performance is done on three subsets of data: the cross-validation dataset, the entire training dataset, and testing data that is held out until after the models have been completed. The first step in model building is separating the data into training and testing data. When it is possible, it is best to split the data in a way that reflects the data collection process. For core data, the most natural split is by well; after all, a petrophysical model is often only useful when it can predict the properties of a new well. This is not possible when re-analyzing the Lucia (1995) data, and therefore we perform random K-fold cross-validation on his data.

### 2.7. Interpreting regression models

After regularization, some facies might be found to have little or no effect on the porosity-permeability transform. This can be useful when deciding which facies to focus on during core logging.

Feature importance is also assessed on each input to the regression. This is done through evaluating the RMSE of the model predictions of log-transformed permeability after randomly shuffling the values (see Molnar, 2019, Section 5.5). Random shuffling has the effect of removing the predictive ability of a predictor variable without otherwise affecting the model. For an important feature, random shuffling would increase the RMSE. Conversely, randomly shuffling an unimportant features would have limited to no effect on the RMSE of the model.

## 3. Results

### 3.1. Exploratory analysis of data

First, we created histograms for the porosity and permeability distributions of each facies from the Lucia dataset (Fig. 1). Class 3 has a bimodal porosity distribution, which can be treated by splitting the class at a cutoff of 20% porosity (Fig. 1a). A Shapiro-Wilk test (1965) confirms that porosity of rock type 3 does not follow a normal distribution with a p-value of less than 0.05. The permeability values are not log-normally distributed, nor unimodal for classes 1 and 2, according to both visual inspection (Fig. 1b) and a Shapiro-Wilk normality test.

Next, we recreated Lucia's porosity-permeability cross-plot, with regression lines and uncertainty bands (Fig. 2a), also providing a plot of the residuals for his transformation (Fig. 2b). The residuals plot shows that the errors are heteroscedastic, that is to say, they do not hold a constant variance as porosity and permeability increase. Performing a Box-Cox transformation of permeability before regressing does not remove the heteroscedasticity from the residuals.

For the SSAU dataset we also created histograms of the porosity and permeability distributions for each lithology (Fig. 3). From this analysis, we identified several cores that had been fractured in the core extraction process and screened those sections from further analysis. The average porosity is highest for grainstone and packstone lithologies (3 and 4) and lowest for mudstone and anhydrite lithologies (5). Porosity for lithology 4 (ooid-peloid grainstone) is multi-modal, suggesting that this lithology could be further subdivided.

Cross-plots for permeability and porosity are shown in Fig. 4. Lithologies 2 and 3 are the most abundant, and also have the highest porosity and permeability values. A linear trend between porosity and permeability can be detected, albeit with significant scatter. The multimodal porosity distribution for lithology 4 does not affect the porosity-permeability trend (This might be due to the small number of samples.).

**Table 3**

Accuracy and residual metrics for several porosity-permeability transforms. The models presented are 1) Lucia (1995) regression, 2) a new regression on the data from Lucia (1995), after careful preprocessing and regression regularization, 3) a lithofacies and porosity model trained on SSAU data, 4) a random forest model trained on SSAU lithofacies data and 5) a model only using porosity, trained on SSAU data. Models 2–4 were trained through cross-validation, then model accuracy was calculated on the training data, cross-validation, and testing data.

| Model | Sample source | Data extent | $R^2$ | RMSE (log-mD) | MAE (log-mD) |
|---|---|---|---|---|---|
| 1. Lucia (1995)[a] | Lucia | Full | 0.65 | 1.40 | 1.09 |
| 2. Lucia rock type, Elastic net | Lucia | Training | 0.69 | 1.21 | 0.96 |
| | | CV | 0.69 | 1.22 | 0.98 |
| | | Testing | 0.59 | 1.29 | 1.04 |
| 3.Lithofacies, Elastic net | SSAU | Training | 0.60 | 1.19 | 0.88 |
| | | CV | 0.59 | 1.17 | 0.88 |
| | | Testing | 0.70 | 1.20 | 0.94 |
| 4.Lithofacies, Random forest | SSAU | Training | 0.66 | 1.11 | 0.83 |
| | | CV | 0.59 | 1.17 | 0.88 |
| | | Testing | 0.68 | 1.22 | 0.97 |
| 5.Porosity (no rock type) | SSAU | Training | 0.58 | 1.21 | 0.90 |
| | | CV | 0.59 | 1.17 | 0.88 |
| | | Testing | 0.72 | 1.18 | 0.92 |

[a] See Table 2 for equations. Metrics are aggregated from all three Lucia rock types.

**Fig. 5.** Feature importance plot for Lucia rock typing on the Lucia data set. Points indicate average importance after 40 shuffling repetitions, while bars indicate 95% confidence intervals. A feature with no importance would have a 95% confidence interval that drops below an importance of 1. All features show importance for this regression. The intercept of each class is the permeability where transformed porosity is zero. The porosity times class X is the slope of log-permeability versus transformed porosity for class X.

**Fig. 6.** Comparison of total porosity versus Lucia's calculated interparticle porosity from point counting. Points indicate individual observations, lines the OLS regression between points of the same rock class, and shading the confidence intervals for those regressions. Color and shape vary with Lucia rock class. Both the x- and y-axes are logarithmic. (For interpretation of the references to color in this figure legend, the reader is referred to the Web version of this article.)

### *3.2. Results of the Lucia model*

In his paper, Lucia (1995) provided best fit lines for each of his petrophysical classes. The results of applying Lucia's proposed permeability transforms (Lucia, 1995, his Figure 12) using his dataset are shown in Table 2. Lucia's transformations do not account for bias from performing the fit in logarithmic space (see Jensen et al., 2000, Chapter 10). Bias is calculated using the relation Bias $= e^{RMSE^2/2}$.

We also ran an elastic net regression on the data from Lucia's Figure 12 with three-repeat ten-fold cross-validation, after randomly selecting 20% of the data to hold out for testing. Porosity was transformed on the training data (the other 80% of the data-set) using Box-Cox, then centering, then scaling to unit standard deviation. Interactions were built between porosity and Lucia Rock Type, and elastic net regression was run. The results of this analysis are shown in Table 3.

The most accurate elastic net regression had no regularization, resulting in OLS regression (much like Fig. 2). The model accuracy for this regression on the three data extents (testing, cross-validation and testing) are provided in Table 3. Each class has a statistically significant difference in its porosity-permeability transformation, as evidenced by the feature importance plot (Fig. 5).

It is desirable to develop a relationship between total porosity and permeability, rather than interparticle porosity, because total porosity is easier to measure from log and core data than interparticle porosity. Jerry Lucia has graciously provided us with total porosity and interparticle porosity measurements. The comparison is plotted in Fig. 6. From this figure, it is clear that there is a strong, unit slope correlation between total and interparticle porosity. The $R^2$ exceeds 0.9 for each rock type.

For all classes, $\varphi_{ip} > \varphi_{total}$. The regression line for class 1 is $\ln\varphi_{ip} = 1.13 \ln \varphi — 0.63$, for class 2, it is $\ln\varphi_{ip} = 1.07 \ln \varphi — 0.28$, and for class 3, it is $\ln\varphi_{ip} = 1.06 \ln \varphi — 0.31$, where porosity is measured in p.u. Thus, in these samples, total porosity overestimates interparticle porosity by less than 15%. We therefore expect total porosity to perform about as well as interparticle porosity in developing permeability predictors for non-vuggy carbonates.

Frequently, Lucia rock types are not determined from measuring the particle size. Instead, core is visually inspected and assigned Dunham rock fabric categories. In theory, grainstone should correspond to Lucia rock type 1, packstone to rock type 2, etc. Therefore, lithofacies interpretation is often an input for determining permeability from porosity data. With the SSAU data, we have the opportunity to compare porosity-permeability transforms arising from lithofacies.

**Fig. 7.** Residuals plot for Elastic-net regressions using the SSAU data. The boxes at the top of each facet provide the lithology, while the y-axis gives the residual (in log-transformed permeability) and the x-axis gives the porosity. An orange line indicates zero residual. Colors for each hexagonal bin give the number of points within, with 1 dark blue, and 18 bright yellow. (For interpretation of the references to color in this figure legend, the reader is referred to the Web version of this article.)

### 3.3. Results of lithofacies model

Creating a testing-training split for the SSAU data was accomplished by holding out the data from the well SSAU #5505R, representing 8.2% of the data, for testing. During preprocessing, porosity was transformed using the same method as above, and interactions were built between porosity and lithofacies. The Box-Cox transformation exponent used to maximize normality of the distribution was 0.640.

Elastic net regression returns an $R^2 =$ 0.60, RMSE = 1.21, and MAE = 0.90 on cross validation. Residuals for the training dataset are shown in Fig. 7. The residuals are slightly heteroscedastic, which disappears if the permeability is transformed using Box-Cox before fitting (unlike in Lucia's dataset).

The best fit elastic net model has a mixing fraction of 0.66 and a regularization parameter of 0.002. The regressor assigns weights to the porosity and the slopes for each lithology. A plot of predicted and observed permeability against depth is given in Fig. 8. Shuffling features indicates that the statistically significant variables are transformed porosity and lithologies 2 and 3 (Fig. 9). Model statistics are reported in Table 3.

Random forest regression yielded the best cross-validated results with 500 trees, 3 randomly selected predictors, a variance split rule, and a minimum node size of 40 points. The features with larger-than-zero importance were porosity, presence of lithology 5, presence of lithology 3, and presence of lithology 2. Shuffling features indicated that both porosity and lithology were important. A plot of residuals is given in Fig. 10, and the permutation importances in Fig. 11. The model statistics are available in Table 3. The random forest slightly underperforms the linear model on cross validation and the testing data.

A reduced model that does not use lithofacies, but instead only uses porosity to predict permeability, has an $R^2 =$ 0.59, RMSE = 1.18, and MAE = 0.90 on the training data (Table 3, last row). This MAE corresponds to $e^{0.90} \approx 2.5$ times the predicted value. For example, if the porosity-only model has $\varphi = 0.067$, it predicts k = 1 mD, and the MAE range is from 0.4 to 2.5 mD. For comparison, the model including lithofacies, with a porosity of 0.067 and lithofacies 3, would predict a permeability of 1.09 mD, with an MAE range of 1.5–2.7 mD.

With the porosity-only model, the regression equation is

$$\log_e k = 13.9\,\frac{\varphi^{0.640} - 1}{0.640} + 17.9$$

where porosity is reported as a volume fraction and permeability is reported in milliDarcy. The accuracy of this regression is shown in Table 2.

Table 3 shows model performance for the Lucia rock type-based model, full core/full lithofacies model, and baseline porosity-permeability model. Each measure is calculated to compare the natural log transformed permeability to its predicted value. The data extents include Full (all data from that sample source), Training (all of the data used in training the final model) CV (cross-validation data, where each fold of the training data is held out of the fitting, then tested), and Testing (data that is never used for building the model, but is blind tested afterwards). The accuracy on each rock type and lithofacies are aggregated to provide the mean accuracy for the data extent.

Using $R^2$ values, the elastic net regression performs better on the SSAU testing data than on the SSAU training data. This is because the accuracy of the model on individual wells varies from an MAE of 0.7–1.3 log-mD, and through chance, one of the better-behaved wells comprised the training data.

## 4. Discussion

### 4.1. Data preprocessing and residuals analysis

This study has set out to inform approaches to ML analyzes and related next generation statistical analyses to ensure that they are interpretable (in the sense of Molnar, 2019). In the first step, the raw data sets were analyzed to establish that they were appropriate for the application of ML algorithms. In his paper on facies classification using machine learning, Hall (2016) noted that "many machine-learning algorithms assume the feature data are normally distributed" (i.e., Gaussian with zero mean and unit variance). Hall suggested that data should be conditioned such that they meet this criterion using includes a Standard Scalar class. This methodology is inadequate for the task. As written in the Sci-kit Learn (2019) manual, the preprocessor used by Hall "ignores the shape of the distribution" and transforms the data "to center it by removing the mean value of each feature", and scaling it "by dividing non-constant features by their standard deviation." This

**Fig. 8.** Plot of permeability versus depth for the testing well in the SSAU data. Measured permeability is the black line, while predicted permeability from the model including porosity and lithology (orange) and using only porosity (blue) are shown as points. The point shape is used to show the interpreted lithology. (For interpretation of the references to color in this figure legend, the reader is referred to the Web version of this article.)

**Fig. 9.** Importance plot for elastic-net regression of permeability for the SSAU data. Dots show the average effect on the RMS error after shuffling each feature. Porosity and lithologies 2 and 3 have a persistent effect on the RMSE after shuffling.

approach does not assure Gaussian distributions for the transformed feature; for instance, it does not remove skew. A superior approach (as noted above), is to first apply a test for normalcy such as the Shapiro-Wilk, followed if needed by a Box-Cox transform. Jensen and Lake (1985) showed that using a Box-Cox transform to provide symmetry is sufficient to improve predictor performance in geostatistical workflows.

In the case of the Lucia (1995) data, a Shapiro-Wilk test confirmed that permeability for rock type 3 is not log-normally distributed, and visual inspection of the distributions show it is not unimodal for classes 1 and 2. Further data analysis revealed that the data Lucia used to build his model is polymodal, and that regressions of such data are heteroscedastic. Heteroscedasticity is characterized by a systematic variation in the spread of the residuals from a regression analysis. Frequently it results from the effects of outliers in the data set or the population being multimodal. Note that ordinary least squares (OLS) regression is based on an assumption that residuals are drawn from a population with constant variance. Heteroscedasticity can result in p-values that are unrealistically small. Bartlett's test for homogeneity of variances (Parra-Frutos, 2013) is one of several tests that can be used to identify heteroscedasticity in data sets.

Utilizing the results of regressions with strongly heteroscedastic residuals will be prone to performing poorly on test data. This can be seen by the large decrease in $R^2$ for the test data using Lucia's rock types. Heteroscedastic residuals that decrease as the prediction increases are indicative of non-Gaussian variables. The heteroscedasticity of Lucia's data cannot be eliminated, even after careful transformation, due to the multi-modal nature of the permeability distribution. If these kinds of tests and data conditioning are not accomplished prior to running ML algorithms, the resultant solutions may not be robust or accurate.

We find that the residuals from the random forest model are heteroscedastic. Not surprisingly, a study by Gelfand (2015) found that heteroscedastic data may have an adverse impact on ML algorithms such as Random Forests (RF) and Gradient Boosting Regressors (GBR). However, Gelfand does note that GBR "may perform better than random forests". Similarly, Henry (2016) concluded that RF algorithms "are inefficient at estimating means when the data are heteroscedastic". He suggested that the effectiveness of RF could be improved by utilizing a "likelihood-based regression trees as a base learner". In general, testing for heteroscedasticity should be a standard procedure in application of ML models to geoscience data sets, particularly if the RF algorithm is to be deployed.

In ML based projects to analyze data sets from reservoirs including rock typing, porosity, permeability and perhaps wireline log data, Elastic Net regression will likely be preferred (in preference to ridge and LASSO regression). If the data is characterized by highly correlated explanatory variables this will be the case. O'Brien (2007) discusses the uses (and abuses) of the Variance Inflation Factor as a measure of the extent of "multi-collinearity of the *i*th independent variable with the other independent variables in regression models."

The elastic net regression run on Lucia's data performed best without regularization. This is because regularization is less likely to be applicable when the number of variables being tested is small. Sufficiently simple models with smaller numbers of variables are already interpretable and explainable in the sense of Molnar (2019), and might not require regularization. Similarly, the data sets that we have analyzed are not sufficiently complex to evaluate the advantages of the Elastic Net regression over less robust alternatives such as the LASSO algorithm. LASSO was used by Al-Mudhafar (2019) to model permeabilities in sandstone reservoirs. He asserted that this approach had resulted in "significant progress in the application of statistical learning models to petrophysical modeling" and had improved reservoir characterization. It would seem that further exploration of Elastic Net Regression as a tool for ML approaches to reservoir characterization could be fruitful.

**Fig. 10.** Plot of residuals for the random forest model trained on lithofacies and porosity for the SSAU data. Each pane represents the lithofacies numbered at the top. An orange line indicates zero residual (a perfect fit). Hexbins are colored from blue (one data point) to yellow (18 data points) based on how many samples had a residual and porosity corresponding to that location. There are only slight differences in the residuals between this model and the residuals of the linear model. (For interpretation of the references to color in this figure legend, the reader is referred to the Web version of this article.)

**Fig. 11.** Feature importances for the random forest model. The dot provides the average importance on the residuals, with the bar representing 95% confidence intervals. Porosity strongly influences the residuals of the model, but lithology is weakly important.

### *4.2. Factors influencing permeability*

Another set of important issues arise when it comes to taking the output from ML algorithms and applying them to making predictions of parameters such as permeability. If permeability is predicted from porosity alone, and then compared to permeability predicted from porosity and lithofacies information, for the SSAU data we find that there is very little improvement of the prediction. The elastic net regression utilizing lithology shows a significant contribution from lithofacies 2 and 3 to the permeability. However, this contribution improves the error metrics in the regression by less than 1% (Table 3, bottom two regressions). The contrasting results (whether lithofacies do or do not improve permeability predictions) show the value of building simple models for benchmarking.

In the SSAU data, we have identified a contribution from lithofacies 2 and 3, but this effect is either too small to impact the regression, or it is not present in the testing data. This indicates that even after regularization, un-useful parameters remain in the elastic net regression of the SSAU data. Therefore, application of the elastic net algorithm has overfit on the training data. These kind of phenomena are likely to occur in more complex ML models, but may go unnoticed unless carefully searched for.

The limited effectiveness of lithofacies information in determining the porosity-permeability transform does not necessarily hold for other types of reservoir. In clastic (Al-Mudhafar (2017)) and mixed clastic-carbonate (Wood, 2019) reservoirs, a much stronger influence of lithofacies on permeability is observed. Also, carbonate reservoirs that have undergone less pervasive dolomitization might have a stronger correlation between lithology and permeability.

On the topic of interparticle porosity versus total porosity, we performed a regression between the two (Fig. 6). These measures of porosity are nearly identical, except in cases where there are significant vugs creating porosity. Vuggy porosity can be disconnected from the flow paths, and therefore should be removed from the porosity when large, disconnected vugs are identified. This result is in keeping with Lucia (1995) conclusions. However, when significant vuggy porosity is not present, total porosity is an accurate measure of the interparticle porosity. The analysis of SSAU data shows that similar model accuracy to the interparticle porosity can be achieved using total porosity.

Finally, we note that despite repeated warnings about de-transforming log-transformed predictions (*e.g.* Jensen and Lake, 1985; Delfiner, 2007), analysts continue to ignore the bias these transforms introduce into the predictions. Given the weak porosity-permeability relationships typical of carbonate rocks, the relationships can under-predict by a factor of 3 or more when bias is ignored. Using the Box-Cox transformation with $\lambda$/=0 helps, because the bias correction term is additive rather than multiplicative to the prediction (Jensen et al., 1987).

### *4.3. Guidelines for future research*

There is a dearth of published data in dolomitized carbonates where the accuracy of porosity-permeability transforms has been systematically measured. For instance, Haro (2004) suggests several permeability models, but does not provide $R^2$, MAE, or RMSE errors for those models. Al-Ajmi and Holditch (2000) offer $R^2$, but neither MAE nor RMSE. (They also build rock groups from the porosity-permeability transforms, rather than the other way around.) Lønøy (2006) and Lucia (1995) provide $R^2$, but neither MAE nor RMSE. None of these papers perform cross-validation, and they do not perform blind well tests of their final models.

In future reservoir studies where core is available, a critical evaluation of lithofacies should be performed with robust statistical checks. This is necessary to verify that differences between porosity-permeability transforms of different lithofacies are significant. When possible, cross-validation should be performed between wells, in an approach similar to the industry-standard blind well test. To compare results with literature, it is valuable to report the $R^2$, mean absolute error, and root-mean squared error.

To build generalizable machine learning models for geoscientific datasets, the statistical character of the data should be carefully examined as part of the exploratory analysis. A testing data set that does not bleed into the model-building data should be selected. The machine learning model needs to have regularization parameters to prevent overfitting, and these parameters need to be tuned with cross-validation. Finally, after model building, the residuals of the model predictions need to be analyzed for the squared error, absolute error, and heteroscedasticity. These are all necessary parts of the geoscience machine learning workflow.

There are other approaches for permeability prediction that have not been analyzed in this study. These include neural networks and gradient boosting regressors, as applied to a clastic reservoir (Al-Mudhafar, 2017), and a nonparametric model applied to a mixed carbonate-clastic reservoir (Wood, 2019). These methods could be applied to carbonate reservoirs such as the Seminole in future studies.

## 5. Conclusions

This study has developed a set of strategies that will support ML studies of reservoir facies and associated petrophysical properties (particularly permeability) being more transparent and/or more robust. The first step involves characterizing the data set to understand key aspects of its statistical distribution. In this study, we generated histogram plots to examine the univariate statistics of porosity and permeability in these rocks. As many ML algorithms require data have approximately normal distributions, tactics such as applying the Box-Cox transform should be utilized.

Following transformation of the data sets, we performed a regularized linear regression on the porosity-permeability. We validated the regression results through cross-validation and test-training splits. Finally, we discussed the fraction of explained variance and expected error for these porosity-permeability transforms.

Polymodal, heteroscedastic, data sets are common in petrophysical studies such as Lucia (1995). In this data set heteroscedasticity was identified from the observed variation in the spread of the residuals from the regression.

In view of the broad interest in the use of porosity-permeability transforms for characterizing carbonate reservoirs, an analysis of Lucia (1995) model (utilizing newly available statistical tools), seems timely. In this paper, we took Lucia's data and another dataset from the Seminole San Andres Unit and performed a robust statistical analysis of his findings. Lucia's results rely upon poorly conditioned data, impacting the generalizability of his work to new datasets. Permeability does not follow a unimodal, log-normal distribution, leading to heteroscedasticity in permeability prediction. Lithofacies interpretations do not lead to permeability predictions that outperform simple porosity-only relations. It was also found that statistically significant effects do not necessarily lead to better performance on holdout data.

This study has used a variety of state of the art Machine Learning tools to analyze the generation of porosity-permeability transforms from core data. Our conclusion has been that the complexity of the data is such that knowledge of the rock type or facies does not result in a significantly improved prediction of permeability, given a porosity measurement. The overarching conclusion of this study is that using Machine Language packages to investigate complex petrophysical and geologic data is likely to be fraught with significant problems if the approach lacks interpretability. If the nature of the data being processed (such as normality and heteroscedasticity) is not understood and accounted for, then model predictions may be erroneous.

## Author contributions

F.M. designed the study. I.J.D. supervised the research and was in charge of overall direction and planning. F.M. performed the data analysis. I.J.D. aided in interpreting the results. F.M. and I.J.D. wrote the manuscript.

## Declaration of interest statement

The authors declare that there is no conflict of interest.

## Acknowledgements

We are grateful to F. Jerry Lucia for providing the raw data, thin sections and image analyses that he used in his 1995 paper. Vinyet Baqués generously provided porosity, permeability, and facies data from the SSAU reservoir as well as providing useful discussion. Statistical analysis was performed in the R language (R Core Team, 2014). Plots were generated using the GGPlot2 package (Wickham, 2009). This study was funded by the US Department of Energy (DOE) grant FE0024375 (PI: Duncan). The authors are in debt to Drs. Jerry Jensen, Larry Lake, Carlos Torres-Verdín, and Bo Ren for valuable conversations and feedback.

## Appendix A. Supplementary data

Supplementary data to this article can be found online at https://doi.org/10.1016/j.petrol.2019.106825.

## References

Agterberg, F.P., 1974. Geomathematics. Elsevier, Amsterdam.
Ahmadi, M.A., Chen, Z., 2018. Comparison of Machine Learning Methods for Estimating Permeability and Porosity of Oil Reservoirs via Petro-Physical Logs. Petroleum.
Al-Ajmi, F.A., Holditch, S.A., 2000. Permeability estimation using hydraulic flow units in a central Arabia reservoir. In: SPE Annual Technical Conference and Exhibition. Society of Petroleum Engineers.
Al-Mudhafar, W.J., 2015. Integrating component analysis & classification techniques for comparative prediction of continuous & discrete lithofacies distributions. In: Offshore Technology Conference. Offshore Technology Conference.
Al-Mudhafar, W.J., 2017. Integrating well log interpretations for lithofacies classification and permeability modeling through advanced machine learning algorithms. J. Petrol. Explor. Product. Technol. 7 (4), 1023–1033.
Al-Mudhafar, W.J., 2019. Bayesian and LASSO regressions for comparative permeability modeling of sandstone reservoirs. Nat. Resour. Res. 28 (1), 47–62.
Archie, G.E., 1952. Classification of carbonate reservoir rocks and petrophysical considerations. AAPG (Am. Assoc. Pet. Geol.) Bull. 36 (2), 278–298.
Box, G.E., Cox, D.R., 1964. An analysis of transformations. J. R. Stat. Soc. Ser. B 26 (2), 211–243.
Breiman, L., 2001. Random forests. Mach. Learn. 45 (1), 5–32.
Caté, A., Perozzi, L., Gloaguen, E., Blouin, M., 2017. Machine learning as a tool for geologists. Lead. Edge 36 (3), 215–219.
Cranganu, C., Luchian, H., Breaban, M.E. (Eds.), 2015. Artificial Intelligent Approaches in Petroleum Geosciences. Springer, Berlin.
Delfiner, P., 2007. Three statistical pitfalls of phi-k transforms. SPE Reserv. Eval. Eng. 10 (6), 609–617.
Dunham, R.J., 1962. Classification of Carbonate Rocks According to Depositional Textures, A038. AAPG Memoir, pp. 108–121.
El-Sebakhy, E.A., Asparouhov, O., Abdulraheem, A.A., Al-Majed, A.A., Wu, D., Latinski, K., Raharja, I., 2012. Functional networks as a new data mining predictive paradigm to predict permeability in a carbonate reservoir. Expert Syst. Appl. 39 (12), 10359–10375.
Elkatatny, S., Mahmoud, M., Tariq, Z., Abdulraheem, A., 2018. New insights into the prediction of heterogeneous carbonate reservoir permeability from well logs using artificial intelligence network. Neural Comput. Appl. 30 (9), 2673–2683.
Gelfand, S., 2015. Understanding the Impact of Heteroscedasticity on the Predictive Ability of Modern Regression Methods. MSc Thesis. *Simon Fraser University*.
Gilpin, L.H., Bau, D., Yuan, B.Z., Bajwa, A., Specter, M., Kagal, L., 2018. October. Explaining explanations: an overview of interpretability of machine learning. In: 2018 IEEE 5th International Conference on Data Science and Advanced Analytics (DSAA). IEEE, pp. 80–89.
Grötsch, J., Mercadier, C., 1999. Integrated 3-D reservoir modeling based on 3-D seismic: the Tertiary Malampaya and Camago buildups, offshore Palawan, Philippines. AAPG Bull. 83 (11), 1703–1728.
Hall, B., 2016. Facies classification using machine learning. Lead. Edge 35 (10), 906–909.
Haro, C.F., 2004. The perfect permeability transform using logs and cores. In: SPE Annual Technical Conference and Exhibition. Society of Petroleum Engineers.
Henry, A.J.D., 2016. Statistical Learning Tools for Heteroskedastic Data. Simon Fraser University. PhD dissertation.
Honarpour, M.M., Nagarajan, N.R., Grijalba Cuenca, A., Valle, M., Adesoye, K., 2010. Rock-fluid characterization for miscible CO2 injection: residual oil zone, Seminole

field, Permian Basin. In: SPE Annual Technical Conference and Exhibition. Society of Petroleum Engineers.

James, G., Witten, D., Hastie, T., Tibshirani, R., 2013. An Introduction to Statistical Learning, vol. 112. Springer, New York, p. 18.

Jensen, J.L., Lake, L.W., 1985. Optimization of regression-based porosity-permeability predictions. In: Transactions of the 10th Formation Evaluation Symposium. Calgary.

Jensen, J.L., Lake, L.W., Hinkley, D.V., 1987. A Statistical Study of Reservoir Permeability: Distributions, Correlations, and Averages, vol. 2. SPE Formation Evaluation, pp. 461–468.

Jensen, J., Lake, L.W., Corbett, P.W., Goggin, D., 2000. Statistics for Petroleum Engineers and Geoscientists, vol. 2. Gulf Professional Publishing.

Kearns, M.J., 1996. A bound on the error of cross validation using the approximation and estimation rates, with consequences for the training-test split. In: Advances in Neural Information Processing Systems, pp. 183–189.

Kerans, C., Lucia, F.J., Senger, R.K., 1994. Integrated characterization of carbonate ramp reservoirs using Permian San Andres Formation outcrop analogs. AAPG (Am. Assoc. Pet. Geol.) Bull. 78 (2), 181–216.

Kohavi, R., 1995. August. A study of cross-validation and bootstrap for accuracy estimation and model selection. In: Ijcai, Vol. 14, pp. 1137–1145, 2.

Lary, D.J., Alavi, A.H., Gandomi, A.H., Walker, A.L., 2016. Machine learning in geosciences and remote sensing. Geosci. Front. 7 (1), 3–10.

Lønøy, A., 2006. Making sense of carbonate pore systems. AAPG Bull. 90 (9), 1381–1405.

Lucia, F.J., 1995. Rock-fabric/petrophysical classification of carbonate pore space for reservoir characterization. AAPG (Am. Assoc. Pet. Geol.) Bull. 79 (9), 1275–1300.

Lucia, F.J., 2007. Carbonate Reservoir Characterization: an Integrated Approach. Springer Science & Business Media.

Mann, C.J., 1987. Misuses of linear regression in earth sciences. In: B Size, W. (Ed.), Use and Abuse of Statistical Methods in the Earth Sciences. OUP, Oxford, pp. 74–106.

Mishra, S., Datta-Gupta, A., 2017. Applied Statistical Modeling and Data Analytics: A Practical Guide for the Petroleum Geosciences. Elsevier.

Molnar, C., 2019. Interpretable Machine Learning: a Guide for Making Black Box Models Explainable, ISBN 9780244768522.

Murdoch, W.J., Singh, C., Kumbier, K., Abbasi-Asl, R., Yu, B., 2019. Interpretable Machine Learning: Definitions, Methods, and Applications arXiv preprint arXiv: 1901.04592.

O'Brien, R.M., 2007. A caution regarding rules of thumb for variance inflation factors. Qual. Quantity 41 (5), 673–690.

Parra-Frutos, I., 2013. Testing homogeneity of variances with unequal sample sizes. Comput. Stat. 28 (3), 1269–1297.

R Core Team, 2017. R: A Language and Environment for Statistical Computing. R Foundation for Statistical Computing, Vienna, Austria. URL. http://www.R-project.org/.

Ren, B., Duncan, I., 2019. Modeling oil saturation evolution in residual oil zones: implications for CO2 EOR and sequestration. J. Pet. Sci. Eng. 177, 528–539.

Rudin, C., 2019. Stop explaining black box machine learning models for high stakes decisions and use interpretable models instead. Nat. Mach. Intell. 1 (5), 206.

Sci-kit Learn, 2019. Standardization, or Mean Removal and Variance Scaling. In: https://scikit-learn.org/stable/modules/preprocessing.html#preprocessing-scaler. (Accessed 29 September 2019).

Seber, G.A.F., 1977. Linear Regression Analysis. J. Wiley, New York.

Shapiro, S.S., Wilk, M.B., 1965. An analysis of variance test for normality (complete samples). Biometrika 52 (3/4), 591–611.

Sonnenfeld, M.D., Canter, L., Meng, H.Z., Wingate, T.P., Zahm, L.C., 2003. Operational sequence stratigraphy for 3-D reservoir modeling of Seminole Andres unit (SSAU), Permian Basin, west Texas. In: Annual AAPG-SEPM Meeting, vol. 5, pp. 11–14. Salt Lake City, UT.

Sudakov, O., Burnaev, E., Koroteev, D., 2019. Driving digital rock towards machine learning: predicting permeability with gradient boosting and deep neural networks. Comput. Geosci. 127, 91–98.

Wang, F.P., Lucia, F.J., Kerans, C., 1998. Integrated reservoir characterization study of a carbonate ramp reservoir: Seminole san Andres unit, Gaines County, Texas. SPE Reserv. Eval. Eng. 1 (2), 105–113.

Wickham, H., 2009. ggplot2: Elegant Graphics for Data Analysis. Springer, New York.

Wood, D.A., 2019. Predicting porosity, permeability and water saturation applying an optimized nearest-neighbour, machine-learning and data-mining network of well-log data. J. Pet. Sci. Eng. 106587.

Zou, H., Hastie, T., 2005. Regularization and variable selection via the elastic net. J. R. Stat. Soc. Ser. B 67 (2), 301–320.

# 7 Diagenesis of the San Andres Formation in the Seminole unit in Central Basin platform, western Texas

Lei Jiang

## ABSTRACT

The San Andres Formation, characterized by massive sulfate cementation (with~10%–30% of rock volume), is one of the most productive units in the Permian Basin. However, little attention has been paid to anhydrites, which affected the San Andres reservoir quality. Coupling petrography with geochemical analysis, this study aims at providing a holistic diagenetic framework in the Seminole San Andres Formation. Advanced evaporation of seawater has resulted in abundant bedded and nodular anhydrite precipitation along with reflux dolomitization. An early stage of bacterial sulfate reduction may have occurred and resulted in pyrite replaced anhydrite nodules. A small downward decreasing of d$^{13}$C in carbonates may be caused by either the secular carbon isotopic change of seawater or the consequence of bacterial sulfate reduction. Fluid inclusion data obtained from anhydrite cements suggest that (1) anhydrite cementation continued to the maximum burial temperature of ~75 ° C and (2) a regional hydrothermal fluid activity with temperatures between 100 ° C and 128 ° C has occurred. Neogene meteoric water from the western uplifted mountain region may have promoted a late-stage bacterial sulfate reduction that caused anhydrite and dolomite dissolution and increased present-day reservoir quality in the residual oil zones. This study emphasizes the dynamics of anhydrite subjected to diagenesis

[redacted]

Manuscript received February 9, 2018; provisional acceptance April 11, 2018; revised manuscript received May 6, 2018; revised manuscript provisional acceptance July 31, 2018; 2nd revised manuscript received September 7, 2018; 2nd revised manuscript provisional acceptance November 12, 2018; 3rd revised manuscript received December 30, 2018; 3rd revised manuscript provisional acceptance April 3, 2019; 4th revised manuscript received May 19, 2019; 4th revised manuscript provisional acceptance August 15, 2019; 5th revised manuscript received September 11, 2019; 5th revised manuscript provisional acceptance January 23, 2020; 6th revised manuscript received February 22, 2020; 6th revised manuscript provisional acceptance March 3, 2020; 7th revised manuscript received March 29, 2020; 7th revised manuscript provisional acceptance July 22, 2020; 8th revised manuscript received August 7, 2020; 8th revised manuscript provisional acceptance January 7, 2021; 9th revised manuscript received January 15, 2021; final acceptance January 24, 2021.
DOI:10.1306/08092118042

[redacted]

that could result in an improved reservoir quality with greater heterogeneity in a mixed carbonate and evaporite system.

## INTRODUCTION

The Permian Basin of western Texas and southeastern New Mexico has produced oil for more than 90 yr and represents the largest oil resource in the United States (Gaswirth et al., 2016). Carbonate reservoirs account for 75% of the total oil production in the Permian Basin, among which the middle Permian San Andres Formation has been the most productive one. The cumulative production of carbonate plays from the San Andres Formation is approximately 10 billion BOE as of 2000 (Dutton et al., 2005), and it is one of the leaders in the Permian Basin for $CO_2$ production above original oil-water contact. Moreover, the San Andres Formation is also one of the biggest producers of oil through $CO_2$-based enhanced oil recovery ($CO_2$-EOR). More than 13,000 BOPD are being produced from residual oil zones (ROZs), with 6500 bbl/day being produced from the ROZs in the Seminole unit alone (Melzer, 2012). The estimated recoverable oil from ROZs in the San Andres Formation and Canyon Reef formation in Permian Basin is 12 billion bbl (Koperna et al., 2006).

The majority of the studies on San Andres carbonate reservoirs were conducted during the 1980s to 1990s. These studies predominantly focused on the reservoir's stratigraphy, depositional models, and reservoir properties (Cowan and Harris, 1986; Sarg and Lehmann, 1986; Kerans and Fitchen, 1995; Lucia et al., 1995). Some workers have modeled reservoir heterogeneity based on outcrop analogues and subsurface rock physical data (Eisenberg et al., 1994; Wang et al., 1998; Dou et al., 2011). Diagenesis studies of the San Andres carbonates in the Permian Basin have been limited in scope and mostly focused on dolomites (Ruppel and Cander, 1988; Saller and Henderson, 1998). Altered rock properties and occasional free sulfur in ROZs formed by anaerobic bacteria in the San Andres Formation has been reported (Melzer, 2012). Recently, Trentham et al. (2015) emphasized the critical role of bacterial sulfate reduction (BSR) in the biodegradation of hydrocarbons as well as the formation of "black sulfur water," $H_2S$, elemental sulfur, and calcite in ROZs. However, the nature of the diagenetic sequence and its impact on reservoir quality have not been documented in detail, neither for the main pay zone nor for the ROZ of the San Andres carbonate reservoirs. This lack of detail hampers understanding mineral precipitation patterns during water injection and $CO_2$ floods, which can cause significant problems for water and oil flow during $CO_2$-EOR (Saller and Stueber, 2018). Further, a better understanding of diagenesis of anhydrite in the San Andres Formation can help constrain the diagenetic effect on reservoir quality. The outcomes from this study can apply to reservoir characterization and $CO_2$-EOR of the ROZs in several other mixed carbonates and evaporite systems in the Permian Basin (Ruppel and Cander, 1988; Lucia and Ruppel, 1996; Saller and Henderson, 1998), as well as many global analogies (e.g., Smackover Formation in the Gulf of Mexico Basin [Heydari, 2000], Feixianguan Formation in the Sichuan Basin [Jiang et al., 2018c], and Khuff Formation in the Arabian Basin [Worden et al., 1995]).

This paper predominantly focuses on the diagenesis of anhydrite and its impacts on reservoir quality in the subsurface San Andres Formation in the Seminole field of the northern Central Basin platform. To characterize the nature and origin of diagenetic anhydrite and carbonate minerals in the Seminole San Andres carbonate reservoir, conventional description techniques of core and thin sections, cathodoluminescence (CL) analysis, scanning electron microscope (SEM) petrography, pore and mineral surface area measurement, fluid-inclusion analysis, and carbon and oxygen isotopic data were used. Combining image-based quantitative data for porosity and different diagenetic products, this paper attempts to address the following questions:

1. What are the characteristics of various types of diagenetic minerals (e.g., dolomite, calcite, and especially anhydrite) within the Seminole San Andres reservoirs?
2. What is the burial-diagenesis model of the Seminole San Andres Formation and how does diagenesis affect reservoir quality?

## GEOLOGICAL SETTING

The Seminole San Andres unit (SSAU) is located on the northeast margin of the Central Basin platform immediately south of the San Simon channel (Figure 1A). The reservoir's surface footprint extends over 60 km$^2$ with approximately 850 wells. A carbonate ramp depositional system (Figure 1B) with the identification of high-frequency stratigraphic cycles provides a detailed framework for reservoir characterization for the San Andres Formation (Eisenberg et al., 1994; Grant et al., 1994; Kerans and Fitchen, 1995; Lucia et al., 1995; Wang et al., 1998; Phelps et al., 2008). The oil field in the SSAU (discovered in 1936) is a solution-gas drive reservoir with a small initial gas cap. The Seminole field is one of several isolated platforms built during early Guadalupian when the lower San Andres composite sequence became linked with the rest of the San Andres platform during the progradation of the upper San Andres sequence (Figure 2) (Lucia et al., 1995).

The lower San Andres is characterized by skeletal (e.g., fusulinid) grainstone, packstone, wackestone, and an open-marine fauna, which was deposited in upward-shallowing, peloidal, shallow subtidal to peritidal cycles (Kerans et al., 1994; Lucia et al., 1995). In contrast, the upper San Andres at the SSAU is largely composed of anhydritic peritidal deposits (Figure 2) (Lucia et al., 1995). Dolomites and anhydrite are major diagenetic minerals in the San Andres Formation, along with other trace amounts of minerals such as quartz, kaolinite, and fluorite (Leary and Vogt, 1987). Generally, the reservoir quality is closely tied to lithotypes and facies, for example, grainstone from ramp crest and grain-dominated packstone and wackestone from the middle to outer ramp have much higher porosity and permeability than mud-dominated fine crystalline dolostones from ramp interior and upper distal outer ramp (Kerans et al., 1994; Lucia et al., 1995; Wang et al., 1998).

## METHODS

New samples for this study were collected from wells SSAU 2309 (*n* = 29), SSAU 2310 (*n* = 56), and SSAU 2504 (*n* = 28) (Figure 1A) in the SSAU. Selected samples were prepared for thin sections (30 μm thick) for optical microscopic studies. Selected polished thin sections were impregnated with blue dye to highlight megapores (greater than 10 μm) and with blue-fluorescent dye to highlight micropores (less than 10 μm) and for SEM-CL and fluid inclusion studies. Additionally, several hundreds of thin sections from wells SSAU 2505 (*n* = 364) and SSAU 5309 (*n* = 209) were kindly provided by Jerry Lucia at the Bureau of Economic Geology of The University of Texas at Austin for the petrological study.

[redacted]

Figure 1. (A) Map of key Permian Basin features and some key fields for enhanced oil recovery and residual oil zones discussions, modified from (Honarpour et al., 2010). Inset shows location of studied wells in the Seminole San Andres unit in Central Basin platform. (B) A generalized depositional model and facies-tract distributions of distally steepened ramp clinothems during the middle Permian for Permian Basin, modified from Phelps and Kerans (2007). GDP 5 grain-dominated packstone; HFC 5 high-frequency cycle.

### Petrography

Selected thin sections, mainly from SSAU 2310 (*n* = 24), were examined by transmitted-light microscopy and SEM-CL along with elemental analysis by energy-dispersive x-ray spectroscopy. The CL images were obtained using a Zeiss Sigma High Vacuum Field Emission SEM equipped with an Oxford X-Max 50-mm$^2$ silicon drift detector for low-energy detectability, a pole piece-mounted backscattered electron detector, and a Gatan MonoCL4 system operated at 5 kV and large sample currents. The CL images were obtained from grayscale images collected using blue filters.

### Quantitative Assessment of Mineralogy and Porosity

Minerals and pore spaces were identified under a petrographic microscope by using plane cross-polarized light. High-resolution thin-section photomicrographs were taken at various scales for quantitative

Figure 2. Lithology, cycles, anhydrite content, and porosity correlation of the San Andres Formation from well SSAU 2505 in the Seminole San Andres unit, modified from Lucia et al. (1995). The facies classification follows Kerans et al. (1994).

image analysis using the JMicrovision v1.27 software. Thereafter, image analysis is performed by using the pixel color and intensity from the photomicrograph to differentiate between various minerals and pores. Submicron to millimeter scale pores and minerals could be extracted along with their geometry parameters. The color deconvolution algorithm was used in image analysis to better differentiate the pores from rock components (minerals). We performed quantitative assessment only on the thin sections from well SSAU 2505 because detailed rock fabric facies, porosity, and permeability data are available in Lucia et al. (1995).

## Fluid Inclusion Microthermometry

Homogenization temperatures ($T_h$) were measured from fluid inclusion assemblages (FIAs) containing two-phase aqueous inclusions in five out of nine doubly polished (50 to 60-μm-thick) wafers from well SSAU 2310. The use of FIAs to determine temperatures of mineral growth, as opposed to lone inclusions, gives confidence that the $T_h$ data are credible and minimizes the effects of artifacts, such as thermal reequilibration (Goldstein and Reynolds, 1994; Goldstein, 2012). Fluid inclusion microthermometry was conducted using a Fluid, Inc. (adapted, US Geological Survey) type, gas-flow heating-freezing stage mounted on an Olympus BX51 microscope equipped with 40× objective (numerical aperture = 0.55) and 15× ocular lenses.

## Carbon and Oxygen Isotopes

Sixty powder samples (~30–50 mg per single sample) of carbonate rocks and cements, from well SSAU 2310, were microdrilled for carbon and oxygen isotope study. The powered samples were heated to remove organic materials and then reacted with anhydrous phosphoric acid, under vacuum, to release $CO_2$ at 25°C for 24 hr. The $CO_2$ was then analyzed for carbon and oxygen isotopes on a Finnigan MAT251 mass spectrometer standardized with NBS-18. All carbon and oxygen data are reported in per mille (‰) units relative to the Vienna Peedee belemnite standard. The precision for both $\delta^{13}C$ and $\delta^{18}O$ measurements is better than ±0.1‰.

# RESULTS

## Diagenetic Products

### Dolomite

In the San Andres Formation, dolomite occurs as very fine crystals (~5–15 μm) (D1), fine crystals (~20–50 μm) (D2), and medium crystals (50–100 μm) (D3). The D1 is commonly present in dolomudstones and wackestones (Figure 3A) and consists of fusulinids in grainstones and packstones (Figure 3C). The D1 dolomite that commonly occurs as planar-e to planar-s crystals is dark brown to black and is homogeneously gray under SEM-CL (Figure 3D). The D2 dolomite is widely present in packstones and grainstones, and it occurs as planar-s to nonplanar-a dolomite rhombs (Figure 3B) and displays white or gray under SEM-CL (Figure 3E). The D3 dolomite is commonly present in grain-rich facies, and it occurs as medium-crystalline, nonplanar-a dolomite rhombs (spherical) (Figure 3C), and displays relatively light (white) color under SEM-CL (Figure 3F).

### Anhydrite

Anhydrite has many occurrences (e.g., beds, nodules, or cement) in the San Andres Formation. Bedded anhydrite (Figure 4A) consists mainly of fine anhydrite crystals ranging from tens to <50 μm in diameter. It occurs predominantly in ramp interior facies with a total thickness of ~110–190 ft in upper San Andres section, and locally in ramp crest and middle to outer ramp facies with a thickness of 1–2 ft in the lower San Andres section. Nodular anhydrite occurs as coalescing or isolated nodules with sizes ranging from tens to hundreds of micrometers in diameter. Coalescing anhydrite nodules (Figure 4B) commonly occur as burrow fillings in the upper San Andres section, whereas isolated anhydrite nodules are widespread in occurrence in the lower San Andres section. Nodular anhydrite displays irregular crystal shapes and crystal lengths ranging from less than 50 μm and up to several hundreds of micrometers (Figure 4C, D), or regular, tube-like shapes with coarse anhydrite crystals up to several centimeters across (Figure 4E). These anhydrites have either homogeneous color (e.g., gray, white, black) or zonation under SEM-CL (Figures 3E, 4I). Anhydrite cements commonly fill in the pore spaces (Figures 3A, E; 4F, G), with single-crystal sizes mostly ranging from 0.2 to 5 mm across, and display homogeneous, or zoned, or nonluminous, under SEM-CL (Figures 3E, F; 4H, I).

### Other Diagenetic Products

Although in a relatively small volume (<0.2% of the total rocks), pyrite is commonly observed in the San Andres Formation. It occurs predominantly as partial replacement of nodular anhydrite, or less commonly as replacing dolomites. Pyrite displays euhedral or irregular and disseminated shapes with sizes ranging from several micrometers to hundreds of micrometers in diameter (Figures 3A; 4G; 5A–C). Calcite is rarely present in the San Andres Formation; it is only observed replacing a few anhydrite nodules in the ROZs of reservoirs (Figures 4B, 5D). Calcite displays either nonluminous or a very dull gray color under SEM-CL (Figure 3E). Stylolites are well developed in mudstone- and wackestone-dominated intervals (Figure 5E), but almost missing in grainstone- and packstone-dominated

Figure 3. Photomicrographs and scanning electron microscopy–cathodoluminescence (SEM-CL) images showing various types of diagenetic minerals observed in the Seminole San Andres unit well SSAU 2310. (A) D1 consists of wackestone-mudstone, anhydrite (An; white) filling mold with some replacive pyrite (Py; red arrow), depth 5179.5 ft. (B) D2 consists of wackestone with abundant intercrystalline pores (BC) (blue), depth 5195.3 ft. (C) D1 consists of the fusulinid grainstone associated with abundant intraparticle pores (IP) (blue) and D3, depth 5261.2 ft. (D) The SEM-CL image of D1 consists of fusulinid grains displaying relatively homogeneous CL color and interparticle porosity (IP), depth 5264.4 ft. (E) The SEM-CL image showing two different gray-scale levels of CL (gray and white) in D2, and relative dark SEM-CL color in An replacive calcite (Ca), depth 5335.4 ft. (F) The SEM-CL image showing lighter (white) CL color in D3, whereas gray CL color in An cement, moldic porosity (Mo) locally present, depth 5200.5 ft. D **5** dolomite.

Figure 4. Core photographs, thin-section photomicrographs, and scanning electron microscopy–cathodoluminescence (SEM-CL) images showing various types of anhydrite (An) in the San Andres Formation. (A) Bedded An and D1 in the upper part of the San Andres Formation, well Seminole San Andres unit (SSAU) 2310, depth 5201 ft. (B) Nodular An locally replaced by calcite (Ca), well SSAU 2310, depth 5335.4 ft. (C) Nodular An displaying irregular and fine crystals, cross-polarized light, well SSAU 2310, depth 5103.3 ft. (D) Nodular An showing irregular medium crystals, cross-polarized light, well SSAU 2310, depth 5200.5 ft. (E) Isolated An nodule showing tube-like, and relatively coarse crystalline, cross-polarized light, well SSAU 2310, depth 5133.8 ft. (F) Various types of An including nodular, cement, fracture-filling showing relatively coarse crystalline, cross-polarized light, well SSAU 5309, depth 5002 ft. (G) Moldic pore filled by a single crystal An cement locally replaced by pyrite (Py; white arrow) at the edge, well SSAU 2310, depth 5200.5 ft. (H) Nonluminescent An cement under SEM-CL, well SSAU 2310, depth 5212.8 ft. (I) Various types of SEM-CL color and local zonation (white arrow) present in An cements, well SSAU 2310, depth 5264.4 ft. D 5 dolomite.

intervals. In ooid-rich grainstones where grain-to-grain contacts are present, some grains display a deformed elliptical shape.

## Pore Systems

Classification of the pore space types follows the methods of Choquette and Pray (1970) for macropores and the methods of Loucks et al. (2013) and Lucia and Loucks (2013) for micropores. In the studied San Andres Formation, seven pore types were recognized and listed in the order of relative abundance as follows: vug, intraparticle pores, intercrystalline pores, interparticle pores, moldic pores, micropores, and fractures (Figures 3, 6).

Figure 5. Photomicrographs showing other diagenetic products in the San Andres Formation. (A) and (B) Pyrite (Py) replacing anhydrite (An) nodule, well Seminole San Andres unit (SSAU) 2310, depth 5107.6 ft for (A); and well SSAU 5309, depth 5084 ft for (B). (C) Py locally replacing bulk dolomite, An cement filling with the pore spaces, well SSAU 2310, depth 5264.4 ft. (D) Calcite (Ca; red) locally replacing An (white) nodule in residual oil zones of well SSAU 2310, depth 5335.4 ft. (E) Stylolites (black; white arrows) commonly present typical serrated shape, well SSAU 5309, depth 5094 ft. D = dolomite.

Vuggy porosity is the volumetric dominant (>50%) pore space type. It most commonly occurs as partial or complete dissolution of rock components, including matrix, grains (e.g., fusulinids), and anhydrite cements with sizes ranging between hundreds of micrometers and up to several millimeters in diameter (Figure 6B, C). Interparticle pores occur mostly in fusulinid grain-rich facies, with pore sizes mainly between 50 and 300 μm (Figures 3C, D; 6A, F). Intercrystalline pores and interparticle pores are commonly observed in mudstone and wackestone (Figure 3B) and grainstone and packstone, respectively (Figure 6A, D). Few moldic pores are observed in grainstone include dissolved crinoids or bivalves, with pore sizes commonly less than 100 μm (Figures 3F). Micropores occur predominantly as dolomite dissolution pores in the middle of microdolomite crystals with sizes ranging from 2 to 10 μm (Figure 6G). They can be observed under blue ultraviolet light (Figure 6H, I) and SEM (Figure 6F, G). Fracture porosity crosscuts all diagenetic minerals and fabrics, commonly in the width of <50 μm and length of up to several centimeters (Figure 6E).

## Quantitative Assessment of Mineralogy and Porosity

Quantitative assessments were performed on porosity occluding minerals, including anhydrite (most commonly) and dolomite in 261 thin sections, which were collected from the reservoir part of well SSAU 2505 at a depth of 5058–5300 ft. Results show that anhydrite content ranges from 0% to >80% of the total rock volume. The average content for anhydrite and dolomite cement is 15% and 5.7% for grainstone, 16.1% and 10.5% for packstone, 10.7% and 14.7% for porous wackestone, 13.3% and 7.3% for nonporous wackestone, and 28.1% and 9.1% for mudstone (Figure 7).

## Geochemical Data

### Stable Carbon and Oxygen Isotopic Analyses

The results of stable isotope (O and C) analyses for 56 bulk dolomite samples (D1 and D2) and four anhydrite-replacive calcites are presented in Figure 8, Figure 9A, and Table 1. Generally, $\delta^{13}C$

Figure 6. Photomicrographs showing various pore types in the San Andres Formation. (A) Abundant pore spaces consist mainly of interparticle pores (BP) and intraparticle pores (IP) in grain-dominated dolostone, well Seminole San Andres unit (SSAU) 5309, depth 5162 ft. (B) Vug with sizes up to several millimeters across in very finely crystalline dolomite (gray) with abundant anhydrite (An) cement, well SSAU 2310, depth 5295.5 ft. (C) Vugs with sizes up to several hundred micrometers are present in An cement filling with moldic pore, well SSAU 2310, depth 5145.1 ft. (D) Abundant interparticle pore (BP) and dolomite moldic pores (Mo; white arrow) are commonly observed in grainstone and packstone, well SSAU 2310, depth 5324.4 ft. (E) Fracture pores (F) are locally present (blue), mostly filled by An (white) cements, well SSAU 2310, depth 5145.1 ft. (F) Abundant micropores (Mi) are present in fusulinid walls composed by D1, which displays abundant IP, well SSAU 2310, depth 5264.4 ft. (G) Micropores (Mi) occur as dissolution of cores in D1, which consists of fusulinid grains, well SSAU 2310, depth 5264.4 ft. (H) Fusulinid packstone displays abundant IP and D3, well SSAU 2310, depth 5261.3 ft. (I) Photomicrograph taken with blue ultraviolet light from (H) results in areas (fusulinid walls) of micropores to luminesce blue. D 5 dolomite.

Figure 7. Box-plot image showing quantitative assessment of mineralogy and porosity results of (A) anhydrite content, and (B) dolomite cement, in different rock types, data were derived from well SSAU 2505 in the Seminole San Andres unit.

decreases downward in the carbonate host rock, but there are no obvious stratigraphic changes in $d^{18}O$ values (Figure 8). Bulk dolomites display a relatively narrow isotopic range for both $d^{13}C$ values (between 3.84‰ and 6.69‰, average at 5.18‰) and $d^{18}O$ values (between—0.18‰ and 3.2‰, average at 1.79‰) (Figure 9A). In contrast, anhydrite-replacive calcites show markedly negative values of $d^{13}C$ (—13.90‰ to —8.01‰, average at—10.93‰) and $d^{18}O$ (—10.16‰ to —9.30‰, average at —9.67‰) (Figure 9A).

## Fluid Inclusion Microthermometry

Two-phase aqueous inclusions are present only in few anhydrite cements, whereas single-phase fluid inclusions were observed in a small part of replacive poikilotopic anhydrite and fine crystalline dolomite. Two groups of primary two-phase aqueous inclusions were obtained from anhydrite cements. One group yielded a relatively low and narrow $T_h$ ranging from 55°C to 75°C (Figure 10; Table 2) with a variation of mostly <10°C within a single FIA. By contrast, the other group yielded much higher $T_h$ ranging from

Figure 8. Lithology, textures, facies, and $d^{13}C$ and $d^{18}O$ isotopic compositions of bulk dolomite (dol) in the San Andres Formation in well SSAU 2310 in the Seminole San Andres unit (SSAU). The facies and texture classification after Lucia et al. (1995) and Kerans et al. (1994). MPZ **5** main pay zone; ROZ **5** residual oil zone.

80 °C to 128 °C (Figure 10; Table 2), with variations from $<$10 °C to ~20 °C within a single FIA.

## DISCUSSION

### Origin of Dolomite

Dolomites in the SSAU display $d^{13}C$ and $d^{18}O$ values similar to several other Permian dolostone intervals in the Permian Basin (Figure 9), which are proven to have formed predominantly during reflux dolomitization (Lloyd, 1966; Ruppel and Cander, 1988; Lucia et al., 1995; Saller and Henderson, 1998; Ruppel and Jones, 2006). Stable isotopes of $d^{13}C$ and $d^{18}O$ for dolomites have been widely used to constrain the fluid temperature and source, diagenetic environment, and thus the correlated dolomitization model (Saller and Dickson, 2011; Jiang et al., 2016). The markedly positive swing of $d^{18}O$ (mostly from 0‰ to 3.2‰) in these dolomites was most plausibly attributable to seawater evaporation, which would lead to increased $d^{18}O_{seawater}$ values (Jiang et al., 2016). The wide occurrence of anhydrites in many Permian intervals suggests a persistent arid climate and strong evaporation in the Permian Basin during the middle to late Permian (Lloyd, 1966; Ruppel and Cander, 1988; Lucia et al., 1995; Saller and Henderson, 1998; Ruppel and Jones, 2006). Therefore, large swings in $d^{18}O$ values among these dolomites may be linked to varying degrees of brine evaporation for reflux dolomitization (Saller and Henderson, 1998; Ruppel and Jones, 2006; Jiang et al., 2016), dolomite recrystallization at various burial depths (Land, 1980; Ruppel and Cander, 1988), or a combination of these factors. Neither evaporation nor recrystallization would change the $d^{13}C$ in precursor dolomites; the

Figure 9. Carbon (carb) and oxygen isotopic compositions of bulk dolomite and diagenetic calcite cement from the Permian units in the Permian Basin. (A) Data measured from the San Andres Formation at the Central Basin platform in this study. (B) The sketch displays the isotopic range of seawater, dolomite, and burial calcite in the Seminole San Andres unit (SSAU), arrows show the trajectory of dolomite in equilibrium with seawater as it evaporates, and the trajectory of calcite produced by bacterial sulfate reduction. VPDB 5 Vienna Peedee belemnite.

small stratigraphic downward decrease in d$^{13}$C, therefore, may imply a secular change of d$^{13}$C in seawater or diagenetic alterations. The latter is evident in many sedimentary basins worldwide through the incorporation of $^{12}$C-rich carbon from oxidation of organic matter to $CO_2$ (e.g., through BSR [Machel, 2001; Saller et al., 2014; Jiang et al., 2019] or meteoric diagenesis [Melim et al., 2001]).

The presence of single-phase fluid inclusion indicates low precipitation temperatures (e.g., <50°C) for D1 dolomite formation (Goldstein and Reynolds, 1994). During San Andres carbonate deposition, the surface temperature may have been higher than that of the present-day (e.g., the average annual temperature of 18.6°C for Midland, Texas). A temperature range of 25°C to 40°C (average at 32.5°C) is invoked

Table 1. Carbon and Oxygen Isotopic Compositions of Bulk Dolomite and Late Diagenetic Calcites in Well SSAU 2310 in the Central Basin Platform

| Sample Number | Depth, ft | Mineral | $d^{18}O_{VPDB}$ | $d^{13}C_{VPDB}$ |
|---|---|---|---|---|
| SSAU-01 | 5008 | Dolomite | 1.47 | 6.23 |
| SSAU-02 | 5013 | Dolomite | −0.18 | 5.62 |
| SSAU-03 | 5019 | Dolomite | 0.96 | 6.18 |
| SSAU-04 | 5019 | Dolomite | 0.97 | 6.17 |
| SSAU-05 | 5024 | Dolomite | 0.28 | 6.25 |
| SSAU-06 | 5035.5 | Dolomite | 1.81 | 6.16 |
| SSAU-07 | 5045.9 | Dolomite | 0.58 | 6.23 |
| SSAU-08 | 5055 | Dolomite | 2.57 | 5.79 |
| SSAU-09 | 5059 | Dolomite | 1.73 | 5.47 |
| SSAU-10 | 5079 | Dolomite | 2.26 | 4.21 |
| SSAU-11 | 5088 | Dolomite | 2.01 | 6.69 |
| SSAU-12 | 5099 | Dolomite | 1.47 | 6.26 |
| SSAU-13 | 5102 | Dolomite | 2.35 | 6.32 |
| SSAU-14 | 5103.2 | Dolomite | 2.08 | 4.03 |
| SSAU-15 | 5106 | Dolomite | 2.06 | 6.30 |
| SSAU-16 | 5108 | Dolomite | 1.52 | 6.37 |
| SSAU-17 | 5111 | Dolomite | 1.64 | 5.87 |
| SSAU-18 | 5118 | Dolomite | 3.03 | 6.63 |
| SSAU-19 | 5133 | Dolomite | 1.65 | 6.07 |
| SSAU-20 | 5137 | Dolomite | 2.11 | 6.29 |
| SSAU-21 | 5145 | Dolomite | 2.00 | 6.10 |
| SSAU-22 | 5146.4 | Dolomite | 2.65 | 5.83 |
| SSAU-23 | 5160 | Dolomite | 2.40 | 6.11 |
| SSAU-24 | 5165 | Dolomite | 2.12 | 5.94 |
| SSAU-25 | 5172.2 | Dolomite | 2.46 | 5.73 |
| SSAU-26 | 5175 | Dolomite | 3.20 | 5.53 |
| SSAU-27 | 5179.5 | Dolomite | 1.91 | 5.74 |
| SSAU-28 | 5190 | Dolomite | 1.22 | 5.29 |
| SSAU-29 | 5201 | Dolomite | 2.72 | 5.13 |
| SSAU-30 | 5203.5 | Dolomite | 2.62 | 4.98 |
| SSAU-31 | 5208 | Dolomite | 2.43 | 5.23 |
| SSAU-32 | 5208.5 | Dolomite | 1.84 | 5.29 |
| SSAU-33 | 5210 | Dolomite | 1.41 | 4.72 |
| SSAU-34 | 5215 | Dolomite | 1.78 | 4.69 |
| SSAU-35 | 5220 | Dolomite | 0.73 | 4.57 |
| SSAU-36 | 5227 | Dolomite | 1.38 | 4.77 |
| SSAU-37 | 5230 | Dolomite | 2.22 | 4.85 |
| SSAU-38 | 5252 | Dolomite | 2.13 | 4.57 |
| SSAU-39 | 5261 | Dolomite | 1.51 | 4.25 |
| SSAU-40 | 5264 | Dolomite | 2.04 | 4.21 |
| SSAU-41 | 5267.5 | Dolomite | 1.32 | 4.46 |
| SSAU-42 | 5269.7 | Dolomite | 1.02 | 4.40 |
| SSAU-43 | 5277 | Dolomite | 2.29 | 4.29 |
| SSAU-44 | 5284.5 | Dolomite | 1.99 | 4.43 |
| SSAU-45 | 5288.4 | Dolomite | 1.40 | 4.55 |
| SSAU-46 | 5293 | Dolomite | 1.78 | 4.56 |
| SSAU-47 | 5299 | Dolomite | 1.81 | 4.21 |
| SSAU-48 | 5302 | Dolomite | 0.86 | 4.07 |
| SSAU-49 | 5307.5 | Dolomite | 1.95 | 4.00 |
| SSAU-50 | 5312 | Dolomite | 2.35 | 3.84 |
| SSAU-51 | 5314 | Dolomite | 1.50 | 3.96 |
| SSAU-52 | 5315 | Dolomite | 1.34 | 4.11 |
| SSAU-53 | 5324.2 | Dolomite | 2.05 | 4.24 |
| SSAU-54 | 5332.5 | Dolomite | 1.79 | 4.26 |
| SSAU-55 | 5333.5 | Dolomite | 1.45 | 3.88 |
| SSAU-56 | 5334.9 | Dolomite | 2.28 | 4.22 |
| SSAU-57 | 5328 | Calcite | −13.90 | −10.16 |
| SSAU-58 | 5333 | Calcite | −12.51 | −9.71 |
| SSAU-59 | 5334.9 | Calcite | −8.01 | −9.45 |
| SSAU-60 | 5335 | Calcite | −9.30 | −9.37 |

Standard deviations for $d^{13}C$ and $d^{18}O$ are 0.01 and 0.04, respectively.

Abbreviations: SSAU = Seminole San Andres unit; *VPDB* = Vienna Peedee belemnite.

for tropics or subtropics surface temperatures during the middle Permian, as revealed by carbonate clumped isotope from fossil brachiopods (Henkes et al., 2018). Assuming a depositional surface temperature of 32.5°C, a geothermal gradient of 20°C/km (Mazzullo and Harris, 1991), this dolomitization event occurred at burial depths ranging from 0 to 2460 ft to generate temperatures between 32.5°C and 50°C. However, the geothermal gradient was probably higher in the past because of meteoric waters circulation that may have cooled most of the current San Andres subsurface (Saller and Stueber, 2018). Hence, the depth of 2460 ft is an estimation of the maximum depth for dolomitization. Diagenesis, including recrystallization, dissolution, and reprecipitation, may have occurred during

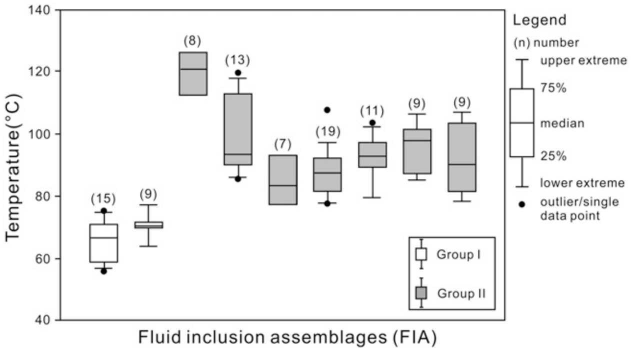

Figure 10. Box-plot image showing homogenization temperatures of two groups of primary inclusions in individual FIA in diagenetic anhydrite cement in the San Andres Formation.

Table 2. Fluid Inclusion Homogenization Temperatures Data of Diagenetic Anhydrites in Well SSAU 2310 in the Central Basin Platform

| FIA Number | Type | $T_h$ Range, °C | Number | Average $T_h$, °C | SD |
|---|---|---|---|---|---|
| 1 | Group I | 55.9–75.3 | 15 | 65.9 | 6.3 |
| 2 | Group I | 64.3–77.5 | 9 | 70.8 | 3.2 |
| 3 | Group II | 111.2–128.2 | 8 | 122.0 | 6.1 |
| 4 | Group II | 85.6–119.6 | 13 | 100.7 | 12.5 |
| 5 | Group II | 76.5–98.2 | 7 | 85.1 | 7.6 |
| 6 | Group II | 79.5–107.7 | 19 | 88.2 | 7.5 |
| 7 | Group II | 79.2–103.5 | 11 | 92.1 | 6.8 |
| 8 | Group II | 85.5–106.5 | 9 | 95.8 | 7.1 |
| 9 | Group II | 78.6–105.4 | 9 | 91.2 | 10.4 |

Abbreviations: SD = standard deviation; SSAU = Seminole San Andres unit; $T_h$ = homogenization temperature.

burial and resulted in varying gray-tones SEM-CL color in the growth zones of D1 dolomites (Figures 3D). In contrast, D2 dolomite displays mixed gray and white (Figure 4H, I), whereas D3 dolomite displays homogeneous gray or white under SEM-CL (Figure 3F), suggesting that they were precipitated from fluids with distinctive chemical compositions at different burial-diagenesis conditions (Leary and Vogt, 1987; Ruppel and Cander, 1988; Major and Holtz, 1990; Saller and Henderson, 1998).

## Origin of Anhydrites

Bedded anhydrite in the San Andres Formation was most likely precipitated in restricted, saline brine bodies (e.g., lagoons) because of strong evaporation under an arid climate condition (Lucia and Ruppel, 1996), whereas anhydrite nodules, especially the coalescing nodules filling burrows, were formed during early diagenesis and probably in parallel with reflux dolomitization (Ruppel and Cander, 1988; Lucia and Ruppel, 1996; Saller and Henderson, 1998). The presence of single-phase fluid inclusions suggests low precipitation temperatures ($<$50°C) for these early anhydrites (Goldstein and Reynolds, 1994). By contrast, late anhydrite cements, occupying various types of pore spaces, were formed during burial diagenesis and likely emplaced after reflux dolomitization (Figure 11). Based on the primary fluid inclusion data, we conclude that anhydrite cementation continued to burial temperatures ranging from $<$55°C to 75°C (Figure 10), corresponding to burial depths lying between ~3355 and 6635 ft, which approached the maximum burial depth for the Seminole San Andres reservoir (Mazzullo and Harris, 1991). Note that the present-day depths for reservoirs in the San Andres Formation are predominantly between 4900 and 5600 ft (Lucia et al., 1995), with temperatures between ~39.1°C and 59.1°C. This is consistent with a measured reservoir temperature of 42°C for the Seminole field (Galloway et al., 1983).

By contrast, some anhydrite cements were precipitated at remarkably high temperatures of 90°C to 128°C, which is much higher than the maximum burial temperatures (60°C–92.6°C) of the Permian strata in the Permian Basin (Mazzullo and Harris, 1991). This suggests the presence of a regional hydrothermal event in the Seminole San Andres carbonates (Warren, 2000; Davies and Smith, 2006; Smith, 2006). The recent discovery of hydrothermal dolomites in several Permian intervals in the Permian Basin (e.g., the Grayburg Formation in the Delaware Basin) ($T_h$ ranging from 113°C to 224°C), the Central Basin platform ($T_h$ ranging from 137°C to 205°C) (Lindsay, 2018), and the Pennsylvanian and lowest Permian carbonates from the Reinecke field in western Texas ($T_h$ ranging from 92°C to 118°C) (Saller and Dickson, 2011), supporting the occurrence of regional hydrotromal event in the Permian units of the Permian Basin. The hydrothermal waters were linked to heating of the Neogene meteoric water sourced from the western uplifted mountain region (Saller and Stueber, 2018) by localized intrusive plutons (Eaton, 2008), before they fluxed into the subsurface area of the Permian strata in the basin. The hydrothermal fluid was likely in equilibrium with dolomite and anhydrite by dissolution of carbonate and evaporite during its pathways (Mazzullo and Harris, 1991) and precipitated hydrothermal minerals in the subsurface reservoirs in Permian strata.

## Bacterial Sulfate Reduction

The BSR, a redox reaction between sulfate and organic matter (including oil) and mediated by sulfate-reducing bacteria, was widespread in ancient rocks during shallow burial at temperatures less than 80°C (Machel, 2001). The observation of small volumes (average $<$ 0.1%) of diagenetic pyrite replacing

Figure 11. Burial depth-temperature curve and paragenetic sequence in the Seminole San Andres unit of the Central Basin platform. Temperature on the basis of geothermal gradient of 20°C/km (5 1.2°F/100 ft). Onset of organic matter maturation and oil charging was modified from Mazzullo and Harris (1991). Paragenetic sequence was established on the basis of petrological evidence combined with homogenization temperatures measured from fluid inclusions. BSR 5 bacterial sulfate reduction.

anhydrite (Figures 3A; 4G; 5A, B) and dolomite (Figure 5C) indicates the occurrence of BSR (Machel, 2001). A small downward decreasing of $\mathrm{d}^{13}\mathrm{C}$ in dolomites with sedimentary facies changing from ramp interior to outer ramp (Figure 8) could be the consequence of enhanced BSR from shallow to deep-water sediments (Machel, 2001; Saller et al., 2014; Jiang et al., 2019). Therefore, syndepositional diagenesis in different sedimentary facies is able to alter primary geochemical signals in carbonates (e.g., C, O, U isotopes) (Jiang et al., 2019). Caution should be paid when applying the geochemistry proxies in marine carbonates for paleoclimate reconstruction.

In this study, anhydrite-replacive calcites, with markedly negative $\mathrm{d}^{13}\mathrm{C}$ values ranging from approximately −30‰ to −10‰ (Figure 9), were observed in the ROZs of the San Andres Formation in well SSAU 2310. This type of calcite has also been documented in several other Permian intervals in the Permian Basin (Leary and Vogt, 1987; Saller and Henderson, 1998; Ruppel and Jones, 2006; Saller and Stueber, 2018). Markedly negative $\mathrm{d}^{13}\mathrm{C}$ values in calcite indicate that a significant contribution of carbon was sourced from the oxidation of hydrocarbons (Wiggins et al., 1993). Diagenetic carbonate cements, with $\mathrm{d}^{13}\mathrm{C}$ values of greater than −10‰, are commonly linked to BSR at burial temperatures of < 80°C (Machel, 2001; Londry and Des Marais, 2003; Saller et al., 2014), or to thermochemical sulfate reduction (TSR) at higher burial temperatures of >100°C (Machel et al., 1995; Worden et al., 1995; Vandeginste et al., 2009; Jiang et al., 2015). The relative low burial temperatures (<75°C; Figure 11) for the studied San Andres Formation appear to support the BSR model. Furthermore, it is evident that a late-stage BSR is likely an ongoing event in the ROZs of the Permian strata in Permian Basin (Leary and Vogt, 1987; Wiggins et al., 1993; Lindsay, 2018; Saller and Stueber, 2018). However, we could not completely rule out the possibility of the TSR model, which may have also promoted calcite precipitation with depleted $\mathrm{d}^{13}\mathrm{C}$ values during the local hydrothermal activities.

## Burial-Diagenesis Model

This study, to my knowledge, is the first holistic diagenesis study that places an emphasis on diagenetic anhydrite and its effects on the Permian carbonate reservoir quality of the San Andres Formation (Figure 11). Mazzullo and Harris (1991) discussed burial-diagenesis models for several Permian intervals in the Permian Basin, which are so far the most detailed documented burial models in the Permian strata.

None of their diagenesis models, however, documented in detail the diagenesis of widespread anhydrites within these carbonate reservoirs (Ruppel and Cander, 1988; Lucia et al., 1995; Saller and Henderson, 1998).

The San Andres carbonates were initially deposited as limestone in a marine ramp system at ambient temperature conditions (Kerans and Fitchen, 1995). As the basin became restricted, intense evaporation elevated seawater salinities under an arid climate condition, resulting in evaporite deposition and early reflux dolomitization (Ruppel and Cander, 1988; Lucia et al., 1995; Saller and Henderson, 1998; Saller et al., 2014). Reflux dolomitization was responsible for the generation of intercrystalline pores and micropores (Figures 3B; 6G, I). Anhydrite deposition, cementation, and replacement may have occurred in parallel with reflux dolomitization (Ruppel and Cander, 1988; Saller et al., 2014; Jiang et al., 2016). The widespread occurrence of the early stage of BSR may have resulted in anhydrite nodules replaced by pyrite (Figure 5A, B), and partial or complete dissolution of dolomites (Figure 6B). The following diagenesis was dominated by anhydrite cementation and recrystallization, dissolution and reprecipitation, mechanical and chemical compaction (Figure 5E), and fracturing (Figure 6E), with diagenetic fluids dominated by evaporative brines. Finally, Neogene tectonism enabled meteoric water from western mountain areas fluxed into the San Andres Formation in Central Basin platform, associated with a late-stage localized hydrothermal event and a late-stage BSR, which resulted in dolomite and anhydrite dissolution and reprecipitation, and growth of calcite in the ROZs (Figure 11).

## Diagenesis Effects on Reservoir Quality

Combining the quantitative assessment of mineral and porosity data with detailed petrology study and a well-established diagenesis frame enables us to evaluate the impact of diagenesis on reservoir quality in facies-dependent rock types of the San Andres Formation (Figure 1B). Generally, reservoir quality for grainstones and packstones is superior to wackestone and mudstone (Figure 12). Porosity data in grainstones and packstones are quite similar, whereas permeability data in grainstones are markedly higher than packstones (Figure 12). The different reservoir quality and heterogeneous in each reservoir type in the San Andres carbonates have been linked to different sedimentary facies and dolomite crystal sizes (Lucia, 1995; Lucia and Ruppel, 1996). However, the origin of porous and finely crystalline wackestones in this study, displaying great reservoir potential (Figure 12), deserves a further explanation. Crucially, the effects of anhydrite cements, which comprise approximately 20%–30% of the total rock volume in the San Andres Formation and many other Permian intervals in Permian Basin, on reservoir development is not well understood (Leary and Vogt, 1987; Ruppel and Cander, 1988; Major and Holtz, 1990; Lucia and Ruppel, 1996; Saller and Henderson, 1998; Ruppel and Jones, 2006).

Anhydrite cements are commonly present in interparticle pore spaces, whereas they are almost absent in areas where grain-to-grain compaction is present, suggesting that early emplacement of anhydrite may have prevented compaction and pressure-dissolution during burial and reserved the original rock structures. This is similar to the appearance and effect of calcite cementation on grain-dominated carbonate reservoirs (Heydari, 2000; Jiang et al., 2018b). However, calcite is relatively stable and precludes most further diagenetic alterations. Once precipitated, it commonly occludes pore spaces and decreases carbonate reservoir quality (Jiang et al., 2018b). By contrast, anhydrite is a more soluble mineral, and it would more easily be removed by normal diagenetic fluids (e.g., meteoric water, seawater, burial and hydrothermal fluids) (Hill, 1990; Jiang et al., 2018a; Saller and Stueber, 2018). Hence, "early-stage" anhydrite cementation may have preserved the primary rock textures, whereas "late-stage" anhydrite dissolution would lead to an enhanced reservoir quality. This dynamic nature of anhydrite subjected to diagenesis may have been underestimated in the reservoir development in the San Andres carbonates (Lucia et al., 1995; Jiang et al., 2018b). The discovery of porous wackestones associated with markedly high porosity and the lowest anhydrite cement volume (Figure 7) from this study is likely attributed to the dynamics of anhydrite during diagenesis. The great heterogeneity and complex

Figure 12. Box-plot image showing the distribution ranges of porosity (A) and permeability (B) in each rock type in the San Andres Formation at well SSAU 2505 in the Seminole San Andres unit (SSAU). Petrophysical data were derived from Lucia et al. (1995) and Wang et al. (1998). Average porosity and permeability for grainstones, packstones, porous wackestones, nonporous wackestone, and mudstone is 10.8%, 10.1%, 13.8%, 8.8%, and 8.3%, and 23.6 md, 5.8 md, 19.8 md, 1.8 md, and 2.4 md, respectively.

pore systems in the present-day San Andres reservoirs are most plausibly linked to a varying degree of diagenesis (e.g., dolomitization and recrystallization) (Lucia and Ruppel, 1996), especially anhydrite cementation and dissolution due to localized hydrothermal fluid or BSR (Figure 11) (Cowan and Harris, 1986; Lucia et al., 1995; Lucia and Ruppel, 1996; Saller and Henderson, 1998; Ehrenberg, 2019). This study may have implications on $CO_2$ EOR of ROZs in the Permian Basin because BSR is likely an ongoing diagenetic event in the present-day reservoirs of the Permian carbonates (Trentham et al., 2015) and on many other mixed carbonate and evaporite systems worldwide (e.g., Sichuan, Tarim, and Ordos Basins in China; Gulf of Mexico Basin; and Arabian Basin).

## CONCLUSIONS

- Carbonate reservoir quality in the SSAU along the Central Basin platform is predominantly controlled by diagenesis including dolomitization, anhydrite and dolomite cementation and dissolution, BSR, and hydrothermal alteration. A new holistic burial-diagenesis model, including anhydrite diagenesis, is provided by this study.

- Reflux dolomitization began syndepositionally and proceeded to a burial depth of up to 2460 ft (875 m). The dolomitizing fluid was evaporated seawater with salinities that vary from normal seawater to brine close to gypsum saturation. Recrystallization, dissolution, and precipitation of dolomite resulted from carbonate compaction and pressure solution, and an early-stage BSR.
- Bedded anhydrites and most nodular anhydrites are syndepositional, whereas isolated nodular anhydrite was likely formed in parallel with reflux dolomitization. Anhydrite cementation may have started along with reflux dolomitization and continued to the maximum burial depth of approximately 6637 ft (~2023 m) and temperature of ~75 °C. A hydrothermal event, with temperatures up to 128 °C, may have occurred in SSAU by influx of meteoric water during the western Neogene uplifting event.
- An early-stage, syndepositional BSR may have occurred and resulted in pyrite replacing anhydrite nodules or cements, coupled with a small downward decreasing of $d^{13}C$ in carbonate host rocks. The occurrence of a late-stage BSR in the ROZs of the San Andres Formation was tied to the Neogene meteoric water recharging event.
- Although sulfate cementation has occupied most of the primary pore spaces, it may have preserved the primary textures and the rest of the pore spaces from carbonate cementation by pressure solution and compaction. Furthermore, dissolution of anhydrite by later diagenesis (e.g., meteoric, hydrothermal, and BSR) may have enhanced present-day reservoir quality along with a greater heterogeneity. Hence, this study offers an ideal example for understanding the dynamics of anhydrite subjected to diagenesis in a mixed carbonate and evaporite system.

## REFERENCES CITED

Choquette, P. W., and L. C. Pray, 1970, Geologic nomenclature and classification of porosity in sedimentary carbonates: AAPG Bulletin, v. 54, no. 2, p. 207–250.

Cowan, P. E., and P. M. Harris, 1986, Porosity distribution in San Andres Formation (Permian), Cochran and Hockley counties, Texas: AAPG Bulletin, v. 70, no. 7, p. 888–897.

Davies, G. R., and L. B. Smith, 2006, Structurally controlled hydrothermal dolomite reservoir facies: An overview: AAPG Bulletin, v. 90, no. 11, p. 1641–1690, doi:10.1306/05220605164.

Dou, Q. F., Y. F. Sun, and C. Sullivan, 2011, Rock-physics-based carbonate pore type characterization and reservoir permeability heterogeneity evaluation, Upper San Andres reservoir, Permian Basin, west Texas: Journal of Applied Geophysics, v. 74, no. 1, p. 8–18, doi:10.1016/j.jappgeo.2011.02.010.

Dutton, S. P., E. M. Kim, R. F. Broadhead, W. D. Raatz, C. L. Breton, S. C. Ruppel, and C. Kerans, 2005, Play analysis and leading-edge oil-reservoir development methods in the Permian basin: Increased recovery through advanced technologies: AAPG Bulletin, v. 89, no. 5, p. 553–576, doi:10.1306/12070404093.

Eaton, G. P., 2008, Epeirogeny in the Southern Rocky Mountains region: Evidence and origin: Geosphere, v. 4, no. 5, p. 764–784, doi:10.1130/GES00149.1.

Ehrenberg, S. N., 2019, Petrophysical heterogeneity in a Lower Cretaceous limestone reservoir, onshore Abu Dhabi, United Arab Emirates: AAPG Bulletin, v. 103, no. 3, p. 527–546, doi:10.1306/09061817298.

Eisenberg, R. A., P. M. Harris, C. W. Grant, D. J. Goggin, and F. J. Conner, 1994, Modeling reservoir heterogeneity within outer ramp carbonate facies using an outcrop analog, San Andres Formation of the Permian Basin: AAPG Bulletin, v. 78, no. 9, p. 1337–1359.

Galloway, W. E., T. E. Ewing, C. M. Garret, N. Tyler, and D. G. Bebout, 1983, Atlas of major Texas oil reservoirs: Austin, Texas, The University of Texas at Austin, Bureau of Economic Geology, 139 p.

Gaswirth, S. B., K. R. Marra, P. G. Lillis, T. J. Mercier, H. M. Leathers-Miller, C. J. Schenk, T. R. Klett, et al., 2016, Assessment of undiscovered continuous oil resources in the Wolfcamp shale of the Midland Basin, Permian Basin Province, Texas, 2016: Washington, DC, US Geological Survey Fact Sheet 2016-3092, 4 p., doi:10.3133/fs20163092.

Goldstein, R. H., 2012, Fluid inclusion geothermometry in sedimentary systems: From paleoclimate to hydrothermal, *in* N. B. Harris and K. E. Peters, eds., Analyzing the thermal history analysis of sedimentary basins; methods and case studies: Tulsa, Oklahoma, SEPM Special Publication 103, p. 45–63.

Goldstein, R. H., and T. J. Reynolds, 1994, Systematics of fluid inclusions in diagenetic minerals: Tulsa, Oklahoma, SEPM Short Course Notes, v. 31, p. 199, doi:10.2110/scn.94.31.

Grant, C. W., D. J. Goggin, and P. M. Harris, 1994, Outcrop analog for cyclic-shelf reservoirs, San Andres Formation of Permian Basin: Stratigraphic framework, permeability distribution, geostatistics, and fluid-flow modeling: AAPG Bulletin, v. 78, no. 1, p. 23–54.

Henkes, G. A., B. H. Passey, E. L. Grossman, B. J. Shenton, T. E. Yancey, and A. P´erez-Huerta, 2018, Temperature evolution and the oxygen isotope composition of Phanerozoic oceans from carbonate clumped isotope thermometry: Earth and Planetary Science Letters, v. 490, p. 40–50, doi:10.1016/j.epsl.2018.02.001.

Heydari, E., 2000, Porosity loss, fluid flow, and mass transfer in limestone reservoirs: Application to the upper Jurassic Smackover formation, Mississippi: AAPG Bulletin, v. 84, no. 1, p. 100–118.

Hill, C. A., 1990, Sulfuric acid speleogenesis of Carlsbad Cavern and its relationship to hydrocarbons, Delaware Basin, New Mexico and Texas: AAPG Bulletin, v. 74, no. 11, p. 1685–1694.

Honarpour, M. M., N. R. Nagarajan, A. Grijalba Cuenca, M. Valle, and K. Adesoye, 2010, Rock-fluid characterization for miscible $CO_2$ injection: residual oil zone, Seminole field, Permian Basin: Society of Petroleum Engineers Annual Technical Conference and Exhibition, Florence, Italy, September 19–22, 2010, SPE-133089-MS, 24 p.

Jiang, L., C. F. Cai, R. H. Worden, S. F. Crowley, L. Q. Jia, K. Zhang, and I. J. Duncan, 2016, Multiphase dolomitization of deeply buried Cambrian petroleum reservoirs, Tarim Basin, north-west China: Sedimentology, v. 63, no. 7, p. 2130–2157, doi:10.1111/sed.12300.

Jiang, L., N. Planavsky, M. Zhao, W. Liu, and X. Wang, 2019, Authigenic origin for a massive negative carbon isotope excursion: Geology, v. 47, no. 2, p. 115–118, doi:10.1130/G45709.1.

Jiang, L., R. H. Worden, and C. F. Cai, 2015, Generation of isotopically and compositionally distinct water during thermochemical sulfate reduction (TSR) in carbonate reservoirs: Triassic Feixianguan Formation, Sichuan Basin, China: Geochimica et Cosmochimica Acta, v. 165, p. 249–262, doi:10.1016/j.gca.2015.05.033.

Jiang, L., R. H. Worden, C. F. Cai, A. J. Shen, and S. F. Crowley, 2018a, Diagenesis of an evaporite-related carbonate reservoir in deeply buried Cambrian strata, Tarim Basin, Northwest China: AAPG Bulletin, v. 102, no. 1, p. 77–102, doi:10.1306/0328171608517048.

Jiang, L., R. H. Worden, C. F. Cai, A. J. Shen, X. Y. He, and L. Y. Pan, 2018b, Contrasting diagenetic evolution patterns of platform margin limestones and dolostones in the Lower Triassic Feixianguan Formation, Sichuan Basin, China: Marine and Petroleum Geology, v. 92, p. 332–351, doi:10.1016/j.marpetgeo.2017.10.029.

Jiang, L., R. H. Worden, and C. Yang, 2018c, Thermochemical sulphate reduction can improve carbonate petroleum reservoir quality: Geochimica et Cosmochimica Acta, v. 223, p. 127–140, doi:10.1016/j.gca.2017.11.032.

Kerans, C., and W. M. Fitchen, 1995, Sequence hierarchy and facies architecture of a carbonate-ramp system: San Andres Formation of Algerita Escarpment and western Guadalupe Mountains, West Texas and New Mexico: Austin, Texas, The University of Texas at Austin, Bureau of Economic Geology, Report of Investigations 235, 89 p.

Kerans, C., F. J. Lucia, and R. K. Senger, 1994, Integrated characterization of carbonate ramp reservoirs using Permian San Andres Formation outcrop analogs: AAPG Bulletin, v. 78, no. 2, p. 181–216.

Koperna, G. J., L. S. Melzer, and V. A. Kuuskraa, 2006, Recovery of oil resources from the residual and transitional oil zones of the Permian Basin: Society of Petroleum Engineers Annual Technical Conference and Exhibition, San Antonio, Texas, September 24–27, 2006, SPE-102972-MS, 18 p.

Land, L. S., 1980, The isotopic and trace element geochemistry of dolomite: The state of the art, *in* D. H. Zenger, J. G. Dunham, and R. L. Ethington, eds., Concepts and models of dolomitization: Tulsa, Oklahoma, SEPM Special Publication 28, p. 87–110.

Leary, D. A., and J. N. Vogt, 1987, Diagenesis of Permian (Guadalupian) San Andres Formation, Central Basin Platform, west Texas, *in* D. G. Bebout and P. M. Harris, eds., Hydrocarbon reservoir studies, San Andres/Grayburg formations, Permian basin: Tulsa, Oklahoma, Permian Basin Section SEPM Publication 86-26, p. 67–68.

Lindsay, R. F., 2018, Hybrid model of dolomitization, Permian basin (abs.): AAPG Annual Convention and Exhibition, Salt Lake City, Utah, May 20–23, 2018, accessed December 16, 2021, https://www.searchanddiscovery.com/abstracts/html/2018/ace2018/abstracts/2843701.html.

Lloyd, R. M., 1966, Oxygen isotope enrichment of sea water by evaporation: Geochimica et Cosmochimica Acta, v. 30, no. 8, p. 801–814, doi:10.1016/0016-7037(66)90133-5.

Londry, K. L., and D. J. Des Marais, 2003, Stable carbon isotope fractionation by sulfate-reducing bacteria: Applied and Environmental Microbiology, v. 69, no. 5, p. 2942–2949, doi:10.1128/AEM.69.5.2942-2949.2003.

Loucks, R. G., F. J. Lucia, and L. E. Waite, 2013, Origin and description of the micropore network within the lower Cretaceous Stuart City Trend tight-gas limestone reservoir in Pawnee Field in South Texas: Austin, Texas, Gulf Coast Association of Geological Societies Journal, v. 2, p. 29–41.

Lucia, F. J., 1995, Rock-fabric/petrophysical classification of carbonate pore space for reservoir characterization: AAPG Bulletin, v. 79, no. 9, p. 1275–1300.

Lucia, F. J., C. Kerans, and F. P. Wang, 1995, Fluid-flow characterization of dolomitized carbonate-ramp reservoirs: San Andres Formation (Permian) of Seminole Field and Algerita Escarpment, Permian Basin, Texas and New Mexico, *in* E. L. Stoudt and P. M. Harris, eds., Hydrocarbon reservoir characterization: Geologic framework and flow unit modeling: Tulsa, Oklahoma, SEPM Short Course 34, p. 129–153.

Lucia, F. J., and R. G. Loucks, 2013, Micropores in carbonate mud: Early development and petrophysics: Austin, Texas, Gulf Coast Association of Geological Societies Journal, v. 2, p. 1–10.

Lucia, F. J., and S. C. Ruppel, 1996, Characterization of diagenetically altered carbonate reservoirs, South Cowden Grayburg reservoir, West Texas: Society of Petroleum Engineers Annual Technical Conference and Exhibition, Denver, Colorado, October 6–9, 1996, SPE-36650-MS, p. 883–893.

Machel, H. G., 2001, Bacterial and thermochemical sulfate reduction in diagenetic settings—Old and new insights: Sedimentary Geology, v. 140, no. 1–2, p. 143–175, doi:10.1016/S0037-0738(00)00176-7.

Machel, H. G., H. R. Krouse, and R. Sassen, 1995, Products and distinguishing criteria of bacterial and thermochemical sulfate reduction: Applied Geochemistry, v. 10, no. 4, p. 373–389, doi:10.1016/0883-2927(95)00008-8.

Major, R., and M. H. Holtz, 1990, Depositionally and diagenetically controlled reservoir heterogeneity at Jordan field: Journal of Petroleum Technology, v. 42, p. 1304–1309.

Mazzullo, S. J., and P. M. Harris, 1991, An overview of dissolution porosity development in the deep-burial environment, with examples from carbonate reservoirs in the Permian Basin, *in* M. P. Candellaria, ed., Permian Basin plays: Tomorrow's technology today: Midland, Texas, West Texas Geological Society Publication No. 91–89, p. 125–138.

Melim, L. E., P. S. Swart, and R. G. Maliva, 2001, Meteoric and marine-burial diagenesis in the subsurface of Great Bahama Bank, *in* R. N. Ginsburg, ed., Subsurface geology of a prograding carbonate platform margin, Great Bahama Bank: Results of the Bahamas Drilling Project: Tulsa, Oklahoma, SEPM Special Publication 70, p. 137–161.

Melzer, S., 2012, Residual oil zones in the Permian basin: Exploiting Mother Nature's waterfloods and rethinking the concept of transition zones: Research Partnership to Secure Energy for America Onshore Production Conference: Technological Keys to Enhance Production Operations, Midland, Texas, April 10, 2012, p. 13–20.

Phelps, R. M., and C. Kerans, 2007, Architectural characterization and three-dimensional modeling of a carbonate channel–levee complex: Permian San Andres Formation, Last Chance Canyon, New Mexico, U.S.A.: Journal of Sedimentary Research, v. 77, no. 11, p. 939–964, doi:10.2110/jsr.2007.085.

Phelps, R. M., C. Kerans, S. Z. Scott, X. Janson, and J. A. Bellian, 2008, Three-dimensional modelling and sequence stratigraphy of a carbonate ramp-to-shelf transition, Permian Upper San Andres Formation: Sedimentology, v. 55, no. 6, p. 1777–1813, doi:10.1111/j.1365-3091.2008.00967.x.

Ruppel, S. C., and H. S. Cander, 1988, Dolomitization of shallow-water platform carbonates by sea water and seawater derived brines San Andres Formation (Guadalupian), West Texas: Sedimentology and geochemistry of dolostones: Tulsa, Oklahoma, SEPM Special Publication 43, p. 245–262.

Ruppel, S. C., and R. H. Jones, 2006, Key role of outcrops and cores in carbonate reservoir characterization and modeling, Lower Permian Fullerton field, Permian basin, United States, *in* P. M. Harris and L. J. Weber, eds., Giant hydrocarbon reservoirs of the world: From rocks to reservoir characterization and modeling: AAPG Memoir 88, p. 355–394.

Saller, A. H., and J. A. D. Dickson, 2011, Partial dolomitization of a Pennsylvanian limestone buildup by hydrothermal fluids and its effect on reservoir quality and performance: AAPG Bulletin, v. 95, no. 10, p. 1745–1762, doi:10.1306/02141110117.

Saller, A. H., and N. Henderson, 1998, Distribution of porosity and permeability in platform dolomites: Insight from the Permian of west Texas: AAPG Bulletin, v. 82, no. 8, p. 1528–1550.

Saller, A. H., D. Pollitt, and J. Dickson, 2014, Diagenesis and porosity development in the First Eocene reservoir at the giant Wafra Field, Partitioned Zone, Saudi Arabia and Kuwait: AAPG Bulletin, v. 98, no. 6, p. 1185–1212, doi:10.1306/12021313040.

Saller, A. H., and A. M. Stueber, 2018, Evolution of formation waters in the Permian Basin, United States: Late Permian evaporated seawater to Neogene meteoric water: AAPG Bulletin, v. 102, no. 3, p. 401–428, doi:10.1306/0504171612517157.

Sarg, J. F., and P. J. Lehmann, 1986, Facies and stratigraphy of lower-upper San Andres shelf crest and outer shelf and lower Grayburg inner shelf: Midland, Texas, Permian Basin Section–SEPM Publication 86-25, p. 9–35.

Smith, L. B., 2006, Origin and reservoir characteristics of Upper Ordovician Trenton–Black River hydrothermal dolomite reservoirs in New York: AAPG Bulletin, v. 90, no. 11, p. 1691–1718, doi:10.1306/04260605078.

Trentham, R. C., L. S. Melzer, D. Vance, V. A. Kuuskraa, and R. Petrusak, 2015, Identifying and developing technology for enabling small producers to pursue the residual oil zone (ROZ) fairways in the Permian Basin San Andres: Houston, Texas, Research Partnership to Secure Energy for America, 504 p.

Vandeginste, V., R. Swennen, S. A. Gleeson, R. M. Ellam, K. Osadetz, and F. Roure, 2009, Thermochemical sulphate reduction in the Upper Devonian Cairn Formation of the Fairholme carbonate complex (South-West Alberta, Canadian Rockies): Evidence from fluid inclusions and isotopic data: Sedimentology, v. 56, no. 2, p. 439–460, doi:10.1111/j.1365-3091.2008.00978.x.

Wang, F. P., F. J. Lucia, and C. Kerans, 1998, Modeling dolomitized carbonate-ramp reservoirs: A case study of the Seminole San Andres unit—Part I, Petrophysical and geologic characterizations: Geophysics, v. 63, no. 6, p. 1866–1875, doi:10.1190/1.1444479.

Warren, J. K., 2000, Dolomite: Occurrence, evolution and economically important associations: Earth-Science Reviews, v. 52, no. 1–3, p. 1–81, doi:10.1016/S0012-8252(00)00022-2.

Wiggins, W. D., P. M. Harris, and R. C. Burruss, 1993, Geochemistry of post-uplift calcite in the Permian Basin of Texas and New Mexico: Geological Society of America Bulletin, v. 105, no. 6, p. 779–790, doi:10.1130/0016-7606(1993)105<0779:GOPUCI>2.3.CO;2.

Worden, R. H., P. C. Smalley, and N. H. Oxtoby, 1995, Gas souring by thermochemical sulfate reduction at 140°C: AAPG Bulletin, v. 79, no. 6, p. 854–863.

# Oil Saturation in Residual Oil Zones and Its Effect on $CO_2$ WAG Injection Strategies

Bo Ren, Frank Male, Yanyong Wang, Vinyet Baqués, Ian Duncan, and Larry Lake, The University of Texas at Austin

This paper was prepared for presentation at the SPE Annual Technical Conference and Exhibition held in Calgary, Alberta, Canada, 30 Sep - 2 October 2019.

## Abstract

The objectives of this work are to understand the characteristics of oil saturation in residual oil zones (ROZs) and to optimize water alternating gas (WAG) injection strategies. ROZs occur in the Permian Basin and elsewhere, and operators are using $CO_2$ injection for enhanced oil recovery (EOR) in these zones. ROZs are thought to be formed by the flushing effect of regional aquifer flow acting over geological time. Both the magnitude of oil saturation and the spatial distribution of oil differ from water-flooded main pay zones (MPZs).

We conducted flow simulations of $CO_2$ injection into both synthetic and realistic geologic reservoirs to find the optimal injection strategies for several scenarios. These simulations of $CO_2$ injection follow either man-made waterflooding or long-term natural waterflooding. We examined the effects of $CO_2$ injection rates, well patterns, reservoir heterogeneity, and permeability anisotropy on optimal WAG ratios. Optimal is defined as being at minimal net $CO_2$ utilization ratios or maximal oil production rates).

Simulations of $CO_2$ EOR show that the optimal WAG ratio for the ROZs is less than 1 (ratio of injected water and $CO_2$ in reservoir volumes), and it depends, but in qualitatively different ways, upon the well pattern and reservoir heterogeneity. The optimal WAG ratio tends to increase with changing from inverted 9-spot (80-acres) to inverted 5-spot (40-acre) or increasing reservoir heterogeneity. The ratios for ROZs are consistently less than those observed in the same geologic models experiencing $CO_2$ injection after traditional (man-made) waterflooding. This is because the water saturation caused by slow regional aquifer flow (~1ft/yr) differs from that created by traditional waterflooding. In ROZs, water prevails almost everywhere and thus it is less needed to ease $CO_2$ channeling as compared to MPZs.

This work demonstrates that optimal WAG ratios for oil production in ROZs are different from those in traditional MPZs because of oil saturation differences. Thus, commingled $CO_2$ injection into both zones or directly copying WAG injection designs from MPZs to ROZs might not optimize production.

## Introduction

A residual oil zone (ROZ) is an oil zone whose oil saturation is at close to residual oil saturation to waterflooding (Melzer, 2013; Koperna et al., 2006). It has been proposed that ROZs are formed from an original main pay zone (MPZ) that has been flushed by regional aquifers ("natural waterflooding" (NWF)) over geological time scales. This type of oil zone is widely distributed in the Permian basin, West Texas, USA (Koperna et al., 2006). ROZs have different types in terms of their origin and evolution. Harouaka et al. (2013) have classified ROZ occurrences into two types: (1) Brownfield ROZs that are located below the oil/water contact of MPZ reservoirs; (2) Greenfield ROZ that are not associated with MPZs. Melzer (2013) divided ROZ into three types (Type I, II and III) resulting from different mechanisms. This work is based on Type III, which is caused by the change in the hydrodynamic of the underlying aquifer. This results in regional groundwater flow and sweeps the lower portion of the oil column in main pay zones (Fig. 1).

**Figure 1—A schematic illustration of the evolution of the Type III ROZ reservoir. As time proceeds from (1) to (3), the bottom part of the original MPZ reservoir is flushed by natural aquifer water, and becomes a ROZ. The upper part of the reservoir is currently under production, so it is called 'producing MPZ'.**

Oil from ROZs can be produced from through $CO_2$ injection, but not from primary production or conventional, man-made waterflooding (MMWF). ROZs in carbonate reservoirs in the Permian Basin of West Texas were initially interpreted from wireline logs as being productive oil zones. However, if these zones were completed for production, they produced water, occasionally with minor oil production. Nevertheless, $CO_2$ injection can make these zones economic to produce, as demonstrated over the last decade in the Permian Basin (Rassenfoss, 2017). For example, Melzer (2013) reported that, by 2012, 13,000 barrels of oil per day were being produced from ROZ, with 6,500 barrels per day being produced from the ROZ in the Seminole San Andres Unit alone. The estimated recoverable oil from the ROZ in both the San Andres and Canyon Reef formations of Permian Basin are estimated by Koperna et al. (2016) to be 12 billion barrels.

By implementing $CO_2$ injection in brownfield ROZs, oil field operators can achieve three goals: extend the life of old oilfields, access extra oil cheaply through repurposing old infrastructures, and storing $CO_2$ in oil reservoirs for climate consideration. As a result, ROZs in the Permian basin and elsewhere have become attractive targets for $CO_2$-EOR and storage.

The mechanisms behind $CO_2$ EOR are well-understood (Lake et al. 2014). They mainly include oil swelling (causing viscosity reduction), $CO_2$/oil interfacial tension reduction, and development of miscibility. Although $CO_2$ EOR has been applied in the oil industry for over 50 years, this technique has targeted main pay zone reservoirs (as secondary or, more commonly, tertiary recovery methods). In this context, many studies have been conducted to understand the effect of heterogeneity and injection strategies on the performance of $CO_2$ EOR (e.g. Ambrose et al., 2007; Bermudez et al., 2007; Bunge and Radke, 1982; Chang et al. 1994; Kulkarni and Rao, 2005; Malik and Islam 2000; Song et al., 2014; Zuo et al., 2014) and to optimize $CO_2$ WAG injection (e.g., Chen et al., 2010; Chen and Reynolds, 2016; Ettehadtavakko et al. 2014;

Nwachukwu et al. 2018; Shehata et al. 2012). One of the main focus of these WAG injection studies is to find optimal WAG ratios (maximal oil production).

The WAG ratio is an important parameter for WAG injection. The WAG ratio is defined as the cumulative volume of water injected divided by the gas injected into reservoirs. High WAG ratios causes the effect of water film blocking (Stalkup, 1970). This leads to oil trapping, and WAG injection performs like waterflooding. Whereas, for small WAG ratios, injected $CO_2$ tends to easily breakthrough or channel, hence compromising oil production rates. Thus, an optimal WAG ratio exists that yields the maximum oil production rates or recovery factors (Afzali et al., 2018; Wu et al. 2004; Rogers and Grigg 2001; Stalkup, 1970).

All the above studies are focused on $CO_2$ injection into MPZs, rather than ROZs. While the controlling physics of $CO_2$-EOR should be the same, the specific characteristics of ROZs will influence the effectiveness of $CO_2$ WAG injection, given the oil saturation difference between ROZs and MPZs after MMWF. This difference would influence the interaction of $CO_2$ and in-situ fluids, which impacts overall sweep and displacement efficiencies. Thus, to maximize the effectiveness of $CO_2$ WAG injection, different strategies should be used.

The main objective of this study is to understand how the optimal $CO_2$ WAG injection scheme is affected by the differences in oil saturation between a ROZ and a MPZ (after MMWF). This understanding will help answer questions like: are the optimal WAG ratios for MPZs still applicable for ROZs? Or, can WAG be used on both the ROZ and MPZ of a pattern at the same time? To accomplish the objective, we conduct systematic flow simulation of the processes of NWF (to generate ROZs), MMWF, and $CO_2$ WAG injection. These simulations were run on both synthetic and realistic geological models. The synthetic models were realized with controlled heterogeneity and well patterns; this enabled us to clearly see how both heterogeneity and pattern geometries impact oil saturation distributions (after NWF and MMWF) and thus $CO_2$ WAG ratios. The overall work provides a general approach for studying ROZs and MPZs when $CO_2$ EOR is considered for both zones.

## Theory and Approach

The work flow chart is in Fig. 2. All simulated cases started from geological models. We built both synthetic and realistic geological models in these simulations. After this step, we conducted flow simulation of both NWF and MMWF. Subsequently, $CO_2$ injection was started at the end of NWF or MMWF to evaluate $CO_2$-EOR performance and find optimal WAG ratios. The Eclipse reservoir flow simulator (Eclipse, 2016) is used in this study. The details of each step are given below.

Figure 2—Work flow chart of each simulated case.

## Generation of Geological Models

***Synthetic Geological Models.*** We generated a series of statistical realizations of permeability fields using sequential gaussion simulation (Remy et al., 2009). The properties of these fields were listed in Table 1. Both inverted 5- and 9-spot well patterns were considered. The permeability fields have different horizontal auto-correlation lengths ($\lambda_x$), and we made the length dimensionless following the work of Li and Lake (1995). Dimensionless horizontal autocorrelation length ($\lambda_{Dx}$) is defined as the ratio of $\lambda_x$ over the domain width in the corresponding directions. $\lambda_x$ indicates how close or how far the permeability is spatially correlated, which is mainly controlled by sedimentary environments and processes. The typical value of $\lambda_{Dx}$ is 2. Three realizations of the permeability field ($\lambda_{Dx}$ =2, inverted 5-spot) are generated to test the effect on simulation results. Layered geological models are also considered through generating the realization of permeability fields with $\lambda_{Dx}$ equal to 100. The permeability anisotropy ($k_v/k_h$) is varied through decreasing $k_v$ while keeping $k_h$ unchanged: 0.001, 0.01, and 0.1. The horizontal permeability ($k_h$) field were statistically realized with different log standard deviations: 0, 1, 2. The corresponding values of the Dykstra-Parsons coefficient are 0, 0.62, 0.85 (with increasing heterogeneity).

Table 1—Properties of synthesized permeability fields.

| Well pattern | Inverted 5-spot | Inverted 9-spot |
|---|---|---|
| Patter size, acre | 40 | 80 |
| Synthetic domain sizes, ft | 1320×1320×96 | 1860×1860×96 |
| Model cell sizes, ft | 30×30×3 | 30×30×3 |
| Model dimensions | 44×44×32 | 62×62×32 |
| Permeability horizontal dimensionless auto-correlation length, $\lambda_{Dx}$ | 0, 2*, 100 | |
| Horizontal permeability log mean, $\mu_{lnk}$ | 5* | |
| Horizontal permeability log standard deviation, $\sigma_{lnk}$ | 0, 1*, 2 | |
| Horizontal permeability Dykstra-Parsons coefficient, $V_{DP}$ | 0, 0.62*, 0.85 | |

*means base case settings

Then, using the Holtz's (2002) porosity-permeability correlation (refer to Eq. 1), we calculated the porosity fields corresponding to the generated permeability fields. In Eq. 1, the units of permeability is mD. The Holtz correlation might be applicable for rock types between the lithofacies packstone and mudstone. As one realizes that the Holtz's correlation does not consider the facies-dependent permeability-porosity characteristic in geological modeling, we considered this in the following realistic geological models.

$$\phi = \left(\frac{k}{7E+7}\right)^{1/9.61} \tag{1}$$

***Realistic Geological Models.*** A realistic geologic model, representing the San Andres residual oil zone, has been built by Ren and Duncan (2019a). The ROZ reservoir is deposited in a carbonate ramp environment on the margin of the Central Basin platform. It consists of carbonates with some evaporite intercalations that developed carbonate-ramp reservoirs during the lower San Andres Formation (early Guadalupian, Middle Permian). Based on the integration of core- and wireline-log data coupled with petrographic analyses, five major depositional environments (lithofacies) with eight carbonate microfacies are identified. The enviroment ranges from intertidale to open marine, with the principle lithofacies including dolowackstone, dolopackstone, and dolograinstone (Sonnenfeld et al., 2003). Common diagenetic effects include dolomite and anhydrite replacement and cementation, silica and pyrite mineralization, and dissolution. The most common pore types include interparticle, moldic, and connected vugs.

All these sedimentary events and lithofacies characteristics created the heterogeneity in permeability and porosity observed today. The porosity field is generated through sequential Gaussian simulation, and then the permeability field is calculated using Lucia's rock typing method (Lucia 2007). The effect of natural fractures on permeability is considered through incorporating the whole-core permeability- porosity correlation. The detailed incorporation procedures are elaborated in the publication by Ren and Duncan (2019a).

From the full-field geologic model, we cut out two sector models: sector #1 represents an inverted 5-spot 40-acre pattern, and sector #2 is an inverted 9-spot 80-acre pattern. The areal sizes of the cells in these models are 100×100 ft with a cell thickness of around 2ft. The petrophysical properties of the two sector models are listed in Table 2. Fig. 3 shows the permeability field for the sector #1.

**Figure 3—High-resolution horizontal permeability field for the sector #1 inverted 5-spot well pattern.**

**Table 2—Statistics of petrophysical properties of the two sector models.**

| Petrophysical property | Sector #1, inverted 5-spot | Sector #2, inverted 9-spot |
|---|---|---|
| Permeability log mean, $\mu_{lnk}$ | 1.17 | 1.87 |
| Permeability log standard deviation, $\sigma_{lnk}$ | 1.05 | 1.48 |
| Permeability anisotropy ($k_v/k_h$) | 0.1 | 0.1 |
| Porosity arithmetic mean, $\mu_\phi$ | 0.10 | 0.12 |
| Porosity standard deviation, $\sigma_\phi$ | 0.03 | 0.04 |

After generating permeability and porosity fields, the corresponding capillary entry pressure fields were calculated using the Leverett j-function (Leverett, 1941), through following the procedures detailed by Ren (2017). The reason for considering capillary entry pressure heterogeneity in simulations is the small regional aquifer flux during ROZ formation. The typical size of aquifer flux during NWF within the Permian Basin is around 10-15 cm/yr (0.33-0.83 ft/d, Trentham (2012)), which is much less than that (1ft/day) of MMWF. Such small flux pronounces the effect of capillary pressure heterogeneity on fluid migration and oil saturations at the end of NWF, as demonstrated in the work by Ren and Duncan (2019b). Thus, capillary pressure heterogeneity was considered in this work, and the implementation procedures are given in the following Section of Rock/Fluid Interaction Models.

## Flow Simulation of NWF and MMWF

***Rock/Fluid Interaction Models.*** We assume the oil phase properties for the ROZ and MPZ are the same, so we use one set of PVT equations for both. The oil properties are adopted from the publication of Honarpour et al. (2010), whose analysis is based on the Seminole San Andres ROZ oil samples. A black oil model is built for the flow modeling of both NWF and MMWF. At the reservoir condition (2119.9 psi and 104 °F), the oil density is 657.71 kg/m$^3$, and the oil viscosity is 1.21 cp. The gas oil ratio (GOR) is 688.15 scf/bbl.

When simulating $CO_2$ WAG injection, we employ a compositional model with the oil compositions shown in Table 3. The Peng Robinson equation of state (PR EOS) is used with the parameter settings in Table 3. The binary interaction coefficients are listed in Table 4. The minimum miscibility pressure for the $CO_2$/oil mixture is around 1400 psi (Honarpour et al. 2010), and the $CO_2$ flooding is set be miscible in simulations.

**Table 3—Crude oil compositions representative of the Seminole San Andres ROZ and the parameter settings for PR EOS (modified from Honarpour et al. (2010) and Jamali and Ettehadtavakkol (2017)).**

| Component | $CO_2$ | $C_1N_2$ | $C_2C_3H_2S$ | $C_4$-$C_6$ | $C_7$-$C_{10}$ | $C_{11}$-$C_{16}$ | $C_{17+}$ |
|---|---|---|---|---|---|---|---|
| Mole fraction, % | 0.02 | 20.14 | 15.9 | 8.99 | 17.29 | 18.42 | 19.24 |
| Critical temperature (R) | 547.56 | 339.21 | 619.38 | 835.43 | 1117.84 | 1344.62 | 1686.57 |
| Critical pressure (psi) | 1071.34 | 666.77 | 722.56 | 491.3 | 389.65 | 277.42 | 159.29 |
| Critical volume (ft$^3$/lb-mole) | 1.51 | 1.56 | 2.71 | 5.02 | 7.73 | 12.13 | 22.15 |
| Critical Z-factor | 0.275 | 0.287 | 0.295 | 0.275 | 0.251 | 0.233 | 0.195 |
| Molecular weights (g/mol) | 44.01 | 16.29 | 36.19 | 70.06 | 114.17 | 180.94 | 358.25 |
| Acentric Factor | 0.225 | 0.0139 | 0.125 | 0.245 | 0.383 | 0.582 | 1.0054 |
| Coefficient $\Omega_a$ | 0.45724 | 0.45724 | 0.45724 | 0.45724 | 0.45724 | 0.45724 | 0.45724 |
| Coefficient $\Omega_b$ | 0.0778 | 0.0778 | 0.0778 | 0.0778 | 0.0778 | 0.0778 | 0.0778 |

**Table 4—Settings of binary interaction coefficients.**

| Component | $CO_2$ | $C_1N_2$ | $C_2C_3H_2S$ | $C_4$-$C_6$ | $C_7$-$C_{10}$ | $C_{11}$-$C_{16}$ | $C_{17+}$ |
|---|---|---|---|---|---|---|---|
| $CO_2$ | 0 | | | | | | |
| $C_1N_2$ | 0.0976 | 0 | | | | | |
| $C_2C_3H_2S$ | 0.1289 | 0.0103 | 0 | | | | |
| $C_4$-$C_6$ | 0.1271 | 0.0019 | 0.0063 | 0 | | | |

| Component | $CO_2$ | $C_1N_2$ | $C_2C_3H_2S$ | $C_4$-$C_6$ | $C_7$-$C_{10}$ | $C_{11}$-$C_{16}$ | $C_{17+}$ |
|---|---|---|---|---|---|---|---|
| $C_7$-$C_{10}$ | 0.1105 | 0.0241 | 0.0196 | 0.003 | 0 | | |
| $C_{11}$-$C_{16}$ | 0.0943 | 0.0494 | 0.0333 | 0.0061 | 0 | 0 | |
| $C_{17+}$ | 0.0997 | 0.1365 | 0.0588 | 0.012 | 0 | 0 | 0 |

We assume the relative permeability and capillary pressure curves (shown in Figs. 4a and 4b) are the same for the two processes of NWF and MMWF for simplicity. Only drainage curves are considered in the flow simulations. As mentioned above, the effect of capillary pressure heterogeneity on water/oil flow was considered in the simulation of NWF. To capture this effect, the capillary pressure curve in Fig. 4b was assigned to the cells with the arithmetic mean of the permeability of a given field, the corresponding capillary pressure curves for other cells were scaled using the Leverett j-function (Ren and Duncan 2019b). For the flow simulation of $CO_2$ WAG injection, the relative permeability curves of gas/oil (Figs. 4a and 4c) are used. The Stone I model (Stone, 1970) is adopted to describe the oil relative permeability during 3-phase flow. The hysteresis in both the relative permeability and capillary pressure curves are omitted for computational efficiency. Both hysteresis and relative permeability has been experimentally shown to be cycle-dependent (Egermann et al., 2000; Element et al., 2003; Skauge and Sorbie, 2014). We believe that considering these cycle-depdent properties will not alter the observations of optimal WAG ratio positions, although they have been shown to cause the difference in oil production rate prediction (Spiteri and Juanes, 2006; Zuo et al., 2014).

**Figure 4—(a) Water/oil relative permeability curves (b) capillary pressure curve for water/oil (c) gas/oil relative permeability curves.**

***Injection/Production Schemes.*** To simulate the NWF process, a line drive geometry was used (Fig. 5a): water injectors are put into every left boundary cell, and producers are put into every right boundary cell.

This uniformly-distributed inlet and outlet conditions are to mimic regional aquifer flow, which has been demonstrated to be physically-applicable in reproducing ROZs (Ren and Duncan 2019b). The inlet water flux is set to be 0.5 ft/yr (15.24 cm/yr). With the inlet flux, the water injection rate is calculated to be 0.0368 rb/day (reservoir bbl/day).

**Figure 5—Illustration of NWF, MMWF, and $CO_2$ WAG simulation setup. The embedded tables on the right column show the corresponding simulation settings for each flow simulation process.**

For MMWF, both the inverted 5-spot 40-acre pattern (Fig. 5b) and inverted 9-spot 80-acre pattern are considered. The middle table in the figure shows the simulation parameter settings for both types of patterns.

For $CO_2$ WAG injection (Fig. 5c), the flow simulation parameters are listed in the lower table of the Fig. 5. The $CO_2$ injection rate is set to be constant at 3000 Mscf/day; varing rates has no effect on optimal WAG ratios although it changes oil production rates (Ren and Duncan, 2019a). The $CO_2$ half-cycle size is 2.5% hydrocarbon pore volume (HCPV), based on the balance of good oil production and the operationability of WAG cycle switches (Ettehadtavakko, 2013; Ren and Duncan, 2019a). The HCPV is calculated at the end of NWF or MMWF. WAG ratio is varied from 0 to 5, through changing water injection duration while keeping $CO_2$ injection duration unchanged in each WAG cycle (see Appendix A for detailed illustration).

The other parameters of the flow simulation of NWF, MMWF and $CO_2$ WAG are all included in Fig. 5. The boundaries of all simulation domains are closed (no flow). All the injectors and producers involved in simulations are vertical, and their perforation is complete (along the depth range of the simulation model).

Additionally, to specifically examine the effect of oil saturation magnitudes on WAG ratios, we manually assign uniform oil saturation ($S_{or}$) to geological models at the beginning of WAG injection. We consider several magnitudes of $S_{or}$: 0.3, 0.35, 0.4, and 0.5. They cover the range of oil saturation magnitudes observed for the virgin ROZ in the Permian Basin (Harouaka et al., 2013; Ren and Duncan, 2019b).

***Metrics of $CO_2$ EOR Performance.*** We report how varying WAG ratios influences the following $CO_2$ EOR performance metrics: net $CO_2$ utilization ratio, averaged oil production rate, and oil recovery factor. Their definitions are:

Net $CO_2$ utilization ratio = (Total $CO_2$ injected-Total $CO_2$ produced) / total oil produced.

Averaged oil production rate = Total oil produced / injection duration/number of oil producers.

Oil recovery factor = cumulative oil produced during $CO_2$ injection / oil in place at the end of MMWF and NWF.

The metric of net $CO_2$ utilization ratio indicates the net use of $CO_2$ to produce 1 bbl of oil. It measures the cost-effectiveness of $CO_2$ injection for enhanced oil recovery (the biggest cost of implementing WAG floods is getting $CO_2$).

## Results

### Results from Synthetic Geological Models

***Oil Saturation Magnitudes and Patterns after MMWF vs. after NWF.*** After 30 years of MMWF, water has swept most of the oil in the bottom part of the reservoir, and the remaining oil is mainly in the upper portion (Figs. 6a and 6c). Correspondingly, the arithmetic mean of remaining oil saturation is around 0.5. However, after $10^6$ years of NWF, the oil saturations for most of the cells of the reservoir have almost reached the end point of relative permeability, and the saturation magnitudes are around 0.35 (Figs. 6e–6h); small rates (large capillary pressure) tend to cancel the effect of reservoir heterogeneity in sweep. For NWF, the distribution of remaining oil saturation is much narrower than that for MMWF. Additionally, heterogeneity always causes much more oil unrecovered than homogeneity does, irrespective of NWF or MMWF.

**Figure 6—Oil saturation fields and oil saturation histograms at the end of MMWF (a-d) and at the end of NWF (e-h). For the heterogeneous geological model used, $V_{DP}$ = 0.62, $\lambda_{Dx}$ = 2. Inverted 5-spot patterns were used.**

***Cumulative Oil Recovery Factors during WAG after NWF vs. after MMWF.*** Generally, the recovery factors are larger for the WAG after MMWF than for the WAG after NWF (Fig. 7a vs. 7b). This is because the oil left in the upper part of the reservoir after MMWF (refer to Figs. 6a and 6c) is effectively swept by the less dense $CO_2$ (compared to oil and water). This gives rise to the better oil recovery factors. Additionally, heterogeneity decreases the ultimate oil recovery efficiencies, but it yields a rapid increase of oil recovery at the beginning of WAG injection.

Well patterns influence oil recovery efficiencies in the studied ranges of PV (Fig. 7). The inverted 9- spot pattern yields a larger recovery factor than the inverted 5-spot does at small pore volume (PV) of injected $CO_2$. This would be due to the larger producer-injector ratio for the former pattern.

**Figure 7—Cumulative oil recovery factor during $CO_2$ WAG injection after MMWF vs. after NWF. For the heterogeneous geological model used, $V_{DP}$ = 0.62, $\lambda_{Dx}$ = 2. The ultimately-injected $CO_2$ PV for the inverted 9-spot is about half of that for the inverted 5-spot, due to both the pattern coverage area difference and the same WAG injection duration.**

***$CO_2$ Net Utilization Ratios.*** The $CO_2$ net utilization ratios for the WAG after NWF are much larger than those for the WAG after MMWF (Fig. 8a vs. 8b). The latter ratios are in the range of 2-10 MScf/Stb, and the former can be as high as 35 MScf/Stb. Such large differences are mainly due to the magnitudes of initial oil saturation at the beginning of WAG injection.

**Figure 8—$CO_2$ net utilization ratios, averaged oil production rates, and oil recovery factors for the inverted 5-spot (40 acre) and inverted 9-spot (80 acre) well patterns. $CO_2$ WAG injection is simulated following the processes of NWF or MMWF. For the heterogeneous geological model used, $V_{DP}$ = 0.62, $\lambda_{Dx}$ = 2. A WAG ratio of 0 means continuous $CO_2$ injection.**

The utilization ratios for both types of WAG (after NWF versus after MMWF) are dependent of the injected WAG ratios, reservoir heterogeneity, and well patterns, but with different trends and extents (Figs. 8a and 8b). For the WAG after NWF, there is an optimal WAG ratio that yields the lowest net utilization ratios, irrespective of the well pattern. The optimal ratio is around 1. However, for WAG after MMWF, the net utilization ratio monotonically decreases with the WAG ratio. The different trend is noteworthy, and we specifically analyze the reason in the following section of "Effect of oil saturation magnitudes on optimal WAG ratios".

Reservoir heterogeneity does not alter these trends, but it leads to different net utilization ratios (Figs. 8a and 8b). Heterogeneity acts on net utilization ratios in different ways for the WAG after NWF versus the WAG after MMWF: heterogeneity leads to larger utilization ratios than homogeneity does for the WAG after NWF, but this is not the case for WAG after MMWF. WAG ratio is a complicated metric that includes both the net amount of $CO_2$ left in reservoirs and the amount of oil produced. Simulated production data indicates that heterogeneity for the WAG after NWF causes the $CO_2$ production increasing effect to be less than the oil production decreasing effect. This gives rise to the higher net utilization ratio for the heterogeneous model than for the homogeneous model.

Well patterns do not alter the above qualitative observations, except that the net utilization ratios for the inverted 9-spot pattern are overall larger than those for the inverted 5-spot. Therefore, using inverted 5-spot patterns can improve the effectiveness of WAG injection to enhance oil recovery. Similar observations of the effect of well patterns on these metrics are made in the layered geological models (see Appendix B).

***Averaged Oil Production Rates and Oil Recovery Factors.*** The averaged oil production rates for the WAG after MMWF are always better than those for the WAG after NWF (about one time higher) (Fig. 8c vs. 8d). The average rates are always negatively impacted by increasing WAG ratios for the $CO_2$ after NWF, whereas, for the WAG after MMWF, heterogeneity necessitates a small WAG ratio (0.25-0.5) to achieve the optimal oil production rates.

The optimal WAG ratios (at maximal oil production rates) are less for virgin ROZs than for the MPZs after MMWF when considering heterogeneous models (Fig. 8c vs. 8d). This is because the $CO_2$ WAG into virgin ROZs starts with high water saturation. Most of the injected $CO_2$ displaces water rather than oil. Thus, water injection during WAG has little effect. However, for the MPZ after MMWF, the zone is relatively rich in oil. Most of the injected $CO_2$ displaces oil, and $CO_2$ tends to break through early because of the mobility ratio contrast between $CO_2$ and oil. Under this condition, the injected water during WAG cycles can divert $CO_2$ and thus improve sweep efficiency. The high water saturation in virgin ROZs attenuates the need for water injection during WAG.

The oil production rate (Stbd/Well) tends to be more heavily impacted by WAG injection for the homogeneous models than for the heterogeneous ones (Fig. 8c vs. 8d). The average oil production rate for the two models crosses at a WAG ratio around 0.5. WAG injection is much more effective for heterogeneous models than for homogenous ones to improve oil production rates.

As the pattern changes from inverted 5-spot to inverted 9-spot, the average oil production rate decreases, as does the oil recovery factor. The oil recovery factor trend versus WAG ratio is very similar to the above trend for the oil production rate versus WAG ratio (Figs. 8e and 8f). This makes sense because the amount of oil in place after NWF and MMWF is similar.

***Effect of Oil Saturation Magnitudes (Sor) on Optimal WAG Ratios.*** As shown in Figs. 6e–6h, the spatial distribution of remaining oil saturation after NWF is almost uniform. This suggests an easy way of generating ROZs: directly assigning a uniform initial oil saturation ($S_{or}$) to create virgin ROZs. Fig. 9 shows the metrics of net utilization ratios and averaged oil production during WAG injection with the different $S_{or}$ for both inverted 5-spot and inverted 9-spot well patterns.

**Figure 9—$CO_2$ net utilization ratios and averaged oil production rates for the inverted 5-spot pattern (a and b) and for the inverted 9- spot pattern (c and d). The initial oil saturation ($S_{or}$) at the beginning of $CO_2$ WAG injection is manually set to be constant. For the heterogeneous geological model used, $V_{DP}$ = 0.85, $\lambda_{Dx}$ = 2. The stars indicate the inflection or optimal points in the curves.**

Initial oil saturations control the curve trend of the net utilization ratio versus the WAG ratio (Fig. 9a and Fig. 9c). At a low $S_{or}$, there is an optimal WAG ratio (minimal net utilization ratio). However, when $S_{or}$ increases to 0.5, the net utilization ratio becomes almost flat as the WAG ratio increases. The approximate inflection point (labelled by a star) moves to the right as the $S_{or}$ increases. This means small $S_{or}$ yields small optimal WAG ratios. This supports our previous analysis that small oil saturation in virgin ROZs decreases the use of water during WAG cycles (i.e., decreasing WAG ratio).

For averaged oil production rates (Fig. 9b and Fig. 9d), the point of optimal return tends to move to a higher WAG ratio as $S_{or}$ increases. In other words, larger $S_{or}$ necessities larger WAG ratios to achieve the best oil production performance. This observation is consistent with that how net utilization ratios are impacted by $S_{or}$.

Well patterns slightly influence optimal WAG ratios (Fig. 9a vs. Fig. 9c and Fig. 9b vs. Fig. 9d). As the well pattern changes from inverted 5-spot to inverted 9-spot, the optimal WAG ratio (either at minimal net utilization ratio or at maximal oil production rates) decreases marginally. The average large injector-producer distance for the inverted 9-spot pattern might need less water to ease $CO_2$ breakthrough. This gives rise to the small optimal WAG ratios.

***Effect of Permeability Anisotropies (kv/kh) on Optimal WAG Ratios for ROZs.*** Increasing permeability anisotropy (the ratio of $k_v/k_h$) improves $CO_2$ net utilization efficiency (Fig. 10a) for ROZs. The net utilization ratio is dropped from about 20 to 10 Mscf/stb when $k_v/k_h$ increases from 0.01 to 1, given a WAG ratio of 1. Large $k_v$ favors $CO_2$ production more than oil production. That is the reason that the $CO_2$ net utilization ratios for the case of $k_v/k_h$ =1 are the smallest, even though the corresponding oil production rate rapidly decreases with the increase in the WAG ratio. Adjusting $k_v/k_h$ has a similar effect on oil production rates (Fig. 10b) as adjusting reservoir heterogeneity (Figs. 8c–8f): oil production decreases as WAG ratio increase.

**Figure 10—$CO_2$ net utilization ratios and averaged oil production rates for the synthetic geological model with different permeability anisotropies. Inverted 5-spot patterns are used. The initial oil saturation ($S_{or}$) at the beginning of $CO_2$ WAG injection is manually set to be constant (0.35). For the heterogeneous geological model used, $V_{DP}$ = 0.62, and $\lambda_{Dx}$ = 2.**

Also, the ratio of $k_v/k_h$ increases the optimal WAG ratio (at the minimal net utilization ratio) (Fig. 10a). Large $k_v$ necessities more water injection to divert injected $CO_2$, and thus $CO_2$ can better sweep the reservoir. This large $k_v$, within the context of structural geology, might be due to vertical fractures. Some vertical fractures have been observed in the cores of the Seminole San Andres ROZ (Duncan, unpublished data). In this sense, the heterogeneity associated vertical natural fractures should be carefully characterized as they have a significant effect on $CO_2$ net utilization ratios.

## Results from Realistic Geological Models

Results (Fig. 11) from the realistic geological models are consistent with the results from synthetic models. The general observations of both the net utilization ratio and oil recovery factor versus the WAG ratio are similar. For instance, the optimal WAG ratios (maximum oil recovery factor, labelled by stars in Fig. 11) are larger for WAG after MMWF than after NWF. This strengthens our key finding that the injected water during WAG cycles for ROZs should be minimized for the EOR purpose.

**Figure 11—$CO_2$ net utilization ratios, averaged oil production rates, and oil recovery factors based on the realistic geological models. Both the inverted 5-spot and inverted 9-spot patterns are considered. $CO_2$ WAG injection is simulated following the processes of NWF or MMWF.**

## Discussion

One of the key findings from the flow simulations is that the optimal WAG ratios for the WAG after NWF is smaller than those for the WAG after MMWF. This has implications in the design of $CO_2$ injection projects. When an operator prepares to target Greenfield ROZs for $CO_2$ flooding, they might benefit from starting the ROZ flood with a very small WAG ratio, less than the typical WAG ratio (=1) used in most of current oilfields (Christensen et al., 2001). For Brownfields, ROZs are hydraulically associated with MPZs. Since optimal WAG ratios for the two different zones are different, additional characterization and simulations need to be conducted to choose the WAG ratio when considering WAG injection into the ROZ. One should not simply deepen wells targeting the MPZ and continue injecting at the same WAG ratio. Instead, WAG injection might be started in the MPZ followed by the ROZ with the optimal WAG ratio specific to each zone. When switching to the ROZ, the commingled production of both zones can be adopted because the injected $CO_2$ into the ROZ might move into the MPZ and help produce oil. Determining the optimal switching time merits further study.

These flow simulations consider the geological heterogeneity variations that essentially control the sweep efficiency of $CO_2$ during WAG injection. In this sense, the optimal WAG ratios should lead to the maximum sweep efficiencies. To examine this point, the analysis method proposed by Walsh and Lake (1989), based on the fractional flow theory, can be adopted to find the optimal WAG ratios in terms of maximizing $CO_2$ displacement efficiency.

The results from flow simulations contain several simplifications. First, inclined producing oil/water contacts, as observed in fields (Honarpour et al., 2010), are not considered in the study. This contact is the oil saturation transition from a MPZ to a ROZ. Considering this contact might have some effects on optimal WAG ratios since such a contact is an oil saturation change. Second, this study assumes the same oil phase properties for both ROZs and MPZs. The experimental characterization of oil samples by Aleidan et al. (2017) demonstrates that the global compositions and overall quality for the both zones are very similar. But, Honarpour et al. (2010) showed that the oil API gravity is different from each other. Further studies are needed to investigate how significant phase property differences would influence the optimal WAG ratios. Third, the optimal WAG ratios are determined based on the $CO_2$ utilization ratios or oil production rates averaged over 20 year of WAG injection (refer to Fig. 5). Since the oil production response varies significantly with time, changing the WAG duration would give different optimal WAG ratios. However, the relative magnitudes of the optimal WAG ratios for ROZs vs. MPZs will not be altered.

Discrepancy of $CO_2$ EOR metrics between realistic and synthetic geological models occur. The magnitudes of net utilization ratios and oil recover factors are different from those for the synthetic models (Fig. 11 vs. Fig. 8), which should be caused by the different petrophysical properties and model thickness of the two types of geological models (Table 1 vs. Table 2). Also, the heterogeneity of the real geological model for the inverted 5-spot is different from that for the inverted 9-spot (refer to Table 2), the effect of well patterns on net utilization ratios and oil recovery factors becomes complicated, so we omit the relevant analysis.

## Conclusions

Understanding the characteristics of oil saturation in residual oil zones (ROZs) and its difference from the remaining oil saturation in main pay zones (MPZs) after man-made waterflooding (MMWF) is essential in both evaluating oil potentials and designing injection strategies of $CO_2$ water alternating gas (WAG) in stacked MPZ and ROZ reservoirs. This work investigated the effect of oil saturation on both $CO_2$ net utilization ratios and oil recovery performance for both synthetic and realistic geological models. Several conclusions can be drawn based on this work:

- After long-term natural waterflooding, the oil saturations in most of the simulation cells are reduced to or close to residual levels.
- Optimal WAG ratios (either at the minimal net utilization ratios or at the maximal averaged oil production rates) for virgin ROZs are consistently smaller than those for MPZs after MMWF. This is essentially because of the prevalent high water saturation (and low oil saturation) in the ROZs.
- The optimal WAG ratio (at the minimal net utilization ratio) increases when i) increasing initial oil saturation (before WAG) ii) the reservoir permeability anisotropy decreases (i.e., the ratio of $k_v/k_h$ increases) iii) the well pattern changes from inverted 9-spot to inverted 5-spot.
- The $CO_2$ net utilization ratios during $CO_2$ WAG injection for virgin ROZs are about 2-3 times larger than those for MPZs after MMWF. The ratios depend on well patterns, reservoir heterogeneity, and WAG ratios.
- Both averaged oil production rates and oil recovery factors for the WAG in virgin ROZs are around ¼-¾ of those for the WAG in the MPZs after MMWF.

## Acknowledgements

This study is part of a long term project investigating ROZ reservoirs in the Permian Basin of Texas being carried out by the Bureau of Economic Geology's (BEG's) State of Texas Advanced Resource Recovery (STARR) Program and funded in part by a US Department of Energy contract under DOE Award

Number FE0024375. Larry W. Lake holds the Shahid and Sharon Ullah Endowed Chair in the Hildebrand Department of Petroleum and Geosystems Engineering at The University of Texas at Austin.

# Nomenclature

## Roman Symbols

| | |
|---|---|
| $k$ | Permeability, mD |
| $k_h$ | Horiozontal permeability, mD |
| $k_v$ | Vertical permeability, mD |
| $S_{or}$ | Initial oil saturation before WAG injection |
| $V_{DP}$ | Dykstra-Parson coefficient |

## Greek Symbols

| | |
|---|---|
| $\lambda_x$ | Horizontal autocorrelation length, ft |
| $\lambda_{Dx}$ | Dimensionless horizontal autocorrelation length |
| $lnk$ | Horizontal permeability log mean, mD |
| $\sigma_{lnk}$ | Horizontal permeability log standard deviation, mD |
| $\phi$ | Porosity, fraction |

## Acronyms

| | |
|---|---|
| EOR | Enhanced Oil Rcovery |
| HCPV | Hydrocarbon Pore Volume |
| PR EOS | Peng Robinson Equation of State |
| GOR | Gas Oil Ratio |
| MPZ | Main Pay Zone |
| MMWF | Man-made Waterflooding |
| NWF | Natural Waterflooding |
| ROZ | Residual Oil Zone |
| WAG | Water Alternating Gas |

## References

Afzali, S., Rezaei, N. and Zendehboudi, S. 2018. A Comprehensive Review on Enhanced Oil Recovery by Water Alternating Gas (WAG) Injection. *Fuel*. **227**, 218–246. https://doi.org/10.1016Zi.fuel.2018.04.015

Aleidan, A., Kwak, H., Muller, H., Zhou, X. 2017. Residual-Oil Zone: Paleo-Oil Characterization and Fundamental Analysis. *SPE Reservoir Evaluation & Engineering*, **20**(02), 260–268. https://doi.org/10.2118/179545-PA

Ambrose, W.A., Lakshminarasimhan, S., Holtz, M.H., Nunez-Lopez, V., Hovorka, S.D., Duncan, I. 2007. Geologic Factors Controlling $CO_2$ Storage Capacity and Permanence: Case Studies Based on Experience with Heterogeneity in Oil and Gas Reservoirs Applied to $CO_2$ Storage. *Environmental Geology*. **54**, 1619–1633. https://doi.org/10.1007/s00254-007-0940-2

Bermudez, L., Johns, R.T., Parakh, H.C. (2007). Parametric Investigation of WAG Floods above the MME. *SPE Journal*. **12**(02), 224–234. https://doi.org/10.2118/84366-PA

Bunge, A. L., Radke, C. J. 1982. $CO_2$ Flooding Strategy in a Communicating Layered Reservoir. *Journal of Petroleum Technology*. **34**(12), 2746–2756. https://doi.org/10.2118/10289-PA

Chang, Y.B., Lim, M.T., Pope, G.A., Sepehrnoori, K. 1994. $CO_2$ Flow Patterns Under Multiphase Flow: Heterogeneous Field-Scale Conditions. *SPE Reservoir Engineering*. **9**, 208–216. https://doi.org/10.2118/22654-PA

Chen, S., Li, H., Yang, D., Tontiwachwuthikul, P. 2010. Optimal Parametric Design for Water-Alternating-Gas (WAG) Process in a $CO_2$- Miscible Flooding Reservoir. *Journal of Canadian Petroleum Technology*. **49**(10), 75–82. https://doi.org/10.2118/141650-PA

Chen, B. and Reynolds, A.C., (2016). Ensemble-based Optimization of the Water-Alternating-Gas-Injection Process. *SPE Journal*. **21**(03), 786–798. https://doi.org/10.2118/173217-PA

Christensen, J. R., Stenby, E. H., Skauge, A. 2001. Review of WAG Field Experience. *SPE Reservoir Evaluation & Engineering*. **4**(02), 97106. https://doi.org/10.2118/71203-PA

Eclipse. 2016. Eclipse User's Guide. Schlumberger, France.

Egermann, P., Vizika, O., Dallet, L., Requin, C., Sonier, F. 2000. Hysteresis in Three-phase Flow: Experiments, Modeling and Reservoir Simulations. Paper SPE-65127-MS presented at SPE European Petroleum Conference, Paris, France, 24-25 October. https://doi.org/10.2118/65127-MS

Element, D. J., Masters, J. H. K., Sargent, N. C., Jayasekera, A. J., Goodyear, S. G. 2003. Assessment of Three-phase Relative Permeability Models Using Laboratory Hysteresis Data. Paper SPE-84903-MS presented at SPE International Improved Oil Recovery Conference in Asia Pacific, Kuala Lumpur, Malaysia, 20-21 October. https://doi.org/10.2118/84903-MS

Ettehadtavakkol, A. 2013. $CO_2$ EOR-Storage Design Optimization under Uncertainty. Ph.D. Dissertation, The University of Texas at Austin. pp46

Ettehadtavakkol, A., Lake, L.W., Bryant, S.L. (2014). $CO_2$-EOR and Storage Design Optimization. *International Journal of Greenhouse Gas Control*. **25**, 79–92. https://doi.org/10.1016/j.ijggc.2014.04.006

Harouaka, A., Trentham, B., Melzer, S. 2013. Long Overlooked Residual Oil Zones (ROZ's) Are Brought to the Limelight. SPE-167209-MS presented at SPE Unconventional Resources Conference Canada, Calgary, Alberta, Canada, 5-7 November. https://doi.org/10.2118/167209-MS

Holtz, M.H. (2002). Residual Gas Saturation to Aquifer Influx: A Calculation Method for 3-D Computer Reservoir Model Construction. SPE- 75502-MS presented at SPE Gas Technology Symposium, Calgary, Alberta, Canada, 30 April-2 May. https://doi.org/10.2118/75502-MS

Honarpour, M.M., Nagarajan, N.R., Grijalba Cuenca, A., Valle, M. and Adesoye, K. 2010. Rock-Fluid Characterization for Miscible $CO_2$ Injection: Residual Oil Zone, Seminole Field, Permian Basin. SPE-133089 presented at the Annual Technical Conference and Exhibition, Florence, Italy, 19-22 September. https://doi.org/10.2118/133089-MS

Koperna, G.J., Melzer, L.S. and Kuuskraa, V.A. (2006). Recovery of Oil Resources from the Residual and Transitional Oil Zones of the Permian Basin. SPE 102972 presented at the Annual Technical Conference and Exhibition, San Antonio, Texas, 24-27 September. https://doi.org/10.2118/102972-MS

Kulkarni, M. M., Rao, D. N. 2005. Experimental Investigation of Miscible and Immiscible Water-Alternating-Gas (WAG) Process Performance. *Journal of Petroleum Science and Engineering*. **48**(1-2), 1–20. https://doi.org/10.1016/j.petrol.2005.05.001

Lake, L.W., Johns, R., Rossen, B., Pope, G. 2014. Enhanced Oil Recovery, 2nd edition. Richardson TX: Society of Petroleum Engineers.

Leverett, M.C. (1941). Capillary Behavior in Porous Solids. *AIMEPetroleum Transactions*. **142**: 152–169. https://doi.org/10.2118/941152-G.

Li, D., Lake, L. W. 1995. Scaling Fluid Flow through Heterogeneous Permeable Media. *SPE Advanced Technology Series*. **3**(01), 188–197. https://doi.org/10.2118/26648-PA

Lucia, F.J. (2007). Carbonate Reservoir Characterization: An Integrated Approach. *Springer Science & Business Media*. pp260.

Malik, Q. M., Islam, M. R. 2000. $CO_2$ Injection in the Weyburn Field of Canada: Optimization of Enhanced Oil Recovery and Greenhouse Gas Storage with Horizontal Wells. SPE-59327-MS presented at SPE/DOE improved oil recovery symposium, Tulsa, Oklahoma, 3-5 April. https://doi.org/10.2118/59327-MS

Melzer, L.S. (2013) Residual Oil Zones (ROZs): A Review of ROZ Science and Engineering. Melzer, L.S. (ed).

Nwachukwu, A., Jeong, H., Sun, A., Pyrcz, M., & Lake, L. W. 2018. Machine Learning-Based Optimization of Well Locations and WAG Parameters under Geologic Uncertainty. SPE 190239 presented at the SPE Improved Oil Recovery Conference, Tulsa, Oklahoma, USA, 14-18 April. https://doi.org/10.2118/190239-MS

Rassenfoss, S. 2017. New Permian Oil Play Requires Pumping and Persistence. *Journal of Petroleum Technology*. **69**(02), 28–31. https://doi.org/10.2118/0217-0028-JPT

Remy, N., Boucher, A., Wu, J. 2009. Applied Geostatistics with SGeMS: a User's Guide. Cambridge University Press. Pp135.

Ren, B. 2017. Local Capillary Trapping and Permeability-Retarded Accumulation during Geological Carbon Sequestration. Ph.D. Dissertation, The University of Texas at Austin, Austin, Texas. pp.17–18. https://repositories.lib.utexas.edu/handle/2152/62236

Ren, B., Duncan, I.J. 2019a. Reservoir Simulation of Carbon Storage Associated with $CO_2$ EOR in Residual Oil Zones, San Andres Formation of West Texas, Permian Basin, USA. *Energy*. **167**, 391–401. https://doi.org/10.1016/j.energy.2018.11.007

Ren, B. and Duncan, I.J. 2019b. Modeling Oil Saturation Evolution in Residual Oil Zones: Implications for $CO_2$ EOR and Sequestration. *Journal of Petroleum Science and Engineering*. **177**, 528–539. https://doi.org/10.1016/j.petrol.2019.02.072

Rogers, J. D., Grigg, R. B. 2001. A Literature Analysis of the WAG Injectivity Abnormalities in the $CO_2$ Process. *SPE Reservoir Evaluation & Engineering*. **4**(05), 375–386. https://doi.org/10.2118/73830-PA

Shehata, A. M., El-banbi, A. H., Sayyouh, H. 2012. Guidelines to Optimize $CO_2$ EOR in Heterogeneous Reservoirs. SPE-151871 presented at the North Africa Technical Conference and Exhibition, Cario, Egypt, 20-22 Feburary. https://doi.org/10.2118/151871-MS.

Skauge, A., Sorbie, K. 2014. Status of Fluid Flow Mechanisms for Miscible and Immiscible WAG. SPE-169747 presented at SPE EOR Conference at Oil and Gas West Asia, Muscat, Oman, 31 March - 2 April. https://doi.org/10.2118/169747-MS

Song, Z., Li, Z., Wei, M., Lai, F., Bai, B. 2014. Sensitivity Analysis of Water-Alternating-$CO_2$ Flooding for Enhanced Oil Recovery in High Water Cut Oil Reservoirs. *Computers & Fluids*. **99**, 93–103. https://doi.org/10.1016/j.compfluid.2014.03.022

Sonnenfeld, M. D., Canter, L., Meng, H. Z., Wingate, T. P., Zahm, L. C. 2003. Operational Sequence Stratigraphy for 3-D Reservoir Modeling of Seminole Andres Unit (SSAU), Permian Basin, West Texas. Abstract presented at Annual AAPG-SEPM Meeting, Salt Lake City, Utah, USA, 11-14 May.

Spiteri, E. J., Juanes, R. 2006. Impact of Relative Permeability Hysteresis on the Numerical Simulation of WAG injection. *Journal of Petroleum Science and Engineering*. **50**(2), 115–139. https://doi.org/10.1016/j.petrol.2005.09.004

Stalkup, F.I., (1970). Displacement of Oil by Solvent at High Water Saturation. *SPE J*. **10**(4): 337–348. https://doi.org/10.2118/2419-PA

Stone, H.L. (1970). Probability Model for Estimating Three-Phase Relative Permeability. *Journal Petroleum Technology*. **22**(2): 214–218. SPE-2116-PA. http://dx.doi.org/10.2118/2116-PA.

Trentham, C.R., Melzer, L.S., Vance, D.B. (2012). Commercial Exploitation and the Origin of Residual Oil Zones: Developing a Case History in the Permian Basin of New Mexico and West Texas. RPSEA Final Report.

Walsh, M. P., Lake, L. W. 1989. Applying Fractional Flow Theory to Solvent Flooding and Chase Fluids. *Journal of Petroleum Science and Engineering*. **2**(4), 281–303. https://doi.org/10.1016/0920-4105(89)90005-3

Wu, X., Ogbe, D. O., Zhu, T., Khataniar, S. 2004. Critical Design Factors and Evaluation of Recovery Performance of Miscible Displacement and WAG Process. PETSOC-2004-192 presented at the Canadian International Petroleum Conference, Calgary, Alberta, 8-10 June. https://doi.org/10.2118/2004-192

Zuo, L., Chen, Y., Zou, D.E., Kamath, J. 2014. Three-phase Relative Permeability Modeling in the Simulation of WAG injection. *SPE Reservoir Evaluation & Engineering*. **17**(03), 326–339. https://doi.org/10.2118/166138-PA

# Appendix A

## WAG Ratio Illustration

This appendix illustrates the design of $CO_2$ WAG injection for different WAG ratios. The ratio is defined as the reservoir volume ratio between injected water and injected $CO_2$ in each WAG cycle. It is increased through increasing water injection duration in each cycle while keeping $CO_2$ injection duration unchanged (Fig. A-1). Thus, when the WAG ratio increases, the amount of cumulatively-injected $CO_2$ is decreased with total water amount increased.

**Figure A-1—Schematic illustration of WAG injection schemes for different WAG ratios.**

# Appendix B

## Net Utilization Ratios and Oil Production Performance for Layered Geological Models

This appendix shows the effect of the WAG ratio and well patterns on the $CO_2$ net utilization ration, average oil production rates, and oil recovery factor during WAG injection in layered synthetic geological models.

**Figure B-1—$CO_2$ net utilization ratios, averaged oil production rates, and oil recovery factors for the inverted 5-spot and inverted 9-spot well patterns. $CO_2$ WAG injection is simulated following the processes of NWF or MMWF. The layered geological model is used with $V_{DP}$ = 0.62, $\lambda_{Dx}$ = 100.**

9

# Economic Assessment of Strategies for $CO_2$-EOR and Storage in Brownfield Residual Oil Zones: A Case Study from the Seminole San Andres Unit

Bo Ren, Ian Duncan, Frank Male, Vinyet Baqués, and Larry Lake, The University of Texas at Austin

This paper was prepared for presentation at the SPE Improved Oil Recovery Conference originally scheduled to be held in Tulsa, OK, USA, 18 – 22 April 2020. Due to COVID-19 the physical event was postponed until 31 August – 4 September 2020 and was changed to a virtual event. The official proceedings were published online on 30 August 2020.

## Abstract

Brownfield residual oil zones (ROZ) may benefit from specific strategies to maximize production. We evaluated several strategies for producing from the Seminole ROZ. This ROZ lies below the main pay zone (MPZ) of the field. Such brownfield ROZs occur in the Permian Basin and elsewhere, formed by the action of regional aquifers over geologic time. $CO_2$ can be injected into these zones to enhance oil recovery and carbon storage. Since brownfield ROZs are hydraulically connected to the MPZs, development sequences and schemes should influence oil production, $CO_2$ storage, and net present value (NPV).

We conducted economic assessments of various $CO_2$ injection/production schemes in the Seminole stacked ROZ-MPZ reservoir based on flow simulations. First, we constructed a high-resolution geocellular model from a seismic survey, wireline logs and core data. To calibrate the geological model and constrain the interface between the ROZ and the MPZ, we performed a comprehensive production-pressure history matching of primary depletion and secondary waterflooding. After this, we conducted flow simulations of water alternating gas (WAG) injection into the reservoir while considering several injection/productions schemes (e.g., switching injection from the MPZ to the ROZ, commingled production). For each scheme, various WAG ratios (i.e., reservoir volume ratio between injected water and $CO_2$) were tested to find the maximum oil production and maximum $CO_2$ storage. We assessed the economic results for each WAG ratio case on NPV.

The results from simulating various injection/production schemes showed that simultaneous $CO_2$ injection into the MPZ and ROZ favors oil production. If instead, $CO_2$ is injected into the MPZ and ROZ, then into the ROZ alone, this leads to increased $CO_2$ storage. Storage performance is influenced by the interplay between the crossflow from the MPZ to ROZ and WAG ratios. As the WAG ratio increases, the amount of $CO_2$ stored decreases more for commingled injection cases than for separated ROZ injection cases. Also, the WAG ratio leading to maximum oil production does not necessarily yield the largest NPV, because of the complicated interactions among $CO_2$ consumption, reservoir heterogeneity, and oil recovery. Brownfield ROZs are common below San Andres reservoirs in the Permian Basin, and they can be exploited to increase oilfields' NPV and carbon storage potential. Our case study on the Seminole MPZ-ROZ is an analog for other similar reservoirs. We demonstrate that development sequences and WAG ratios

influence the performance of $CO_2$ EOR and storage. Thus, this work provides valuable insights into the further optimization of brownfield ROZ development and helps operators to plan flexible storage goals for stacked ROZ-MPZ reservoirs.

## Introduction

Brownfield ROZs are hydraulically connected to previously-exploited oil reservoirs (Harouaka et al., 2016; Melzer, 2017). Many brownfield ROZs have been found in Permian Basin (Melzer, 2017) and other places around the world (Webb, 2019). These ROZs have been flooded by regional aquifers over a geological time, and the remaining oil saturation ranges from 10-40% (Harouaka et al., 2016; Ren et al., 2019; Roueche and Karacan, 2018; Webb, 2019). These huge reservoir potentials can be unlocked by improved oil recovery techniques. One such technique of $CO_2$ injection has been demonstrated to be effective in producing oil from these ROZs (Melzer, 2017). One challenge of developing brownfield ROZs when using $CO_2$ injection is balancing the economics and carbon storage potentials between the ROZ and MPZ. Since these ROZs are linked to MPZs, the interaction between the two zones should influence production performance and development strategies. Some possible strategies include MPZ/ROZ commingled injection, switching from MPZ to ROZ or MPZ/ROZ at a certain time (e.g., when the produced gas-oil-ratio is larger than a given value in the MPZs), separate injection of $CO_2$ into MPZ and ROZ but commingled production, and partial or full ROZ completion when developing ROZs. Selection of these strategies should be based on: i) understanding the reservoir/geological characteristics; ii) estimating $CO_2$ EOR and storage potentials in the reservoirs; and iii) strategic goals for oil production and carbon storage. Several reservoir flow simulations have been conducted to evaluate the influence of some of the above strategies on metrics (e.g., oil production) of $CO_2$ EOR and storage. For example, Koperna et al. (2006), studying the Seminole San Andres unit, concluded that "simultaneously implementing the flood in both the ROZ and MPZ" is a superior approach to "separately completing either the MPZ or the ROZ" in term of cumulative oil production. Jamali and Ettehadtavakkol (2017) showed that early expansion into brownfield ROZs compromises project economics. Webb (2019) studied the Nobel field (brownfield) in the Illinois basin and found that complete perforation in both MPZ and ROZ may not substantially increase oil production compared to the perforation in MPZ alone. The author found that for comingled injection, the perforation interval in the ROZ injectors affects the fluid flow interaction between the MPZ and ROZ, and thus significantly influences oil production.

This paper is focused on development strategies for brownfield ROZs to maximize oil recovery and $CO_2$ storage in the Seminole San Andres Unit (SSAU) oilfield. Compared to previous works by Wang et al. (1998), Koperna et al. (2006), Jamali and Ettehadtavakkol (2017), and Webb (2019), our contributions include:

i. We built a high-resolution geological model for both the MPZ and ROZ from high quality subsurface data, including seismic, well logs, cores, production/injection. This allowed us to decrease the uncertainties in both history matching and predicting $CO_2$ EOR and storage potentials compared to similar papers.
ii. We conducted an extensive investigation of how various development scenarios designed in the work influence the brownfield ROZ project economics, oil production, and carbon storage. For the development scenarios, we focused on how to manage the development of brownfield ROZ to achieve the best project economics, given proposed carbon credits.
iii. We found and compared two optimized WAG ratios (one is that which results in the maximum NPV, and the other is at the maximum cumulative oil production). The relevant economic influential factors were examined through conducting a thorough economic sensitivity analysis, including lifting cost and carbon credit. We emphasize the interaction between oil sales and potential carbon credits. The influence of this interaction on desired WAG ratio and NPV was specifically examined.

The whole work provides a reference to the study of other similar brownfield ROZ reservoirs.

## Seminole San Andres Unit (SSAU)

The SSAU oil field is located in the north-east corner of the terminus of the Central Basin Platform (Fig. 1). The field was previously owned by Hess, and it was then acquired by Oxy in 2017. By 2010, the field had produced approximately 700 million barrels of oil, dominantly from the MPZs of the Permian carbonate San Andres Formation. Fig. 2 shows the brief history of the field. Before waterflooding in the late 1960s, cumulative oil production was 200 million, less than 17 percent of the estimated 1.2 to 1.4 billion barrels of OOIP (original oil in place). Waterflooding, through to the early 1980s, resulted in the recovery of an additional 300 million barrels. $CO_2$ injection into the Seminole MPZ begun in the early 1980s slowed the production decline associated with the mature water flood operation.

For the SSAU ROZ, two phases of $CO_2$ injection pilots were implemented. Phase 1, in July 1996, tested the use of line drive patterns. Phase 2, initiated in June 2004, was based on 40-acre inverted 5-spot patterns (Honarpour, 2012). Following the two pilot phases, three stages of full-field commercial ROZ development began in Oct 2007, May 2011, and July 2013 (Melzer, 2017).

**Figure 1—Paleogeographic map of the Permian Basin showing the location of the study area (red box) in west Texas. Modified from Ruppel et al. (1995) and Dutton et al. (2005).**

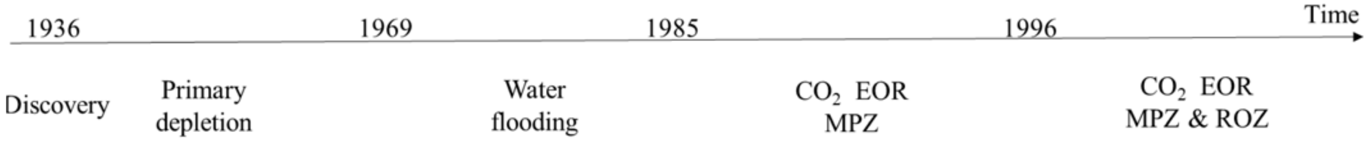

**Figure 2—A brief production history of the SSAU oilfield.**

## Methods

### Geological Characterization

The San Andres Formation is one of the several shallow water platform carbonate and mixed siliciclastic-carbonate units that developed on shelves of the Permian basin in west Texas and New Mexico during the

Permian (Leonardian-Guadalupian) (Ward et al., 1986). This formation corresponds to the Upper Permian (Guadalupian) oil play. From the sequence studies of SSAU sequences by Kerans et al. (1994) and Lucia et al. (1995), multiple shallowing-up cycles were interpreted. These cycles consist of basal mudstones and wackestones grading upward into grain-dominated packstones and grainstones. True crossbedded ooid grainstones are rare, but grain-dominated packstones and grainstones are common. The uppermost part of these cycles consists of fenestral peritidal deposits, and in some cases anhydrite was precipitated (caprock).

Seven carbonate microfacies and one anhydrite dominated microfacies have been described from 10 continuous cores in the northern and central part of the Seminole Field (Baqués and Duncan in prep). The cores exhibit well-developed cyclic depositional sequences, with at least five cycles of sedimentation. The identified microfacies includes: i) crinoidal-fusilinid packstones and grainstones and fusilinid mudstones/packstones representing deep-water facies (into the ROZ); ii) bryozoan packstones/wackestones and boundstones (bafflestones); iii) peloidal-oolitic packstones/grainstones representing near-shoal and shoal deposition; iv) dascyclad-peloidal packstones that are capped by tidal flat deposits with fenestral fabrics; v) restricted subtidal peloidal deposits, overlying tidal flat deposits, grade up into well-developed tidal flat deposits with pisolites, fenestral fabric, mud clasts, storm layers and anhydrite. In summary, the cores exhibit a very thick lower cycle of sedimentation, dominated almost entirely by open-marine facies. Upper cycles are thinner and exhibit a greater proportion of shallow restricted subtidal and tidal flat facies.

All facies in the Seminole San Andres Unit are pervasively dolomitized. Ruppel and Cander (1988) observed that porosity preservation that in these reservoirs was a consequence of dolomitization. Fusilinid mudstones/packstones exhibit variably-preserved porosities. The crinodal-rich facies, prevalent into the ROZ, contains moderate to large amounts (up to greater than 20%) of preserved porosity. Most of this porosity is secondary in origin. Intercrystalline porosity is variably occluded by anhydrite cement. Bryozoan facies in the lower part of the cores have moderate porosities, generally ranging between 10-15%. Pelodial-oolitic shoal deposits have quite variable porosities, ranging from a few percent up to 22%. Most of the grainstones have their primary porosity reduced by anhydrite cements. Packstones exhibit high intercrystalline and leached dolomite rhomb porosity.

## Reservoir Modeling

We integrated a 3D seismic, well logs, and core description results into the geological modeling. The cored-wells' logs (including spontaneous potential, gamma, and neutron porosity) were analyzed, and through this we assigned facies to non-cored wells. Next, we conducted semi-variogram analysis of each facies group in each zone, adopting an exponential variogram model. Then, we employed sequential indictor simulation to generate facies for the geomodel. Then, we employed sequential Gaussian simulation to generate 10 realizations of porosity fields. The corresponding permeability fields are created using Lucia's (1995) rock fabric method (with details in Ren and Duncan (2019a and b), Ren et al. (2019)).

After building a full-field high resolution (cell size 20×20×2 ft) geological model, we generated a coarser, upscaled model with the cell size of 100×100×2 ft. Then, we cut a sector model (Fig. 3d), upon which we conducted history matching of primary depletion and waterflooding for calibration. The calibrated model was then used for the prediction of $CO_2$ EOR and storage potentials. For the simulation input, the rock/fluid interaction models (including fluid properties, relative permeability, and capillary pressure curves) refer to Ren et al. (2019).

When predicting the performance of $CO_2$ EOR and storage, water alternating gas (WAG) injection was considered. Inverted 9-spot 80-acre patterns were adopted, which are currently being used in the development of the MPZ (Honarpour, 2012). The $CO_2$ injection rate is set to 3000 Mscf/day, and water injection rate is 1400 rb/day (reservoir barrel/day). The injection target pressure is at the reservoir fracturing pressure of 3900 psi (Alcorn et al., 2019). Bottom hole pressure for producers is set to be the minimum miscibility pressure, which was measured as 1400 psi (Honarpour et al., 2010). The WAG ratio (i.e., reservoir volume ratio between injected water and $CO_2$) was varied from 0 to 4, through changing water injection duration while keeping $CO_2$ injection duration unchanged in each WAG cycle. The WAG ratio equal to 1 (base case) corresponds to 90 days of water injection alternating with 70 days of $CO_2$ injection. We run WAG injection for 40 years.

All the injectors and producers involved in simulations are vertical, and perforated according to the development scenarios as shown in Table 1. Different switching schedules and injection/production schemes were considered. Buffered boundary conditions as described by Ren and Duncan (2019a) were used in all flow simulations.

**Table 1—Designed development scenarios for the brownfield ROZ**

| Scenario # | Injection Schemes | Production Schemes | Notes |
|---|---|---|---|
| 1 | MPZ & ROZ 40 yr commingled injection | MPZ & ROZ 40 yr comingled production | Develop MPZ & ROZ at the start |
| 2 | MPZ 40 yr injection | MPZ 40 yr production | Develop only MPZ |
| 3 | MPZ 20 yr injection + MPZ & ROZ 20 yr injection | MPZ 20 yr + MPZ & ROZ 20 yr | Develop MPZ initially and then develop MP & ROZ |
| 4 | MPZ & ROZ 20 yr injection + ROZ 20 yr injection | MPZ & ROZ 40 yr | Develop MPZ & ROZ and then develop ROZ |

## Economic Modeling

We calculated the cumulative net present values (NPV) for all the development scenarios. For these scenarios, we assumed CAPEX (mainly drilling costs at the beginning of MPZ development and installation of $CO_2$ clean-up/recycle plants) is the same, and thus the difference in calculated NPV will be attributed to different injection and production rates and the incurred expense and revenues. We focused on the comparison of different scenarios, so the CAPEX is not included in NPV calculation.

For the purposes of this analysis, the NPV is assumed to consist of four components: oil revenue, carbon credit, operational expenses, and cost of well deepening into the ROZ. For simplicity, we treated the carbon credit as a revenue stream. The operational expenses include $CO_2$ purchase, $CO_2$ recycle, produced water management, and liquid lifting. The formula used to estimate NPV is in equation 1. The following equations 2–9 show how to calculate all these components. The cost assumptions are listed in Table 2. Sensitivity analysis of these parameters was also conducted using the range in Table 2.

**Table 2—The settings of economic parameters in NPV calculation. These settings are based on the publications by Chen and Reynolds (2016), Godec (2014), Hultzsch et al. (2007).**

| Component | Base Settings | Range |
|---|---|---|
| Oil price ($/STB) | 60 | 30-120 |
| Carbon credit ($/Tonne) | 0 | 0-40 |
| CO2 purchase price ($/Tonne) | Oil price × 0.42* | Oil price × (0.33-0.50) |
| Gas recycling cost ($/MSCF) | Oil price × 1% | - |
| **Produced water management cost ($/STB) | 0.64 | - |
| Liquid lifting cost ($/STB) | 1.0*** | 0.40-1.50 |
| Deepening cost ($/ft) | 150 | - |
| Annual discount rate | 0.12 | - |

* assuming natural $CO_2$. The price of $CO_2$ sold varies according to oil price, and conversion factor is 0.42 for base settings.

** produced water management cost consists of water injection, water recycling, and water disposal.

*** this is the liquid lifting cost for wells perforated in the MPZ only. The cost for other wells perforated in the ROZ or both the MPZ and ROZ is assumed to linearly increase with reservoir depth.

$$NPV = \sum_{n=1}^{N} \frac{Oil\_\ \ revenue_n + Carbon\_price_n \ \ - Recurrent\_cost_n - Welldeepen\_cost_n}{(1+r)^n} \tag{1}$$

$$Oil\_revenue_n = \left[Q_{op(n)} - Q_{op(n-1)}\right] \times Oil\_price \tag{2}$$

$$Carbon\_price_n = ([Q_{gi(n)} - Q_{gi(n-1)}] - [Q_{gp(n)} - Q_{gp(n-1)}] \ \ ) \times Storagetax \tag{3}$$

$$Recurrent\_cost_n = Gaspur_n + Gasrecy_n + \ \ Water\_cost_n + Liquid\_lift_n \tag{4}$$

$$Gaspur_n = (\left[Q_{gi(n)} - Q_{gi(n-1)}\right] - \left[Q_{gp(n)} - Q_{gp(n-1)}\right] \ \ ) \times Gaspur\_price \tag{5}$$

$$Gasrecy_n = \left[Q_{gp(n)} - Q_{gp(n-1)}\right] \ \ \times Gasrecy\_cost \tag{6}$$

$$Water\_cost_n = (\left[Q_{wp(n)} - Q_{wp(n-1)}\right] \ \ - \left[Q_{wi(n)} - Q_{wi(n-1)}\right]) \times Water\_cost \tag{7}$$

$$Liquid\_Lift_n = \left(\left[Q_{op(n)} - Q_{op(n-1)}\right] + \left[Q_{wp(n)} - Q_{wp(n-1)}\right]\right) \times Lift\_cost \tag{8}$$

$$Welldeepen\_cost_n = Cost\_perft * Deepen\_length \tag{9}$$

In the above equations,

$Oil\_\ revenue_n$, revenue from oil production at the $n_{th}$ year, \$

$Carbon\_price_n$, price of carbon as incentive for carbon storage at the $n_{th}$ year, \$

$Recurrent\_cost_n$, recurrent operation cost at the $n_{th}$ year, \$

$Welldeepen\_cost_n$, well deepening cost for ROZ development at the $n_{th}$ year, \$

$r$, annual discount rate

$n$, year numbering since the start of development

$_{op(n)}$, cumulative oil production till the $n_{th}$ year, STB

$Q_{op(n-1)}$, cumulative oil production till the $(n\text{-}1)_{th}$ year, STB

$Oil\_price$, the price of oil, \$/STB

$Q_{gi(n)}$, cumulative gas injection till the $n_{th}$ year, MSCF

$Q_{gi(n-1)}$, cumulative gas injection till the $(n\text{-}1)_{th}$ year, MSCF

$Q_{gp(n)}$, cumulative gas production till the $n_{th}$ year, MSCF

$Q_{gp(n-1)}$, cumulative gas production till the $(n\text{-}1)_{th}$ year, MSCF

$Storagetax$, carbon credit for storage, \$/Tonne

$Gaspur_n$, $CO_2$ purchase cost at the $n_{th}$ year, \$

$Gasrecy_n$, $CO_2$ recycling cost at the $n_{th}$ year, \$

$Water\_cost_n$, produced water management cost at the $n_{th}$ year, \$

$Liquid\_lift_n$, produced liquid lifting cost at the $n_{th}$ year, \$

$Gaspur\_price$, $CO_2$ purchase price, \$/Tonne

$Gasrecy\_cost$, $CO_2$ recycling cost, \$/MSCF

$Q_{wp(n)}$, cumulative water production till the $n_{th}$ year, STB

$_{wp(n-1)}$, cumulative water production till the $(n\text{-}1)_{th}$ year, STB

$Q_{wi(n)}$, cumulative water injection till the $n_{th}$ year, STB

$Q_{wi(n-1)}$, cumulative water injection till the $(n\text{-}1)_{th}$ year, STB

$Water\_cost$, cost of produced water management, \$/STB

$Lift\_cost$, cost of liquid lifting, \$/STB

$Cost\_perft$, cost of deepening wells into ROZ, \$/ft

$Deepen\_length$, depth of deepening for wells into ROZ, \$

## Metrics Used to Evaluate $CO_2$ EOR and Storage Performance

In addition to traditional EOR performance metrics (e.g., cumulative oil production), we also calculated metrics used to measure the performance of $CO_2$ storage in the brownfield ROZ.

Stored $CO_2$ amount = injected $CO_2$ amount – produced $CO_2$ amount.

$CO_2$ retention fraction = stored $CO_2$ amount / injected $CO_2$ amount.

All these $CO_2$ EOR and storage metrics change with time; the results given here are the values after 40 years.

## Results and Discussion

### Geological Models

Fig. 3 shows the full-field porosity and permeability, along with permeability for the sector model. This porosity/permeability is selected from the batch of realizations that conform to geological characterizations and reservoir heterogeneity. The cut sector consists of 25 inverted 9-spot 80-acre patterns, with 25 vertical injectors and 94 vertical producers.

**Figure 3—(a) The Petrel unit boundary of full-field geological model for Seminole with the dashed square in (a) representing the outer boundaries of a cut sector model. (b) Porosity fence diagram. (c) Permeability field with the two sectional cut for direct visualization. Four zones (gas cap, MPZ, ROZ, and water leg) are differentiated with different colors for easy look. The depth cutoff for the three contacts are 1725 ft (gas-oil-contact), 1935 ft (producing water-oil-contact or the contact between the MPZ and ROZ), and 2200 ft (free water level). (d) Permeability field of the cut sector with all the vertical well locations shown on the top of model.**

## History Matching

The purpose of history matching was to: i) calibrate petrophysical properties, including permeability, porosity, and compressibility; ii) calibrate the depth of the producing water-oil contact (interface between the MPZ and ROZ) and gas-oil contact. Fig. 4 shows the achieved good match of oil production rate, water cut, and reservoir pressure. The history match of gas-oil-ratio (GOR) is challenging. GOR matching is hindered by the lack of both the information about the gas cap size and knowledge of the vertical fracture permeability of the reservoir. The GOR curve indicates that gas-solution-drive is the main driving mechanism during primary depletion (1936-1969).

**Figure 4—History matching of oil production rate (a), water cut (b), gas-oil-ratio (c), and reservoir pressure (d) during primary depletion and waterflooding periods. Large dots are field measurements, and lines represent simulation results.**

## Comparison of Different Development Scenarios

Fig. 5 compares the $CO_2$ EOR and storage metrics for all the development scenarios. Comingled injection and production (scenario #1) yields the largest oil production and NPV, and comingled injection followed by ROZ injection only (scenario #4) gives the highest $CO_2$ storage amount and retention fraction. The least favorable scenario is #2, MPZ development only. The corresponding EOR and storage metrics are the smallest among all scenarios.

The commingled $CO_2$ injection (scenario #1) increases the contact of $CO_2$ to rocks and thus favors both oil production and carbon storage, as compared to MPZ injection only (scenario #2). For the latter scenario #2, most of the injected $CO_2$ is very likely to channel into producers and was then recycled (as revealed by

Fig. 6). As a comparison, scenario # 4 with the largest $CO_2$ storage only perforated wells in the ROZ interval at the late period, which helps decrease $CO_2$ production. This should be because the ROZ has a large initial water saturation (~60%), and displacing water is more difficult than displacing oil by $CO_2$ (Ren et al., 2019).

Here, we purposely compared scenario #1 to #4. Wide variations of both oil production and NPV with the WAG ratio are observed for scenario #1, as compared to scenario #4 (Figs. 5a and 5d). Meanwhile, as the WAG ratio increases, the amount of $CO_2$ stored decreases more rapidly for scenario #1 than for scenario #4 (Fig. 5b). We found similar results in the $CO_2$ retention fraction comparison (Fig. 5c).

Further comparison between scenario #1 and #4 shows the large difference in oil production (Fig. 5a) but with similar $CO_2$ storage amount (Fig. 5b) when adjusting the WAG ratio. This indicates that gravity segregation of $CO_2$ might not be significant (i.e., $CO_2$ migration is probably confined into each zone because of the interlayered low permeability flow barriers/baffles (refer to Fig. 3c)). Such indication was also supported through surveying $CO_2$ saturation fields.

**Figure 5—Comparison of $CO_2$ EOR and storage metrics for different development scenarios at the end of WAG injection (at 40 years). (a) final oil production; (b) final amount of $CO_2$ stored; (c) final retention fraction of $CO_2$; (d) final NPV. The WAG ratio is in the range of 0-4. The final NPV is calculated using the base settings in Table 2.**

Fig. 6 shows the cost bar charts for scenarios #1, #2, and #4 after 40 years of development. For scenario #4 with the largest $CO_2$ storage, the associated cost fraction of liquid lifting and water management is a little larger than those for scenario #1 (commingled injection/production for 40 years, Fig. 6a). Most of the costs for both scenarios is from $CO_2$ recycling and purchasing. For MPZ only development (scenario #2, Fig. 6c), the fraction of $CO_2$ recycling costs is much higher (75.5% versus 41.4% for comingled injection/production).

When moving from the MPZ to ROZ development, it appears that the large water saturation in the ROZ does not greatly increase the fractions of the costs associated with liquid lifting and water management. The cost fractions are specific to each reservoir and depend on reservoir characteristics and dynamics during $CO_2$ injection.

Comparison between scenario #1 and #4 shows that the cost fraction of $CO_2$ recycling is less for scenario #4 (38.7%) than for #1 (41.4%). This should indicate that $CO_2$ tends to be difficult to be produced out when switching from the MPZ to ROZ (where water prevails), which is consistent with our above analysis of the production metrics.

**Figure 6—Bar charts for 40 years of cost for development scenarios #1 (a) and # 4 (b). Both of them are associated with ROZ development. For comparison to only MPZ development, the cost pie charts for the scenario #2 (c) was also included in the figure. The WAG ratio is 1 (i.e., 70 days of $CO_2$ half-cycle alternating with 90 days of water half-cycle). Base settings for economic parameters in Table 2 were used. The cost of well deepening into the ROZ is minimal, so it was not included in the charts.**

## Sensitivity Analysis

Fig. 7 compares two types of WAG ratios: the WAG ratios at the maximum oil production versus the WAG ratios at the maximum NPV. We focused on the effects of economic parameters (oil price, carbon credit and conversion factor (from oil price to $CO_2$ purchasing price)), rather than geological parameters. The main observation from Fig. 7 is that, for most of the cases studied here, the WAG ratios that yield the maximum oil production do not necessarily give the maximum NPV. Generally, large oil price increases the optimal WAG ratio for NPV, whereas large carbon credit decreases it. Cheap $CO_2$ (small conversion factor from oil price to $CO_2$ purchasing price) decreases the optimal WAG ratio. The lifting cost shows no effect on the WAG ratio comparison.

**Figure 7—Comparison between the WAG ratio corresponding to maximum cumulative oil production (at 40 year) and the WAG ratio corresponding to maximum cumulative NPV for all the development scenarios. The settings for economical parameters are for the base case (refer to Table 2). The effects of changing oil price, carbon credit, and conversion factor (from oil price to $CO_2$ purchasing price) on the comparison between the two types of WAG ratios are shown in the figure.**

Fig. 8 shows the sensitivity of NPV to several economic parameters (i.e., oil price, carbon credit, lifting cost, conversion factor). The WAG ratio, as an example of engineering parameters, was also included to show how different considerations of $CO_2$ EOR and storage will influence the NPV. For scenario #1, with the largest oil production, the NPV is more sensitive to the WAG ratio than for the scenario #4, with largest $CO_2$ storage ((Fig. 8a vs. Fig. 8b). This indicates the complexity of the interaction between economic parameters and engineering ones. The effect of this interaction on the emphasis of some parameters should be considered when switching $CO_2$ injection from MPZs to ROZs.

**Figure 8—Tornado plots of final NPV for development scenario #1 (a) and #4 (b).**

## Summary, Conclusions, and Recommendations

We built a high-resolution geological model for both the main pay zone (MPZ) and residual oil zone (ROZ) of the Seminole San Andres Unit based on integrated geological and reservoir characterization. The model was calibrated with historical primary and secondary production data matches. We used the geological model to economically evaluate different development strategies and their associated uncertainties through integrated full-physics flow simulation and economic assessment. To better compare these scenarios, we defined and calculated a series of metrics for $CO_2$ EOR and storage. Water alternating gas (WAG) ratios were tuned to maximize either oil production or net present value (NPV). The influence of economic parameters (e.g., oil price and carbon credit) on favorable WAG ratios were examined. We found that:

i. Simultaneous injection into both the MPZ and ROZ favors oil production, whereas, switching from comingled injection to only ROZ injection in the later time period of projects helps $CO_2$ storage. The optimal switching time needs further study.
ii. The WAG ratios at the maximum oil production are not equal to those at the maximum NPV for most of the cases due to the uncertainties in economic parameters.
iii. The sensitivity of NPV to economic and engineering parameters changes when considering the goals of increasing oil production versus maximizing $CO_2$ storage.

The whole work provides a basis for future optimization of $CO_2$ EOR and storage in brownfield ROZs.

## Acknowledgements

We thank Robin Dommisse for valuable assistance in outputting the geomodel from Petrel. This study is part of a long term project investigating ROZ reservoirs in the Permian Basin of Texas being carried out by the Bureau of Economic Geology's (BEG's) State of Texas Advanced Resource Recovery (STARR) Program and funded in part by a US Department of Energy contract under DOE Award Number FE0024375 (PI: Duncan). The opinions of the authors do not necessarily reflect those of the United States Government or any agency thereof. Larry W. Lake holds the Shahid and Sharon Ullah Endowed Chair in the Hildebrand Department of Petroleum and Geosystems Engineering at The University of Texas at Austin.

## References

Alcorn, Z. P., Fredriksen, S. B., Sharma, M., Rognmo, A. U., Føyen, T. L., Fernø, M. A., Graue, A. 2019. An Integrated Carbon-Dioxide-Foam Enhanced-Oil-Recovery Pilot Program with Combined Carbon Capture, Utilization, and Storage in an Onshore Texas Heterogeneous Carbonate Field. *SPE Reservoir Evaluation & Engineering*. **78** (2), 181–216. https://doi.org/10.2118/190204-PA

Baqués, V., Duncan, I.J. 2020. Diagenetic Evolution of the Residual Oil Zone (ROZ) Platform Carbonates San Andres Seminole Unit, Permian Basin, West Texas: Constraints from C, O and Sr isotopes. In preparation

Chen, B., Reynolds, A.C., 2016. Ensemble-based Optimization of the Water-Alternating-Gas-Injection Process. *SPE Journal*. **21**(03), 786–798. https://doi.org/10.2118/173217-PA

Dutton, S.P., Kim, E.M., Broadhead, R.F., Raatz, W.D., Breton, C.L., Ruppel, S.C. Kerans, C., 2005, Play Analysis and Leading-Edge Oil-Reservoir Development Methods in the Permian Basin: Increased Recovery through Advanced Technologies. *AAPG bulletin*. **89**(5), 553–576. https://doi.org/10.1306/12070404093

Godec, M. L. 2014. Acquisition and Development of Selected Cost Data for Saline Storage and Enhanced Oil Recovery (EOR). *United States*. https://www.osti.gov/servlets/purl/1557133

Harouaka, A., Trentham, B., Melzer, S. 2013. Long Overlooked Residual Oil Zones (ROZ's) Are Brought to the Limelight. SPE-167209-MS presented at SPE Unconventional Resources Conference Canada, Calgary, Alberta, Canada, 5-7 November. https://doi.org/10.2118/167209-MS

Honarpour, M.M., Nagarajan, N.R., Grijalba Cuenca, A., Valle, M., Adesoye, K. 2010. Rock-Fluid Characterization for Miscible $CO_2$ Injection: Residual Oil Zone, Seminole Field, Permian Basin. SPE-133089 presented at the Annual Technical Conference and Exhibition, Florence, Italy, 19-22 September. https://doi.org/10.2118/133089-MS

Hultzsch, P., Lake, L. W., Gilbert, R. B. 2007. Decision and Risk Analysis Through the Life of the Field. In Hydrocarbon Economics and Evaluation Symposium. SPE-107704-MS presented at SPE Hydrocarbon Economics and Evaluation Symposium, Dallas, Texas, 1-3 April. https://doi.org/10.2118/107704-MS

Jamali, A., Ettehadtavakkol, A. 2017. $CO_2$ Storage in Residual Oil Zones: Field-scale Modeling and Assessment. *International Journal of Greenhouse Gas Control*. **56**, 102–115. https://doi.org/10.1016/j.ijggc.2016.10.005

Kerans, C., Lucia, F.J., Senger, R.K. 1994, Integrated Characterization of Carbonate Ramp Reservoirs Using Permian San Andres Formation Outcrop Analogs. *AAPG Bulletin*. **78** (2), 181–216. https://doi.org/10.1306/BDFF905A-1718-11D7-8645000102C1865D

Koperna, G.J., Melzer, L.S. and Kuuskraa, V.A. 2006. Recovery of Oil Resources from the Residual and Transitional Oil Zones of the Permian Basin. SPE-102972-MS presented at the SPE Annual Technical Conference and Exhibition, San Antonio, Texas, 24-27 September. https://doi.org/10.2118/102972-MS

Lucia, F.J., Kerans, C., Wang, F.P. 1995, Fluid-Flow Characterization of Dolomitized Carbonate-Ramp Reservoirs: San Andres Formation (Permian) of Seminole Field and Algerita escarpment, Permian Basin, Texas and New Mexico. *SEPM*, **SC34**, 129–153. https://doi.org/10.2110/scn.95.34.0129

Melzer, L. S., Kuuskraa, V. A., Koperna, G. J. 2006. The Origin and Resource Potential of Residual Oil Zones. SPE 102964-MS presented at the SPE Annual Technical Conference and Exhibition, San Antonio, Texas, 24-27 September. https://doi.org/10.2118/102964-MS

Melzer, L. S. 2017. Residual Oil Zones Changing Commercial Reservoir Models. *Oil & Gas Journal*. **115**(4), 52–55.

Ren, B., Duncan, I.J. 2019a. Reservoir Simulation of Carbon Storage Associated with $CO_2$ EOR in Residual Oil Zones, San Andres Formation of West Texas, Permian Basin, USA. *Energy*. **167**, 391–401. https://doi.org/10.1016/j.energy.2018.11.007

Ren, B. and Duncan, I.J. 2019b. Modeling Oil Saturation Evolution in Residual Oil Zones: Implications for $CO_2$ EOR and Sequestration. *Journal of Petroleum Science and Engineering*. **177**, 528–539. https://doi.org/10.1016/j.petrol.2019.02.072

Ren, B., Male, F., Wang, Y., Baqués, V., Duncan, I.J., Lake, L.W. 2019. Oil Saturation in Residual Oil Zones and Its Effect on $CO_2$ WAG Injection Strategies. SPE-196230-MS presented at the SPE Annual Technical Conference and Exhibition, Calgary, Alberta, 30 September-2 October. https://doi.org/10.2118/196230-MS

Roueché, J. N., Karacan, C. Ö. 2018. Zone Identification and Oil Saturation Prediction in a Waterflooded Field: Residual Oil Zone, East Seminole Field, Texas, USA, Permian Basin. SPE-190170-MS presented at the SPE Improved Oil Recovery Conference, Tulsa, Oklahoma, 14-18 April. https://doi.org/10.2118/190170-MS

Ruppel, S.C., Cander, H.S., 1988, Dolomitization of Shallow Water Platform Carbonates by Seawater and Seawater-Derived Brines: the San Andres Formation (Guadalupian), West Texas, in Shukla, V., and Baker, P.A., eds., *Sedimentology and Geochemistry of Dolostones: SEPM Spec. Publ*. **43**, 245–262. https://doi.org/10.2110/pec.88.43.0245

Ruppel, S. C., Kerans, C., Major, R. P., Holtz, M. H., 1995, Controls on Reservoir Heterogeneity in Permian Shallow Water Carbonate Platform Reservoirs, Permian Basin: Implications for Improved Recovery: The University of Texas at Austin, *Bureau of Economic Geology Geological Circular GC9502*.

Wang, F. P., Lucia, F. J., Kerans, C. 1998. Integrated Reservoir Characterization Study of a Carbonate Ramp Reservoir: Seminole San Andres Unit, Gaines County, Texas. *SPE Reservoir Evaluation & Engineering*. **1**(02), 105–113. https://doi.org/10.2118/36515-PA

Ward, R., Kendall, C. G. St. C., Harris P. M., 1986, Upper Permian (Guadalupian) facies and their association with hydrocarbons Permian Basin: West Texas and New Mexico. *AAPG*. **70**, 239–262. https://doi.org/10.1306/9488566F-1704-11D7-8645000102C1865D

Webb, N. 2019. A Nonconventional $CO_2$-EOR Target in the Illinois Basin: Oil Reservoirs of the Thick Cypress Sandstone (No. DOE-UofI-24431). *United States*. https://www.osti.gov/servlets/purl/1545654.

10

# Analysis of Vertical Permeability and Its Influence on $CO_2$ EOR and Storage in a Carbonate Reservoir

Bo Ren, Jerry Jensen, Larry Lake, Ian Duncan, and Frank Male, The University of Texas at Austin

This paper was prepared for presentation at the 2021 SPE Annual Technical Conference and Exhibition held in Dubai, UAE, 21 - 23 September 2021.

## Abstract

The objective of this study is to improve understanding of the geostatistics of vertical (bed-normal) permeability ($k_z$) and its influence on reservoir performance during $CO_2$ enhanced oil recovery (EOR) and storage. $k_z$ is scrutinized far less often than horizontal permeability ($k_x$, $k_y$) in most geological and reservoir modeling. However, our work indicates that it is equally important to understand $k_z$ characteristics to better evaluate their influence on $CO_2$ EOR and storage performance prediction.

We conducted this study on about 9,000 whole-core triaxial permeability ($k_x$, $k_y$, $k_z$) measurements from 42 wells in a San Andres carbonate reservoir. We analyzed $k_z$ data, including heterogeneity, correlation, and sample sufficiency measures. We analyzed wells with the largest and smallest fractions of points with $k_z > k_{max} = \max(k_x, k_y)$, to explore geological factors that coincided with large $k_z$. We quantified these geological effects through conditional probabilities on potential permeability barriers (e.g., stylolites).

Every well had at least some whole-cores where $k_z > k_{max}$. This is a statistically justifiable result; only where Prob($k_z > k_{max}$) is statistically different from 1/3 are core samples non-isotropic. In conventional core data interpretation, however, modelers usually assume $k_z$ is less than $k_{max}$. For the well with the smallest fraction (11%) of cores where $k_z > k_{max}$, the cumulative distribution functions differ and coincides with the presence of stylolites. We found that $k_z$ is about twice as variable as $k_x$ in many wells. This makes $k_z$ more difficult to interpret because it was (and usually is) heavily undersampled.

To understand the influence of $k_z$ heterogeneity on $CO_2$ flow, we built a series of flow simulation models that captured these geostatistical characteristics of permeability, while considering $k_z$ realizations, flow regimes (e.g., buoyant flow), $CO_2$ injection strategies, and reservoir heterogeneity. $CO_2$ flow simulations showed that, for viscous flow, assuming variable $k_x$ similar to the reservoir along with a constant $k_z/k_x = 0.1$ yields a close (within 0.5%) cumulative oil production to the simulation case with both $k_x$ and $k_z$ as uncorrelated variables. However, for buoyant flow, oil production differs by 10% (at 2.0 hydrocarbon pore volume HCPV of $CO_2$ injected) between the two cases. Such flows could occur for small $CO_2$ injection rates and long injection times, in interwell regions, and/or with vertically permeable conduits.

Our geostatistical characterization demonstrates the controls on $k_z$ in a carbonate reservoir and how to improve conventional interpretation practices. This study can help $CO_2$ EOR and storage operators refine injection development programs, particularly for reservoirs where buoyant flow exists. More broadly,

the findings potentially apply to other similar subsurface buoyancy-driven flow displacements, including hydrogen storage, geothermal production, and aquifer $CO_2$ sequestration.

## Introduction

Vertical permeability ($k_z$) is important in many subsurface processes where there is a density difference between fluids, including gas (e.g., $CO_2$) enhanced oil recovery (EOR) and geologic storage, geothermal production, hydrogen storage, compressed air storage, tracer flow, steam injection, and water coning (Bryant et al., 2008; Hassanpouryouzband et al., 2021; Hinton and Woods, 2019; Silin et al., 2009; Yang and Butler, 1992). Specifically, for $CO_2$ EOR and storage in oil reservoirs, $k_z$ characterization is important for reservoir management and development endeavors, including optimization of injector/producer placement, design of completion strategies, and deployment of reservoir monitoring programs during $CO_2$ injection as well as post-injection periods.

Vertical permeability ($k_z$) can be measured at several scales. At core scales (i.e., cm and dm), whole core samples are convenient because permeability is measured in three directions on the same sample. Core plugs drilled orthogonal to local bedding planes can also be used. At larger scales, formation testers (e.g., Ayan et al., 1994; Onur et al., 2011), history-matched reservoir simulation (e.g., Sutton et al., 2013), analytical and semi-analytical calculations (e.g., Haldorsen and Lake, 1984; Begg and King, 1985), ocean tide pressure variations (e.g., Wannell and Morrison, 1990) may be used to estimate $k_z$. Of all these methods, core-scale measurements are perhaps the most common.

Core-scale $k_z$ is often compared with the horizontal permeability ($k_x$) measured at the same or a nearby location by calculating the ratio $k_z/k_x$. There appear to be two main reasons for using the ratio. First, one may expect that $k_z$ and $k_x$ are positively correlated, so that $k_z/k_x$ is less variable than either $k_z$ or $k_x$. The less variable a reservoir characteristic is, the easier it is to predict for areas beyond the wellbore. Second, $k_x$ measurements are typically more abundant than $k_z$ measurements, so that a knowledge of $k_x$ and $k_z/k_x$ will provide $k_z$ estimates at the same frequency as $k_x$ values. Typically, log-log plots of $k_z$ versus $k_x$ (Fig. 1) offer a useful assessment of the $k_z/k_x$ values present in a reservoir.

**Fig. 1—Sherwood Sandstone core plug data from a strongly laminated fluvio-aeolian reservoir with $k_z/k_x$ lines drawn to evaluate core-scale anisotropy. $k_z/k_x$ varies by approximately four orders of magnitude while either $k_z$ or $k_x$ change by six orders of magnitude. With 232 bi-directional pairs for this figure, Prob ($k_z/k_x > 1$) = 63/232 = 0.27 (probabilities are equivalent to frequencies in this work). Because this probability is much different than ½, it is extremely unlikely (probability of approximately $2 \times 10^{-12}$) to get only 63 out of 232 samples with $k_z/k_x > 1$ if the core-scale permeability is isotropic for this data. See Morton et al. (2002) for more details on the Sherwood Sandstone.**

The use of $k_z/k_x$ ratio is a common way of modeling $k_z$. Then the question to be answered: what are the consequences of avoiding $k_z$ measurements by using $k_x$ measurements instead? Several associated questions also arise: i) is $k_z$ always dependent on $k_x$ or is it independent? ii) Do both permeabilities have the same/similar statistical properties? iii) What are the influential factors of $k_z$ /$k_x$ ratio? The $k_z/k_x$ ratio is typically assumed to be 0.1. However, several studies on sandstones (Jones et al., 1987; Hanks et al., 2011, Baker et al., 2005) and carbonates (Sun et al., 2017; Dernaika et al., 2018; Chandra et al., 2013), including the work presented here, showed the occurrences where $k_z > k_x$. The underlying geological causes should be well understood for reliable geomodels and multiphase flow simulations.

A considerable number of studies have focused on the influence of $k_z$ on flow prediction. Unfortunately, most flow simulations that consider $k_z$ typically treated the $k_z/k_x$ ratio as a sensitivity parameter and examined its influence on defined metrics (e.g., Abdelaal et al., 2021; Chang et al., 1994; Ren and Duncan, 2021). Campero et al. (2014) made an analysis of $k_z/k_x$ based on the geological datasets collected in a field and evaluated the influence of $k_z/k_x$ ratio on history match and prediction during waterflooding. However, all these studies avoided a fundamental question: how good is using a constant $k_z$ /$k_x$ ratio to populate vertical permeability for flow prediction as compared to having variable $k_z$?

Our objectives here are to: i) deepen our understanding of the statistical properties of $k_z$; ii) examine $k_z$'s influence on $CO_2$ flow, storage, and production prediction; and iii) specifically compare performance prediction between the case of using true $k_z$ versus the traditional wisdom of assuming a ratio for $k_z/k_x$.

Our study is based on a San Andres carbonate reservoir. The San Andres Formation is one of the richest oil formations in the Permian Basin, and many $CO_2$ EOR projects are active in the formation (Jarrell et al., 2002; Lake et al., 2018). It could be expected that $CO_2$ storage incidental to EOR will likely be implemented into those Permian Basin carbonate formations in near future. In this sense, our case study on the carbonate reservoir should provide a good reference for the understanding of $k_z$ and its influence on $CO_2$ EOR and storage.

We conducted $k_z$ -related exploratory plots, including permeability profiles, histograms, heterogeneity measures, and semivariogram analyses. Then, based on the geostatistical analysis, we selected the wells with the extreme fractions of $k_z > k_x$. We analyzed whole core, thin sections, and core plug datasets of the selected wells to explore the geological factors of $k_z$. We also conducted probability analyses conditioned by potential permeability barriers to quantify geological parameters. We then built a series of generic flow simulation models based on these geostatistical understanding, while considering various injection strategies and flow regimes, to quantify the influence of $k_z$ realizations on $CO_2$ EOR and storage performance.

## San Andres Formation

The carbonate facies of the San Andres Formation (SAF) developed on the shelves of the Permian Basin in west Texas and New Mexico during the Permian (Leonardian-Guadalupian) ages (Ward et al., 1986). The SAF is one of several shallow water platform carbonate and mixed siliciclastic-carbonate units. From the sequence stratigraphy studies by Kerans et al. (1994), Lucia et al. (1995), and Wang et al. (1998), several upward-shallowing cycles were interpreted from their facies description. These cycles consist of basal mudstones and wackestones grading upward into grain-dominated packstones and grainstones. A total of 5 facies groups were identified from a 4002-feet-thick continuous core from 10 wells with both MPZ and ROZ intervals. More complete studies for the MPZ were reported by Kerans et al. (1994) and Lucia et al. (1995).

The most common pore types include interparticle, moldic, and vugs. Dolomitization is a key diagenetic process that influences porosity distribution in the reservoir. Stylolites, which are common in the SAF, are intergranular pressure solution features usually with wavy surfaces (Heap et al., 2014; Koepnick, 1987). Most of the stylolites are sutured with cements, but some have solution seams. The stylolite-bearing horizons could be laterally extensive (100s of meters). They may act as barriers or paths for fluid flow depending on both stylolite features and their extents relative to the flow directions. Vertical fractures are common but and mostly filled in by anhydrite or dolomite cement.

## Datasets

The $k_z$ -related dataset come from a SAF reservoir and include whole-core measurements (by Core Labs), core plugs, as well as descriptions of lithology and diagenetic history. For the reservoir we studied, nearly 9,000 whole-core permeabilities from over 4 wells were available from Core Labs reports. We conducted careful quality checks and cleaning of these datasets before exploratory analyses. Data cleaning consisted of: i) removing measurement values below the threshold (e.g., < 0.001 md) for some evaluations, such as averages, standard deviation, and semivariograms; and ii) removing incomplete measurements. Samples where only $k_x$ was available without $k_z$, might be from core plugs. For the collected whole cores, over 6000 samples have core lithology descriptions. Core descriptions in these reservoirs provide sedimentological information such as textures, sedimentary structures, and post-depositional features.

A whole-core has a larger diameter and length than a conventional core plug (Fig. 2), thus the whole-core includes more larger-scale geological information. The main advantage of whole cores is that they are or approach exhaustive sampling. Whole cores are often used in reservoir characterization to measure three-directional permeabilities: $k_x$, $k_y$, $k_z$ (Fig. 2). The horizontal (x, y) direction are varying randomly, and usually $k_{max} = \max(k_x, k_y)$ and $k_{90} = \min(k_x, k_y)$. More details of whole-core-based permeabilities and their comparison to core plugs and probe permeameter measurements can be found in Camargo and Jensen (2012), Honarpour et al. (2005), and Ringrose et al. (2005).

Fig. 2—Whole cores versus core plugs. Note that the measurements are not exactly on the same scale.

## Theory and Approaches

### Statistical Characterization

Based on the above datasets, it is helpful to begin with comprehensive geostatistical analysis on $k_z$ to understand its characteristics as compared to $k_x$. This will also guide the synthesis of generic geomodels used in the flow simulations to examine the influence of $k_z$ realizations on performance prediction during $CO_2$ EOR and storage.

Based on the 42 wells' whole core measurements, we created a series of $k_z$-related exploratory plots, including vertical profiles for the three permeabilities. The histograms, well-based Dykstra-Parson coefficient, semivariograms, $k_z$ - $k_x$ cross plots, and permeability-porosity cross plots, Lorenz plots, and

Koval plots (Koval, 1963) were produced. A Koval plot is the plot of *(1-F)/F* versus *(1-C)/C* where *F* is flow capacity, and *C* is storage capacity. The vertical location of the curves on the plot measures the heterogeneity that gives clues to vertical sweep efficiency (Salazar, 2018). Detailed explanations of the Koval plot and its physical meaning are in Lake et al. (2014) and Salazar and Lake (2020).

When viewing plots such as Fig. 1 or listings of $k_z/k_x$ values, it is tempting to assume that $k_z/k_x$ should nearly always be less than one (e.g., Dernaika et al., 2018; Pamungkas et al., 2020), so there must be a problem with the measurements if $k_z/k_x > 1$ for significant portions of the data set. This assumption may be incorrect for reasons listed below and it is therefore useful to keep the questions below in mind when assessing $k_z/k_x$ values. We will use these considerations during analysis of data from the field.

i. Are the data from one geological unit (e.g., rock type or facies) or do they represent a larger domain? A clearer picture of the $k_z/k_x$ behavior is likely to emerge from unit-based data, so that characteristic $k_z/k_x$ values and how the values change can be identified.

ii. Is the formation isotropic? If the permeability is isotropic and a deterministic variable, then $k_x = k_y = k_z$. However, if we assume permeability to be isotropic and a random variable, then $k_x$, $k_y$, and $k_z$ have the same probability distribution but might be unequal for any given sample. In that case, the probability of $k_z/k_x > 1$ should be 1/3 (written as Prob($k_z/k_x > 1$) = 1/3) for tri-directional samples and ½ for bi-directional samples. Also, while the formation may not be locally isotropic, it may behave at the larger scales as being isotropic because some areas have $k_z/k_x > 1$ while other areas have $k_z/k_x < 1$. There may be good geological reasons why some $k_z/k_x$ data exceed 1. For examplfne, in sandstone reservoirs having burrowing or dewatering horizons, $k_z/k_x > 1$ (Jones et al., 1987; Hanks et al., 2011). Carbonates also may show $k_z/k_x > 1$ in dissolution enhanced or stylolite-bearing samples (e.g., Sun et al., 2017; Dernaika et al., 2018; Chandra et al., 2013).

## Flow Simulation

We ran flow simulations (using the Eclipse® simulator), to quantify the influence of $k_z$ on $CO_2$ flow/sweep and performance prediction during $CO_2$ EOR and storage. First, we synthesized a series of permeability fields according to the geostatistical analysis. Second, we conducted flow simulations of $CO_2$ injection into these synthetic models while considering the reservoir ROZ rock-fluid properties. Third, we compared various $k_z$ realizations (including direct $k_z$ statistical realizations or true $k_z$ versus assuming $k_z/k_x = 0.1$) in terms of simulation prediction for $CO_2$ EOR and storage.

Our procedure for generating permeability fields is to: i) employ the Box-Cox method (Box and Cox, 1964) to transform the reservoir permeability distributions to be more Gaussian; ii) use sequential Gaussian simulation to generate permeability fields with a given set of heterogeneity indicators; iii) back-transform to get the synthetic permeability field. Appendix A includes more details of the procedure and demonstrates that the synthetic fields reproduce the global permeability statistics.

Table 1 shows the properties of the synthetic permeability fields. Simulation models for inverted 5-spot and inverted 9-spot well patterns were created. The corresponding model dimensions and cell sizes are also in the table. The porosity was set to be constant at 0.11, the arithmetic average of the reservoir ROZ, since porosity is far less variable than permeability. It was known that vertical cell size influences miscible flood predictions, especially when gravity is important (Stalkup, 1990). This work adopted a fixed cell size since the simulation studies are designed for general sensitivity analysis.

Table 1—Properties of synthetic permeability fields

| Well pattern | Inverted 5-spot | Inverted 9-spot |
|---|---|---|
| Pattern size, acre | 40 | 80 |
| Model domain sizes, ft | 1320×1320×96 | 1860×1860×96 |
| Model cell sizes, ft | 30×30×3 | 30×30×3 |
| Model dimensions | 44×44×32 | 62×62×32 |
| Horizontal dimensionless auto-correlation length | 0.2, 2', 20 | |
| Horizontal permeability log mean | 1.5* | |
| Vertical permeability log standard deviation | 1.8* | |
| Vertical permeability log mean | 0.5* | |
| Vertical permeability log standard deviation | 2.3* | |

* Based on reservoir permeability geostatistics.

For the reservoir simulation model, the settings for the rock, fluids, and their interactions, including oil properties, PVT models, relative permeability and capillary pressure curves, were described in Ren and Duncan (2021). Since the whole simulation study is designed to examine the sensitivity of vertical permeability on $CO_2$ EOR and storage performance, we used a single set of relative permeability and capillary pressure curves. More details are included in Appendix B.

Initially, the reservoir pressure is 2119.9 psi, and the reservoir temperature is 104 °F. Uniform fluid saturations were assigned as per the average saturation magnitudes of the the reservoir ROZ (Ren and Duncan, 2019), with an initial oil saturation of 0.4 and the rest of the pore space water.

We designed injection-production schemes with a focus on the effects of $k_z$ on flow. To achieve this, we use a buoyancy number $N_{bu}$ (Shook et al., 1992, Eq. 1) to measure the relative importance of buoyant force ($k_z$-related) over viscous force (injection rate-related). The variation of $N_{bu}$ along the distance from an injector is in Fig. 3. $CO_2$ flow is dominated by the buoyant force ($N_{bu}$ >1) in most of the inter-well areas (around 115 to 1300 ft away from the injector). Thus, most of the $CO_2$ flow will tend to be gravity segregated. Our study covers a wide $N_{bu}$ range of 0.0022 to 22 through adjusting either injection rates or $k_z$ in simulation cases (see Table 2).

$N_{\mathrm{bu}}$ is defined as

$$N_{bu} = \frac{\Delta \rho g k_z H \cos\alpha}{u_h \mu L} \tag{1}$$

where $\Delta\rho$ is the density difference between $CO_2$ and the mixture of brine and oil, $g$ is the gravitational constant, $k_z$ is vertical permeability, $H$ is the well perforation height, $\alpha$ is the formation dip angle, $u_h$ is $CO_2$ entry velocity at the wellbore (it was calculated using $CO_2$ injection rate in a radial flow geometry), $\mu$ is the $CO_2$ viscosity at reservoir conditions, and $L$ is the horizontal length of the simulation domain (same as the distance from an injector in Fig. 3).

Table 2—Values for the cases of CO2 flow simulations. The "truth" cases are for the case with both variable kx and variable kz 2 realizations (i.e., case #4, 8, 12, 13, 16, 17, 19, and 23).

| Case # | $k_x$ mD | $k_z$, mD | Injection Rate, MScf/d | Injector BHP, psi | Buoyancy Number[a] | WAG ratio | Autocorrelation $\lambda_{DX}$ | Well Pattern | Notes |
|---|---|---|---|---|---|---|---|---|---|
| 1 | Constant | | 3000 | NA | 2.2E-2 | 0 | 2 | Inverted-5<br>& 40 acre | Base settings: Injection rate: WAG ratio; Horizontal dimensionless autocorrelation; |
| 2 | Constant[d] | Constant[d] | 3000 | NA | 1.4E-2 | 0 | 2 | inverted-5<br>& 40 acre | |
| 3 | Variable | $k_x$ | 3000 | NA | 2.2E-2 | 0 | 2[b] | inverted-5<br>& 40 acre | |
| 4 | Variable | Variable | 3000 | NA | 1.4E-2 | 0 | 2 | inverted-5<br>& 40 acre | |
| 1a | Variable | 10×kx[c] | 3000 | NA | 2.2E-1 | 0 | 2 | inverted-5<br>& 40 acre | Effect of buoyancy number |
| 3a | Variable | 0.1×$k_x$ | 3000 | NA | 2.2E-3 | 0 | 2 | inverted-5<br>& 40 acre | |
| 3b | Variable | 0.1 × $k_x$ | 30 | NA | 2.2E-1 | 0 | 2 | inverted-5<br>& 40 acre | |
| 5 | Constant | $k_x$ | 30 | NA | 2.2 | 0 | 2 | Inverted-5<br>&40 acre | |
| 6 | Constant | Constant | 30 | NA | 1.4 | 0 | 2 | inverted-5<br>& 40 acre | |
| 7 | Variable | $K_x$ | 30 | NA | 2.2 | 0 | 2 | inverted-5<br>& 40 acre | |
| 8 | Variable | Variable | 30 | NA | 1.4 | 0 | 2 | inverted-5<br>& 40 acre | |
| 9 | Variable | 10×$k_x$[c] | 30 | NA | 2.2 E+1 | 0 | 2 | inverted-5<br>& 40 acre | |
| 10 | Variable | $k_x$ | 3000 | NA | 2.2E-2 | 1 | 2 | inverted-5<br>& 40 acre | Effect of WAG ratio |
| 11 | Variable | $k_x$ | 3000 | NA | 2.2E-2 | 4 | 2 | inverted-5<br>& 40 acre | |
| 12 | Variable | Variable | 3000 | NA | 1.4E-2 | 1 | 2 | inverted-5<br>& 40 acre | |
| 13 | Variable | Variable | 3000 | NA | 1.4E-2 | 4 | 2 | inverted-5<br>& 40 acre | |
| 14 | Variable | $k_x$ | 3000 | NA | 2.2E-2 | 0 | 0.2 | Inverted-5<br>& 40 acre | Effect of horizontal autocorrelation length |
| 15 | Variable | $k_x$ | 3000 | NA | 2.2E-2 | 0 | 20 | Inverted-5<br>& 40 acre | |
| 16 | Variable | Variable | 3000 | NA | 1.4E-2 | 0 | 0.2 | inverted-5<br>& 40 acre | |
| 17 | Variable | Variable | 3000 | NA | 1.4E-2 | 0 | 20 | inverted-5<br>& 40 acre | |
| 18 | Variable | $k_x$ | 3000 | NA | 2.2E-2 | 0 | 2 | inverted-9<br>& 80 acre | Effect of well pattern |
| 19 | Variable | Variable | 3000 | NA | 1.4E-2 | 0 | 2 | inverted-9<br>& 80 acre | |
| 20 | Constant | $k_x$ | NA | 2800 | NA | 0 | 2 | Inverted-5<br>&40 acre | Injectivity |
| 21 | Constant | Constant | NA | 2800 | NA | 0 | 2 | inverted-5<br>& 40 acre | |

| Case # | $k_x$ mD | $k_z$, mD | Injection Rate, MScf/d | Injector BHP, psi | Buoyancy Number[a] | WAG ratio | Autocorrelation $\lambda_{DX}$ | Well Pattern | Notes |
|---|---|---|---|---|---|---|---|---|---|
| 22 | Variable | $k_x$ | NA | 2800 | NA | 0 | 2 | inverted-5 & 40 acre | |
| 23 | Variable | Variable | NA | 2800 | NA | 0 | 2 | inverted-5 & 40 acre | |
| 22a | Variable | $0.1 \times k_x$ | NA | 2800 | NA | 0 | 2 | inverted-5 & 40 acre | |
| 22b | Variable | $0.01 \times k_x$ | NA | 2800 | NA | 0 | 2 | inverted-5 & 40 acre | |

a These values of buoyancy number $N_{bu}$ are along the wellbore. Note $N_{bu}$ changes with the distance as shown in Fig. 3.

b Three realizations of permeability fields were created for the inverted-5 well pattern.

c With vertical fractures.

d Constant $k_x$ is 17.5 md, and constant $k_z$ is 11.1 md as per the reservoir arithmetic averages of permeabilities.

**Fig. 3—The change of buoyancy number $N_{bu}$ along the distance from a given $CO_2$ vertical injector. $N_{bu}$ is larger than 1 when the distance is larger than 115 ft. This means that buoyant flow prevails in a large area between an injector to producers (the interwell distance is 933 ft for the 40-acre inverted 5-spot and 1319 ft for the 80-acre inverted 9-spot well patterns). Under r reservoir conditions, the $CO_2$ density is 768kg/m$^3$, and $CO_2$ viscosity is 0.07 cp. The brine density is 915 kg/m$^3$. The vertical permeability arithmetic average is 11.1 md, and the perforation length is 96 ft (same as the thickness of the synthetic model in Table 1). The injection rate used for the calculation is 3000 MScf/d (based on settings in Table 2).**

We considered four scenarios, the details of which are listed in Table 2. We provide a brief description of the four scenarios below. Simulation predictions based on the settings in Scenario #4 (using true $k_z$) are considered to be "truth case" in the result analysis.

Scenario #1: constant $k_x$ and $k_z = 0.1\ k_x$;

Scenario #2: constant $k_x$ and $k_z$ from the reservoir arithmetic mean (i.e., average $k_x$ and average $k_z$);

Scenario # 3: variable $k_x$ with the reservoir geostatistics, and $k_z = 0.1\ k_x$;

Scenario #4: variable $k_x$ and $k_z$ with the reservoir geostatistics.

Several other parameters were also examined, including WAG ratios, horizontal dimensionless auto-correlation length ($\lambda_{Dx}$), and injector constraints. The WAG ratio is defined as the ratio of the reservoir volumes of injected water to injected $CO_2$ for a cycle; The WAG ratio 0 represents continuous $CO_2$ injection. The range of reported WAG ratios is 0 to 5 (Ettehadtavakkol et al., 2014). The ratio in this work was adjusted through changing water half-cycle size while keeping $CO_2$ half-cycle size unchanged at 2.5% HCPV. Dimensionless horizontal auto-correlation length, $\lambda_{Dx}$, is the horizontal auto-correlation length divided by the domain horizontal length. For the base case, we set $\lambda_{Dx} = 2$ considering the permeability variogram analysis for the reservoir wells. We also examined two extreme values of $\lambda_{Dx}$: 0.2 (very weak lateral autocorrelation) and 20 (strong layering). The vertical dimensionless auto-correlation length is 0.

The base case injection schemes are: $CO_2$ injection rate is 3000 MScf/day, water injection rate is 1400 bbl/day, and the total injection duration is 20 years with the WAG ratio 0 (Table 2). The base sets 200% HCPV $CO_2$ injected considering carbon sequestration, which is larger than the typical range of 30-80% HCPV for $CO_2$ EOR (Merchant, 2010). Such a large HCPV, as demonstrated in our work, tends to interact with $k_z$ in influencing $CO_2$ EOR and storage performance. The injection duration for other cases proportionally varies with injection rates for a given HCPV $CO_2$. Both constant injection rate and constant bottom hole pressure for injectors were considered, and producers were assigned a constant bottom hole pressure (minimum $CO_2$-oil miscible pressure). Other details for the settings of these parameters are in Table 2. These numerical simulations are designed for general purposes, and the understanding from them might could also be revealed from scaling groups that were mathematically derived from relatively simplistic models (e.g., Shook et al., 1992; Sikandar, 1994).

The metrics used are typical ones (Lake et al., 2019) to measure the influence of $k_z$ realizations on $CO_2$ flow: the cumulative oil production (for EOR) and cumulative $CO_2$ retention fraction (for storage). The retention fraction is (cumulative $CO_2$ injected – cumulative $CO_2$ produced) / cumulative $CO_2$ injected. It measures the efficiency of injected $CO_2$ that is stored in an oil reservoir.

## Results and Discussion

### Geological and Geostatistical Analysis Results

***Statistical Analysis for An Example Well.*** A comprehensive geostatistical analysis is essential for understanding the properties (e.g., variability, auto-correlation, and anisotropy) of $k_z$ as compared to $k_x$. In this section, $k_x$ and $k_y$ corresponds to $k_{max}$, and $k_{90}$, respectively, as termed by Honarpour et al. (2005). Fig. 4 shows a set of $k_z$ -related exploratory plots for one example well, including permeability profiles, histograms, semivariograms, Lorenz plots, Koval plots, and $k_z$ - $k_x$ cross plots.

$k_z$ tends to be overall less than $k_x$; 74.7% of the whole cores have $k_z < k_x$ (Fig. 4a). Several cycles of vertical permeability variation can be observed from the permeability profiles. Semivariograms (SVs) for log base 10 permeability (Fig. 4b) showed that $k_x$ and $k_y$ are virtually the same but $k_z$ shows much more variability. This observation is consistent with the permeability profiles (Fig. 4a): several spikes of small $k_z$ appear with small-scale cycles. Log-permeability SVs reveal more small-scale variability than untransformed permeability SVs, similar to behaviors observed by Jensen et al. (2000). Untransformed SVs (not shown) indicate that $k_x$ and $k_z$ are virtually the same, which implies that large-scale correlation and variability for both permeabilities are similar, a behavior also reported by Lucia et al. (1995). These analyses indicate that $k_z$ shows both small- and large-scale variability and that it should be more variable than $k_x$ spatially.

**Fig. 4—A series of $k_z$-related exploratory plots for example well A: (a) vertical profiles for three permeabilities (depths indicated are not actual values); (b) semi-variograms for log permeability; (c) permeability histograms with $V_{dp}$ included; (d) Lorenz plots; (e) Koval plots; (f) $k_z$-$k_x$ cross plot with the 1:1 line included; (g) permeability-porosity cross plots.**

This observation is also supported by the plots for global statistics: permeability histograms (Fig. 4c), Lorenz plots (Fig. 4d), and Koval plots (Fig. 4e). All permeability histograms are skewed right. This must

Fig. 6—CDFs of whole core permeability of wells B (a) and C (b).

Possible reasons for the different $k_z/k_x$ behaviors of wells B and C were furthers investigated. Core descriptions for both wells (by Core Labs) suggest predominant dolomite lithology with varying amounts of anhydrite—mostly as nodules-and very fine silts. Stylolites and associated cements are also present. For well B, the upper section (025 to 255 feet) has $k_z/k_x$ values similar to those of C and similar densities of stylolites; the upper section having 86% of the core samples with stylolites compared to 95% for well 5512R. The lower section of B (255 to 600 feet) has 37% of the samples with stylolites present. The Core Lab data we had does not specify the number of stylolites in each whole core sample; it simply recorded if one or more stylolites was present in the sample. To further test if there is a $k_z/k_x$ relationship with stylolites, we evaluated the conditional probability of $k_z \geq k_x$ when stylolites are present, Prob($k_z \geq k_x$ | stylolites). For well C, Prob($k_z \geq k_x$ | stylolites) = 0.08 while for well B we obtained 0.26 for the upper section and 0.38 for the lower section. Thus, the well C values suggest a strong linkage between stylolites and permeability anisotropy, while well B shows that there maybe a reduced impact of stylolites on the core-scale anisotropy.

***Statistics of $k_z$ versus $k_x$ Heterogeneities for All Wells.*** Fig. 7 shows the comparison of Dykstra-Parsons coefficient ($V_{\mathrm{dp}}$, Fig. 7a) between $k_z$ and $k_x$, along with the similar plot for the Lorenz coefficient ($L_{\mathrm{c}}$, Fig. 7b). From the scatter point distribution, it appears that both $k_z$ and $k_x$ have similar heterogeneity levels, i.e., both coefficients are mostly in the range of 0.6-0.9. However, $k_z$ tends to be a little more heterogeneous than $k_x$ at the same well. The clustering behavior of points seen in Fig. 7a is a reflection of $V_{dp}$ to compress large variability changes between wells into the small interval of 0.6 to 0.9 (Jensen and Lake, 1988).

Considering that vertical flow is over a larger area but a with smaller pressure drop than horizontal flow, even a very small $k_z$ could permit non-negligible vertical flow. Thus, the prediction of flow response to $k_z$ may have a larger uncertainty than that to $k_x$. Additionally, greater heterogeneity of $k_z$ as compared to $k_x$ cannot be honored when assuming a fixed $k_z/k_x$ ratio in reservoir simulations. We examined the consequences of this in the flow simulation section.

[redacted]

**Fig. 7—Compilation of Dykstra-Parsons coefficient $V_{dp}$ (a) and Lorenz coefficient $L_c$ (b) for both $k_z$ and $k_x$ for the 42 wells with whole-core measurements.**

## Reservoir Flow Simulation Results

***Base Case Results.*** Fig. 8 shows the influence of various $k_z$ field realizations (corresponding to cases #1-4, Table 2) on the predicted $CO_2$ EOR and storage results. At small buoyancy number $N_{bu}$, assuming $k_z = k_x$ gives comparable oil production (Fig. 8a) to variable $k_z$, but $CO_2$ retention (Fig. 8b) deviates by 6.3%. This means that $CO_2$ flow is more sensitive to $k_z$ than oil flow, which agrees with our intuition. The differences in metrics for homogeneous fields (black lines) are caused by different constants of permeabilities (17.5 vs. 11.1md, refer to Table 2).

[redacted]

**Fig. 8—The variation of cumulative oil production (a) and $CO_2$ retention fraction (b) along with injected $CO_2$ HCPV. The buoyant number are very similar for the four cases ($N_{bu}$ ≈ 2E-2). Refer to the case #1-4 in Table 2 for detailed settings.**

***Influence of Buoyancy Number on Metrics.*** Fig. 9 shows the influence of the buoyancy number $N_{bu}$ on the defined metrics when adjusting only injection rates. Increasing injection rates smears or decreases the influence of $k_z$ realizations on oil production estimates (Fig. 9a). This is intuitive since the two factors (i.e., injection rate and $k_z$) have opposite influences on $N_{bu}$ (Eq. 1). The influence of $k_z$ realizations on $CO_2$

retention forecasts (Fig. 9b) is stronger as the injection rate increases. This is because high rates cause large $CO_2$ plume volumes, which tends to be more sensitive to $k_z$ compared to small plume volumes caused by low rates.

**Fig. 9—Influence of buoyancy number $N_{bu}$ on the cumulative oil production (a) and $CO_2$ retention fraction (b). The change of $N_{bu}$ is through adjusting injection rates while keeping $k_z$ equal to $k_x$. The four runs (in the sequence of legends) correspond to the cases #3-4 and cases #7-8 in Table 2.**

Comparing Fig. 8 to Fig. 9 shows that, at large $N_{bu}$, assuming $k_z = k_x$ causes a large deviation (9.9%) in the estimated ultimate oil production. However, the different $k_z$ field realizations have a negligible influence on $CO_2$ retention. This is because buoyant flow (large $N_{bu}$) prevails in the $CO_2$ plume, and the accessed volume tends be small (reduced sweep).

Fig. 10 shows the $CO_2$ spatial distribution for $N_{bu} = 2$ at 0.5 HCPV $CO_2$ injected. Areally, the patches that are swept by $CO_2$ vary significantly for different realizations of $k_z$, particularly in the upper and middle layers. Vertically, the $CO_2$ distributions and saturations also show differences, particularly near the wellbore.

Fig. 11 shows the influence of $N_{bu}$ on the metrics when adjusting the $k_z/k_x$ ratio. At large injection rates, $k_z = 0.1\ k_x$ yields a close agreement of both oil production (Fig. 11a) and $CO_2$ retention (Fig. 11b) to the truth case (variable $k_z$), even though the $N_{bu}$ for the two cases are almost 10 times different. This implies that using the wellbore-based $N_{bu}$ cannot capture the influence of $k_z$ on flow. As $N_{bu}$ increases because of increasing $k_z$, the ultimate oil production increases, as does the ultimate $CO_2$ retention fraction. This is because the increase in $k_z$ makes the reservoir less anisotropic, and thus the injected $CO_2$ contacts more oil.

**Fig. 10—$CO_2$ areal distribution (a) in the three selected layers and $CO_2$ vertical distribution (b) along the vertical slice across the injector along the I-direction for the four cases (#5-8 in Table 2). The buoyancy number $N_{bu}$ is around 2.0 for all cases. The areal distributions show much difference in both the upper and middle layers because of vertical permeability distribution.**

At a small injection rate, using $k_z = 0.1\ k_x$ causes an underestimation of ultimate oil production by 6% (Fig. 11c). The deviation is larger than that for the large injection rate (Fig. 11c versus 11a). This is consistent with the influence of $N_{bu}$ on production and retention as explained above. Also, at the small injection rate, the instantaneous retention fraction differs (e.g., in the interval 0.2-1.0 HCPV) and slightly decrease as $N_{bu}$ increases, however, the ultimate $CO_2$ retention fractions ((Fig. 11d) were very similar regardless of the $k_z$ realizations. This is because: in the late injection period, $CO_2$ flow paths form mostly in the upper portion of the reservoir, and thus $N_{bu}$ or $k_z$ realizations exert a negligible influence on $CO_2$ retention.

**Fig. 11—Influence of buoyancy number on simulated performance. (a) and (b) are cumulative oil production and $CO_2$ retention fraction, respectively, when varying buoyancy numbers (through changing $k_z$) at a fixed *large* injection rate of 3000 MScf/d, whereas (c) and (d) are the equivalents at a fixed *small* injection rate of 30 MScf/d. The scale factors seem to work even the permeability field is heterogeneous. The four runs (in the sequence of legends) in the upper row correspond to Cases #3a, 3, 1a, and 4 in Table 2, and the runs in the lower row are from the Cases # 3b, and 7-9.**

***Influence of WAG ratio on Metrics.*** Figs. 12a and 12b show the influence of WAG ratios on the estimated performance. As the WAG ratio increases, the deviation between the case $k_z = k_x$ and the truth case (variable $k_z$) for cumulative oil production estimation increases (Fig. 12a). An opposite influence is observed for the $CO_2$ retention fraction estimation (Fig. 12b). At the same WAG ratio, setting $k_z = k_x$ yields larger oil production than variable $k_z$.

**Fig. 12—The change of simulated cumulative oil production (left) and $CO_2$ retention fraction (right) with the HCPV $CO_2$ injected through adjusting WAG ratios (a and b), horizontal dimensionless autocorrelation length $\lambda_{Dx}$ (c and d), and well pattern geometries (e and f). Two main scenarios are compared: $k_z = k_x$ versus variable $k_z$. $N_{bu}$ is around 2E-2 for all cases. In (a), The WAG ratio at 1 corresponds to 21 days (2.5% HCPV) of $CO_2$ injection alternating with 21 days of water injection.**

As the WAG ratio increases, the $k_z$ realization shows negligible influence on the ultimate $CO_2$ retention fraction (Fig. 12b). This is because a large WAG ratio means more water injected and effective diversion of $CO_2$ away from channeled paths and thus better sweep overall. In other words, large WAG ratios decrease the sensitivity in $k_z$ spatial distributions for $CO_2$ retention efficiencies for small $N_{bu}$.

***Influence of Horizontal Auto-correlation Length on Metrics.*** Figs. 12c and 12d show the influence of horizontal auto-correlation length $\lambda_{Dx}$ on oil production and $CO_2$ retention. At intermediate $\lambda_{Dx}$ (< 2), $k_z$ exerts a limited influence on these results. At large $\lambda_{Dx}$, however, there is a large effect. As $\lambda_{Dx}$ increases, both the ultimate oil production and $CO_2$ retention decrease. This is because large autocorrelated regions of permeability give rise to lateral flow channels, which cause early $CO_2$ breakthrough and sub-optimal results. The early breakthrough can also be seen from the very starting point of $CO_2$ retention decrease in Fig. 12d. In particular, at the early injection period (< 0.8 HCPV), the retention fraction overall decreases as $\lambda_{Dx}$ increases for the variable $k_z$ realization cases. The ultimate retention is less influenced by $\lambda_{Dx}$ when it is large (>2). This may be because large $\lambda_{Dx}$ cases represent moderately- to strongly-layered systems where the $CO_2$ flow paths become well-established by late injection.

***Influence of Well Pattern Geometries on Metrics.*** Figs. 12e and 12f show the influence of well pattern geometries on $CO_2$ EOR and storage performance. Assigning $k_z = k_x$ does not affect oil production for either the inverted 5-spot or inverted 9-spot well patterns. However, the configuration affects the $CO_2$ retention prediction more for the inverted 5-spot than inverted 9-spot (6.3% vs. 0.1%).

***Influence of $k_z$ on $CO_2$ Cumulative Injection.*** The above results (Figs. 8–12) are based on constant injection rates. Fig. 13 shows the influence of $k_z$ field realizations on the metrics when constraining the injector to have constant bottom hole pressure. Under this constraint, if we assume $k_z = 0.1\ k_x$, then simulations can give good estimates for oil production (Fig. 13a), $CO_2$ retention fraction (Fig. 13b), and ultimate $CO_2$ injected volume (Fig. 13c). Among the three $k_z/k_x$ ratios, the use of $k_z = 0.01\ k_x$ yields the largest errors.

**Fig. 13—The variation of cumulative oil production (a) and $CO_2$ retention fraction (b) along with the HCPV $CO_2$ injected for different $k_z$ realizations. (c) is the cumulative volume of $CO_2$ injected versus $CO_2$ injection duration for these realizations. Constant bottom hole pressure is imposed for the injector. Refer to Table 2 for the detailed case settings.**

## Comparison to Literature and Discussion

***Anisotropy ($k_z/k_x$) and Its Controls.*** Wang et al. (1998) also studied the $k_z/k_x$ behavior in the Seminole Field, in an area similar in geology to wells B and C. They suggest a core-scale formation average $k_z/k_x$ = 0.3 with $0.1 < k_z/k_x < 1$. Examination of their Fig. 12a, however, shows many data with $k_z/k_x > 1$, especially when $k_x < 3$ md. Of the 144 points shown in their data, about 1/3rd (50 points) have $k_z/k_x \geq 1$, suggesting that the formation might be considered as isotropic at the core scale. The lower section of well B, which is similar to the area studied by Wang et al. (1998), shows similar behavior to their data (Fig. 14a). However, well C exhibits smaller $k_z/k_x$ values than Wang et al. (1998) reported (Fig. 14b).

**Fig. 14—Whole core vertical and horizontal permeabilities for wells B (a) and C (b). The $k_z/k_x$ = 0.02 line is the lower value Wang et al. (1998) found appropriate by reservoir simulation. $k_z < k_x$ for nearly all the points on the right plot.**

Koepnick (1987) presents a nice description of stylolite characteristics. Whether stylolites represent flow barriers depends on conditions during and after they form, leading to mixed reports of their flow effects. Ahr (2011), for example, states that "The literature is replete with references to stylolites … and how they form permeability barriers…." but he cautions that "post-stylolite diagenesis can create porosity and permeability in previously tight rocks …." Other studies have observed stylolites to form occasional large-scale flow barriers (Koepnick, 1987), but the evidence largely suggests they only form local impediments to vertical flow (Koepnick, 1987; Heap et al., 2014; Al-Amrie et al., 2012). Data from wells B and C suggest that when stylolites are abundant, the core-scale $k_z/k_x$ values are reduced. This core-scale information will be useful for defining the larger-scale $k_z/k_x$ value.

Our work through conditional probability analysis, identified the feature of stylolite that may influence the core-scale $k_z/k_x$ ratio for this carbonate reservoir. Comparing this result with the behavior of $k_z/k_x$ and associated factors in sandstone reservoirs can prove instructive. At core scales, sandstone permeability anisotropies are caused by small-scale structures, e.g., silt beds and shale patches (Clavaud et al., 2008; Dernaika et al., 2018). Campero et al. (2014) noted that the $k_z$ /$k_x$ ratio is also a function of lithofacies (mud fraction) in a sandstone reservoir. Similar observations were made by Armitage et al. (2011) and Ringrose et al. (2005). These small-scale structures and lithofacies are difficult to explicitly model in the large scale, except for some simple deterministic distributions of shale barriers with regular geometries (Sikandar, 1994). Baker et al. (2015) showed that, in a sandstone reservoir, the $k_z$ - $k_x$ cross plot show only a few points with $k_z > k_x$, while their carbonate example shows many more $k_z > k_x$ values. Their fraction of $k_z > k_x$ is less than that in our carbonate case.

***Scale Dependence of $k_z/k_x$.*** What do the core-based anisotropic values imply for the large-scale $k_z/k_x$? Lishman (1970) states, "it is not logical to transfer anisotropy measurements made on a core sample … to a reservoir" and thus, for this large-scale $k_z/k_x$ values, geological factors beyond the wellbore must play a role. Core-scale $k_z/k_x$ values are largely controlled by small-scale geological heterogeneities (Lake, 1988; Clavaud et al., 2008). At the larger scales, different geological heterogeneities may dominate and thereby change the $k_z/k_x$ values (Dernaika et al., 2018). For example, for large-scale sedimentary environments, wave-dominated shoreface deposits tend to have more $k_z > k_x$ than river-dominated deltaic deposits (Hanks et al., 2011).

Reports on the relationship of core- to large-scale $k_z/k_x$ values is very limited, but Baker et al. (2015) show a decrease of $k_z/k_x$ by 2 to 3 orders of magnitude from core- to large-scale in three clastic formations. Morton et al. (2002) undertook a detailed comparison of core plugs, probe permeameter, and wireline tester $k_z/k_x$ values in one of the formations reported by Baker et al. (2015). Generally, they find agreement between the upscaled probe (using arithmetic and harmonic averages) and tester values. They also determined that core plugs sampled the heterogeneities insufficiently to give agreement with either the probe or tester values. Thus, Morton et al.'s (2002) results suggest extrapolation of core-scale $k_z/k_x$ ratios depends not only on how the local heterogeneities compare with the large-scale heterogeneities, but on having sufficient sampling at the core scale to render statistically meaningful values.

Unlike clastics, carbonates appear to show weaker $k_z/k_x$ trends with scale, perhaps decreasing by 1 or 2 orders of magnitude from core- to large-scale (e.g., Chandra et al., 2013; Wang et al., 1994; Pamungkas et al., 2020). This smaller change than sandstones may be partly due to better core-scale sampling, since carbonates tend to be well consolidated, have good core recoveries, and are exhaustively measured (in the vertical direction) when using whole core samples. For example, Wang et al. (1998) suggest large-scale simulation-based $k_z/k_x$ values of 0.02 to 0.04 for the area they studied in the Seminole Field. Using harmonic and arithmetic averages of data from 3 wells, they predict $k_z/k_x = 0.05$ to 0.06 from the whole core permeabilities (Wang et al., 1994). The reasonably good agreement between upscaled core and simulation $k_z/k_x$ values suggests the core-based values need only modest "adjustment" to represent larger-scale properties. In contrast, the report of Chandra et al. (2013) is a case study where core plug permeabilities were inadequate to characterize the $k_z/k_x$ in their carbonate field.

All these demonstrate the scale dependence of anisotropies or $k_z/k_x$ ratios. The core-scale $k_z/k_x$ ratio thus may not be the ratio at other scales (e.g., grid blocks in reservoir simulations), particularly if poor sampling is done. The geological controls of $k_z/k_x$ ratio can be scale-dependent, and a geologically guided procedure may be needed to scale up the ratio from cores to grid-blocks. For scales larger than grid cells, the formation anisotropy could be evaluated through using interference well tests and possibly seismic (Ayan et al., 1994; Onur et al., 2011; Wannell and Morrison, 1990).

***Influence of $k_z$ Realizations on $CO_2$ Flow/Injectivity, Retention, and Implications.*** Our direct comparison of heterogeneity between $k_z$ and $k_x$ based on the whole-core datasets showed that $k_z$ tends to be more heterogeneous and complicated than $k_x$ for this carbonate reservoir. A similar observation was made by Ringrose et al. (2005), and they found that traditional estimation functions for $k_x$ cannot give a satisfactory prediction of $k_z$ in a sandstone reservoir. Their sandstone study, along with our carbonate one here, strongly indicate that the flow influenced by $k_z$ will be more complicated than that by $k_x$, and thus flow prediction will be much more difficult.

Such flow here mostly refers to buoyant flow, and it occurs in subsurface porous media where two contrasting-density fluids exist (e.g., aquifer $CO_2$ storage (Bryant et al., 2008; Ren et al., 2018) and subsurface hydrogen storage (Hassanpouryouzband et al., 2021; Heinemann et al., 2021)). In this sense, the geological characterization of $k_z$ for these processes should be even more important than for $k_x$. Since permeability is related with capillary pressure, the latter heterogeneity on buoyant flow has received considerable attention in the context of aquifer $CO_2$ storage. It has been shown that capillary pressure heterogeneity tends to exert much more influence on small-scale upward flow paths and associated trapping quantification than permeability does (Krishnamurthy et al., 2019; Saadatpoor et al., 2018; Trevisan et al., 2017).

For the influence of $k_z$ on $CO_2$ storage, Abdelaal et al. (2021) studied the effect of the $k_z/k_x$ ratio on ultimate $CO_2$ storage capacities in a saline aquifer undergoing $CO_2$ injection. Our result (Fig. 13) showed similar findings that, at the initial period of injection, cumulative $CO_2$ injected are almost independent of $k_z/k_x$ ratios. However, at late injection, the cumulatively injected amount becomes different for these ratios. We showed that, for the studied carbonate reservoir, using the $k_z/k_x$ ratio equal to 1 is better than 0.1 in terms of $CO_2$ injection estimation (Fig. 13). The effect is however very limited for the time scale we investigated. Our work further shows that, as the injection duration increases, its effects on oil production become large when varying the $k_z/k_x$ ratio. This threshold point is around 60-100% HCPV as revealed from Figs. 9–12. This is because a long injection duration causes more $CO_2$ to be affected by buoyant flow, and the influence of $k_z$ on $CO_2$ displacing oil is thereby enhanced.

Campero et al. (2014) found that using constant $k_z/k_x$ to populate vertical permeability works in homogeneous reservoirs but fails in heterogeneous reservoirs having complex depositional environments (related to autocorrelation length). This is consistent with our findings that the oil production and $CO_2$ retention metrics change as the horizontal autocorrelation length increases. Further, our distinct contribution here is that we demonstrated the injection strategies (i.e., injection rates and WAG ratio choices) interact with reservoir heterogeneity in influencing both oil production and $CO_2$ retention prediction (Figs. 12 and 15). This interplay makes the influence of $k_z/k_x$ on flow complicated.

Generally, at the same buoyancy number ($N_{bu} \approx$ 2E-2), assuming $k_z = k_x$ overestimates both the cumulative oil recovery factor and $CO_2$ retained HCPV compared to the true case (Fig. 15). This assumption, therefore, affects the vertical positions of inflection points at which $CO_2$ retained HCPV flattens with the increase in $CO_2$ injection (Fig. 15b). The point represents the maximum injection duration for increased storage, and, after that point, injected $CO_2$ cannot be further retained. It appears that large WAG ratios and small autocorrelation lengths (less heterogeneity) shorten the time duration of reaching the inflection points. These points were not extensively observed in the report by Lake et al. (2018) because of the relatively short (1 HCPV) $CO_2$ injection duration for the reviewed projects. More work is needed to understand the controlling factors of the inflection point and possible operational strategies for moving the point toward the left top in the figure (i.e., rapid and large $CO_2$ retention) for CCUS storage. The understanding of improving volumetric sweep efficiency strategies and their interplay with reservoir heterogeneity should be the key here (Lake et al., 2018, 2019).

**Fig. 15—The change of cumulative oil recovery (HCPV, left column) and cumulative $CO_2$ retention (HCPV, right column) change cumulative $CO_2$ injection (HCPV) through adjusting WAG ratios (a and b) and horizontal autocorrelation length (c and d). $N_{bu}$ is around 2E-2 for all cases. The figure is similar to Fig. 12a-d except two changes: i) produced oil and retained $CO_2$ was measured by HCPV; ii) the x-axis was extended from 2 to 4 HCPV.**

Another noteworthy aspect of Fig. 15d is that, for continuous $CO_2$ injection, the retained $CO_2$ can be larger than 1 HCPV as injection proceeds. After 1 HCPV $CO_2$ retention, the subsequently injected $CO_2$ must occupy the space that was previously occupied by water (i.e., water displacement must be occurring). The combined voidage replacement and dissolution/miscibility analysis, as demonstrated by Lake et al (2018), is very helpful to understand $CO_2$ storage mechanisms here.

More generally, what is the $k_z/k_x$ value that would be important as a threshold if a formation appears to be anisotropic? This value depends on the flow process under consideration. For example, performance differences between $k_z/k_x = 1$ and $k_z/k_x < 0.7$ might be significant for steam-assisted gravity drainage (Azom and Srinivasan, 2011) while $k_z/k_x = 0.05$ might be the threshold value for gas coning (Addington, 1981). For our study on $CO_2$ EOR and storage here, it appears that the threshold $k_z/k_x$ ratio for flow simulations is in the range of 0.1 to 1, which can give a good forecast of both oil production and carbon sequestration performance.

## Summary, Conclusions, and Recommendations

For $CO_2$ EOR and storage in oil reservoirs, it is important to understand the intrinsic geological controls of $k_z$ to better evaluate $CO_2$ flow/sweep, oil production, and $CO_2$ storage performance. We conducted analyses of the effect of different $k_z$ estimates based on a San Andres carbonate reservoir dataset, including whole-core measurements, core facies, and thin sections. We also conducted generic flow simulations based on the geostatistical understanding of the reservoir and studied the influence of $k_z$ on $CO_2$ EOR and storage performance prediction. Our conclusions are:

1. $k_z$ tends to be more heterogeneous and complicated than $k_x$, as revealed from heterogeneity measurements. This means that assuming a fixed $k_z/k_x$ ratio is not representative; if $k_z/k_x$ ratios are taken as constants they should have the same variability.
2. $k_z > k_x$ is not unusual and, indeed, should be expected for isotropic sediments. For the reservoir studied, it appears that stylolites show statistically significant effects on $k_z$ for the core-scale anisotropy.
3. $k_z$ versus $k_x$ crossplots need care when being evaluated for characteristic $k_z/k_x$ values, paying particular attention to how many samples have $k_z > k_x$. The assumption that $k_z/k_x < 1$ can bias interpretation of these plots and give $k_z/k_x$ estimates which are too small.
4. The change of $k_z/k_x$ with increasing scale depends primarily on two factors: the change(s) of geological features controlling fluid flow and on how well the permeability measurements fully represent the core-scale heterogeneities. Whole-core measurements of carbonates may better capture the core-scale controls and thereby reduce the change in $k_z/k_x$ as scale increases.
5. The influence of $k_z$ on performance predictions depends on the flow process and regimes. The buoyancy number proved to be a useful method to characterize the gravity-viscous competition.
6. The accuracy of results by assuming a constant $k_z/k_x$ ratio for flow performance prediction is heavily influenced by WAG ratios and autocorrelation lengths, but less by well patterns.
7. As $CO_2$ injection duration increases, the influence of $k_z$ on flow also increases. $k_z$ shows limited influence on cumulative $CO_2$ injected volumes.

To evaluate $CO_2$ EOR and storage performance, we recommend a serial of flow numerical tests on $k_z$, as shown in this work, before any large or full-field scale flow simulation efforts.

## Acknowledgements

We thank Robin Dommisse for valuable discussions during this work. Bo Ren would like to thank Dr. Tingwei "Lucy" Ko for the discussion on geological features and data collection. We thank an anonymous operator for allowing us to access the Core Lab data. This study is part of a long-term project investigating ROZ reservoirs in the Permian Basin of Texas being carried out by the Bureau of Economic Geology's (BEG's) State of Texas Advanced Resource Recovery (STARR) Program. Larry W. Lake holds the Shahid and Sharon Ullah Endowed Chair in the Hildebrand Department of Petroleum and Geosystems Engineering at The University of Texas at Austin. This document is published with the approval of the Director of the Bureau of Economic Geology.

## Nomenclature

| | |
|---|---|
| $C$ | Storage capacity |
| $F$ | Flow capacity |
| $H$ | Well perforation length |
| $k_{rg}$ | Gas relative permeability |
| $k_{rw}$ | Water relative permeability |
| $k_{ro}$ | Oil relative permeability |

| | |
|---|---|
| $k_x$ | x-direction permeability |
| $k_y$ | y-direction permeability |
| $k_z$ | Vertical permeability |
| $k_{max}$ | Maximum horizontal permeability |
| $k_{90}$ | Minimum horizontal permeability |
| $L$ | Lateral length of the simulation domain |
| $L_c$ | Lorenz coefficient |
| $N_{bu}$ | Buoyancy Number |
| $u_h$ | $CO_2$ entry velocity at the wellbore |
| $V_{dp}$ | Dykstra-Parsons coefficient |
| $\alpha$ | Formation dip angle |
| $\lambda_{Dx}$ | Horizontal dimensionless auto-correlation length |
| $\rho$ | Phase density |
| $\Delta$ | Difference |
| $\mu$ | Phase viscosity |

## References

Abdelaal, M., Zeidouni, M. and Duncan, I.J. 2021. Effects of injection well operation conditions on $CO_2$ storage capacity in deep saline aquifers. *Greenhouse Gases: Science and Technology*. **0**:1–16. https://doi.org/10.1002/ghg.2076

Addington, D.V. 1981. An approach to gas-coning correlations for a large grid cell reservoir simulator. *Journal of Petroleum Technology*. **33**(11): 2267–2274. https://doi.org/10.2118/8332-PA

Ahr, W.M., 2011. Geology of Carbonate Reservoirs: the identification, description, and characterization of hydrocarbon reservoirs in carbonate rocks. John Wiley & Sons.

Al-Amrie, O.Y., Ben-Saad, M.A., Al Marzouqi, K.I., Kshirsagar, A.H. and Coskun, S.B. 2012. The use of formation tester to characterize the permeability and vertical communication across the stylolite zones in carbonate reservoir. Paper presented at the Abu Dhabi International Petroleum Conference and Exhibition, Abu Dhabi, UAE, 11-14 November. SPE-160956-MS. https://doi.org/10.2118/160956-MS

Armitage, P.J., Faulkner, D.R., Worden, R.H., Aplin, A.C., Butcher, A.R. and Iliffe, J., 2011. Experimental measurement of, and controls on, permeability and permeability anisotropy of caprocks from the $CO_2$ storage project at the Krechba Field, Algeria. *Journal of Geophysical Research: Solid Earth*. **116**(B12). https://doi.org/10.1029/2011JB008385

Ayan, C., Colley, N., Cowan, G., Ezekwe, E., Goode, P., Halford, F., Joseph, J., Mongini, A., Obondoko, G., Pop, J. 1994. Measuring permeability anisotropy: The latest approach. *Oilfield Review*;(Netherlands), **6**(4).

Azom, P.N., Srinivasan, S. 2011. Modeling the effect of permeability anisotropy on the steam-assisted gravity drainage (SAGD) process. Paper presented at the Canadian Unconventional Resources Conference, Calgary, Alberta, Canada, 15-17 November. SPE-149274-MS. https://doi.org/10.2118/149274-MS

Baker, R.O., Yarranton, H.W., Jensen, J. L. 2015. *Practical Reservoir Engineering and Characterization*. Gulf Professional Publishing.

Box, G.E. and Cox, D.R. 1964. An analysis of transformations. *Journal of the Royal Statistical Society: Series B (Methodological)*. **26**(2), 211–243. https://www.jstor.org/stable/2984418

Bryant, S.L., Lakshminarasimhan, S. and Pope, G.A. 2008. Buoyancy-dominated multiphase flow and its effect on geological sequestration of $CO_2$. *SPE Journal*. **13**(04): 447–454. https://doi.org/10.2118/99938-PA

Camargo, J.E.N. and Jensen, J.L. 2012. Analysis of fault permeability using mapping and flow modeling, Hickory Sandstone Aquifer, Central Texas. *Natural Resources Research*. **21**(3): 395–409. https://doi.org/10.1007/s11053-012-9181-5

Campero, M.F., Nwonodi, C., Onwuchekwa, C., Eke, K., Adenaiye, O., Igogo, A., Adekoya, O. and Anosike, E. 2014. $K_v/K_h$ in heterogeneous reservoirs of a brown field of the Niger delta of Nigeria-valuable uncertain parameter for assisted history matching. Paper presented at the SPE Nigeria Annual International Conference and Exhibition, Lagos, Nigeria, 5-7 August. SPE-172450-MS. https://doi.org/10.2118/172450-MS

Chandra, V.S., Geiger, S., Corbett, P., Steele, R., Milroy, P., Barnett, A. and Wright, P.V. 2013. Using near wellbore upscaling to improve reservoir characterisation and simulation in highly heterogeneous carbonate reservoirs. Paper presented at the SPE Reservoir Characterization and Simulation Conference and Exhibition, Abu Dhabi, UAE, 16-18 September. https://doi.org/10.2118/166033-MS

Clavaud, J.B., Maineult, A., Zamora, M., Rasolofosaon, P., Schlitter, C. 2008. Permeability anisotropy and its relations with porous medium structure. *Journal of Geophysical Research: Solid Earth*. **113**(B1). https://doi.org/10.1029/2007JB005004

Dernaika, M., Al Mansoori, M., Singh, M., Al Dayyani, T., Kalam, Z., Bhakta, R., Koronfol, S. and Uddin, Y.N. 2018. Digital and conventional techniques to study permeability heterogeneity in complex carbonate rocks. *Petrophysics*. **59**(03): 373–396. https://doi.org/10.30632/PJV59N3-2018a6

Ettehadtavakkol, A., Lake, L.W. and Bryant, S.L. 2014. $CO_2$-EOR and storage design optimization. *International Journal of Greenhouse Gas Control*. **25**: 79–92. https://doi.org/10.1016/j.ijggc.2014.04.006

Haldorsen, H.H. and Lake, L.W., 1984. A new approach to shale management in field-scale models. *SPE Journal*. **24**(04): 447–457. https://doi.org/10.2118/10976-PA

Hanks, C., Shimer, G., Davis, J., Wentz, R., Godabrelidze, V., Shukla, C., Levi-Johnson, O., Huckaby, A., McCarthy, P., Mongrain, J. and Dandekar, A. 2011. Production of Light Oil from a Shallow Frozen Reservoir: A Redevelopment Case Study of the Umiat Oil Field, Northern Alaska. Paper presented at the OTC Arctic Technology Conference, Houston, Texas, USA, 7-9 February. OTC-22064-MS. https://doi.org/10.4043/22064-MS

Hassanpouryouzband, A., Joonaki, E., Edlmann, K., Haszeldine, R.S. 2021. Offshore geological storage of hydrogen: Is this our best option to achieve net-zero? *ACS Energy Letters*. **6**:2181–2186. https://doi.org/10.1021/acsenergylett.1c00845

Heap, M.J., Baud, P., Reuschlé, T. and Meredith, P.G. 2014. Stylolites in limestones: Barriers to fluid flow? *Geology*. **42**(1): 51–54. https://doi.org/10.1130/G34900.1

Heinemann, N., Alcalde, J., Miocic, J.M., Hangx, S.J., Kallmeyer, J., Ostertag-Henning, C., Hassanpouryouzband, A., Thaysen, E.M., Strobel, G.J., Schmidt-Hattenberger, C., Edlmann, K. 2021. Enabling large-scale hydrogen storage in porous media–the scientific challenges. *Energy & Environmental Science*. **14**(2): 853–864. https://doi.org/10.1039/d0ee03536j

Hinton, E. M. Woods, A. W. 2019. The effect of vertically varying permeability on tracer dispersion. *Journal of Fluid Mechanics*. **860**: 384–407. https://doi.org/10.1017/jfm.2018.891

Honarpour, M.M., Djabbarah, N.F. and Sampath, K. 2005. Whole core analysis-experience and challenges. *SPE Reservoir Evaluation & Engineering*. **8**(06): 460–469. https://doi.org/10.2118/81575-PA

Jarrell, P.M., Fox, C.E., Stein, M.H. and Webb, S.L., 2002. Practical aspects of $CO_2$ flooding (Vol. **22**, p.2002). Richardson, TX: Society of Petroleum Engineers.

Jensen, J.L., Hinkley, D.V. and Lake, L.W. 1987. A statistical study of reservoir permeability: distributions, correlations, and averages. *SPE Formation Evaluation*. **2**(04): 461–468. https://doi.org/10.2118/14270-PA

Jensen, J. L., and Lake, L. W., 1988. The influence of sample size and permeability distribution on heterogeneity measures. *SPE Reservoir Engineering*. **3**(02): 629–637. https://doi.org/10.2118/15434-PA

Jensen, J.L., Glasbey, C.A. Corbett, P.W.M. 1994. On the interaction of geology, measurement, and statistical analysis of small-scale permeability measurements. *Terra Nova*. **6**(4): 397–403. https://doi.org/10.1111/j.1365-3121.1994.tb00513.x

Jensen, J. L., Lake, L. W., Corbett, P. W. M., Goggin, D. J., 2000, *Statistics for Petroleum Engineers and Geoscientists*, 2nd ed., Elsevier.

Jones, J.R., Scott, A.J. and Lake, L.W. 1987. The geologic aspects of reservoir characterization for numerical simulation: Mesaverde meanderbelt sandstone, northwestern Colorado. *SPE Formation Evaluation*. **2**(01): 97–107. https://doi.org/10.2118/13052-PA

Kerans, C., Lucia, F.J., Senger, R.K. 1994. Integrated characterization of carbonate ramp reservoirs using Permian San Andres Formation Outcrop Analogs. *AAPG Bulletin*. **78** (2): 181–216. https://doi.org/10.1306/BDFF905A-1718-11D7-8645000102C1865D

Koepnick, R.B. 1987. Distribution and permeability of stylolite-bearing horizons within a Lower Cretaceous carbonate reservoir in the Middle East. *SPE Formation Evaluation*. **2**(02): 137–142. https://doi.org/10.2118/14173-PA

Koval, E. 1963. A method for predicting the performance of unstable miscible displacement in heterogeneous media. *SPE Journal*. **3**(02): 145–154. https://doi.org/10.2118/450-PA

Krishnamurthy, P.G., Meckel, T.A., DiCarlo, D. 2019. Mimicking geologic depositional fabrics for multiphase flow experiments. *Water Resources Research*. **55**(11): 9623–9638. https://doi.org/10.1029/2019WR025664

Lake, L.W. 1988. The origins of anisotropy (includes associated papers 18394 and 18458). *Journal of Petroleum Technology*. **40**(04): 395–396. https://doi.org/10.2118/17652-PA

Lake, L. W., Lotfollahi, M., Bryant, S. L. 2018. Fifty years of field observations: Lessons for $CO_2$ storage from $CO_2$ enhanced oil recovery. Paper presented at the 14th international conference on greenhouse gas control technologies (GHGT-14), Melbourne, Australia, 21-25 October. http://dx.doi.org/10.2139/ssrn.3366254

Lake, L.W., Lotfollahi, M., Bryant, S.L. 2019. $CO_2$ enhanced oil recovery experience and its messages for $CO_2$ storage. *In Science of Carbon Storage in Deep Saline Formations* (pp. 15–31), Elsevier. https://doi.org/10.1016/B978-0-12-812752-0.00002-2

Lake, L.W., Johns, R., Rossen, B., Pope, G. 2014. *Enhanced Oil Recovery*, 2nd edition. Richardson TX: Society of Petroleum Engineers.

Lishman, J.R. 1970. Core permeability anisotropy. *Journal of Canadian Petroleum Technology*. **9**(02): 79–85. https://doi.org/10.2118/70-02-01

Lucia, F.J. 1995. Rock-fabric/petrophysical classification of carbonate pore space for reservoir characterization. *AAPG Bulletin*.**79**(9): 1275–1300. https://doi.org/10.1306/7834D4A4-1721-11D7-8645000102C1865D

Lucia, F.J., Kerans, C., Wang, F.P. 1995. Fluid-flow characterization of dolomitized carbonate-ramp reservoirs: San Andres Formation (Permian) of Reservoir Field and Algerita escarpment, Permian Basin, Texas and New Mexico. *Hydrocarbon Reservoir Characterization: Geologic Framework and Flow Unit Modeling*, E.L. Stoudt and P.M. Harris (eds.), SEPM Short Course No. 34 (1995) 129–153 SEPM, SC34, 129-153. https://doi.org/10.2110/scn.95.34.0129

Merchant, D.H. 2010. Life Beyond 80: A look at conventional WAG recovery beyond 80% HCPV injected in $CO_2$ tertiary floods. Paper presented at the SPE International Conference on CO2 Capture, Storage, and Utilization, New Orleans, Louisiana, USA, 10-12 November. SPE-139516-MS. https://doi.org/10.2118/139516-MS

Morton, K., Thomas, S., Corbett, P. W. M., and Davies, D. 2002. Detailed analysis of probe permeameter and interval pressure transient test data measurements in a heterogeneous reservoir. *Petroleum Geoscience*. **8**:209–216. https://doi.org/10.1144/petgeo.8.3.209

Pamungkas, S., Gueye, T., Al Hammadi, F.Y.A. and Al Saadi, H.A. 2020. A novel technique to constrains kv/kh of carbonate reservoir, a valuable uncertain parameter for history match process. Paper presented at the Abu Dhabi International Petroleum Exhibition & Conference, Abu Dhabi, UAE, 9-12 November. SPE-202832-MS. https://doi.org/10.2118/202832-MS

Ren, B., Delaney, J.M., Lake, L.W. and Bryant, S.L. 2018. Interplay between permeability retardation and capillary trapping of rising carbon dioxide in storage reservoirs. *SPE Journal*. **23**(05): 1866–1879. https://doi.org/10.2118/187356-PA

Ren, B., Duncan, I. 2019. Modeling oil saturation evolution in residual oil zones: Implications for $CO_2$ EOR and sequestration. *Journal of Petroleum Science and Engineering*. **177**: 528–539. https://doi.org/10.1016/j.petrol.2019.02.072

Ren, B., Duncan, I.J. 2021. Maximizing oil production from water alternating gas ($CO_2$) injection into residual oil zones: The impact of oil saturation and heterogeneity. *Energy*. **222**, 119915119915. https://doi.org/10.1016/j.energy.2021.119915

Ringrose, P., Nordahl, K., Wen, R. 2005. Vertical permeability estimation in heterolithic tidal deltaic sandstones. *Petroleum Geoscience*. **11**(1): 29–36. https://doi.org/10.1144/1354-079303-614

Saadatpoor, E., Bryant, S.L., Sepehrnoori, K. 2010. New trapping mechanism in carbon sequestration. *Transport in porous media*. **82**(1): 3–17. https://doi.org/10.1007/s11242-009-9446-6

Salazar, J.J. 2018. Heterogeneity study of the Little Creek field from petrophysical data. Master Thesis. The University of Texas at Austin.

Salazar, J.J. and Lake, L.W. 2020. The physical meaning of the Koval factor. *Mathematical Geosciences*. **52**(8): 1017–1033. https://doi.org/10.1007/s11004-020-09883-0

Shook, M., Li, D. and Lake, L.W. 1992. Scaling immiscible flow through permeable media by inspectional analysis. *In Situ*. **16**: 311–311.

Sikandar, A.S. 1994. A study of barrier efficiency. Master Thesis. The University of Texas at Austin.

Silin, D., Patzek, T., Benson, S.M. 2009. A model of buoyancy-driven two-phase countercurrent fluid flow. *Transport in Porous Media*, **76**(3): 449–469. https://doi.org/10.1007/s11242-008-9257-1

Stalkup, F. I., Lo. L. L., Dean, R.H. 1990. Sensitivity to gridding of miscible flood predictions made with upstream differenced simulators. Paper presented at the SPE/DOE Enhanced Oil Recovery Symposium, Tulsa, Oklahoma, 22-25 April. SPE-20178-MS. https://doi.org/10.2118/20178-MS

Sun, H., Vega, S. and Tao, G. 2017. Analysis of heterogeneity and permeability anisotropy in carbonate rock samples using digital rock physics. *Journal of petroleum science and engineering*.**156**: 419–429. https://doi.org/10.1016/j.petrol.2017.06.002

Trevisan, L., Krishnamurthy, P.G., Meckel, T.A. 2017. Impact of 3D capillary heterogeneity and bedform architecture at the sub-meter scale on $CO_2$ saturation for buoyant flow in clastic aquifers. *International Journal of Greenhouse Gas Control*. **56**: 237–249. https://doi.org/10.1016/j.ijggc.2016.12.001

Wang, F. P., Lucia, F. J., Kerans, C. 1994. Critical scales, upscaling, and modeling of shallow-water carbonate reservoirs. Paper presented at the Permian Basin Oil and Gas Recovery Conference, Midland, Texas, 16-18 March. SPE-27715-MS. https://doi.org/10.2118/27715-MS

Wang, F.P., Lucia, F.J., Kerans, C. 1998. Integrated reservoir characterization study of a carbonate ramp reservoir: Reservoir San Andres Unit, Gaines County, Texas. *SPE Reservoir Evaluation & Engineering*. **1**(02): 105–113. https://doi.org/10.2118/36515-PA

Wannell, M.J. and Morrison, S.J. 1990. Vertical permeability measurement in new reservoirs using tidal pressure changes. Paper presented at the SPE Annual Technical Conference and Exhibition, New Orleans, Louisiana, 23-26 September. SPE-20532-MS. https://doi.org/10.2118/20532-MS

Ward, R., Kendall, C. G. St. C., Harris P. M. 1986. Upper Permian (Guadalupian) facies and their association with hydrocarbons Permian Basin: West Texas and New Mexico. *AAPG*. **70**: 239–262. https://doi.org/10.1306/9488566F-1704-11D7-8645000102C1865D

Yang, G., Butler, R.M. 1992. Effects of reservoir heterogeneities on heavy oil recovery by steam-assisted gravity drainage. *Journal of Canadian Petroleum Technology*. **31**(08): 37–43. https://doi.org/10.2118/92-08-03

# Appendix A

## Reproduction of Reservoir Permeability Geostatistics in Synthetic Models

This appendix illustrates detailed procedures of using both the Box-Cox method and sequential Gaussian simulation to reproduce the permeability statistics in synthetic models. For the Box-Cox method, the transformation of Y has the form: $Y(\lambda) = (Y^{\lambda} - 1)/\lambda$, if $\lambda \neq 0$; $Y(\lambda) = \log Y$, if $\lambda = 0$. Based on the reservoir whole-core measurements of $k_{max}$ (see the light blue curve in Fig.A-1(a)), we calculated that the optimal $\lambda$ is 0.081 that results in the best approximation of a normal distribution of $k_{max}$. Then, based on the global statistics of normal distribution, we generated the corresponding three-dimensional permeability field with a set of other constraints (including model dimensions and autocorrelation length) using sequential gaussian simulation. After this step, we substituted the generated permeability back into the Box-Cox equation and back-calculated Y to get the simulated permeabilities. They are compared to the core permeability in Fig. A-1. Both the cumulative distribution function and Q-Q plot demonstrate that the global permeability statistics of the reservoir are captured in the synthetic permeability field.

**Fig. A-1—Comparative plots used to show the reproduction of the core permeability through using the proposed procedures. (a) is the permeability cumulative distribution function for cores versus the simulated permeability field with the horizontal dimensionless autocorrelation length 2 for an inverted 5-spot well pattern. (b) The Q-Q plot for the two permeability datasets (cores vs. simulated).**

# Appendix B

## Reservoir Simulation Model Inputs

This appendix lists the main inputs for the reservoir flow simulation model. These inputs include crude oil properties, $CO_2$-oil interaction, relative permeability curves. The reservoir oil viscosity is 1.2 cp with the density of 657.7 kg/$m^3$ at the reservoir condition. The minimum miscibility pressure for the $CO_2$-oil system is around 1400 psi. Peng-Robinson equation of state (EOS) was used to model the PVT behaviors. More details are in Ren and Duncan (2021). Table B-1 shows the oil compositions, and Table B-2 are the binary interaction coefficients for pseudo components. Fig. B-1 shows the relative permeability curves for the oil-water and oil-gas systems. The Stone I model was used to calculate oil relative permeability during 3-phase flow. Hysteresis was not considered, and its influence on performance prediction was discussed in Ren and Duncan (2021). End-point scaling is used to consider the influence of permeability variations on relative permeability curves in flow simulations.

**Table B-1—Representative crude oil compositions for the San Andres ROZ.**

| Component | $CO_2$ | $C_1N_2$ | $C_2C_3H_2S$ | $C_4$-$C_6$ | $C_7$-$C_{10}$ | $C_{11}$-$C_{16}$ | $C_{17+}$ |
|---|---|---|---|---|---|---|---|
| Mole fraction, % | 0.02 | 20.14 | 15.9 | 8.99 | 17.29 | 18.42 | 19.24 |
| Critical temperature (R) | 547.56 | 339.21 | 619.38 | 835.43 | 1117.84 | 1344.62 | 1686.57 |
| Critical pressure (psi) | 1071.34 | 666.77 | 722.56 | 491.3 | 389.65 | 277.42 | 159.29 |
| Critical volume ($ft^3$/lb-mole) | 1.51 | 1.56 | 2.71 | 5.02 | 7.73 | 12.13 | 22.15 |
| Critical Z-factor | 0.275 | 0.287 | 0.295 | 0.275 | 0.251 | 0.233 | 0.195 |
| Molecular weights (g/mol) | 44.01 | 16.29 | 36.19 | 70.06 | 114.17 | 180.94 | 358.25 |
| Acentric Factor | 0.225 | 0.0139 | 0.125 | 0.245 | 0.383 | 0.582 | 1.0054 |
| Coefficient $\Omega_a$ | 0.457 | 0.457 | 0.457 | 0.457 | 0.457 | 0.457 | 0.457 |
| Coefficient $\Omega_b$ | 0.077 | 0.077 | 0.077 | 0.077 | 0.077 | 0.077 | 0.077 |

**Table B-2—Binary interaction coefficients for pseudo components.**

| Component | $CO_2$ | $C_1N_2$ | $C_2C_3H_2S$ | $C_4$-$C_6$ | $C_7$-$C_{10}$ | $C_{11}$-$C_{16}$ | $C_{17+}$ |
|---|---|---|---|---|---|---|---|
| $CO_2$ | 0 | | | | | | |
| $C_1N_2$ | 0.0976 | 0 | | | | | |
| $C_2C_3H_2S$ | 0.1289 | 0.0103 | 0 | | | | |
| $C_4$-$C_6$ | 0.1271 | 0.0019 | 0.0063 | 0 | | | |
| $C_7$-$C_{10}$ | 0.1105 | 0.0241 | 0.0196 | 0.003 | 0 | | |
| $C_{11}$-$C_{16}$ | 0.0943 | 0.0494 | 0.0333 | 0.0061 | 0 | 0 | |
| $C_{17+}$ | 0.0997 | 0.1365 | 0.0588 | 0.012 | 0 | 0 | 0 |

Fig. B-1—Relative permeability curves for oil-water (a) and oil-gas (b) systems.

# Appendix C

## Koval Plots and $k_z$–$k_x$ Crossplots for Other Wells

This appendix shows the compilation of Koval plots and $k_z$-$k_x$ crossplots for other wells.

**Fig. C-1—Koval plots for several selected wells. The curves for $k_x$($k_{max}$) and $k_y$($k_{90}$) are virtually identical because they are from unoriented cores.**

**Fig. C-2—Vertical permeability versus maximum horizontal permeability cross plots for several selected wells. Both permeability measurements are reported on a log scale. A 1:1 line is provided for reference. The probability of $k_z > k_x$ is included in each plot.**

# Analysis of Vertical Permeability and Its Influence on CO2 Enhanced Oil Recovery and Storage in a Carbonate Reservoir

**Bo Ren[1]*, Jerry L. Jensen[1], Larry W. Lake[1], Ian J. Duncan[1], and Frank Male[1,2]**

[1]The University of Texas at Austin
[2]Now with Shell Oil Company

## Summary

The objective of this study is to improve understanding of the geostatistics of vertical (bed-normal) permeability ($k_z$) and its influence on reservoir performance during $CO_2$ enhanced oil recovery (EOR) and storage. $k_z$ is scrutinized far less often than horizontal permeability ($k_x$, $k_y$) in most geological and reservoir modeling. However, our work indicates that it is equally important to understand $k_z$ characteristics to better evaluate their influence on $CO_2$ EOR and storage performance prediction.

We conducted this study on approximately 9,000 whole-core triaxial permeability ($k_x$, $k_y$, $k_z$) measurements from 42 wells in a San Andres carbonate reservoir. We analyzed $k_z$ data, including heterogeneity, correlation, and sample sufficiency measures. We analyzed wells with the largest and smallest fractions of points with $k_z > k_{\max} = \max(k_x, k_y)$ to explore geological factors that coincided with large $k_z$. We quantified these geological effects through conditional probabilities on potential permeability barriers (e.g., stylolites).

Every well had at least some whole cores where $k_z > k_{\max}$. This is a statistically justifiable result; only where Prob($k_z > k_{\max}$) is statistically different from 1/3 are core samples nonisotropic. In conventional core data interpretation, however, modelers usually assume $k_z$ is less than $k_{\max}$. For the well with the smallest fraction (11%) of cores where $k_z > k_{\max}$, the cumulative distribution functions (CDFs) differ and coincide with the presence of stylolites. We found that $k_z$ is approximately twice as variable as $k_x$ in many wells. This makes $k_z$ more difficult to interpret because it was (and usually is) heavily undersampled.

To understand the influence of $k_z$ heterogeneity on $CO_2$ flow, we built a series of flow simulation models that captured these geostatistical characteristics of permeability, while considering $k_z$ realizations, flow regimes (e.g., buoyant flow), $CO_2$ injection strategies, and reservoir heterogeneity. $CO_2$ flow simulations showed that, for viscous flow, assuming variable $k_x$ similar to the reservoir along with a constant $k_z/k_x = 0.1$ yields a close (within 0.5%) cumulative oil production to the simulation case with both $k_x$ and $k_z$ as uncorrelated variables. However, for buoyant flow, oil production differs by 10% [at 2.0 hydrocarbon pore volume (HCPV) of $CO_2$ injected] between the two cases. Such flows could occur for small $CO_2$ injection rates and long injection times, in interwell regions, and/or with vertically permeable conduits.

Our geostatistical characterization demonstrates the controls on $k_z$ in a carbonate reservoir and how to improve conventional interpretation practices. This study can help $CO_2$ EOR and storage operators refine injection development programs, particularly for reservoirs where buoyant flow exists. More broadly, the findings potentially apply to other similar subsurface buoyancy-driven flow displacements, including hydrogen storage, geothermal production, and aquifer $CO_2$ sequestration.

## Introduction

Vertical permeability is important in many subsurface processes where there is a density difference between fluids, including gas (e.g., $CO_2$) EOR and geologic storage, geothermal production, hydrogen storage, compressed air storage, tracer flow, steam injection, and water coning (Bryant et al. 2008; Hassanpouryouzband et al. 2021; Hinton and Woods 2018; Yang and Butler 1992; Silin et al. 2008). Specifically, for $CO_2$ EOR and storage in oil reservoirs, $k_z$ characterization is important for reservoir management and development endeavors, including optimization of injector/producer placement, design of completion strategies, and deployment of reservoir monitoring programs during $CO_2$ injection as well as post-injection periods.

Vertical permeability can be measured at several scales. At core scales (i.e., cm and dm), whole-core samples are convenient because permeability is measured in three directions on the same sample. Core plugs drilled orthogonal to local bedding planes can also be used. At larger scales, formation testers (e.g., Ayan et al. 1994; Onur et al. 2011), history-matched reservoir simulation (Sutton et al. 2013), analytical and semianalytical calculations (e.g., Haldorsen and Lake 1984; Begg and King 1985), and ocean tide pressure variations (e.g., Wannell and Morrison 1990) may be used to estimate $k_z$. Of all these methods, core-scale measurements are perhaps the most common.

Core-scale $k_z$ is often compared with the horizontal permeability measured at the same or a nearby location by calculating the ratio $k_z/k_x$. There appear to be two main reasons for using the ratio. First, one may expect that $k_z$ and $k_x$ are positively correlated, so that $k_z/k_x$ is less variable than either $k_z$ or $k_x$. The less variable a reservoir characteristic is, the easier it is to predict for areas beyond the wellbore. Second, $k_x$ measurements are typically more abundant than $k_z$ measurements, so that a knowledge of $k_x$ and $k_z/k_x$ will provide $k_z$ estimates at the same frequency as $k_x$ values. Typically, log-log plots of $k_z$ vs. $k_x$ **(Fig. 1)** offer a useful assessment of the $k_z/k_x$ values present in a reservoir.

The use of $k_z/k_x$ ratio is a common way of modeling $k_z$. Then the question to be answered is: What are the consequences of avoiding $k_z$ measurements by using $k_x$ measurements instead? Several associated questions also arise: (i) Is $k_z$ always dependent on $k_x$ or is it independent? (ii) Do both permeabilities have the same/similar statistical properties? (iii) What are the influential factors of $k_z/k_x$ ratio? The $k_z/k_x$ ratio is typically assumed to be 0.1. However, several studies on sandstones (Jones et al. 1987; Hanks et al. 2011; Baker et al. 2015) and

---

*Corresponding author; email: bo.ren@beg.utexas.edu

This paper (SPE 205995) was accepted for presentation at the SPE Annual Technical Conference and Exhibition, Dubai, UAE, 21–23 September 2021, and revised for publication. Original manuscript received for review 12 July 2021. Revised manuscript received for review 21 September 2021. Paper peer approved 21 October 2021.

**Fig. 1—Sherwood Sandstone core plug data from a strongly laminated fluvio-aeolian reservoir with $k_z/k_x$ lines drawn to evaluate core-scale anisotropy. $k_z/k_x$ varies by approximately four orders of magnitude while either $k_z$ or $k_x$ change by six orders of magnitude. With 232 bidirectional pairs for this figure, Prob($k_z/k_x > 1$) = 63/232 = 0.27 (probabilities are equivalent to frequencies in this work). Because this probability is much different from ½, it is extremely unlikely (probability of approximately $2\times10^{-12}$) to get only 63 out of 232 samples with $k_z/k_x > 1$ if the core-scale permeability is isotropic for these data. See Morton et al. (2002) for more details on the Sherwood Sandstone.**

carbonates (Chandra et al. 2013; Sun et al. 2017; Dernaika et al. 2018), including the work presented here, showed the occurrences where $k_z > k_x$. The underlying geological causes should be well understood for reliable geomodels and multiphase flow simulations.

A considerable number of studies have focused on the influence of $k_z$ on flow prediction. Unfortunately, most flow simulations that consider $k_z$ typically treat the $k_z/k_x$ ratio as a sensitivity parameter and examine its influence on defined metrics (e.g., Kerans et al. 1994; Ren and Duncan 2021; Abdelaal et al. 2021). Campero et al. (2014) went further and analyzed $k_z/k_x$ based on the geological data sets collected in a field and evaluated the influence of $k_z/k_x$ ratio on history match and prediction during waterflooding. However, all these studies avoided a fundamental question: How good is using a constant $k_z/k_x$ ratio for each facies or reservoir to populate vertical permeability for flow prediction as compared to having variable $k_z$?

Our objectives here are to deepen our understanding of the statistical properties of $k_z$, examine $k_z$'s influence on $CO_2$ flow, storage, and production prediction, and specifically compare performance prediction between the case of using true $k_z$ vs. the traditional approach of assuming a ratio for $k_z/k_x$.

Our study is based on a San Andres carbonate reservoir. The San Andres Formation (SAF) is one of the richest oil formations in the Permian Basin, and many $CO_2$ EOR projects are active in the formation (Jarrell et al. 2002; Lake et al. 2018). It could be expected that $CO_2$ storage incidental to EOR will likely be implemented in those Permian Basin carbonate formations in the near future. In this sense, our case study on the carbonate reservoir should provide a good reference for the understanding of $k_z$ and its influence on $CO_2$ EOR and storage.

We conducted $k_z$-related exploratory plots, including permeability profiles, histograms, heterogeneity measures, and semivariogram (SV) analyses. Then, based on the geostatistical analysis, we selected the wells with the extreme fractions of $k_z > k_x$. We analyzed whole core, thin sections, and core plug data sets of the selected wells to explore the geological factors of $k_z$. We also conducted probability analyses conditioned by potential permeability barriers to quantify geological parameters. We then built a series of generic flow simulation models based on this geostatistical understanding, while considering various injection strategies and flow regimes, to quantify the influence of $k_z$ realizations on $CO_2$ EOR and storage performance.

## San Andres Formation

The carbonate facies of the SAF developed on the shelves of the Permian Basin in west Texas and New Mexico during the Permian (Leonardian-Guadalupian) ages (Ward et al. 1986). The SAF is one of several shallow-water platform carbonate and mixed siliciclastic-carbonate units. From the sequence stratigraphy studies by Kerans et al. (1994), Lucia et al. (1995), and Wang et al. (1998), several upward-shallowing cycles were interpreted from their facies description. These cycles consist of basal mudstones and wackestones grading upward into grain-dominated packstones and grainstones. A total of five facies groups were identified from a 4,002-ft-thick continuous core from 10 wells with both main pay zone (MPZ) and residual oil zone (ROZ) intervals. More complete studies for the MPZ were reported by Kerans et al. (1994) and Lucia et al. (1995).

The most common pore types include interparticle, moldic, and vugs. Dolomitization is a key diagenetic process that influences porosity distribution in the reservoir. Stylolites, which are common in the SAF, are intergranular pressure solution features usually with wavy surfaces (Koepnick 1987; Heap et al. 2014). Most of the stylolites are sutured with cement, but some have solution seams. The stylolite-bearing horizons could be laterally extensive (100s of meters). They may act as barriers or paths for fluid flow depending on both stylolite features and their extents relative to the flow directions. Vertical fractures are common and mostly filled in by anhydrite or dolomite cement.

## Data Sets

The $k_z$-related data set comes from an SAF reservoir and includes whole-core measurements (by Core Laboratories, Houston, Texas, USA), core plugs, as well as descriptions of lithology and diagenetic history. For the reservoir we studied, nearly 9,000 whole-core permeabilities from more than four wells were available from Core Laboratories reports. We conducted careful quality checks and cleaning of these data sets before exploratory analyses. Data cleaning consisted of (i) removing measurement values below the threshold (e.g., <0.001 md) for some evaluations, such as averages, standard deviation, and SVs; and (ii) removing incomplete measurements. Samples where only $k_x$ was available without $k_z$ might be from core plugs. For the collected whole cores, over 6,000 samples have core lithology descriptions. Core descriptions in these reservoirs provide sedimentological information, such as textures, sedimentary structures, and post-depositional features.

A whole core has a larger diameter and length than a conventional core plug **(Fig. 2),** thus the whole-core includes more larger-scale geological information. The main advantage of whole cores is that they are or approach exhaustive sampling. Whole cores are often used in reservoir characterization to measure three-directional permeabilities: $k_x$, $k_y$, $k_z$ **(Fig. 2)**. The horizontal ($x$, $y$) direction varies randomly and usually $k_{\max} = \max(k_x, k_y)$ and $k_{90} = \min(k_x, k_y)$. More details of whole-core-based permeabilities and their comparison to core plugs and probe permeameter measurements can be found in Honarpour et al. (2005), Nieto Camargo and Jensen (2012), and Ringrose et al. (2005).

**Fig. 2—Whole cores vs. core plugs. Note that the measurements are taken on very different rock volumes.**

## Theory and Approaches

**Statistical Characterization.** Based on the above data sets, it is helpful to begin with a comprehensive geostatistical analysis on $k_z$ to understand its characteristics as compared to $k_x$. This will also guide the synthesis of generic geomodels used in the flow simulations to examine the influence of $k_z$ realizations on performance prediction during $CO_2$ EOR and storage.

Based on the 42 wells' whole-core measurements, we created a series of $k_z$-related exploratory plots, including vertical profiles for the three permeabilities. The histograms, well-based Dykstra-Parson coefficient, SVs, $k_z$-$k_x$ crossplots, and permeability-porosity crossplots, Lorenz plots, and Koval plots (Koval 1963) were produced. A Koval plot is the plot of $(1 - F)/F$ vs. $(1- C)/C$, where $F$ is flow capacity and $C$ is storage capacity. The vertical location of the curves on the plot measures the heterogeneity that gives clues to vertical sweep efficiency (Salazar 2018). Detailed explanations of the Koval plot and its physical meaning are in Lake et al. (2014) and Salazar and Lake (2020).

When viewing plots, such as **Fig. 1**, or listings of $k_z/k_x$ values, it is tempting to assume that $k_z/k_x$ should nearly always be less than one (e.g., Dernaika et al. 2018; Pamungkas et al. 2020), so there must be a problem with the measurements if $k_z/k_x > 1$ for significant portions of the data set. This assumption may be incorrect for reasons listed below and it is therefore useful to keep the questions below in mind when assessing $k_z/k_x$ values. We will use these considerations during analysis of data from the field.

1. Are the data from one geological unit (e.g., rock type or facies) or do they represent a larger domain? A clearer picture of the $k_z/k_x$ behavior is likely to emerge from unit-based data so that characteristic $k_z/k_x$ values and how the values change can be identified.
2. Is the formation isotropic? If the permeability is isotropic and a deterministic variable, then $k_x = k_y = k_z$. However, if we assume permeability to be isotropic and a random variable, then $k_x$, $k_y$, and $k_z$ have the same probability distribution but might be unequal for any given sample. In that case, the probability of $k_z/k_x > 1$ should be 1/3 [written as $\text{Prob}(k_z/k_x > 1) = 1/3$] for tri-directional samples and ½ for bidirectional samples. Also, while the formation may not be locally isotropic, it may behave at the larger scales as being isotropic because some areas have $k_z/k_x > 1$ while other areas have $k_z/k_x < 1$. There may be good geological reasons why some $k_z/k_x$ data exceed 1. For example, in sandstone reservoirs with burrowing or dewatering horizons, $k_z/k_x > 1$ (Jones et al. 1987; Hanks et al. 2011). Carbonates also may show $k_z/k_x > 1$ in dissolution enhanced or stylolite-bearing samples (e.g., Chandra et al. 2013; Sun et al. 2017; Dernaika et al. 2018).

**Flow Simulation.** We ran flow simulations (using the Eclipse® simulator) to quantify the influence of $k_z$ on $CO_2$ flow/sweep and performance prediction during $CO_2$ EOR and storage. First, we synthesized a series of permeability fields according to the geostatistical analysis. Second, we conducted flow simulations of $CO_2$ injection into these synthetic models while considering the reservoir ROZ rock-fluid properties. Third, we compared various $k_z$ realizations (including direct $k_z$ statistical realizations or true $k_z$ vs. assuming $k_z/k_x = 0.1$) in terms of simulation prediction for $CO_2$ EOR and storage.

Our procedure for generating permeability fields is to (i) use the Box-Cox method (Box and Cox 1964) to transform the reservoir permeability distributions to be more Gaussian; (ii) use sequential Gaussian simulation to generate permeability fields with a given set of heterogeneity indicators; and (iii) back-transform to get the synthetic permeability field. Appendix A includes more details of the procedure and demonstrates that the synthetic fields reproduce the global permeability statistics.

**Table 1** shows the properties of the synthetic permeability fields. Simulation models for inverted 5-spot and inverted 9-spot well patterns were created. The corresponding model dimensions and cell sizes are also in **Table 1**. The porosity was set to be constant at 0.11, the arithmetic average of the reservoir ROZ, because porosity is far less variable than permeability. It was known that vertical cell size influences miscible flood predictions, especially when gravity is important (Stalkup and Dean 1990). This work adopted a fixed cell size because the simulation studies are designed for general sensitivity analysis.

| Well Pattern | Inverted 5-Spot | Inverted 9-Spot |
|---|---|---|
| Pattern size (acre) | 40 | 80 |
| Model domain sizes (ft) | 1,320×1,320×96 | 1,860×1,860×96 |
| Model cell sizes (ft) | 30×30×3 | 30×30×3 |
| Model dimensions | 44×44×32 | 62×62×32 |
| Horizontal dimensionless autocorrelation length | 0.2, 2*, 20 | |
| Horizontal permeability log mean | 1.5* | |
| Vertical permeability log standard deviation | 1.8* | |
| Vertical permeability log mean | 0.5* | |
| Vertical permeability log standard deviation | 2.3* | |

*Based on SAF reservoir permeability statistics.

Table 1—Properties of synthetic permeability fields.

For the reservoir simulation model, the settings for the rock, fluids, and their interactions, including oil properties, pressure/volume/temperature models, relative permeability, and capillary pressure curves, were described in Ren and Duncan (2021). Because the whole simulation study is designed to examine the sensitivity of vertical permeability on $CO_2$ EOR and storage performance, we used a single set of relative permeability and capillary pressure curves. More details are included in Appendix B.

Initially, the reservoir pressure is 2,119.9 psi, and the reservoir temperature is 104°F. Uniform fluid saturations were assigned the average saturation magnitudes of the reservoir ROZ (Ren and Duncan 2019), with an initial oil saturation of 0.4 and the rest of the pore space water.

**Fig. 3—The change of buoyancy number $N_{bu}$ along the distance from a given $CO_2$ vertical injector. $N_{bu}$ is larger than 1 when the distance is larger than 115 ft. This means that buoyant flow prevails in a large area between an injector to producers (the interwell distance is 933 ft for the 40-acre inverted 5-spot and 1,319 ft for the 80-acre inverted 9-spot well patterns). Under reservoir conditions, the $CO_2$ density is 768 kg/m$^3$, and $CO_2$ viscosity is 0.07 cp. The brine density is 915 kg/m$^3$. The vertical permeability arithmetic average is 11.1 md, and the perforation length is 96 ft (same as the thickness of the synthetic model in Table 1). The injection rate used for the calculation is 3,000 Mscf/D (based on settings in Table 2).**

We designed injection-production schemes with a focus on the effects of $k_z$ on flow. To achieve this, we use a buoyancy number $N_{bu}$ (Shook et al. 1992, Eq. 1) to measure the relative importance of buoyant force ($k_z$-related) over viscous force (injection rate-related). The variation of $N_{bu}$ along the distance from an injector is in **Fig. 3.** $CO_2$ flow is dominated by the buoyant force ($N_{bu} > 1$) in most of the interwell areas (around 115 to 1,300 ft away from the injector). Thus, most of the $CO_2$ flow will tend to be gravity segregated. Our study covers a wide $N_{bu}$ range of 0.0022 to 22 through adjusting either injection rates or $k_z$ in simulation cases (see **Table 2**).

| Case No. | $k_x$ (md) | $k_z$ (md) | Injection Rate (Mscf/D) | Injector Bottomhole Pressure (psi) | Buoyancy Number[a] | WAG Ratio | Autocorrelation, $\lambda_{Dx}$ | Well Pattern | Notes |
|---|---|---|---|---|---|---|---|---|---|
| 1 | Constant | $k_x$ | 3,000 | NA | $2.2 \times 10^{-2}$ | 0 | 2 | Inverted-5 and 40 acre | Base settings: injection rate;<br>WAG ratio;<br>autocorrelation; |
| 2 | Constant[d] | Constant[d] | 3,000 | NA | $1.4 \times 10^{-2}$ | 0 | 2 | Inverted-5 and 40 acre | |
| 3 | Variable | $k_x$ | 3,000 | NA | $2.2 \times 10^{-2}$ | 0 | 2[b] | Inverted-5 and 40 acre | |
| 4 | Variable | Variable | 3,000 | NA | $1.4 \times 10^{-2}$ | 0 | 2 | Inverted-5 and 40 acre | |
| 1a | Variable | $10 \times k_x$[c] | 3,000 | NA | $2.2 \times 10^{-1}$ | 0 | 2 | Inverted-5 and 40 acre | Effect of buoyancy number |
| 3a | Variable | $0.1 \times k_x$ | 3,000 | NA | $2.2 \times 10^{-3}$ | 0 | 2 | Inverted-5 and 40 acre | |
| 3b | Variable | $0.1 \times k_x$ | 30 | NA | $2.2 \times 10^{-1}$ | 0 | 2 | Inverted-5 and 40 acre | |
| 5 | Constant | $k_x$ | 30 | NA | 2.2 | 0 | 2 | Inverted-5 and 40 acre | |
| 6 | Constant | Constant | 30 | NA | 1.4 | 0 | 2 | Inverted-5 and 40 acre | |
| 7 | Variable | $k_x$ | 30 | NA | 2.2 | 0 | 2 | Inverted-5 and 40 acre | |
| 8 | Variable | Variable | 30 | NA | 1.4 | 0 | 2 | Inverted-5 and 40 acre | |
| 9 | Variable | $10 \times k_x$[c] | 30 | NA | $2.2 \times 10^{1}$ | 0 | 2 | Inverted-5 and 40 acre | |
| 10 | Variable | $k_x$ | 3,000 | NA | $2.2 \times 10^{-2}$ | 1 | 2 | Inverted-5 and 40 acre | Effect of WAG ratio |
| 11 | Variable | $k_x$ | 3,000 | NA | $2.2 \times 10^{-2}$ | 4 | 2 | Inverted-5 and 40 acre | |
| 12 | Variable | Variable | 3,000 | NA | $1.4 \times 10^{-2}$ | 1 | 2 | Inverted-5 and 40 acre | |
| 13 | Variable | Variable | 3,000 | NA | $1.4 \times 10^{-2}$ | 4 | 2 | Inverted-5 and 40 acre | |
| 14 | Variable | $k_x$ | 3,000 | NA | $2.2 \times 10^{-2}$ | 0 | 0.2 | Inverted-5 and 40 acre | Effect of horizontal autocorrelation length |
| 15 | Variable | $k_x$ | 3,000 | NA | $2.2 \times 10^{-2}$ | 0 | 20 | Inverted-5 and 40 acre | |
| 16 | Variable | Variable | 3,000 | NA | $1.4 \times 10^{-2}$ | 0 | 0.2 | Inverted-5 and 40 acre | |
| 17 | Variable | Variable | 3,000 | NA | $1.4 \times 10^{-2}$ | 0 | 20 | Inverted-5 and 40 acre | |
| 18 | Variable | $k_x$ | 3,000 | NA | $2.2 \times 10^{-2}$ | 0 | 2 | Inverted-9 and 80 acre | Effect of well pattern |
| 19 | Variable | Variable | 3,000 | NA | $1.4 \times 10^{-2}$ | 0 | 2 | Inverted-9 and 80 acre | |
| 20 | Constant | $k_x$ | NA | 2,800 | NA | 0 | 2 | Inverted-5 and 40 acre | Injection rates |
| 21 | Constant | Constant | NA | 2,800 | NA | 0 | 2 | Inverted-5 and 40 acre | |
| 22 | Variable | $k_x$ | NA | 2,800 | NA | 0 | 2 | Inverted-5 and 40 acre | |
| 23 | Variable | Variable | NA | 2,800 | NA | 0 | 2 | Inverted-5 and 40 acre | |
| 22a | Variable | $0.1 \times k_x$ | NA | 2,800 | NA | 0 | 2 | Inverted-5 and 40 acre | |
| 22b | Variable | $0.01 \times k_x$ | NA | 2,800 | NA | 0 | 2 | Inverted-5 and 40 acre | |

[a] These values of buoyancy number $N_{bu}$ are along the wellbore. Note $N_{bu}$ changes with the distance as shown in Fig. 3.

[b] Three realizations of permeability fields were created for this case.

[c] With vertical fractures.

[d] Constant $k_x$ is 17.5 md, and constant $k_z$ is 11.1 md as per the reservoir arithmetic averages of permeabilities.

Table 2—Values for the cases of $CO_2$ flow simulations. The “truth” cases are for the case with both variable $k_x$ and variable $k_z$ realizations (i.e., Cases 4, 8, 12, 13, 16, 17, 19, and 23).

$N_{bu}$ is defined as:

$$N_{bu} = \frac{\Delta\rho g k_z H \cos\alpha}{u_h \mu L}, \tag{1}$$

where $\Delta\rho$ is the density difference between $CO_2$ and the mixture of brine and oil, $g$ is the gravitational constant, $k_z$ is the vertical permeability, $H$ is the well perforation height,  is the formation dip angle, $u_h$ is the $CO_2$ entry velocity at the wellbore (it was calculated using $CO_2$ injection rate in a radial flow geometry), $\mu$ is the $CO_2$ viscosity at reservoir conditions, and $L$ is the horizontal length of the simulation domain (same as the distance from an injector referred to in **Fig. 3**).

We considered four scenarios, the details of which are listed in **Table 2**. We provide a brief description of the four scenarios below. Simulation predictions based on the settings in Scenario 4 (using true $k_z$) are considered to be "truth case" in the results analysis.

Scenario 1: constant $k_x$ and $k_z = 0.1\ k_x$;
Scenario 2: constant $k_x$ and $k_z$ from the reservoir arithmetic averages (i.e., average $k_x$ and average $k_z$);
Scenario 3: variable $k_x$ with the reservoir geostatistics, and $k_z = 0.1\ k_x$;
Scenario 4: variable $k_x$ and $k_z$ with the reservoir geostatistics.

Several other parameters were also examined, including water alternating gas (WAG) ratios, horizontal dimensionless autocorrelation length ($\lambda_{Dx}$), and injector constraints. The WAG ratio is defined as the ratio of the reservoir volumes of injected water to injected $CO_2$ for a cycle; the WAG ratio 0 represents continuous $CO_2$ injection. The range of reported WAG ratios is 0 to 5 (Ettehadtavakkol et al. 2014). The ratio in this work was adjusted through changing water half-cycle size while keeping $CO_2$ half-cycle size unchanged at 2.5% HCPV. Dimensionless horizontal autocorrelation length, $\lambda_{Dx}$, is the horizontal autocorrelation length divided by the domain horizontal length. For the base case, we set $\lambda_{Dx}=2$ considering the permeability variogram analysis for the reservoir wells. We also examined two extreme values of $\lambda_{Dx}$: 0.2 (very weak lateral autocorrelation) and 20 (strong layering). The vertical dimensionless autocorrelation length is 0.

The base case injection schemes are $CO_2$ injection rate is 3,000 Mscf/D, water injection rate is 1,400 B/D, and the total injection duration is 20 years with the WAG ratio 0 (**Table 2**). The base sets 200% HCPV $CO_2$ injected considering carbon sequestration, which is larger than the typical range of 30 to 80% HCPV for $CO_2$ EOR (Merchant 2010). Such a large HCPV, as demonstrated in our work, tends to interact with $k_z$ in influencing $CO_2$ EOR and storage performance. The injection duration for other cases proportionally varies with injection rates for a given HCPV $CO_2$. Both constant injection rate and constant bottomhole pressure for injectors were considered, and producers were assigned a constant bottomhole pressure (minimum $CO_2$-oil miscible pressure). Other details for the settings of these parameters are in **Table 2**. These numerical simulations are designed for general purposes, and the understanding from them might also be revealed from scaling groups that were mathematically derived from relatively simplistic models (e.g., Shook et al. 1992; Sikandar 1994).

The metrics used are typical ones (Lake et al. 2019) to measure the influence of $k_z$ realizations on $CO_2$ flow: the cumulative oil production (for EOR) and cumulative $CO_2$ retention fraction (for storage). The retention fraction is (cumulative $CO_2$ injected − cumulative $CO_2$ produced)/cumulative $CO_2$ injected. It measures the efficiency of injected $CO_2$ that is stored in an oil reservoir.

## Results and Discussion

**Geological and Geostatistical Analysis Results.** ***Statistical Analysis for an Example Well.*** A comprehensive geostatistical analysis is essential for understanding the properties (e.g., variability, autocorrelation, and anisotropy) of $k_z$ as compared to $k_x$. In this section, $k_x$ and $k_y$ correspond to $k_{\max}$ and $k_{90}$, respectively, as termed by Honarpour et al. (2005). **Fig. 4** shows a set of $k_z$-related exploratory plots for one example well, including permeability profiles, histograms, SVs, Lorenz plots, Koval plots, and $k_z$-$k_x$ crossplots.

$k_z$ tends to be overall less than $k_x$; 74.7% of the wholecores have $k_z < k_x$ **(Fig. 4a)**. Several cycles of vertical permeability variation can be observed from the permeability profiles. SVs for log base 10 permeability **(Fig. 4b)** showed that $k_x$ and $k_y$ are virtually the same but $k_z$ shows much more variability. This observation is consistent with the permeability profiles **(Fig. 4a)**: Several spikes of small $k_z$ appear with small-scale cycles. Log-permeability SVs also indicate more small-scale variability than untransformed permeability SVs, similar to behaviors observed by Jensen et al. (2000). Untransformed SVs (not shown) indicate that $k_x$ and $k_z$ are virtually the same, which implies that large-scale correlation for both permeabilities is similar, a behavior also reported by Lucia et al. (1995). These analyses indicate that $k_z$ shows both small- and large-scale variability and that it should be more variable than $k_x$ spatially.

This observation is also supported by the plots for global statistics: permeability histograms **(Fig. 4c)**, Lorenz plots **(Fig. 4d)**, and Koval plots **(Fig. 4e)**. All permeability histograms are skewed right. This must be considered when populating permeability fields or estimating other permeability-related parameters (Jensen et al. 1987). Both the Dykstra-Parsons and Lorenz coefficients are statistically significantly larger for vertical permeability than for horizontal ones. The well-based Koval plots **(Fig. 4e)** showed the horizontal permeability holds a different trend as compared with that of vertical permeability. Similar observations were made in the plots for other wells (Appendix C).

**Fig. 4f** shows the $k_z$-$k_x$ crossplots for the example well. Approximately 25% of the points have $k_z > k_x$, where $k_x$ is large (>10 md). In fact, the anisotropic behavior is observed for more wells (Appendix C). These wells, and indeed all wells analyzed, show the existence of points with $k_z > k_x$, with the fractions ranging from 11 to 35%. Considering the importance of anisotropy and its implications to both geomodeling and flow, we further analyze the anisotropy and its geological controls in the next section.

The permeability-porosity crossplots **(Fig. 4g)** show that, at a given porosity, vertical permeability tends to be less than horizontal permeabilities (consistent with **Fig. 4a**). It appears that log $k_z$ is better correlated with porosity than the other two permeabilities.

***Anisotropy Analysis for Two Contrasting Wells.*** We chose two wells for $k_z/k_x$ analysis to further identify causes for that anisotropy. As a first step, depth plots and CDFs show two distinct behaviors **(Figs. 5 and 6).** Well B shows $k_z$ and $k_x$ behaving similarly, with $k_z/k_x$ values fluctuating around unity **(Fig. 5a)**. The well's CDFs **(Fig. 6a)** show some differences between $k_z$ and $k_x$ values and, on closer inspection, the uppermost 230 ft show decreased $k_z/k_x$ values compared to the bottom 340 ft **(Fig. 5a)**. This change appears to be primarily a result of the number of stylolites; lithology differences are quite small. Well C, on the other hand, has $k_z$ a factor of 10 smaller than $k_x$ (**Figs. 5b and 6b**) and looks to have similar behavior throughout the cored section.

**Fig. 4—A series of $k_z$-related exploratory plots for example Well A: (a) vertical profiles for three permeabilities (depths indicated are not actual values); (b) SVs for log permeability; (c) permeability histograms with $V_{dp}$ included; (d) Lorenz plots; (e) Koval plots; (f) $k_z$-$k_x$ crossplot with the 1:1 line included; (g) permeability-porosity crossplots.**

[redacted]

Fig. 5—Vertical profiles of $k_z/k_x$ ratios for Wells B (a) and C (b). Depths shown are not actual values.

[redacted]

Fig. 6—CDFs of whole-core permeability of Wells B (a) and C (b).

Possible reasons for the different $k_z/k_x$ behaviors of Wells B and C were further investigated. Core descriptions for both wells (by Core Laboratories) suggest predominant dolomite lithology with varying amounts of anhydrite—mostly as nodules—and very fine silts. Stylolites and associated cements are also present. For Well B, the upper section (025 to 255 ft) has $k_z/k_x$ values similar to those of C and similar densities of stylolites; the upper section has 86% of the core samples with stylolites compared to 95% for Well C. The lower section of B (255 to 600 ft) has 37% of the samples with stylolites present. The Core Laboratories data we had do not specify the number of stylolites in each whole-core sample; they simply recorded if one or more stylolites was present in the sample. To further test if there is a $k_z/k_x$ relationship with stylolites, we evaluated the conditional probability of $k_z \geq k_x$ when stylolites are present, Prob($k_z \geq k_x$ | stylolites). For Well C, Prob($k_z \geq k_x$ | stylolites) = 0.08 while for Well B we obtained 0.26 for the upper section and 0.38 for the lower section. Thus, the Well C values suggest a strong linkage between stylolites and permeability anisotropy, while Well B shows that there may be a reduced impact of stylolites on the core-scale anisotropy.

***Statistics of $k_z$ vs. $k_x$ Heterogeneities for All Wells.*** **Fig. 7** shows the comparison of the Dykstra-Parsons coefficient ($V_{dp}$, **Fig. 7a**) between $k_z$ and $k_x$, along with a similar plot for the Lorenz coefficient ($L_c$, **Fig. 7b**). From the scatter point distribution, it appears that both $k_z$ and $k_x$ have similar heterogeneity levels (i.e., both coefficients are mostly in the range of 0.6–0.9). However, $k_z$ tends to be more heterogeneous than $k_x$ at the same well. The clustering behavior of points seen in **Fig. 7a** is a reflection of $V_{dp}$ to compress large variability changes between wells into the small interval of 0.6 to 0.9 (Jensen and Lake 1988).

Considering that vertical flow is over a larger area but with a smaller pressure drop than horizontal flow, even a very small $k_z$ could permit nonnegligible vertical flow. Thus, the prediction of flow response to $k_z$ may have a larger uncertainty than that to $k_x$. Additionally, greater heterogeneity of $k_z$ as compared to $k_x$ cannot be honored when assuming a fixed $k_z/k_x$ ratio in reservoir simulations. We examined the consequences of this in the flow simulation section.

**Reservoir Flow Simulation Results.** ***Base Case Results.*** **Fig. 8** shows the influence of various $k_z$ field realizations (corresponding to Cases 1–4, **Table 2**) on the predicted $CO_2$ EOR and storage results. At small buoyancy number $N_{bu}$, assuming $k_z = k_x$ gives comparable

**Fig. 7—Compilation of Dykstra-Parsons coefficient $V_{dp}$ (a) and Lorenz coefficient $L_c$ (b) for both $k_z$ and $k_x$ for the 42 wells with whole-core measurements.**

**Fig. 8—The variation of cumulative oil production (a) and $CO_2$ retention fraction (b) along with injected $CO_2$ HCPV. The buoyancy numbers are very similar for the four cases ($N_{bu}$ ≈ 2E−2). Refer to Cases 1–4 in Table 2 for detailed settings.**

oil production **(Fig. 8a)** to variable $k_z$, but $CO_2$ retention **(Fig. 8b)** deviates by 6.3%. This means that $CO_2$ flow is more sensitive to $k_z$ than oil flow, which agrees with our intuition. The differences in metrics for homogeneous fields (black lines) are caused by different constant permeability values (17.5 vs. 11.1 md, refer to **Table 2**).

***Influence of Buoyancy Number on Metrics.*** **Fig. 9** shows the influence of $N_{bu}$ on the defined metrics when adjusting only injection rates. Increasing injection rates smears or decreases the influence of $k_z$ realizations on oil production estimates **(Fig. 9a)**. This is as expected because the two factors (i.e., injection rate and $k_z$) have opposite influences on $N_{bu}$ (Eq. 1). The influence of $k_z$ realizations on $CO_2$ retention forecasts **(Fig. 9b)** is stronger when the injection rate increases. This is because high rates cause large $CO_2$ plume volumes, which tend to be more sensitive to $k_z$ compared to small plume volumes caused by low rates.

Comparing **Fig. 8** to **Fig. 9** shows that, at large $N_{bu}$, assuming $k_z = k_x$ causes a large deviation (9.9%) in the estimated ultimate oil production. However, the different $k_z$ field realizations have a negligible influence on $CO_2$ retention. This is because buoyant flow (large $N_{bu}$) prevails in the $CO_2$ plume, and the accessed volume tends to be small (reduced sweep).

**Fig. 10** shows the $CO_2$ spatial distribution for $N_{bu} = 2$ at 0.5 HCPV $CO_2$ injected. Areally, the patches that are swept by $CO_2$ vary significantly for different realizations of $k_z$, particularly in the upper and middle layers. Vertically, the $CO_2$ distributions and saturations also show differences, particularly near the wellbore.

**Fig. 11** shows the influence of $N_{bu}$ on the production and retention metrics when adjusting the $k_z/k_x$ ratio. At large injection rates, $k_z = 0.1\ k_x$ yields close agreement of both oil production **(Fig. 11a)** and $CO_2$ retention **(Fig. 11b)** to the truth case (variable $k_z$), even though the $N_{bu}$ for the two cases are almost 10 times different. This implies that using the wellbore-based $N_{bu}$ cannot capture the influence of $k_z$ on flow. As $N_{bu}$ increases because of increasing $k_z$, the ultimate oil production increases, as does the ultimate $CO_2$ retention fraction. This is because the increase in $k_z$ makes the reservoir less anisotropic, and thus the injected $CO_2$ contacts more oil.

At a small injection rate, using $k_z = 0.1\ k_x$ causes an underestimation of ultimate oil production by 6% **(Fig. 11c)**. The deviation is larger than that for the large injection rate (**Fig. 11c** vs. **Fig. 11a**). This is consistent with the influence of $N_{bu}$ on production and retention as explained above. Also, at the small injection rate, the instantaneous retention fraction differs (e.g., in the interval 0.2–1.0 HCPV) and slightly decreases when $N_{bu}$ increases; however, the ultimate $CO_2$ retention fractions **(Fig. 11d)** were very similar regardless of the $k_z$

**Fig. 9—Influence of buoyancy number $N_{bu}$ on the cumulative oil production (a) and $CO_2$ retention fraction (b). The change of $N_{bu}$ is through adjusting injection rates while keeping $k_z$ equal to $k_x$. The four runs (in the sequence of legends) correspond to Cases 3–4 and Cases 7–8 in Table 2.**

**Fig. 10—$CO_2$ areal distribution (a) in the three selected layers and $CO_2$ vertical distribution (b) along the vertical slice across the injector along the I-direction for the four cases (Cases 5–8 in Table 2). The buoyancy number $N_{bu}$ is around 2.0 for all cases. The areal distributions show large difference in both the upper and middle layers because of vertical permeability distribution.**

realizations. This is because in the late injection period, $CO_2$ flow paths form mostly in the upper portion of the reservoir, and thus $N_{bu}$ or $k_z$ realizations exert a negligible influence on $CO_2$ retention.

***Influence of WAG Ratio on Metrics.*** **Figs. 12a and 12b** show the influence of WAG ratios on the estimated performance. As the WAG ratio increases, the deviation between the case $k_z = k_x$ and the truth case (variable $k_z$) for cumulative oil production estimation increases **(Fig. 12a)**. An opposite influence is observed for the $CO_2$ retention fraction estimation **(Fig. 12b)**. At the same WAG ratio, setting $k_z = k_x$ yields larger oil production than variable $k_z$.

**Fig. 11—Influence of buoyancy number on simulated performance. (a) and (b) are cumulative oil production and $CO_2$ retention fraction, respectively, when varying buoyancy numbers (through changing $k_z$) at a fixed *large* injection rate of 3,000 Mscf/D, whereas (c) and (d) are the equivalents at a fixed *small* injection rate of 30 Mscf/D. The scale factors seem to work, even the permeability field is heterogeneous. The four runs (in the sequence of legends) in the upper row correspond to Cases 3a, 3, 1a, and 4 in Table 2, and the runs in the lower row are from Cases 3b and 7–9.**

As the WAG ratio increases, the $k_z$ realization shows its negligible influence on the ultimate $CO_2$ retention fraction **(Fig. 12b)**. This is because a large WAG ratio means more water injected and effective diversion of $CO_2$ away from channeled paths and thus better sweep overall. In other words, large WAG ratios decrease the sensitivity in $k_z$ spatial distributions for $CO_2$ retention efficiencies for small $N_{bu}$.

***Influence of Horizontal Autocorrelation Length on Metrics.*** **Figs. 12c and 12d** show the influence of horizontal autocorrelation length $\lambda_{Dx}$ on oil production and $CO_2$ retention. At intermediate $\lambda_{Dx}$ (<2), $k_z$ exerts a limited influence on these results. At large $\lambda_{Dx}$, however, there is a large effect. As $\lambda_{Dx}$ increases, both the ultimate oil production and $CO_2$ retention decrease. This is because large autocorrelated regions of permeability give rise to lateral flow channels, which cause early $CO_2$ breakthrough and suboptimal results. The early breakthrough can also be seen from the very starting point of $CO_2$ retention decrease in **Fig. 12d**. In particular, at the early injection period (<0.8 HCPV), the retention fraction overall decreases as $\lambda_{Dx}$ increases for the variable $k_z$ realization cases. The ultimate retention is less influenced by $\lambda_{Dx}$ when it is large (>2). This may be because large $\lambda_{Dx}$ cases represent moderately to strongly layered systems where the $CO_2$ flow paths become well-established by late injection.

***Influence of Well Pattern Geometries on Metrics.*** **Figs. 12e and 12f** show the influence of well pattern geometries on $CO_2$ EOR and storage performance. Assigning $k_z = k_x$ does not affect oil production for either the inverted 5-spot or inverted 9-spot well patterns. However, the configuration affects the $CO_2$ retention prediction more for the inverted 5-spot than inverted 9-spot (6.3% vs. 0.1%).

***Influence of $k_z$ on $CO_2$ Cumulative Injection.*** The above results **(Figs. 8–12)** are based on constant injection rates. **Fig. 13** shows the influence of $k_z$ field realizations on the metrics when constraining the injector to have constant bottomhole pressure. Under this constraint, if we assume $k_z = 0.1\ k_x$, then simulations can give good estimates for oil production **(Fig. 13a)**, $CO_2$ retention fraction **(Fig. 13b)**, and ultimate $CO_2$ injected volume **(Fig. 13c)**. Among the three $k_z/k_x$ ratios, the use of $k_z = 0.01\ k_x$ yields the largest errors.

**Comparison to Literature and Discussion.** ***Anisotropy ($k_z/k_x$) and Its Controls.*** Wang et al. (1998) also studied the $k_z/k_x$ behavior in the Seminole Field, in an area similar in geology to Wells B and C. They suggest a core-scale formation average $k_z/k_x = 0.3$ with $0.1 < k_z/k_x < 1$. Examination of their figure, however, shows many data with $k_z/k_x > 1$, especially when $k_x < 3$ md. Of the 144 points shown in their data, approximately 1/3 (50 points) have $k_z/k_x > 1$, suggesting that the formation might be considered as isotropic at the core scale. The lower section of Well B, which is similar to the area studied by Wang et al. (1998), shows similar behavior to their data **(Fig. 14a).** However, Well C exhibits smaller $k_z/k_x$ values than Wang et al. (1998) reported **(Fig. 14b)**.

Koepnick (1987) presents a nice description of stylolite characteristics. Whether stylolites represent flow barriers depends on conditions during and after they form, leading to mixed reports of their flow effects. Ahr (2011), for example, states that "The literature is replete with references to stylolites … and how they form permeability barriers…." but he cautions that "post-stylolite diagenesis can create porosity and permeability in previously tight rocks ….". Other studies have observed stylolites to form occasional large-scale flow barriers (Koepnick 1987), but the evidence largely suggests they only form local impediments to vertical flow (Koepnick 1987; Al-Amrie et al. 2012; Heap et al. 2014). Data from Wells B and C suggest that when stylolites are abundant, the core-scale $k_z/k_x$ values are reduced. This core-scale information will be useful for defining the larger-scale $k_z/k_x$ value.

Using conditional probability analysis, we can assess the influence of stylolites on the core-scale $k_z/k_x$ ratio for this carbonate reservoir. Comparing this result with the behavior of $k_z/k_x$ and associated factors in sandstone reservoirs can prove instructive. At core scales, sandstone permeability anisotropies are caused by small-scale structures (e.g., silt beds and shale patches) (Clavaud et al. 2008; Dernaika et al.

**Fig. 12—The change of simulated cumulative oil production (left) and $CO_2$ retention fraction (right) with the HCPV $CO_2$ injected through adjusting WAG ratios (a and b), horizontal dimensionless autocorrelation length $\lambda_{Dx}$ (c and d), and well pattern geometries (e and f). Two main scenarios are compared: $k_z = k_x$ vs. variable $k_z$. $N_{bu}$ is around 2E−2 for all cases. In (a), the WAG ratio at 1 corresponds to 21 days (2.5% HCPV) of $CO_2$ injection alternating with 21 days of water injection.**

2018). Campero et al. (2014) noted that the $k_z/k_x$ ratio is also a function of lithofacies (mud fraction) in a sandstone reservoir. Similar observations were made by Armitage et al. (2011) and Ringrose et al. (2005). These small-scale structures and lithofacies are difficult to explicitly model in the large scale, except for some simple deterministic distributions of shale barriers with regular geometries (Sikandar 1994). Baker et al. (2015) showed that, in a sandstone reservoir, the $k_z$-$k_x$ crossplot show only a few points with $k_z > k_x$, while their carbonate example shows many more $k_z > k_x$ values. Their fraction of $k_z > k_x$ is less than that in our carbonate case.

***Scale Dependence of*** $k_z/k_x$**.** What do the core-based anisotropic values imply for the large-scale $k_z/k_x$? Lishman (1970) states, "it is not logical to transfer anisotropy measurements made on a core sample … to a reservoir" and, thus, for these large-scale $k_z/k_x$ values, geological factors beyond the wellbore must play a role. Core-scale $k_z/k_x$ values are largely controlled by small-scale geological heterogeneities (Lake 1988; Clavaud et al. 2008). At the larger scales, different geological heterogeneities may dominate and thereby change the $k_z/k_x$ values (Dernaika et al. 2018). For example, for large-scale sedimentary environments, wave-dominated shoreface deposits tend to have more $k_z > k_x$ values than river-dominated deltaic deposits (Hanks et al. 2011).

Reports on the relationship of core- to large-scale $k_z/k_x$ values are very limited, but Baker et al. (2015) show a decrease of $k_z/k_x$ by 2 to 3 orders of magnitude from the core- to large-scale in three clastic formations. Morton et al. (2002) undertook a detailed comparison of core plugs, probe permeameter, and wireline tester $k_z/k_x$ values in one of the formations reported by Baker et al. (2015). Generally, they find agreement between the upscaled probe (using arithmetic and harmonic averages) and tester values. They also determined that core plugs sampled the heterogeneities insufficiently to give agreement with either the probe or tester values. Thus, Morton et al.'s (Morton et al. 2002) results suggest extrapolation of core-scale $k_z/k_x$ ratios depends not only on how the local heterogeneities compare with the large-scale heterogeneities but on having sufficient sampling at the core scale to render statistically meaningful values.

Unlike clastics, carbonates appear to show weaker $k_z/k_x$ trends with scale, perhaps decreasing by 1 or 2 orders of magnitude from the core- to large-scale (e.g., Wang et al. 1994; Chandra et al. 2013; Pamungkas et al. 2020). This smaller change than sandstones may be partly resulting from better core-scale sampling because carbonates tend to be well consolidated, have good core recoveries, and are exhaustively measured (in the vertical direction) when using whole-core samples. For example, Wang et al. (1998) suggest large-scale simulation-based $k_z/k_x$ values of 0.02 to 0.04 for the area they studied in the Seminole Field. Using harmonic and arithmetic averages of data from three wells, they predict $k_z/k_x$ = 0.05 to 0.06 from the whole-core permeabilities (Wang et al. 1994). The reasonably good agreement between upscaled core and simulation $k_z/k_x$ values suggests the core-based values need only modest "adjustment" to represent

Fig. 13—The variation of cumulative oil production (a) and $CO_2$ retention fraction (b) along with the HCPV $CO_2$ injected for different $k_z$ realizations. (c) The cumulative volume of $CO_2$ injected vs. $CO_2$ injection duration for these realizations. Constant bottomhole pressure is imposed for the injector. Refer to Table 2 for the detailed case settings.

Fig. 14—Whole-core vertical and horizontal permeabilities for Wells B (a) and C (b). The $k_z/k_x = 0.02$ line is the lower value Wang et al. (1998) found appropriate by reservoir simulation. $k_z < k_x$ for nearly all the points on the right plot.

larger-scale properties. In contrast, the report of Chandra et al. (2013) is a case study where core plug permeabilities were inadequate to characterize the $k_z/k_x$ in their carbonate field.

**Fig. 15—The change of cumulative oil recovery (HCPV, left column) and cumulative $CO_2$ retention (HCPV, right column) with cumulative $CO_2$ injection (HCPV) through adjusting WAG ratios (a and b) and horizontal autocorrelation length (c and d). $N_{bu}$ is around 2E-2 for all cases. The figure is similar to Figs. 12a–12d except two changes: (i) produced oil and retained $CO_2$ was measured by HCPV; (ii) the *x*-axis was extended from 2 to 4 HCPV.**

All these demonstrate the scale dependence of anisotropies on $k_z/k_x$ ratios. The core-scale $k_z/k_x$ ratio thus may not be the ratio at other scales (e.g., gridblocks in reservoir simulations), particularly if poor sampling is done. The geological controls of $k_z/k_x$ ratios can be scale-dependent, and a geologically guided procedure may be needed to scale up the ratio from cores to gridblocks. For scales larger than grid cells, the formation anisotropy could be evaluated through using interference well tests and possibly seismic (Ayan et al. 1994; Onur et al. 2011; Wannell and Morrison 1990).

***Influence of $k_z$ Realizations on $CO_2$ Flow/Injectivity, Retention, and Implications.*** Our direct comparison of $k_z$ and $k_x$ based on the whole-core data sets showed that $k_z$ tends to be more heterogeneous and complicated than $k_x$ for this carbonate reservoir. A similar observation was made by Ringrose et al. (2005), and they found that traditional estimation functions for $k_x$ cannot give a satisfactory prediction of $k_z$ in a sandstone reservoir. Their sandstone study, along with our carbonate one here, strongly indicates that the flow influenced by $k_z$ will be more complicated than that by $k_x$, and thus flow prediction will be much more difficult.

Such flow here mostly refers to buoyant flow, and it occurs in subsurface porous media where two contrasting-density fluids exist [e.g., aquifer $CO_2$ storage (Bryant et al. 2008; Ren et al. 2018) and subsurface hydrogen storage (Hassanpouryouzband et al. 2021; Heinemann et al. 2021)]. In this sense, the geological characterization of $k_z$ for these processes should be even more important than for $k_x$. Because permeability is related with capillary pressure, the latter heterogeneity on buoyant flow has received considerable attention in the context of aquifer $CO_2$ storage. It has been shown that capillary pressure heterogeneity tends to exert much more influence on small-scale upward flow paths and associated trapping quantification than permeability does (Krishnamurthy et al. 2019; Saadatpoor et al. 2010; Trevisan et al. 2017).

For the influence of $k_z$ on $CO_2$ storage, Abdelaal et al. (2021) studied the effect of the $k_z/k_x$ ratio on ultimate $CO_2$ storage capacities in a saline aquifer undergoing $CO_2$ injection. Our results **(Fig. 13)** showed similar findings that, at the initial period of injection, cumulative $CO_2$ injected is almost independent of $k_z/k_x$ ratios. However, at late injection, the cumulatively injected amount becomes different for these ratios. We showed that, for the studied carbonate reservoir, using the $k_z/k_x$ ratio equal to 1 is better than 0.1 in terms of $CO_2$ injection estimation **(Fig. 13)**. The effect is, however, very limited for the time scale we investigated. Our work further shows that, as the injection duration increases, its effects on oil production become large when varying the $k_z/k_x$ ratio. This threshold point is around 60 to 100% HCPV as revealed from **Figs. 9–12**. This is because as injection time lengthens, it causes more $CO_2$ to be affected by buoyant flow, and the influence of $k_z$ on $CO_2$ displacing oil is thereby enhanced.

Campero et al. (2014) found that using constant $k_z/k_x$ to populate vertical permeability works in homogeneous reservoirs but fails in heterogeneous reservoirs with complex depositional environments (related to autocorrelation length). This is consistent with our findings that the oil production and $CO_2$ retention metrics change as the horizontal autocorrelation length increases. Furthermore, our distinct contribution here is that we demonstrated the injection strategies (i.e., injection rates and WAG ratio choices) interact with reservoir heterogeneity in influencing both oil production and $CO_2$ retention prediction **(Figs. 12 and 15).** This interplay makes the influence of $k_z/k_x$ on flow complicated.

Generally, at the same buoyancy number ($N_{bu} \approx$ 2E-2), assuming $k_z = k_x$ overestimates both the cumulative oil recovery factor and $CO_2$ retained HCPV compared to the true case **(Fig. 15)**. This assumption, therefore, affects the vertical positions of inflection points at which $CO_2$ retained

HCPV flattens with the increase in $CO_2$ injection **(Fig. 15b)**. The point represents the maximum injection duration for increased storage, and, after that point, injected $CO_2$ cannot be further retained. It appears that large WAG ratios and small autocorrelation lengths (less heterogeneity) shorten the time duration of reaching the inflection points. These points were not extensively observed in the report by Lake et al. (2018) because of the relatively short (1 HCPV) $CO_2$ injection duration for the reviewed projects. More work is needed to understand the controlling factors of the inflection point and possible operational strategies for moving the point toward the left top in the figure (i.e., rapid and large $CO_2$ retention) for storage. The understanding of improving volumetric sweep efficiency strategies and their interplay with reservoir heterogeneity should be the key here (Lake et al. 2018, 2019).

Another noteworthy aspect of **Fig. 15d** is that, for continuous $CO_2$ injection, the retained $CO_2$ can be larger than 1 HCPV as injection proceeds. After 1 HCPV $CO_2$ retention, the subsequently injected $CO_2$ must occupy the space that was previously occupied by water (i.e., water displacement must be occurring). The combined voidage replacement and dissolution/miscibility analysis, as demonstrated by Lake et al. (2018), is very helpful to understand $CO_2$ storage mechanisms here.

More generally, what is the $k_z/k_x$ threshold value if a formation appears to be anisotropic? This value depends on the flow process under consideration. For example, performance differences between $k_z/k_x = 1$ and $k_z/k_x < 0.7$ might be significant for steam-assisted gravity drainage (Azom and Srinivasan 2011) while $k_z/k_x = 0.05$ might be the threshold value for gas coning (Addington 1981). For our study on $CO_2$ EOR and storage here, it appears that the threshold $k_z/k_x$ ratio for flow simulations is in the range of 0.1 to 1, which can give a good forecast of both oil production and carbon sequestration performance.

## Conclusions and Recommendations

For $CO_2$ EOR and storage in oil reservoirs, it is important to understand the intrinsic geological controls of $k_z$ to better evaluate $CO_2$ flow/sweep, oil production, and $CO_2$ storage performance. We conducted analyses of the effect of different $k_z$ estimates based on a San Andres carbonate reservoir data set, including whole-core measurements and core facies. We also conducted generic flow simulations based on the geostatistical understanding of the reservoir and studied the influence of $k_z$ on $CO_2$ EOR and storage performance prediction. Our conclusions are:

1. $k_z$ tends to be more heterogeneous and complicated than $k_x$, as revealed from heterogeneity measurements. This means that assuming a fixed $k_z/k_x$ ratio is not representative; if $k_z/k_x$ ratios are taken as constants they should have the same variability.
    a. $k_z > k_x$ is not unusual and, indeed, should be expected for isotropic sediments. For the reservoir studied, it appears that stylolites show statistically significant effects on $k_z$ for the core-scale anisotropy.
2. $k_z$ vs. $k_x$ crossplots need to be carefully prepared when evaluating for characteristic $k_z/k_x$ values, paying particular attention to how many samples have $k_z > k_x$. The assumption that $k_z/k_x < 1$ can bias interpretation of these plots and give $k_z/k_x$ estimates that are too small.
3. The change of $k_z/k_x$ with increasing scale depends primarily on two factors: the change(s) of geological features controlling fluid flow and on how well the permeability measurements fully represent the core-scale heterogeneities. Whole-core measurements of carbonates may better capture the core-scale controls and thereby reduce the change in $k_z/k_x$ as scale increases.
4. The influence of $k_z$ on performance predictions depends on the flow process and regimes. The buoyancy number proved to be a useful method to characterize the gravity-viscous competition.
5. The accuracy of results by assuming a constant $k_z/k_x$ ratio for flow performance prediction is heavily influenced by WAG ratios and autocorrelation lengths but less by well patterns.
6. As $CO_2$ injection duration increases, the influence of $k_z$ on flow also increases. $k_z$ shows limited influence on cumulative $CO_2$ injected volumes.

To evaluate $CO_2$ EOR and storage performance, we recommend a serial of flow numerical tests on $k_z$, as shown in this work, before undertaking any large or full-field scale flow simulation efforts.

## Nomenclature

$C$ = storage capacity
$F$ = flow capacity
$H$ = well perforation length
$k_{90}$ = minimum horizontal permeability
$k_{\max}$ = maximum horizontal permeability
$k_{rg}$ = gas relative permeability
$k_{ro}$ = oil relative permeability
$k_{rw}$ = water relative permeability
$k_x$ = $x$-direction permeability
$k_y$ = $y$-direction permeability
$k_z$ = vertical permeability
$L$ = lateral length of the simulation domain
$L_c$ = Lorenz coefficient
$N_{bu}$ = buoyancy number
$u_h$ = $CO_2$ entry velocity at the wellbore
$V_{dp}$ = Dykstra-Parsons coefficient
$\alpha$ = formation dip angle
$\Delta$ = difference
$\mu$ = phase viscosity
$\lambda_{Dx}$ = horizontal dimensionless autocorrelation length
$\rho$ = phase density

## Acknowledgments

We thank Robin Dommisse for valuable discussion during this work. Bo Ren would like to thank Dr. Tingwei “Lucy” Ko for the discussion on geological features and data collection. We thank an anonymous operator for allowing us to access the Core Laboratories data. This study is part of a long-term project investigating ROZ reservoirs in the Permian Basin of Texas being carried out by the Bureau of Economic Geology’s (BEG’s) State of Texas Advanced Resource Recovery (STARR) Program. Larry W. Lake holds the Shahid and Sharon Ullah Endowed Chair in the Hildebrand Department of Petroleum and Geosystems Engineering at The University of Texas at Austin. This document is published with the approval of the Director of the Bureau of Economic Geology.

## References

Abdelaal, M., Zeidouni, M., and Duncan, I. J. 2021. Effects of Injection Well Operation Conditions on $CO_2$ Storage Capacity in Deep Saline Aquifers. *Greenhouse Gas Sci Technol* **11** (4): 734–749. https://doi.org/10.1002/ghg.2076.

Addington, D. V. 1981. An Approach to Gas-Coning Correlations for a Large Grid Cell Reservoir Simulator. *J Pet Technol* **33** (11): 2267–2274. SPE-8332-PA. https://doi.org/10.2118/8332-PA.

Ahr, W. M. 2011. *Geology of Carbonate Reservoirs: The Identification, Description, and Characterization of Hydrocarbon Reservoirs in Carbonate Rocks*. England, UK: John Wiley & Sons.

Al-Amrie, O. Y., Saad, M. A., Marzouqi, K. I. et al. 2012. The Use of a Formation Tester to Characterize Permeability and Vertical Communication across Stylolite Zones in a Carbonate Reservoir - Case Study. Paper presented at the Abu Dhabi International Petroleum Conference and Exhibition, Abu Dhabi, UAE, 11–14 November. SPE-160956-MS. https://doi.org/10.2118/160956-MS.

Armitage, P. J., Faulkner, D. R., Worden, R. H. et al. 2011. Experimental Measurement of, and Controls on, Permeability and Permeability Anisotropy of Caprocks from the $CO_2$ Storage Project at the Krechba Field, Algeria. *J. Geophys. Res* **116**. https://doi.org/10.1029/2011JB008385.

Ayan, C., Colley, N., Cowan, G. et al. 1994. Measuring Permeability Anisotropy: The Latest Approach. *Oilfield Review* **6** (4).

Azom, P. N. and Srinivasan, S. 2011. Modeling the Effect of Permeability Anisotropy on the Steam-Assisted Gravity Drainage (SAGD) Process. Paper presented at the Canadian Unconventional Resources Conference, Calgary, Alberta, Canada, 15–17 November. SPE-149274-MS. https://doi.org/10.2118/149274-MS.

Baker, R. O., Yarranton, H. W., and Jensen, J. L. 2015. *Practical Reservoir Engineering and Characterization*. Houston, Texas, USA: Gulf Professional Publishing.

Begg, S. H. and King, P. R. 1985. Modelling the Effects of Shales on Reservoir Performance: Calculation of Effective Vertical Permeability. Paper presented at the SPE Reservoir Simulation Symposium, Dallas, Texas, USA, 10–13 February. SPE-13529-MS. https://doi.org/10.2118/13529-MS.

Box, G. E. P. and Cox, D. R. 1964. An Analysis of Transformations. *J R Stat Soc Series B Stat Methodol* **26** (2): 211–243. https://doi.org/10.1111/j.2517-6161.1964.tb00553.x.

Bryant, S. L., Lakshminarasimhan, S., and Pope, G. A. 2008. Buoyancy-Dominated Multiphase Flow and Its Effect on Geological Sequestration of $CO_2$. *SPE J.* **13** (4): 447–454. SPE-99938-PA. https://doi.org/10.2118/99938-PA.

Campero, M. F., Nwonodi, C., Onwuchekwa, C. et al. 2014. Kv/Kh in Heterogeneous Reservoirs of a Brown Field of the Niger Delta of Nigeria – Valuable Uncertain Parameter for Assisted History Matching. Paper presented at the SPE Nigeria Annual International Conference and Exhibition, Lagos, Nigeria, 5–7 August. SPE-172450-MS. https://doi.org/10.2118/172450-MS.

Chandra, V., Geiger, S., Corbett, P. W. et al. 2013. Using Near Wellbore Upscaling to Improve Reservoir Characterization and Simulation in Highly Heterogeneous Carbonate Reservoirs. Paper presented at the SPE Reservoir Characterization and Simulation Conference and Exhibition, Abu Dhabi, UAE, 16–18 September. SPE-166033-MS. https://doi.org/10.2118/166033-MS.

Clavaud, J.-B., Maineult, A., Zamora, M. et al. 2008. Permeability Anisotropy and Its Relations with Porous Medium Structure. *J. Geophys. Res* **113**. https://doi.org/10.1029/2007JB005004.

Dernaika, M., Al Mansoori, M., Singh, M. et al. 2018. Digital and Conventional Techniques to Study Permeability Heterogeneity in Complex Carbonate Rocks. *Petro S Journ* **3** (59): 373–396. https://doi.org/10.30632/PJV59N3-2018a6.

Ettehadtavakkol, A., Lake, L. W., and Bryant, S. L. 2014. $CO_2$-EOR and Storage Design Optimization. *Ternational J Greenh Gas Control* **25**: 79–92. https://doi.org/10.1016/j.ijggc.2014.04.006.

Haldorsen, H. H. and Lake, L. W. 1984. A New Approach to Shale Management in Field-Scale Models. *SPE J.* **24** (4): 447–457. SPE-10976-PA. https://doi.org/10.2118/10976-PA.

Hanks, C., Shimer, G., Davis, J. et al. 2011. Production of Light Oil from a Shallow Frozen Reservoir: A Redevelopment Case Study of the Umiat Oil Field, Northern Alaska. Paper presented at the OTC Arctic Technology Conference, Houston, Texas, USA, 7–9 February. OTC-22064-MS. https://doi.org/10.4043/22064-MS.

Hassanpouryouzband, A., Joonaki, E., Edlmann, K. et al. 2021. Offshore Geological Storage of Hydrogen: Is This Our Best Option to Achieve Net-Zero? *ACS Energy Lett.* **6** (6): 2181–2186. https://doi.org/10.1021/acsenergylett.1c00845.

Heap, M. J., Baud, P., Reuschlé, T. et al. 2014. Stylolites in Limestones: Barriers to Fluid Flow? *Geology* **42** (1): 51–54. https://doi.org/10.1130/G34900.1.

Heinemann, N., Alcalde, J., Miocic, J. M. et al. 2021. Enabling Large-Scale Hydrogen Storage in Porous Media – the Scientific Challenges. *Energy Environ. Sci.* **14** (2): 853–864. https://doi.org/10.1039/D0EE03536J.

Hinton, E. M. and Woods, A. W. 2018. The Effect of Vertically Varying Permeability on Tracer Dispersion. *J. Fluid Mech.* **860**: 384–407. https://doi.org/10.1017/jfm.2018.891.

Honarpour, M. M., Djabbarah, N. F., and Sampath, K. 2005. Whole Core Analysis - Experience and Challenges. *SPE Res Eval & Eng* **8** (06): 460–469. SPE-81575-PA. https://doi.org/10.2118/81575-PA.

Jarrell, P. M., Fox, C. E., Stein, M. H. et al. 2002. *Practical Aspects of $CO_2$ Flooding*. Richardson, TX, USA: Society of Petroleum Engineers.

Jensen, J. L., Hinkley, D. V., and Lake, L. W. 1987. A Statistical Study of Reservoir Permeability: Distributions, Correlations, and Averages. *SPE Form Eval* **2** (04): 461–468. SPE-14270-PA. https://doi.org/10.2118/14270-PA.

Jensen, J. L. and Lake, L. W. 1988. The Influence of Sample Size and Permeability Distribution on Heterogeneity Measures. *SPE Res Eng* **3** (02): 629–637. SPE-15434-PA. https://doi.org/10.2118/15434-PA.

Jensen, J. L., Lake, L. W., Corbett, P. W. M. et al. 2000. *Statistics for Petroleum Engineers and Geoscientists*, second edition. Amsterdam, The Netherlands: Elsevier.

Jones, J. R., Scott, A. J., and Lake, L. W. 1987. The Geologic Aspects of Reservoir Characterization for Numerical Simulation: Mesaverde Meanderbelt Sandstone, Northwestern Colorado. *SPE Form Eval* **2** (01): 97–107. SPE-13052-PA. https://doi.org/10.2118/13052-PA.

Kerans, C., Lucia, F. J., and Senger, R. K. 1994. Integrated Characterization of Carbonate Ramp Reservoirs Using Permian San Andres Formation Outcrop Analogs. *Bulletin* **78** (2): 181–216. https://doi.org/10.1306/BDFF905A-1718-11D7-8645000102C1865D.

Koepnick, R. B. 1987. Distribution and Permeability of Stylolite-Bearing Horizons Within a Lower Cretaceous Carbonate Reservoir in the Middle East. *SPE Form Eval* **2** (02): 137–142. SPE-14173-PA. https://doi.org/10.2118/14173-PA.

Koval, E. J. 1963. A Method for Predicting the Performance of Unstable Miscible Displacement in Heterogeneous Media. *SPE J.* **3** (2): 145–154. SPE-450-PA. https://doi.org/10.2118/450-PA.

Krishnamurthy, P. G., Meckel, T. A., and DiCarlo, D. 2019. Mimicking Geologic Depositional Fabrics for Multiphase Flow Experiments. *Water Resour. Res.* **55** (11): 9623–9638. https://doi.org/10.1029/2019WR025664.

Lake, L. W. 1988. The Origins of Anisotropy (Includes Associated Papers 18394 and 18458). *J Pet Technol* **40** (04): 395–396. SPE-17652-PA. https://doi.org/10.2118/17652-PA.

Lake, L. W., Johns, R., Rossen, B. et al. 2014. *Enhanced Oil Recovery*, second edition. Richardson, Texas, USA: Society of Petroleum Engineers.

Lake, L. W., Lotfollahi, M., and Bryant, S. L. 2018. Fifty Years of Field Observations: Lessons for $CO_2$ Storage from $CO_2$ Enhanced Oil Recovery. Paper presented at the 14th International Conference on Greenhouse Gas Control Technologies, Melbourne, Australia. https://doi.org/10.2139/ssrn.3366254.

Lake, L. W., Lotfollahi, M., and Bryant, S. L. 2019. $CO_2$ Enhanced Oil Recovery Experience and Its Messages for $CO_2$ Storage. In *Science of Carbon Storage in Deep Saline Formations*, 15–31. N.p.: Elsevier. https://doi.org/10.1016/B978-0-12-812752-0.00002-2.

Lishman, J. R. 1970. Core Permeability Anisotropy. *J Can Pet Technol* **9** (02): 79–85. PETSOC-70-02-01. https://doi.org/10.2118/70-02-01.

Lucia, F. J., Kerans, C., and Wang, F. P. 1995. Fluid-Flow Characterization of Dolomitized Carbonate-Ramp Reservoirs: San Andres Formation (Permian) of Reservoir Field and Algerita Escarpment, Permian Basin, Texas and New Mexico. In *Hydrocarbon Reservoir Characterization: Geologic Framework and Flow Unit Modeling*, ed. E. L. Stoudt and P. M. Harris, 129–153. N.p.: SEPM Short Course No. 34.

Merchant, D. H. 2010. Life Beyond 80: A Look at Conventional WAG Recovery Beyond 80% HCPV Injection in $CO_2$ Tertiary Floods. Paper presented at the SPE International Conference on $CO_2$ Capture, Storage, and Utilization, New Orleans, Louisiana, USA, 10–12 November. SPE-139516-MS. https://doi.org/10.2118/139516-MS.

Morton, K., Thomas, S., Corbett, P. et al. 2002. Detailed Analysis of Probe Permeameter and Interval Pressure Transient Test Permeability Measurements in a Heterogeneous Reservoir. *Petroleum Geoscience* **8** (3): 209–216. https://doi.org/10.1144/petgeo.8.3.209.

Nieto Camargo, J. E. and Jensen, J. L. 2012. Analysis of Fault Permeability Using Mapping and Flow Modeling, Hickory Sandstone Aquifer, Central Texas. *Nat Resour Res* **21** (3): 395–409. https://doi.org/10.1007/s11053-012-9181-5.

Onur, M., Hegeman, P. S., Gok, I. M. et al. 2011. A Novel Analysis Procedure for Estimating Thickness-Independent Horizontal and Vertical Permeabilities From Pressure Data at an Observation Probe Acquired by Packer-Probe Wireline Formation Testers. *SPE Res Eval & Eng* **14** (4): 477–492. SPE-148403-PA. https://doi.org/10.2118/148403-PA.

Pamungkas, S., Gueye, T., Al Hammadi, F. Y. A. et al. 2020. A Novel Technique to Constrains Kv/Kh of Carbonate Reservoir, A Valuable Uncertain Parameters for History Match Process. Paper presented at the Abu Dhabi International Petroleum Exhibition & Conference, Abu Dhabi, UAE, 9–12 November. SPE-202832-MS. https://doi.org/10.2118/202832-MS.

Ren, B., Delaney, J. M., Lake, L. W. et al. 2018. Interplay Between Permeability Retardation and Capillary Trapping of Rising Carbon Dioxide in Storage Reservoirs. *SPE J.* **23** (5): 1866–1879. SPE-187356-PA. https://doi.org/10.2118/187356-PA.

Ren, B. and Duncan, I. 2019. Modeling Oil Saturation Evolution in Residual Oil Zones: Implications for $CO_2$ EOR and Sequestration. *J Pet Sci Eng* **177**: 528–539. https://doi.org/10.1016/j.petrol.2019.02.072.

Ren, B. and Duncan, I. J. 2021. Maximizing Oil Production from Water Alternating Gas ($CO_2$) Injection into Residual Oil Zones: The Impact of Oil Saturation and Heterogeneity. *Energy* **222**. https://doi.org/10.1016/j.energy.2021.119915.

Ringrose, P., Nordahl, K., and Wen, R. 2005. Vertical Permeability Estimation in Heterolithic Tidal Deltaic Sandstones. *Petroleum Geoscience* **11** (1): 29–36. https://doi.org/10.1144/1354-079303-614.

Saadatpoor, E., Bryant, S. L., and Sepehrnoori, K. 2010. New Trapping Mechanism in Carbon Sequestration. *Transp Porous Med* **82** (1): 3–17. https://doi.org/10.1007/s11242-009-9446-6.

Salazar, J. J. 2018. *Heterogeneity Study of the Little Creek Field from Petrophysical Data*. Master Thesis, The University of Texas at Austin, Austin, Texas.

Salazar, J. J. and Lake, L. W. 2020. The Physical Meaning of the Koval Factor. *Math Geosci* **52** (8): 1017–1033. https://doi.org/10.1007/s11004-020-09883-0.

Shook, M., Li, D., and Lake, L. W. 1992. Scaling Immiscible Flow through Permeable Media by Inspectional Analysis. *Situ* **16**: 311–311.

Sikandar, A. S. 1994. *A Study of Barrier Efficiency*. Master thesis, The University of Texas at Austin, Austin, Texas.

Silin, D., Patzek, T., and Benson, S. M. 2008. A Model of Buoyancy-Driven Two-Phase Countercurrent Fluid Flow. *Transp Porous Med* **76** (3): 449–469. https://doi.org/10.1007/s11242-008-9257-1.

Stalkup, F. I. and Dean, R. H. 1990. Sensitivity to Gridding of Miscible Flood Predictions Made with Upstream Differenced Simulators. Paper presented at the SPE/DOE Enhanced Oil Recovery Symposium, Tulsa, Oklahoma, USA, 22–25 April. SPE-20178-MS. https://doi.org/10.2118/20178-MS.

Sun, H., Vega, S., and Tao, G. 2017. Analysis of Heterogeneity and Permeability Anisotropy in Carbonate Rock Samples Using Digital Rock Physics. *J Pet Sci Eng* **156**: 419–429. https://doi.org/10.1016/j.petrol.2017.06.002.

Sutton, J. T., Glenton, P. N., Fittall, M. E. et al. 2013. Reservoir Simulation to Investigate the Effect of Flow Baffles in a Basin-Floor Fan, Scarborough Field, North West Shelf, Australia. Paper presented at the SPE Middle East Oil and Gas Show and Conference, Manama, Bahrain, 10–13 March. SPE-164268-MS. https://doi.org/10.2118/164268-MS.

Trevisan, L., Krishnamurthy, P. G., and Meckel, T. A. 2017. Impact of 3D Capillary Heterogeneity and Bedform Architecture at the Sub-Meter Scale on $CO_2$ Saturation for Buoyant Flow in Clastic Aquifers. *International J Greenh Gas Control* **56**: 237–249. https://doi.org/10.1016/j.ijggc.2016.12.001.

Wang, F. P., Lucia, F. J., and Kerans, C. 1994. Critical Scales, Upscaling, and Modeling of Shallow-Water Carbonate Reservoirs. Paper presented at the Permian Basin Oil and Gas Recovery Conference, Midland, Texas, USA, 16–18 March. SPE-27715-MS. https://doi.org/10.2118/27715-MS.

Wang, F. P., Lucia, F. J., and Kerans, C. 1998. Integrated Reservoir Characterization Study of a Carbonate Ramp Reservoir: Seminole San Andres Unit, Gaines County, Texas. *SPE Res Eval & Eng* **1** (02): 105–113. SPE-36515-PA. https://doi.org/10.2118/36515-PA.

Wannell, M. J. and Morrison, S. J. 1990. Vertical Permeability Measurement in New Reservoirs Using Tidal Pressure Changes. Paper presented at the SPE Annual Technical Conference and Exhibition, New Orleans, Louisiana, USA, 23–26 September. SPE-20532-MS. https://doi.org/10.2118/20532-MS.

Ward, R., Kendall, C. G., and Harris, P. M. 1986. Upper Permian (Guadalupian) Facies and Their Association with Hydrocarbons--Permian Basin, West Texas and New Mexico. *Am Assoc Pet Geol Bull* **70**: 239–262. https://doi.org/10.1306/9488566F-1704-11D7-8645000102C1865D.

Yang, G. and Butler, R. M. 1992. Effects Of Reservoir Heterogeneities On Heavy Oil Recovery By Steam-Assisted Gravity Drainage. *J Can Pet Technol* **31** (08): 37–43. PETSOC-92-08-03. https://doi.org/10.2118/92-08-03.

## Appendix A—Reproduction of Reservoir Permeability Geostatistics in Synthetic Models

This appendix illustrates detailed procedures of using both the Box-Cox method and sequential Gaussian simulation to reproduce the permeability statistics in synthetic models. For the Box-Cox method, the transformation of a random variable $X$ has the form: $Y(X, \lambda) = (X^{\lambda} - 1)/\lambda$, if $\lambda \neq 0$; $Y(X, 0) = \log X$. Based on the reservoir whole-core measurements of $k_{\max}$ (see the light blue curve in **Fig. A-1a),** we calculated that the optimal $\lambda = 0.081$ that results in the best approximation of a normal distribution of $k_{\max}$. Then, based on the global statistics of normal distribution, we generated the corresponding 3D permeability field with a set of other constraints (including model dimensions and autocorrelation length) using sequential Gaussian simulation. After this step, we substituted the generated permeability back into the Box-Cox equation and back-calculated Y to get the simulated permeabilities. They are compared to the core permeability in **Fig. A-1**. Both the CDF and Q-Q plots demonstrate that the global permeability statistics of the reservoir are captured in the synthetic permeability field.

**Fig. A-1—Comparative plots used to show the reproduction of the core permeability through using the proposed procedures. (a) The permeability CDF for cores vs. the simulated permeability field with the horizontal dimensionless autocorrelation length 2 for an inverted 5-spot well pattern. (b) The Q-Q plot for the two permeability data sets (cores vs. simulated).**

## Appendix B—Reservoir Simulation Model Inputs

This appendix lists the main inputs for the reservoir flow simulation model. These inputs include crude oil properties, $CO_2$-oil interaction, and relative permeability curves. The reservoir oil viscosity is 1.2 cp with a density of 657.7 $kg/m^3$ at reservoir conditions. The minimum miscibility pressure for the $CO_2$-oil system is around 1,400 psi. The Peng-Robinson equation of state was used to model the pressure/volume/temperature behaviors. More details are in Ren and Duncan (2021). **Table B-1** shows the oil compositions, and **Table B**-2 lists the binary interaction coefficients for pseudocomponents. **Fig. B-1** shows the relative permeability curves for the oil-water and oil-gas systems. The Stone I model was used to calculate oil relative permeability during three-phase flow. Hysteresis was not considered, and its influence on performance prediction was discussed in Ren and Duncan (2021). Endpoint scaling was used to consider the influence of permeability variations on relative permeability curves in flow simulations.

| Component | $CO_2$ | $C_1N_2$ | $C_2C_3H_2S$ | $C_4$-$C_6$ | $C_7$-$C_{10}$ | $C_{11}$-$C_{16}$ | $C_{17+}$ |
|---|---|---|---|---|---|---|---|
| Mole fraction (%) | 0.02 | 20.14 | 15.9 | 8.99 | 17.29 | 18.42 | 19.24 |
| Critical temperature (°R) | 547.56 | 339.21 | 619.38 | 835.43 | 1,117.84 | 1,344.62 | 1,686.57 |
| Critical pressure (psi) | 1,071.34 | 666.77 | 722.56 | 491.3 | 389.65 | 277.42 | 159.29 |
| Critical volume ($ft^3$/lb-mole) | 1.51 | 1.56 | 2.71 | 5.02 | 7.73 | 12.13 | 22.15 |
| Critical Z-factor | 0.275 | 0.287 | 0.295 | 0.275 | 0.251 | 0.233 | 0.195 |
| Molecular weights (g/mol) | 44.01 | 16.29 | 36.19 | 70.06 | 114.17 | 180.94 | 358.25 |
| Acentric factor | 0.225 | 0.0139 | 0.125 | 0.245 | 0.383 | 0.582 | 1.0054 |
| Coefficient, $\Omega_a$ | 0.457 | 0.457 | 0.457 | 0.457 | 0.457 | 0.457 | 0.457 |
| Coefficient, $\Omega_b$ | 0.077 | 0.077 | 0.077 | 0.077 | 0.077 | 0.077 | 0.077 |

Table. B-1—Representative crude oil compositions for the San Andres ROZ.

| Component | $CO_2$ | $C_1N_2$ | $C_2C_3H_2S$ | $C_4$-$C_6$ | $C_7$-$C_{10}$ | $C_{11}$-$C_{16}$ | $C_{17+}$ |
|---|---|---|---|---|---|---|---|
| $CO_2$ | 0 | | | | | | |
| $C_1N_2$ | 0.0976 | 0 | | | | | |
| $C_2C_3H_2S$ | 0.1289 | 0.0103 | 0 | | | | |
| $C_4$-$C_6$ | 0.1271 | 0.0019 | 0.0063 | 0 | | | |
| $C_7$-$C_{10}$ | 0.1105 | 0.0241 | 0.0196 | 0.003 | 0 | | |
| $C_{11}$-$C_{16}$ | 0.0943 | 0.0494 | 0.0333 | 0.0061 | 0 | 0 | |
| $C_{17+}$ | 0.0997 | 0.1365 | 0.0588 | 0.012 | 0 | 0 | 0 |

Table. B-2—Binary interaction coefficients for pseudo-components.

[redacted]

Fig. B-1—Relative permeability curves for oil-water (a) and oil-gas (b) systems.

## Appendix C—Koval Plots and $k_z$-$k_x$ Crossplots for Other Wells

This appendix shows the compilation of Koval plots and $k_z$-$k_x$ crossplots for more wells (**Figs. C-1 and C-2**).

[redacted]

Fig. C-1—Koval plots for several selected wells. The curves for $k_x(k_{\max})$ and $k_y(k_{90})$ are virtually identical because they are from unoriented cores.

[redacted]

Fig. C-2—Vertical permeability vs. maximum horizontal permeability crossplots for several selected wells. Both permeability measurements are reported on a log scale. A 1:1 line is provided for reference. The probability of $k_z > k_x$ is included in each plot.

## 12

# $CO_2$ EOR and Associated Storage in Residual Oil Zones: Modelling the Evolution and Significance of Oil Saturation in Residual Oil Zones

Bo Ren[a], Ian J. Duncan[b]*

[a]*Hildebrand Department of Petroleum and Geosystems Engineering, The University of Texas at Austin, Austin, TX 78712, USA*
[b]*Bureau of Economic Geology, The University of Texas at Austin, Austin, TX 78713, USA*

---

### Abstract

Residual oil zones (ROZs) are reservoirs in which oil is largely at levels of residual saturation. Such reservoirs cannot be produced by conventional production techniques. ROZs in carbonate reservoirs in the Permian Basin of West Texas were initially interpreted (from wireline logs), as being productive oil zones. If these zones were completed for production, they produced largely water. Over the last decade it has been demonstrated that $CO_2$ injection can make these zones economic to produce. As a result, ROZs in the Permian basin and elsewhere have become attractive targets for $CO_2$-EOR ($CO_2$ enhanced oil recovery) and have a large potential for $CO_2$ sequestration consequential to the EOR activity. The viability of $CO_2$ EOR in ROZs is currently being demonstrated by the results of $CO_2$ injection into the ROZs at the Seminole, Wasson Denver Unit, and Goldsmith oil field. The recoverable oil from ROZs in both the San Andres and Canyon Reef formations of Permian Basin, have been estimated as 12 billion barrels. A key question is the capacity of ROZs to sequester $CO_2$.

The current project is the first study of ROZs based on extensive studies of cores, wireline logs, and production data from several ROZs in the San Andreas Formation. Understanding the magnitude of oil saturation and how it varies within ROZs is important to modelling both EOR and sequestration. The commonly accepted model for the formation of ROZ is based on the hydrodynamic effects of tectonically-controlled increased water flows in aquifer at the base of oil fields. In this work, the nature of this process was modelled using a commercial reservoir simulator. These flow simulations were designed to understand how the effects of strength of aquifer flow, flow direction, and capillary pressure on the nature and distribution of oil saturations in ROZs. A special emphasis was on understanding the impact of reservoir heterogeneity on the variation of capillary pressures throughout ROZs. Heterogeneities in capillary pressures appear to dominate the distribution of oil saturation within the ROZ and will also strongly influence the performance for both oil production from $CO_2$ injection, as well as associated $CO_2$ storage. Finally, we discuss the implications of our results to the understanding of both $CO_2$ EOR and storage in ROZs.

*Keywords:* Oil Saturation, Residual Oil Zone, $CO_2$ EOR and Storage, Flow Modeling.

---

### 1. Introduction

Residual oil zones (ROZs) can be defined as an oil reservoir in which the oil is at, or is close to, residual oil saturation. ROZs have the apparent characteristics of a reservoir after the completion of a water flood. ROZs in carbonate reservoirs in the Permian Basin of Texas were initially interpreted from wireline logs as being productive

---

* Corresponding author. Tel.: +1-512-471-5117; fax: +1-512-471-0140
*E-mail address:* ian.duncan@beg.utexas.edu

oil zones. However, if these zones were completed for production, they produced water only occasionally with traces of oil. Thus, ROZs can be produced by neither conventional pumping nor water flooding. Rather, producing from these zones requires some form of enhanced oil recovery such as $CO_2$-EOR (providing incidental sequestration of $CO_2$).

ROZs have different types in terms of their origin and evolution [1]: (i) an oil accumulation is subject to a tilt (from differential subsidence or tectonic movements), resulting in re-equilibration of water-oil contacts and the formation of ROZs; (ii) the original oil accumulation leaks through seal (perhaps temporally), again leading to ROZ formation; (iii) a change in the hydrodynamics of the underlying aquifer resulting in regional groundwater flow. This flow sweeps the lower portion of oil columns, resulting in the development of ROZs. The consensus of opinions is that the ROZs in the Permian Basin represent the third of these categories and the simulations made in the current study are based on this scenario.

As a result of many years of testing and analysis by Permian Basin petroleum engineers and geologists, it has been demonstrated that $CO_2$ injection enables economically viable oil production from ROZs [1-4]. The San Andres Formation has over 10 Billion bbls of cumulative production. Estimates of the volume remaining from the original oil in place (OOIP) vary between 50 to 80%. $CO_2$ EOR in ROZs is currently taking place in eight San Andres oil fields in the Permian Basin, including the Seminole San Andres Unit, the East Seminole field, the Goldsmith San Andreas Unit, the Wasson Denver Unit, Tall Cotton, Hanford field, Means, and the Vacuum San Andres field. Significant volumes of $CO_2$ are being sequestered incidental to these $CO_2$-EOR projects, providing a possible path for large scale market-driven carbon capture and storage (CCS). The estimated recoverable oil from ROZs in both the San Andres and Canyon Reef formations of Permian Basin, are estimated by Koperna et al. [5] as 12 billion barrels. This represents a little over a third of the estimated original oil in place. Bachu et al. [6] noted that ROZs are "regarded in the industry as the most optimum part of oil reservoirs to store $CO_2$". They based this on: the typically large volume of ROZs; their high water saturation; and "hydrocarbon availability".

Unfortunately, almost all the research on ROZ formation and characteristics has not been published in refereed journals but rather is available in contract reports, presentations, and conference proceedings. Trentham and his coworkers [7] have assumed that, high aquifer flow rates would have been initially established across the San Andreas formation from the uplift of the Guadalupe Mountains along the western margin of the Permian Basin. This uplift apparently peaked around 20 Ma associated with the formation of the Rio Grande Rift [8]. Subsequent erosion of these mountains would have reduced hydraulic heads in the regional aquifer lowering flow rates. Harouaka et al. [9] suggested that the hydrodynamic impact continued unabated, "albeit at a very slow pace like one foot/1000 years", an assertion they based on "analytical modeling" using the analysis of Hubbert [10]. A recent study by Trentham et al. [7] attempted to model the probable flow pathways, of what they termed "hydrodynamic fairways". However, absent a creation of a set of robust regional groundwater flow models extending back to the regional uplift event in the Permian Basin, the groundwater flow directions cannot be well constrained. Jamali and Ettehadtavakkol [11] modelled the ROZ formation process through mimicking the natural waterflooding process, however, their specific simulation is based on a simplified static reservoir model and physics.

This paper is the first attempt to use multiphase and full-physics flow simulations to make a comprehensive study of the hydrodynamic model for the development of (and the implications of for $CO_2$-EOR) ROZs in the San Andres Formation. In the following, we describe our modeling approach and analyze several factors that are potentially significant in the evolution of ROZs. Finally, we evaluate the significance of these results to both oil production and incidental $CO_2$ sequestration in future $CO_2$-EOR projects in these zones.

## 2. Methodology

This project set out to study the formation of ROZs in the San Andres Formation, based on creating simulations modelling the "natural waterflood" scenario. We create simulations of these reservoirs that aim to explore the nature and spatial patterns of oil saturation in ROZs in response to variations in the flow of regional aquifers. The simulator used is Eclipse-E100 [12], an efficient and multidimensional black-oil simulator.

Our modeling is based on the reservoir characteristics of the residual oil zone associated with the Seminole Field, however, we do not model this field specifically. A three-dimensional (3D) static reservoir model, representative of the geology and petrophysical variation of the ROZ underlying the Seminole Field, was built from the published reservoir property data [13-15]. The model was populated using data from these published sources and from petrophysical measurements made on cores, and interpretation of wireline logs from the BEG log library.

Two 2-D section geologic models were cut from the 3-D reservoir model: one is along the E-W (X-Z slice, the approximate dip direction), and the other is along the N-S (Y-Z slice, the approximate strike direction). The purpose of selecting these two sections is to examine how flow direction affects evolution the oil saturation in the ROZ. The two vertical sections cross along a vertical line. This line overlaps a drilled vertical well with detailed well properties published by Honarpour et al. [15]. Specifically, this well has an oil saturation profile, based on measurements (made prior to $CO_2$ injection into the ROZ) from sponge cores. This data provides an important way for us to validate the reasonableness of our simulations.

The corner point grid system is used, and the dimensions of each model is 63×100. The cell size in the horizontal direction is 100 ft., and the vertical cell size varies in different layers with the average ~2ft. The two 2-D orthogonal models have similar means and standard deviation for the porosity and permeability (Table 1). Published permeability measurements by Honarpour et al. [15] show that the horizontal and vertical permeability's are largely similar. These authors note that the presence of low permeability layers of fine-grained, anhydrite-rich facies, creates a strongly anisotropic permeability. They suggest the resultant vertical component is approximately one tenth of the horizontal component. Initially, hydrostatic pressure is set for the reservoir with the middle depth pressure at 2119.9 psi, and the reservoir temperature is 104 °F. The oil saturation is initialized using the gravity-capillary equilibrium method.

A capillary entry pressure field is generated using the Leverett j-function [16] that links permeability, porosity, and capillary pressure. The reference capillary pressure curve is assigned to the cells with the permeability of 16 mD as this reference curve is measured on the core with this permeability. These cells are considered as reference cells. The other cells in the model are assigned with different capillary pressure curves by scaling the capillary pressure of each cell with the corresponding permeability and porosity. The interfacial tension for each cell is assumed to be the same, and contact angle has the same assumption. So each cell can be assigned with a capillary pressure curve that is consistent with its upscaled permeability and porosity while omitting interfacial tension and contact angle.

Flow simulations are designed to model the key relevant physics for understanding the ROZ origin associated with the San Andreas Formation in the Permian Basin. To understand the relevant physics, we first introduce a gravity number ($N_{gr}$), and this number describes the influence of competitive gravity versus viscous forces on water flooding. $N_{gr}$ is a dimensionless ratio of the gravitational force acting on the fluids to the viscous force that drives water migration.

In the 2D models, the volume of water injected is approximately 27 pore volumes (PV) for the base case (corresponding to the regional water flux of 0.5 ft./yr.). This PV is consistent with the suggestions of Trentham et al., [7] about the time scale and flux of regional natural water flooding impacting the ROZs within the Permian Basin. The sensitivity of the magnitude of oil saturation in the ROZs to varying the magnitude and duration of regional hydraulic head, is also investigated. The regional hydraulic head was varied over three orders of magnitude. Additionally, changes in the nature of ROZs (e.g., oil saturation and geometry) in response to the lowering of hydraulic head are examined. This lowering decreases regional water flow rate, so the study is designed to approximate the decreasing rate of flow through three sequential simulation processes with the decreasing water fluxes from 5ft/yr, 0.5ft/yr to 0.05 ft/yr, with each modeled time period lasting for 50,000 years (refer to case #12 in Table 2). More importantly, both single and heterogeneous capillary pressure are purposely considered in these simulations. Single capillary pressure means that the capillary pressure curve is used for all the cells in the domain, whereas, heterogeneous capillary pressure means that scaled capillary pressure curves are employed.

Table 1 Injection simulation schemes in the 2D models

| Water flux entering formation from wellbore, ft./yr. | Injection rate, rb/d** | Injection duration, Year | Total injected water, PV | $N_{gr}$ along the wellbore | Dominant force |
|---|---|---|---|---|---|
| 5.0 | 183.4 | 50k | 268 | 4.7E+3 | Gravity |
| 0.5* | 18.3* | 50k* | 26.8* | 4.7E+4* | Gravity |
| 0.05 | 1.83 | 50k | 2.7 | 4.7E+5 | Gravity |

*means base case settings; ** rb means reservoir barrel

A vertical injector and a producer are used to mimic regional water filtration in the ROZ, and the two wells are placed on the left and right boundary cells, respectively. Both wells are perforated along the intervals of both the producing ROZ and the water leg, for which, their heights are approximated through the field tests and measurements [15]. Constant water rate is imposed on the injector with the values shown in Table 2, and the same rate of liquid production is imposed on the right producer. Boundary settings in the N-S slice are the same. The condition settings for all the simulated cases are summarized in Table 2.

Table 2 Summary of conditions for simulations. The time duration in parentheses, correspond to the adjacent PV.

| Case No | Water flux, ft/yr | Injected PV | Flow direction | Capillary pressure |
|---|---|---|---|---|
| 1 | 0.5 | 26.8 (50k yrs) | W-E | w/o |
| 2 | 0.5 | 32.1 (60k yrs) | W-E | w/o |
| 3 | 0.5 | 26.8 | W-E | Single |
| 4 | 0.5 | 26.8, 268, 536 (1MM yrs) | W-E | Heterogeneous |
| 5 | 5.0 | 268 | W-E | Single |
| 6 | 5.0 | 268 | W-E | Heterogeneous |
| 7 | 0.05 | 2.7 | W-E | Single |
| 8 | 0.05 | 2.7, 27, 54 (1MM yrs) | W-E | Heterogeneous |
| 10 | 0.5 | 26.8 | N-S | Heterogeneous |

## 3. Results

We firstly describe the evolution of oil saturation fields during the ROZ formation process. Particularly, we emphasize the effect of the interplay between water flux magnitude and capillary pressure on the remaining oil saturation in the ROZ. Next, we compare our simulation results to the down the well measurements of oil saturation in the San Andres Seminole Field.

### *3.1 Effect of the duration of regional aquifer flow on oil saturation in ROZs*

To evaluate the effect of the duration of regional aquifer flow on the nature of ROZ formation, we started with the case that considers no capillary pressure (#1 in Table 2). This case shows a similar oil saturation field as another case that considers single capillary pressure (#3 in Table 2). For the MPZ, the oil saturation is initialized using the gravity-capillary equilibrium, and the initial oil saturation is high and around 0.8. The capillary transition zone in these simulations is very small and almost not observable as shown around the interface between the yellow and blue areas. As water influx proceeds (T=10,000 to 50,000 yrs.), the vertical extent of the ROZ increases. At a timescale of 50,000 years, further changes in the magnitude and spatial distribution of oil saturation values are negligible.

The variation of oil saturation with depth is perhaps the most important feature of ROZs. The intervals with high saturation represent the low permeability/low porosity (<0.05) areas, and this oil cannot be efficiently displaced by water as shown in Fig. 1. To quantify oil saturation vertical profiles, we plot the change of oil saturation along depth at different times (Fig. 2). Overall, the oil saturation profiles attained an approximate or pseudo-steady state after approximately 50,000 years. The attainment of pseudo-steady-state oil saturation is further illustrated in Fig. 3 that shows the evolution cell oil saturation in several selected depths. It appears that, in this simulation, the upper part of the ROZ requires a much longer time to reach this pseudo-steady state (note the light blue line in Fig.3).

Fig. 1. The evolution of oil saturation fields considering single capillary pressure. The water inlet flux is 0.5 ft/yr. X/Z aspect ratio is 5.7.

Fig. 2. The change of oil saturation vertical oil saturation profiles with time. These profiles correspond to the middle column cells (along the well with measured oil saturation in the ROZ) of the oil saturation fields in Fig. 6.

Fig. 3. The change of cell oil saturation with time at several different selected depth points. These points are all in the ROZ: 5370 ft is around the ROZ top, the two depths of 5425 and 5450 ft are in the middle, and 5475 ft is at the bottom.

### *3.2 Effect of the interplay between inlet flux magnitude and capillary pressure*

We first analyze the effect of water flux magnitude (aquifer flow-rate) on ROZs when considering single capillary pressure (left column in Fig. 4). ROZ thickness is sensitive to the magnitude of the upstream water flux in the aquifer. This is because of the competition between the viscous and gravitational forces (the ratio is gravity number $N_{gr}$,): large viscous force (large water flux) suppresses the effect of water gravity on the displacement profile, and a thick ROZ is created. Additionally, the contact between the MPZ (yellow in Fig. 4) and ROZ (light blue) becomes less inclined as water flux decreases; this is obviously because decreasing water flux tends to create hydrostatic distribution of oil/water.

Next, we focus on the imposed upstream water flux of 0.5 ft/yr (the middle row in Fig. 4) and analyse the effect of capillary pressure heterogeneity on the development of ROZs in response to this water flow. When capillary pressure heterogeneity is taken into account, the producing water-oil contact is enlarged (relative to single capillary pressure). In addition, the transition zone (black circled area in the middle row) between the ROZ and the MPZ is distinct, with a thickness of 10-15 ft. The oil saturation in this transition zone varies significantly, from around 0.30 in light green spots to 0.80 in the light yellow patches. However, for the case considering single capillary pressure, the transition zone is thin and poorly defined (refer to the middle left oil saturation field in Fig. 4).

Fig. 4. Oil saturation fields at 50000 yrs of flow simulation. Each row represents different regional water fluxes. The left column considers single capillary pressure, whereas, the right column considers heterogeneous capillary pressure. The dashed lines represent the approximated transition areas between the top of producing ROZ and the base of producing MPZs. X/Z aspect ratio is 5.7.

More importantly, the interplay between capillary pressure heterogeneity and upstream water flux largely influences the thickness of the upper transition zone (the dashed circle area). Through comparing the middle saturation field to the lower one in the right column in Fig. 4, it can be seen that the upper transition zone becomes thick as the upstream water flux decreases. Again, this is because of the lower viscous force, which in turn enhances the effect of capillary dispersion on oil saturation.

The above analyses concentrate on the evolution of oil saturation in ROZs. The time scale of achieving quasi steady-state oil saturation in a ROZ is much less than the geologic time of mountain uplift and erosion (~Ma). Generally, the evolution of oil saturation in a given cell is mainly controlled by both relative permeability curves and imposed pressure gradient (equivalent to inlet water flux). Thus, any changes in both of them would cause different time consumed to achieve steady states.

### *3.3 Effect of regional water flow directions*

The noteworthy issue is the nature of oil-water contacts (dashed blue lines in Fig. 5) for the two different regional water flow directions. The inclination of the contact along the strike direction is smaller than in the dip direction. This observation is consistent with greater lateral sedimentary continuity along the strike.

Fig. 5. Impact of flow direction on oil saturation fields in the ROZ. The oil saturation is at the 50,000 yrs of flow simulation with capillary pressure heterogeneity considered. The black dashed lines circle the oil stripes with large oil saturation in the ROZ, and the blue dashed lines approximate the inclined producing water-oil contacts. The imposed water flux for both oil saturation fields is 0.5 ft/yr. Left: X/Z aspect ratio is 5.7. Right: Y/Z ratio is 7.7.

## 4. Discussion

This study has not attempted to specifically model the Seminole Field, rather, we have modelled the formation of a generic ROZ by starting with an oil-saturated reservoir. Its thickness is equivalent to the sum of current SSAU ROZ and producing MPZ. Our simulations reproduce many of the features reported from San Andreas ROZ reservoirs. The simulation results are consistent with an effectively steady state being reached (at least with respect to oil saturation) on a time scale of 50 thousand years. It is significant that, even after 1MM yrs of regional water flush, the oil saturation in several patches remains similar to the initialized values (0.7~0.8). These patches are local areas of lower porosity and permeability. This observation is consistent with the observed presence of oil stains in the less permeable patches of San Andres core samples.

The influence of capillary pressure heterogeneity on the flow paths of water/oil and thus on the ROZ characteristics, is one of the key discoveries of this study. Heterogeneous capillary pressures are known to be significant for a number of subsurface processes that are characterized by slow flow rates, e.g., buoyant flow of $CO_2$ during geological carbon sequestration [17,18] and secondary hydrocarbon migration/ accumulation [19]. Even for conventional water flooding with flow rates three orders of magnitudes larger than that associated with the hydraulic head gradient and consequent subsurface regional aquifer flow rates preferred in this study, capillary pressure heterogeneity apparently significantly affects oil saturation under some conditions [20, 21].

This study is subject to several limitations. First, the predictions of average oil saturation in the ROZs from our simulations are marginally larger than those measured by Honarpour et al. [15]. One possibility is that, in some cells, the 50,000 years of the flow simulations presented is insufficient to achieve a steady state. This is the consequence of the fractional flow curve for water. The fractional flow of oil is reduced to a very small value (<0.008) when water saturation increases to 0.5. Another complication is the impact of our limited ability to accurately model the heterogeneous nature of the reservoir. The simulations in this study utilized a cell size of 100 ft. × ~2 ft. However, the estimates of porosity and permeability were based on measurements of core plugs with the size of 1~2 inches. Upscaling these detailed measurements to the scale of the simulation grid inevitably averages out the true heterogeneous nature of the reservoir. Additionally, the water-oil-rock interaction might need to be studied to examine its effect on oil properties and reservoir petrophysical properties. Such geochemical reactions have been demonstrated to be important in other similar subsurface flow dynamics [22, 23].

The capacity of ROZs to store $CO_2$ associated with EOR is not well understood. Commercial scale ROZ floods have only been implemented in the last decade and no studies of ROZ reservoirs have been published. Bachu et al. [6] suggested that the oil industry regard ROZs as a superior target for geological carbon storage. They noted that $CO_2$-EOR will provide a mechanism to defray the costs of carbon capture and storage (CCS) projects. The current study can be used as the basis for developing strategies to utilize $CO_2$ injection to optimize oil production and sequestration. For example, heterogeneities in permeability, porosity, and capillary pressures are highly likely to result in three-dimensional spatial heterogeneities in oil saturation. Such patches and layers of higher saturation could be exploited by using multiple horizontal wells. Additionally, the extensive distribution of water in ROZs should have some effects in selecting and optimizing $CO_2$ injection strategies. This extensive water distribution is different from that in MPZ after man-made water flooding since, for MPZ, water saturations are locally high around the water streamlines connecting injectors and producers. This difference would bring different optimized schemes of WAG injection into ROZ reservoirs, including water cycle size and WAG ratio.

## 5. Conclusions and Recommendations

The key characteristic of residual oil zones (ROZs) is the spatial and depth dependant variation of oil saturation. This information is important essential to assess reserves, design $CO_2$-EOR projects, and estimate the sequestration capacity in ROZs. This study has demonstrated that the key features of ROZs can be simulated using a commercial, full-physics, multi-phase flow simulator. The results support the plausibility of the hydrodynamic model suggested by earlier researchers, but do not rule out other models for the origin of ROZs.

The magnitudes of water flux (aquifer flow rate) and capillary pressure within the reservoir influences the variation of oil saturation (both spatially and temporally) and geometry of ROZs. Larger water fluxes result in thicker ROZs, and heterogeneous capillary pressures will lead to development of diffuse water-oil contacts. During the formation of ROZ, the evolving oil saturation is controlled by the relative permeability curves. A very large amount of oil resides in ROZ reservoirs in the San Andres Formation and these reservoirs are attractive targets for $CO_2$ EOR and associated storage. Additionally, the spatial distribution of oil in ROZs are different from that in MPZs undergoing water flooding. This difference will be important in the optimization of $CO_2$ EOR and storage in ROZs.

## Acknowledgements

This study is part of a long term project investigating ROZ reservoirs in the Permian Basin of Texas being carried out by the Bureau of Economic Geology's (BEG's) State of Texas Advanced Resource Recovery (STARR) Program and funded in part by a US Department of Energy contract under DOE Award Number FE0024375 (PI: Duncan). The opinions of the authors do not necessarily reflect those of the United States Government or any agency thereof. The research was also supported by endowed funds from the Jackson School of Geological Sciences at The University of Texas at Austin. Publication authorized by the Director, Bureau of Economic Geology.

## References

[1] Melzer LS. Residual oil zones (ROZ): a review of ROZ science and engineering. In: enhanced oil recovery's tensleep III workshop. University of Wyoming; 2013.

[2] Trentham CR, Melzer LS. Case studies of the ROZ $CO_2$ flood and the combined ROZ/MPZ $CO_2$ flood at the Goldsmith Landreth Unit, Ector County, Texas. DOE Final Report; 2015

[3] Kuuskraa V, Petrusak R, Wallace M. Residual oil zone "fairways" and discovered oil resources: expanding the options for carbon negative storage of $CO_2$. Energy Procedia 2017;114:5438-5450.

[4] Godec ML, Kuuskraa VA, Dipietro P. Opportunities for using anthropogenic $CO_2$ for enhanced oil recovery and $CO_2$ storage. Energ Fuel 2013; 27(8):4183-4189.

[5] Koperna GJ, Melzer LS, Kuuskraa VA. Recovery of oil resources from the residual and transitional oil zones of the Permian Basin. SPE 102972 presented at the Annual Technical Conference and Exhibition, San Antonio, Texas, 24-27 September 2006.

[6] Bachu S, Pires P, Li MY, Guzman F, Eide LI, Aleidan A, Ackiewicz M, Melzer LS. Technical challenges in the conversion of $CO_2$-EOR projects to $CO_2$ storage projects, Report Prepared by the CSLF Task Force on Technical Challenges in the Transition from $CO_2$ EOR to CCS, http://www.cslforum.org/publications/documents/CO₂- EORtoCCS_FinalReport.pdf, 2013.

[7] Trentham CR, Melzer LS, Vance DB. Commercial exploitation and the origin of residual oil zones: Developing a case history in the Permian Basin of New Mexico and West Texas. RPSEA Final Report; 2012.

[8] Horak RL. Tectonic and hydrocarbon maturation history in the Permian Basin: Oil Gas J 1985;83(21):124–129.

[9] Harouaka A, Trentham B, Melzer LS. Long overlooked residual oil zones (ROZ's) are brought to the limelight. SPE-167209 presented at the SPE Unconventional Resources Conference, Calgary, Canada, 5-7 November 2013.

[10] Hubbert MK. "Entrapment of petroleum under hydrodynamic conditions," AAPG Bulletin 1953;37(8):1954-2028.

[11] Jamali A, Ettehadtavakkol A. $CO_2$ storage in residual oil zones: Field-scale modeling and assessment. Int J Greenh Gas Con 2017;56:102-115.

[12] Eclipse-E100, 2016. Eclipse Users' Manual. Schlumberger, France.

[13] Wang F, Lucia F, Kerans C. Integrated reservoir characterization study of a carbonate ramp reservoir: Seminole San Andres Unit, Gaines County, Texas. SPE Reserv Eval Eng 1998;1(02):105–113.

[14] Lucia FJ. Carbonate reservoir characterization: An integrated approach, Springer Science & Business Media. Berlin, Germany; 2007

[15] Honarpour MM, Nagarajan NR, Grijalba CA, Valle M, Adesoye K. Rock-fluid characterization for miscible $CO_2$ injection: Residual oil zone, Seminole Field, Permian Basin. SPE-133089 presented at the Annual Technical Conference and Exhibition, Florence, Italy, 19-22 September 2010.

[16] Leverett MC. Capillary behavior in porous solids. AIME Petroleum Transactions 1941;142:152-169.

[17] Saadatpoor E, Bryant SL, Sepehrnoori K. New trapping mechanism in carbon sequestration. Transport In Porous Media 2009; 82(1):3-17.

[18] Trevisan L, Krishnamurthy PG, Meckel TA. Impact of 3D capillary heterogeneity and bedform architecture at the sub-meter scale on $CO_2$ saturation for buoyant flow in clastic aquifers. Int J Greenh Gas Con 2017;56:237-249.

[19] Carruthers DJF. Transport modelling of secondary oil migration using gradient-driven invasion percolation techniques. Ph.D. Dissertation, Heriot-Watt University, Edinburgh, UK; 1998

[20] Chang J, Yortsos YC. Effect of capillary heterogeneity on Buckley-Leverett displacement. SPE Reserv Eng 1992;7(2):285-293.

[21] Lasseter TJ, Waggoner JR, Lake LW. Reservoir heterogeneities and their influence on ultimate recovery, in: Lake, L.W., Carroll, B.C. (Eds.), Reservoir Characterization. Amsterdam: Elsevier Inc., 1986. p. 545-559.

[22] Luhmann AJ, Tutolo BM, Tan C, Moskowitz BM, Saar MO, Seyfried WE. Whole rock basalt alteration from CO2-rich brine during flow-through experiments at 150°C and 150bar. Chem Geol 2017;453:92-110.

[23] Cui G, Zhang L, Tan C, Ren S, Zhuang Y, Enechukwu C. Injection of supercritical $CO_2$ for geothermal exploitation from sandstone and carbonate reservoirs: $CO_2$–water–rock interactions and their effects. J $CO_2$ Util 2017;20:113-128.

# 13 $CO_2$ EOR and Associated Storage in Residual Oil Zones: Modelling the Evolution and Significance of Oil Saturation in Residual Oil Zones

Bo Ren[a], Ian J. Duncan[b]*

[a]Hildebrand Department of Petroleum and Geosystems Engineering, The University of Texas at Austin, Austin, TX 78712, USA
[b]Bureau of Economic Geology, The University of Texas at Austin, Austin, TX 78713, USA

---

## Abstract

Residual oil zones (ROZs) are reservoirs in which oil is largely at levels of residual saturation. Such reservoirs cannot be produced by conventional production techniques. ROZs in carbonate reservoirs in the Permian Basin of West Texas were initially interpreted (from wireline logs), as being productive oil zones. If these zones were completed for production, they produced largely water. Over the last decade it has been demonstrated that $CO_2$ injection can make these zones economic to produce. As a result, ROZs in the Permian basin and elsewhere have become attractive targets for $CO_2$-EOR ($CO_2$ enhanced oil recovery) and have a large potential for $CO_2$ sequestration consequential to the EOR activity. The viability of $CO_2$ EOR in ROZs is currently being demonstrated by the results of $CO_2$ injection into the ROZs at the Seminole, Wasson Denver Unit, and Goldsmith oil field. The recoverable oil from ROZs in both the San Andres and Canyon Reef formations of Permian Basin, have been estimated as 12 billion barrels. A key question is the capacity of ROZs to sequester $CO_2$.

The current project is the first study of ROZs based on extensive studies of cores, wireline logs, and production data from several ROZs in the San Andreas Formation. Understanding the magnitude of oil saturation and how it varies within ROZs is important to modelling both EOR and sequestration. The commonly accepted model for the formation of ROZ is based on the hydrodynamic effects of tectonically-controlled increased water flows in aquifer at the base of oil fields. In this work, the nature of this process was modelled using a commercial reservoir simulator. These flow simulations were designed to understand how the effects of strength of aquifer flow, flow direction, and capillary pressure on the nature and distribution of oil saturations in ROZs. A special emphasis was on understanding the impact of reservoir heterogeneity on the variation of capillary pressures throughout ROZs. Heterogeneities in capillary pressures appear to dominate the distribution of oil saturation within the ROZ and will also strongly influence the performance for both oil production from $CO_2$ injection, as well as associated $CO_2$ storage. Finally, we discuss the implications of our results to the understanding of both $CO_2$ EOR and storage in ROZs.

*Keywords:* Oil Saturation, Residual Oil Zone, $CO_2$ EOR and Storage, Flow Modeling.

---

## 1. Introduction

Residual oil zones (ROZs) can be defined as an oil reservoir in which the oil is at, or is close to, residual oil saturation. ROZs have the apparent characteristics of a reservoir after the completion of a water flood. ROZs in carbonate reservoirs in the Permian Basin of Texas were initially interpreted from wireline logs as being productive

---

* Corresponding author. Tel.: +1-512-471-5117; fax: +1-512-471-0140
*E-mail address:* ian.duncan@beg.utexas.edu

oil zones. However, if these zones were completed for production, they produced water only occasionally with traces of oil. Thus, ROZs can be produced by neither conventional pumping nor water flooding. Rather, producing from these zones requires some form of enhanced oil recovery such as $CO_2$-EOR (providing incidental sequestration of $CO_2$).

ROZs have different types in terms of their origin and evolution [1]: (i) an oil accumulation is subject to a tilt (from differential subsidence or tectonic movements), resulting in re-equilibration of water-oil contacts and the formation of ROZs; (ii) the original oil accumulation leaks through seal (perhaps temporally), again leading to ROZ formation; (iii) a change in the hydrodynamics of the underlying aquifer resulting in regional groundwater flow. This flow sweeps the lower portion of oil columns, resulting in the development of ROZs. The consensus of opinions is that the ROZs in the Permian Basin represent the third of these categories and the simulations made in the current study are based on this scenario.

As a result of many years of testing and analysis by Permian Basin petroleum engineers and geologists, it has been demonstrated that $CO_2$ injection enables economically viable oil production from ROZs [1-4]. The San Andres Formation has over 10 Billion bbls of cumulative production. Estimates of the volume remaining from the original oil in place (OOIP) vary between 50 to 80%. $CO_2$ EOR in ROZs is currently taking place in eight San Andres oil fields in the Permian Basin, including the Seminole San Andres Unit, the East Seminole field, the Goldsmith San Andreas Unit, the Wasson Denver Unit, Tall Cotton, Hanford field, Means, and the Vacuum San Andres field. Significant volumes of $CO_2$ are being sequestered incidental to these $CO_2$-EOR projects, providing a possible path for large scale market-driven carbon capture and storage (CCS). The estimated recoverable oil from ROZs in both the San Andres and Canyon Reef formations of Permian Basin, are estimated by Koperna et al. [5] as 12 billion barrels. This represents a little over a third of the estimated original oil in place. Bachu et al. [6] noted that ROZs are "regarded in the industry as the most optimum part of oil reservoirs to store $CO_2$". They based this on: the typically large volume of ROZs; their high water saturation; and "hydrocarbon availability".

Unfortunately, almost all the research on ROZ formation and characteristics has not been published in refereed journals but rather is available in contract reports, presentations, and conference proceedings. Trentham and his coworkers [7] have assumed that, high aquifer flow rates would have been initially established across the San Andreas formation from the uplift of the Guadalupe Mountains along the western margin of the Permian Basin. This uplift apparently peaked around 20 Ma associated with the formation of the Rio Grande Rift [8]. Subsequent erosion of these mountains would have reduced hydraulic heads in the regional aquifer lowering flow rates. Harouaka et al. [9] suggested that the hydrodynamic impact continued unabated, "albeit at a very slow pace like one foot/1000 years", an assertion they based on "analytical modeling" using the analysis of Hubbert [10]. A recent study by Trentham et al. [7] attempted to model the probable flow pathways, of what they termed "hydrodynamic fairways". However, absent a creation of a set of robust regional groundwater flow models extending back to the regional uplift event in the Permian Basin, the groundwater flow directions cannot be well constrained. Jamali and Ettehadtavakkol [11] modelled the ROZ formation process through mimicking the natural waterflooding process, however, their specific simulation is based on a simplified static reservoir model and physics.

This paper is the first attempt to use multiphase and full-physics flow simulations to make a comprehensive study of the hydrodynamic model for the development of (and the implications of for $CO_2$-EOR) ROZs in the San Andres Formation. In the following, we describe our modeling approach and analyze several factors that are potentially significant in the evolution of ROZs. Finally, we evaluate the significance of these results to both oil production and incidental $CO_2$ sequestration in future $CO_2$-EOR projects in these zones.

## 2. Methodology

This project set out to study the formation of ROZs in the San Andres Formation, based on creating simulations modelling the "natural waterflood" scenario. We create simulations of these reservoirs that aim to explore the nature and spatial patterns of oil saturation in ROZs in response to variations in the flow of regional aquifers. The simulator used is Eclipse-E100 [12], an efficient and multidimensional black-oil simulator.

Our modeling is based on the reservoir characteristics of the residual oil zone associated with the Seminole Field, however, we do not model this field specifically. A three-dimensional (3D) static reservoir model, representative of the geology and petrophysical variation of the ROZ underlying the Seminole Field, was built from the published reservoir property data [13-15]. The model was populated using data from these published sources and from petrophysical measurements made on cores, and interpretation of wireline logs from the BEG log library.

Two 2-D section geologic models were cut from the 3-D reservoir model: one is along the E-W (X-Z slice, the approximate dip direction), and the other is along the N-S (Y-Z slice, the approximate strike direction). The purpose of selecting these two sections is to examine how flow direction affects evolution the oil saturation in the ROZ. The two vertical sections cross along a vertical line. This line overlaps a drilled vertical well with detailed well properties published by Honarpour et al. [15]. Specifically, this well has an oil saturation profile, based on measurements (made prior to $CO_2$ injection into the ROZ) from sponge cores. This data provides an important way for us to validate the reasonableness of our simulations.

The corner point grid system is used, and the dimensions of each model is 63×100. The cell size in the horizontal direction is 100 ft., and the vertical cell size varies in different layers with the average ~2ft. The two 2-D orthogonal models have similar means and standard deviation for the porosity and permeability (Table 1). Published permeability measurements by Honarpour et al. [15] show that the horizontal and vertical permeability's are largely similar. These authors note that the presence of low permeability layers of fine-grained, anhydrite-rich facies, creates a strongly anisotropic permeability. They suggest the resultant vertical component is approximately one tenth of the horizontal component. Initially, hydrostatic pressure is set for the reservoir with the middle depth pressure at 2119.9 psi, and the reservoir temperature is 104 °F. The oil saturation is initialized using the gravity-capillary equilibrium method.

A capillary entry pressure field is generated using the Leverett j-function [16] that links permeability, porosity, and capillary pressure. The reference capillary pressure curve is assigned to the cells with the permeability of 16 mD as this reference curve is measured on the core with this permeability. These cells are considered as reference cells. The other cells in the model are assigned with different capillary pressure curves by scaling the capillary pressure of each cell with the corresponding permeability and porosity. The interfacial tension for each cell is assumed to be the same, and contact angle has the same assumption. So each cell can be assigned with a capillary pressure curve that is consistent with its upscaled permeability and porosity while omitting interfacial tension and contact angle.

Flow simulations are designed to model the key relevant physics for understanding the ROZ origin associated with the San Andreas Formation in the Permian Basin. To understand the relevant physics, we first introduce a gravity number ($N_{gr}$), and this number describes the influence of competitive gravity versus viscous forces on water flooding. $N_{gr}$ is a dimensionless ratio of the gravitational force acting on the fluids to the viscous force that drives water migration.

In the 2D models, the volume of water injected is approximately 27 pore volumes (PV) for the base case (corresponding to the regional water flux of 0.5 ft./yr.). This PV is consistent with the suggestions of Trentham et al., [7] about the time scale and flux of regional natural water flooding impacting the ROZs within the Permian Basin. The sensitivity of the magnitude of oil saturation in the ROZs to varying the magnitude and duration of regional hydraulic head, is also investigated. The regional hydraulic head was varied over three orders of magnitude. Additionally, changes in the nature of ROZs (e.g., oil saturation and geometry) in response to the lowering of hydraulic head are examined. This lowering decreases regional water flow rate, so the study is designed to approximate the decreasing rate of flow through three sequential simulation processes with the decreasing water fluxes from 5ft/yr, 0.5ft/yr to 0.05 ft/yr, with each modeled time period lasting for 50,000 years (refer to case #12 in Table 2). More importantly, both single and heterogeneous capillary pressure are purposely considered in these simulations. Single capillary pressure means that the capillary pressure curve is used for all the cells in the domain, whereas, heterogeneous capillary pressure means that scaled capillary pressure curves are employed.

Table 1 Injection simulation schemes in the 2D models

| Water flux entering formation from wellbore, ft./yr. | Injection rate, rb/d** | Injection duration, Year | Total injected water, PV | $N_{gr}$ along the wellbore | Dominant force |
|---|---|---|---|---|---|
| 5.0 | 183.4 | 50k | 268 | 4.7E+3 | Gravity |
| $0.5^*$ | 18.3* | 50k* | 26.8* | 4.7E+4* | Gravity |
| 0.05 | 1.83 | 50k | 2.7 | 4.7E+5 | Gravity |

*means base case settings; ** rb means reservoir barrel

A vertical injector and a producer are used to mimic regional water filtration in the ROZ, and the two wells are placed on the left and right boundary cells, respectively. Both wells are perforated along the intervals of both the producing ROZ and the water leg, for which, their heights are approximated through the field tests and measurements [15]. Constant water rate is imposed on the injector with the values shown in Table 2, and the same rate of liquid production is imposed on the right producer. Boundary settings in the N-S slice are the same. The condition settings for all the simulated cases are summarized in Table 2.

Table 2 Summary of conditions for simulations. The time duration in parentheses, correspond to the adjacent PV.

| Case No | Water flux, ft/yr | Injected PV | Flow direction | Capillary pressure |
|---|---|---|---|---|
| 1 | 0.5 | 26.8 (50k yrs) | W-E | w/o |
| 2 | 0.5 | 32.1 (60k yrs) | W-E | w/o |
| 3 | 0.5 | 26.8 | W-E | Single |
| 4 | 0.5 | 26.8, 268, 536 (1MM yrs) | W-E | Heterogeneous |
| 5 | 5.0 | 268 | W-E | Single |
| 6 | 5.0 | 268 | W-E | Heterogeneous |
| 7 | 0.05 | 2.7 | W-E | Single |
| 8 | 0.05 | 2.7, 27, 54 (1MM yrs) | W-E | Heterogeneous |
| 10 | 0.5 | 26.8 | N-S | Heterogeneous |

## 3. Results

We firstly describe the evolution of oil saturation fields during the ROZ formation process. Particularly, we emphasize the effect of the interplay between water flux magnitude and capillary pressure on the remaining oil saturation in the ROZ. Next, we compare our simulation results to the down the well measurements of oil saturation in the San Andres Seminole Field.

### *3.1 Effect of the duration of regional aquifer flow on oil saturation in ROZs*

To evaluate the effect of the duration of regional aquifer flow on the nature of ROZ formation, we started with the case that considers no capillary pressure (#1 in Table 2). This case shows a similar oil saturation field as another case that considers single capillary pressure (#3 in Table 2). For the MPZ, the oil saturation is initialized using the gravity-capillary equilibrium, and the initial oil saturation is high and around 0.8. The capillary transition zone in these simulations is very small and almost not observable as shown around the interface between the yellow and blue areas. As water influx proceeds (T=10,000 to 50,000 yrs.), the vertical extent of the ROZ increases. At a timescale of 50,000 years, further changes in the magnitude and spatial distribution of oil saturation values are negligible.

The variation of oil saturation with depth is perhaps the most important feature of ROZs. The intervals with high saturation represent the low permeability/low porosity (<0.05) areas, and this oil cannot be efficiently displaced by water as shown in Fig. 1. To quantify oil saturation vertical profiles, we plot the change of oil saturation along depth at different times (Fig. 2). Overall, the oil saturation profiles attained an approximate or pseudo-steady state after approximately 50,000 years. The attainment of pseudo-steady-state oil saturation is further illustrated in Fig. 3 that shows the evolution cell oil saturation in several selected depths. It appears that, in this simulation, the upper part of the ROZ requires a much longer time to reach this pseudo-steady state (note the light blue line in Fig.3).

Fig. 1. The evolution of oil saturation fields considering single capillary pressure. The water inlet flux is 0.5 ft/yr. X/Z aspect ratio is 5.7.

Fig. 2. The change of oil saturation vertical oil saturation profiles with time. These profiles correspond to the middle column cells (along the well with measured oil saturation in the ROZ) of the oil saturation fields in Fig. 6.

Fig. 3. The change of cell oil saturation with time at several different selected depth points. These points are all in the ROZ: 5370 ft is around the ROZ top, the two depths of 5425 and 5450 ft are in the middle, and 5475 ft is at the bottom.

### *3.2 Effect of the interplay between inlet flux magnitude and capillary pressure*

We first analyze the effect of water flux magnitude (aquifer flow-rate) on ROZs when considering single capillary pressure (left column in Fig. 4). ROZ thickness is sensitive to the magnitude of the upstream water flux in the aquifer. This is because of the competition between the viscous and gravitational forces (the ratio is gravity number $N_{gr}$,): large viscous force (large water flux) suppresses the effect of water gravity on the displacement profile, and a thick ROZ is created. Additionally, the contact between the MPZ (yellow in Fig. 4) and ROZ (light blue) becomes less inclined as water flux decreases; this is obviously because decreasing water flux tends to create hydrostatic distribution of oil/water.

Next, we focus on the imposed upstream water flux of 0.5 ft/yr (the middle row in Fig. 4) and analyse the effect of capillary pressure heterogeneity on the development of ROZs in response to this water flow. When capillary pressure heterogeneity is taken into account, the producing water-oil contact is enlarged (relative to single capillary pressure). In addition, the transition zone (black circled area in the middle row) between the ROZ and the MPZ is distinct, with a thickness of 10-15 ft. The oil saturation in this transition zone varies significantly, from around 0.30 in light green spots to 0.80 in the light yellow patches. However, for the case considering single capillary pressure, the transition zone is thin and poorly defined (refer to the middle left oil saturation field in Fig. 4).

Fig. 4. Oil saturation fields at 50000 yrs of flow simulation. Each row represents different regional water fluxes. The left column considers single capillary pressure, whereas, the right column considers heterogeneous capillary pressure. The dashed lines represent the approximated transition areas between the top of producing ROZ and the base of producing MPZs. X/Z aspect ratio is 5.7.

More importantly, the interplay between capillary pressure heterogeneity and upstream water flux largely influences the thickness of the upper transition zone (the dashed circle area). Through comparing the middle saturation field to the lower one in the right column in Fig. 4, it can be seen that the upper transition zone becomes thick as the upstream water flux decreases. Again, this is because of the lower viscous force, which in turn enhances the effect of capillary dispersion on oil saturation.

The above analyses concentrate on the evolution of oil saturation in ROZs. The time scale of achieving quasi steady-state oil saturation in a ROZ is much less than the geologic time of mountain uplift and erosion (~Ma). Generally, the evolution of oil saturation in a given cell is mainly controlled by both relative permeability curves and imposed pressure gradient (equivalent to inlet water flux). Thus, any changes in both of them would cause different time consumed to achieve steady states.

### *3.3 Effect of regional water flow directions*

The noteworthy issue is the nature of oil-water contacts (dashed blue lines in Fig. 5) for the two different regional water flow directions. The inclination of the contact along the strike direction is smaller than in the dip direction. This observation is consistent with greater lateral sedimentary continuity along the strike.

Fig. 5. Impact of flow direction on oil saturation fields in the ROZ. The oil saturation is at the 50,000 yrs of flow simulation with capillary pressure heterogeneity considered. The black dashed lines circle the oil stripes with large oil saturation in the ROZ, and the blue dashed lines approximate the inclined producing water-oil contacts. The imposed water flux for both oil saturation fields is 0.5 ft/yr. Left: X/Z aspect ratio is 5.7. Right: Y/Z ratio is 7.7.

## 4. Discussion

This study has not attempted to specifically model the Seminole Field, rather, we have modelled the formation of a generic ROZ by starting with an oil-saturated reservoir. Its thickness is equivalent to the sum of current SSAU ROZ and producing MPZ. Our simulations reproduce many of the features reported from San Andreas ROZ reservoirs. The simulation results are consistent with an effectively steady state being reached (at least with respect to oil saturation) on a time scale of 50 thousand years. It is significant that, even after 1MM yrs of regional water flush, the oil saturation in several patches remains similar to the initialized values (0.7~0.8). These patches are local areas of lower porosity and permeability. This observation is consistent with the observed presence of oil stains in the less permeable patches of San Andres core samples.

The influence of capillary pressure heterogeneity on the flow paths of water/oil and thus on the ROZ characteristics, is one of the key discoveries of this study. Heterogeneous capillary pressures are known to be significant for a number of subsurface processes that are characterized by slow flow rates, e.g., buoyant flow of $CO_2$ during geological carbon sequestration [17,18] and secondary hydrocarbon migration/ accumulation [19]. Even for conventional water flooding with flow rates three orders of magnitudes larger than that associated with the hydraulic head gradient and consequent subsurface regional aquifer flow rates preferred in this study, capillary pressure heterogeneity apparently significantly affects oil saturation under some conditions [20, 21].

This study is subject to several limitations. First, the predictions of average oil saturation in the ROZs from our simulations are marginally larger than those measured by Honarpour et al. [15]. One possibility is that, in some cells, the 50,000 years of the flow simulations presented is insufficient to achieve a steady state. This is the consequence of the fractional flow curve for water. The fractional flow of oil is reduced to a very small value (<0.008) when water saturation increases to 0.5. Another complication is the impact of our limited ability to accurately model the heterogeneous nature of the reservoir. The simulations in this study utilized a cell size of 100 ft. × ~2 ft. However, the estimates of porosity and permeability were based on measurements of core plugs with the size of 1~2 inches. Upscaling these detailed measurements to the scale of the simulation grid inevitably averages out the true heterogeneous nature of the reservoir. Additionally, the water-oil-rock interaction might need to be studied to examine its effect on oil properties and reservoir petrophysical properties. Such geochemical reactions have been demonstrated to be important in other similar subsurface flow dynamics [22, 23].

The capacity of ROZs to store $CO_2$ associated with EOR is not well understood. Commercial scale ROZ floods have only been implemented in the last decade and no studies of ROZ reservoirs have been published. Bachu et al. [6] suggested that the oil industry regard ROZs as a superior target for geological carbon storage. They noted that $CO_2$-EOR will provide a mechanism to defray the costs of carbon capture and storage (CCS) projects. The current study can be used as the basis for developing strategies to utilize $CO_2$ injection to optimize oil production and sequestration. For example, heterogeneities in permeability, porosity, and capillary pressures are highly likely to result in three-dimensional spatial heterogeneities in oil saturation. Such patches and layers of higher saturation could be exploited by using multiple horizontal wells. Additionally, the extensive distribution of water in ROZs should have some effects in selecting and optimizing $CO_2$ injection strategies. This extensive water distribution is different from that in MPZ after man-made water flooding since, for MPZ, water saturations are locally high around the water streamlines connecting injectors and producers. This difference would bring different optimized schemes of WAG injection into ROZ reservoirs, including water cycle size and WAG ratio.

## 5. Conclusions and Recommendations

The key characteristic of residual oil zones (ROZs) is the spatial and depth dependant variation of oil saturation. This information is important essential to assess reserves, design $CO_2$-EOR projects, and estimate the sequestration capacity in ROZs. This study has demonstrated that the key features of ROZs can be simulated using a commercial, full-physics, multi-phase flow simulator. The results support the plausibility of the hydrodynamic model suggested by earlier researchers, but do not rule out other models for the origin of ROZs.

The magnitudes of water flux (aquifer flow rate) and capillary pressure within the reservoir influences the variation of oil saturation (both spatially and temporally) and geometry of ROZs. Larger water fluxes result in thicker ROZs, and heterogeneous capillary pressures will lead to development of diffuse water-oil contacts. During the formation of ROZ, the evolving oil saturation is controlled by the relative permeability curves. A very large amount of oil resides in ROZ reservoirs in the San Andres Formation and these reservoirs are attractive targets for $CO_2$ EOR and associated storage. Additionally, the spatial distribution of oil in ROZs are different from that in MPZs undergoing water flooding. This difference will be important in the optimization of $CO_2$ EOR and storage in ROZs.

## Acknowledgements

This study is part of a long term project investigating ROZ reservoirs in the Permian Basin of Texas being carried out by the Bureau of Economic Geology's (BEG's) State of Texas Advanced Resource Recovery (STARR) Program and funded in part by a US Department of Energy contract under DOE Award Number FE0024375 (PI: Duncan). The opinions of the authors do not necessarily reflect those of the United States Government or any agency thereof. The research was also supported by endowed funds from the Jackson School of Geological Sciences at The University of Texas at Austin. Publication authorized by the Director, Bureau of Economic Geology.

## References

[1] Melzer LS. Residual oil zones (ROZ): a review of ROZ science and engineering. In: enhanced oil recovery's tensleep III workshop. University of Wyoming; 2013.

[2] Trentham CR, Melzer LS. Case studies of the ROZ $CO_2$ flood and the combined ROZ/MPZ $CO_2$ flood at the Goldsmith Landreth Unit, Ector County, Texas. DOE Final Report; 2015

[3] Kuuskraa V, Petrusak R, Wallace M. Residual oil zone "fairways" and discovered oil resources: expanding the options for carbon negative storage of $CO_2$. Energy Procedia 2017;114:5438-5450.

[4] Godec ML, Kuuskraa VA, Dipietro P. Opportunities for using anthropogenic $CO_2$ for enhanced oil recovery and $CO_2$ storage. Energ Fuel 2013; 27(8):4183-4189.

[5] Koperna GJ, Melzer LS, Kuuskraa VA. Recovery of oil resources from the residual and transitional oil zones of the Permian Basin. SPE 102972 presented at the Annual Technical Conference and Exhibition, San Antonio, Texas, 24-27 September 2006.

[6] Bachu S, Pires P, Li MY, Guzman F, Eide LI, Aleidan A, Ackiewicz M, Melzer LS. Technical challenges in the conversion of $CO_2$-EOR projects to $CO_2$ storage projects, Report Prepared by the CSLF Task Force on Technical Challenges in the Transition from $CO_2$ EOR to CCS, http://www.cslforum.org/publications/documents/CO2- EORtoCCS_FinalReport.pdf, 2013.

[7] Trentham CR, Melzer LS, Vance DB. Commercial exploitation and the origin of residual oil zones: Developing a case history in the Permian Basin of New Mexico and West Texas. RPSEA Final Report; 2012.

[8] Horak RL. Tectonic and hydrocarbon maturation history in the Permian Basin: Oil Gas J 1985;83(21):124–129.

[9] Harouaka A, Trentham B, Melzer LS. Long overlooked residual oil zones (ROZ's) are brought to the limelight. SPE-167209 presented at the SPE Unconventional Resources Conference, Calgary, Canada, 5-7 November 2013.

[10] Hubbert MK. "Entrapment of petroleum under hydrodynamic conditions," AAPG Bulletin 1953;37(8):1954-2028.

[11] Jamali A, Ettehadtavakkol A. $CO_2$ storage in residual oil zones: Field-scale modeling and assessment. Int J Greenh Gas Con 2017;56:102-115.

[12] Eclipse-E100, 2016. Eclipse Users' Manual. Schlumberger, France.

[13] Wang F, Lucia F, Kerans C. Integrated reservoir characterization study of a carbonate ramp reservoir: Seminole San Andres Unit, Gaines County, Texas. SPE Reserv Eval Eng 1998;1(02):105–113.

[14] Lucia FJ. Carbonate reservoir characterization: An integrated approach, Springer Science & Business Media. Berlin, Germany; 2007

[15] Honarpour MM, Nagarajan NR, Grijalba CA, Valle M, Adesoye K. Rock-fluid characterization for miscible $CO_2$ injection: Residual oil zone, Seminole Field, Permian Basin. SPE-133089 presented at the Annual Technical Conference and Exhibition, Florence, Italy, 19-22 September 2010.

[16] Leverett MC. Capillary behavior in porous solids. AIME Petroleum Transactions 1941;142:152-169.

[17] Saadatpoor E, Bryant SL, Sepehrnoori K. New trapping mechanism in carbon sequestration. Transport In Porous Media 2009; 82(1):3-17.

[18] Trevisan L, Krishnamurthy PG, Meckel TA. Impact of 3D capillary heterogeneity and bedform architecture at the sub-meter scale on $CO_2$ saturation for buoyant flow in clastic aquifers. Int J Greenh Gas Con 2017;56:237-249.

[19] Carruthers DJF. Transport modelling of secondary oil migration using gradient-driven invasion percolation techniques. Ph.D. Dissertation, Heriot-Watt University, Edinburgh, UK; 1998

[20] Chang J, Yortsos YC. Effect of capillary heterogeneity on Buckley-Leverett displacement. SPE Reserv Eng 1992;7(2):285-293.

[21] Lasseter TJ, Waggoner JR, Lake LW. Reservoir heterogeneities and their influence on ultimate recovery, in: Lake, L.W., Carroll, B.C. (Eds.), Reservoir Characterization. Amsterdam: Elsevier Inc., 1986. p. 545-559.

[22] Luhmann AJ, Tutolo BM, Tan C, Moskowitz BM, Saar MO, Seyfried WE. Whole rock basalt alteration from CO2-rich brine during flow-through experiments at 150°C and 150bar. Chem Geol 2017;453:92-110.

[23] Cui G, Zhang L, Tan C, Ren S, Zhuang Y, Enechukwu C. Injection of supercritical $CO_2$ for geothermal exploitation from sandstone and carbonate reservoirs: $CO_2$–water–rock interactions and their effects. J $CO_2$ Util 2017;20:113-128.